



City Research Online

City, University of London Institutional Repository

Citation: El-Shawish, J. M. (2004). Investigation of variable transformers by finite element modelling. (Unpublished Doctoral thesis, City, University of London)

This is the accepted version of the paper.

This version of the publication may differ from the final published version.

Permanent repository link: <https://openaccess.city.ac.uk/id/eprint/30410/>

Link to published version:

Copyright: City Research Online aims to make research outputs of City, University of London available to a wider audience. Copyright and Moral Rights remain with the author(s) and/or copyright holders. URLs from City Research Online may be freely distributed and linked to.

Reuse: Copies of full items can be used for personal research or study, educational, or not-for-profit purposes without prior permission or charge. Provided that the authors, title and full bibliographic details are credited, a hyperlink and/or URL is given for the original metadata page and the content is not changed in any way.



City University
London

School of Engineering and Mathematical Sciences

Investigation of Variable Transformers by Finite Element Modelling

by

Jamal M. El-Shawish

A thesis submitted in partial fulfilment of the
requirements for the degree of

Doctor of Philosophy in Electrical Engineering

Computer Aided Modelling and Design
Department of Electrical, Electronic and Information Engineering
Northampton square, London EC1V 0HB, UK

July 2004

Table of Contents

List of Tables	iv
List of Figures	v
Symbols and Abbreviations	xiv
Acknowledgements	xvi
Declaration	xvii
Abstract	1
Chapter 1. Introduction and Background	3
1.1. Introduction	3
1.2. Review of Previous Work on the topic	4
1.3. The Need for Design Methodologies for Variable Transformers	5
1.4. Aims and Objectives of the Work	7
1.5. Structure of the Thesis	8
1.6. The Basic Principle of an Autotransformer	9
1.6.1. Principle of a variable transformer	13
1.6.2. Operation of a Variable Transformer	16
1.7. The Basic Construction Features and Physical Processes in Variable Transformers	19
1.7.1. The magnetic circuit	19
1.7.2. The winding	20
1.7.3. The brushes and commutation	22
Chapter 2. Finite Element Modelling of Variable Transformers	24
2.1. Introduction	24
2.2. Mathematical Formulation of 3D Magnetic Field Distribution in Variable Transformers	25
2.2.1. Basic equations	25
2.2.2. Fields in non-conducting media	26

2.2.3.	Field in conducting media	29
2.2.4.	“Cuts” in total and vector potential regions	31
2.3.	The finite element method (FEM) and its basic procedures	32
2.4.	Assumptions	33
2.5.	Boundary Conditions	34
2.6.	Estimation of Errors in Finite Element Modelling	35
Chapter 3. Realisation of 3D Finite Element Models of Commercial Variable Transformers		37
3.1.	Introduction	37
3.2.	Development of basic finite element model of single-phase commercial variable transformer	43
3.2.1.	Finite Element Model Definition	44
3.3.	Definition of conductors	56
Chapter 4. Experimental Investigation of Magnetic Fields in Variable Transformers and Validation of Finite Element models		66
4.1.	Introduction	66
4.2.	Experimental Models for Investigations	68
4.2.1.	Experimental apparatus	68
4.2.2.	The experimental models	72
4.3.	Results of Flux Density Measurements	79
4.3.1.	Results for Model 1:	79
4.3.2.	Results for model 2:	87
4.3.3.	Results for Model 3:	94
4.4.	Validation of Finite Element Models	96
4.4.1.	Comparison of modelling Results with Experimental Data for Model 1.	96
4.4.2.	Comparison of modelling Results with Experimental Data for Model 2.	104
4.4.3.	Comparison of modelling Results with Experimental Data for Model 3.	108

Chapter 5. Investigation of Commercial Variable Transformers by Finite Element Modelling	114
5.1. Introduction	114
5.2. Investigation of the core for various Design Parameters	114
5.2.1. Calculation of winding parameters	117
5.2.2. Variation of outer diameter of the core	120
5.2.3. Effects of design parameters on field distribution in the core	121
5.2.4. Effects of brush and tap positions	128
5.2.5. Effects of core saturation on the top plate	137
5.3. Study of the Effects of Higher Harmonics	141
Chapter 6. Conclusions	147
6.1. Work done	147
6.2. Future work	149
References	150
Appendix 1: Technical Features and Specifications of the Instruments used in Experimental Measurements	157
Appendix 2: Command input files used in FE Modelling	164
Appendix 3: Calculations of winding resistance (R) for various conductor sizes	181
Appendix 4: Main geometric and parameters of one of the designs of type TS1225 variable transformer.	183
Appendix 5: Experimental Measurements of Flux Density	184
Appendix 6: Experimental and Simulation flux density Measurements used for FE Modelling Validation	216
Publications	237

List of Tables

- Table 3.1 Types of normal and tangential boundary conditions used by the software.
- Table 3.2 Various coordinate system, and geometric parameters used to define a general racetrack conductor.
- Table 4.1 Current distribution in transformer for experimental case-1.
- Table 4.2 Current distribution in the transformer for experimental case-2.
- Table 4.3 The sensor positions (in mm) for magnetic field measurements surrounding the toroidal core (Fig. 4.9).
- Table 4.4 The sensor positions (in mm) for magnetic field measurements above the toroidal core (Fig. 4.9 and Fig. 4.13).
- Table 5.1 combination of core parameters used for various cases of modelling investigation; L_w – total winding length, R_w – winding resistance.
- Table 5.2 Conductor parameters for first layer of winding turns for reduced core dimensions w and h .
- Table 5.3 Conductor parameters for second layer of winding turns for reduced core dimensions w and h .
- Table 5.4 Maximum Eddy-current, J_{\max} (A/mm^2) at various sections through the top plate thickness and due different frequencies.

List of Figures

- Fig. 1.1 Basic arrangement of an autotransformer
- Fig. 1.2 Typical two-winding single phase conventional transformer: (a) core and electrically isolated windings, (b) simplified schematic of the electrical circuit.
- Fig. 1.3 Phase diagram of transformer on no-load
- Fig. 1.4 Primary and secondary windings of conventional transformer connected in series.
- Fig. 1.5 Circuit diagram of fixed tap autotransformer (a) core and electrically connected windings, (b).simplified schematic of the electrical circuit.
- Fig. 1.6 Circuit of basic variable transformer
- Fig. 1.7 Constant copper-loss current versus output voltage ('a' represent any number between zero and unity).
- Fig. 1.8 Autotransformer step-up connections
- Fig. 1.9 Load current versus ratio of input to output voltage (a represent any number between zero and unity).
- Fig. 1.10 Output current versus transformation ratio.
- Fig. 1.11 commutation in variable transformers: (a) one turn is short-circuited (bridged) by the brush, (b) equivalent circuit of the brush arrangement.
- Fig. 2.1 Schematic diagram shows the cut in total potential region.
- Fig. 2.2 Longitudinal view of the FE model showing the boundary condition.
- Fig. 3.1 Typical commercial variable transformers investigated: (a) transformer type TS1225; (b) it's simplified longitudinal section showing main constructive elements (not drawn to scale).
- Fig. 3.2 Magnetization curve of Unisil 30M5 grain-oriented silicon steel used in TS 1225 transformer core.
- Fig. 3.3 Schematic diagram of the TS1225 transformer showing some of the main geometric parameters (dimension in mm, not drawn to scale)
- Fig. 3.4 Schematic diagram of the top plate: (a) bottom view and (b) longitudinal section through A-A; (dimensions in mm, not drawn to scale).
- Fig. 3.5 Schematic diagram of the toroidal core: (a) top view, (b) longitudinal section through A-A (dimensions in mm, not drawn to scale)
- Fig. 3.6 Shematic diagram of the base plate: (a) top view and (b) longitudinal section through A-A, (dimensions in mm and not drawn to scale).

- Fig. 3.7 Definition of construction lines outlining all major geometric features on the base plane.
- Fig. 3.8 Use of construction lines to define points giving the geometric features of the transformer.
- Fig. 3.9 Definition of 2D surfaces (facets) on the base plane by connecting predefined points.
- Fig. 3.10 Subdivision of facets on the base plane.
- Fig. 3.11 2D wire-frame representation of the extruded 3D finite element model of the variable transformer TS 1225, showing the main constructive features.
- Fig. 3.12 Schematic diagram of the transformer (a); part of the cross-section A-A (b) and part of the cross-section B-B (c).
- Fig. 3.13 Top view of the FE model showing mesh subdivision.
- Fig. 3.14 The 3D model is obtained by extrusion of the base plane in the third, Z direction by moving points on mesh planes and transforming sets of points on mesh planes (winding not shown).
- Fig. 3.15 The actual boundary conditions used for the 3D model.
- Fig. 3.16 Global and local coordinate systems used for definition of conductors.
- Fig. 3.17 Wire frame representation of the generally oriented racetrack conductor showing the local and global coordinate systems and defining conductor geometric parameters.
- Fig. 3.18 Schematic diagram showing the positions of odd turns from 15 to 309; total number of turns 148 (not drawn to scale).
- Fig. 3.19 Schematic diagram showing the positions of even turns from 16 to 310; total number of turns 148 (not drawn to scale).
- Fig. 3.20 Schematic diagram showing the generation of single-turn coils on the toroidal core; (a) odd turns, (b) odd and even turns, (c) longitudinal section through A-A showing the over-lapping of turns, (d) 3D view of the overlapping turns (dimensions in mm not drawn to scale).
- Fig. 3.21 Top view of the 3D FE model of the variable transformer showing half of the conductor turns.
- Fig. 3.22 Top view of the 3D FE model of the variable transformer showing all the conductor turns.
- Fig. 3.23 Full 3D FE model of the commercial variable transformer type TS1225 used for modelling investigations.
- Fig. 4.1 Simplified diagram of the experimental apparatus (made of non-magnetic material) used for experimental investigation of variable transformers (not drawn to scale).

- Fig. 4.2 Top view of the transformer core (without top plate) placed concentrically on the experimental apparatus: (a) without Gauss-meter, (b) with Gauss-meter.
- Fig. 4.3 Arrangement of experimental apparatus for the measurement of magnetic field above the toroidal core of the transformer: (a) schematic diagram, (b) photograph showing the actual transformer used (brush gear not shown).
- Fig. 4.4 Arrangement of experimental apparatus for the measurement of magnetic field around the toroidal core of the transformer: (a) schematic diagram, (b) photograph showing the actual transformer used (brush gear not shown).
- Fig. 4.5 Schematic diagram of the transformer for various models: (a) without top and bottom plates for various tap and brush positions. (b) taps T₁ at turn no. 1, T₅ at turn no. 296 and brush position T₃ (T_b) at turn no. 149 (Models 1, 2 case 1); (c) taps T₁, T₄ and T₅ – at turns 1, 257 and 296 respectively, and brush positions T_{b1}, T_{b2} and T_{b3} – at turns 100, 154 and 207 respectively (Model 3 case 2).
- Fig. 4.6 Schematic diagram showing various tap and brush positions on the winding for experimental cases 1 (a) and 2 (b).
- Fig. 4.7 Full circuit diagram for experimental investigation of autotransformer (experimental case 1).
- Fig. 4.8 Full circuit diagram for experimental investigation of autotransformer (experimental case 2).
- Fig. 4.9 Schematic diagram showing sensor positions in r , θ , z for experimental Model 1.
- Fig. 4.10 Schematic diagram showing dimensions along r (mm) direction (not drawn to scale).
- Fig. 4.11 Schematic diagram showing dimensions along z direction.
- Fig. 4.12 Schematic diagram of the transformer for Model 2 (a) with top plate, (b) taps T₁ at turn no. 1, T₅ at turn no. 296 and T₃ at turn no. 148 (brush position T_b).
- Fig. 4.13 Schematic diagram showing sensor positions in r , θ , z for experimental Model 2.
- Fig. 4.14 No load v - i characteristics of TS1225 autotransformer for tap positions corresponding to experimental cases 1 (graph 1) and 2 (graph 2).
- Fig. 4.15 Variation of the vertical component of flux density B_z above the toroidal core with r , θ and z in the absence of the top plate: $r = r_1 = 35$ mm, $z = 91$ (z₄), 103 (z₅), 117 (z₆), 230 (z₉) mm, $\theta = 0 - 360^\circ$ (Fig. 4.9)
- Fig. 4.16 Variation of the vertical component of flux density B_z above the toroidal core with r , θ and z in the absence of the top plate: $r = r_3 =$

- 110 mm, $z = 91$ (z_4), 103 (z_5), 117 (z_6), 230 (z_9) mm, $\theta = 0 - 360^\circ$ (Fig. 4.9).
- Fig. 4.17 Variation of the vertical component of flux density B_z above the toroidal core with r , θ and z in the absence of the top plate: $r = r_7 = 140$ mm, $z = 91$ (z_4), 103 (z_5), 117 (z_6), 230 (z_9) mm, $\theta = 0 - 360^\circ$ (Fig. 4.9).
- Fig. 4.18 Variation of the vertical component of flux density B_z above the toroidal core with r , θ and z in the absence of the top plate: $z = z_4 = 91$ mm, $r = 35$ (r_1), 110 (r_3), 140 (r_7) mm, $\theta = 0 - 360^\circ$ (Fig. 4.9).
- Fig. 4.19 Variation of flux density B surrounding the toroidal core with r , θ and z in the absence of the top plate: $z = z_1 = 13$ mm, $r = 134$ (r_6), 140 (r_7), 150 (r_8), 170 (r_9) mm, $\theta = 0 - 360^\circ$ (Fig. 4.9).
- Fig. 4.20 Variation of flux density B surrounding the toroidal core with r , θ and z in the absence of the top plate: $z = z_2 = 41$ mm, $r = 134$ (r_6), 140 (r_7), 150 (r_8), 170 (r_9) mm, $\theta = 0 - 360^\circ$ (Fig. 4.9).
- Fig. 4.21 Variation of flux density B surrounding the toroidal core with r , θ and z in the absence of the top plate: $z = z_3 = 70$ mm, $r = 134$ (r_6), 140 (r_7), 150 (r_8), 170 (r_9) mm, $\theta = 0 - 360^\circ$ (Fig. 4.9).
- Fig. 4.22 Variation of the vertical component of flux density B_z above the toroidal core with r , θ and z in the presence of the top plate: $r = r_1 = 35$ mm, $z = 117$ (z_6), 170 (z_7), 200 (z_8), 230 (z_9) mm, $\theta = 0 - 360^\circ$ (Fig. 4.13).
- Fig. 4.23 Variation of the vertical component of flux density B_z above the toroidal core with r , θ and z in the presence of the top plate: $r = r_3 = 110$ mm, $z = 117$ (z_6), 170 (z_7), 200 (z_8), 230 (z_9) mm, $\theta = 0 - 360^\circ$ (Fig. 4.13).
- Fig. 4.24 Variation of the vertical component of flux density B_z above the toroidal core with r , θ and z in the presence of the top plate: $r = r_7 = 140$ mm, $z = 117$ (z_6), 170 (z_7), 200 (z_8), 230 (z_9) mm, $\theta = 0 - 360^\circ$ (Fig. 4.13).
- Fig. 4.25 Variation of the flux density B surrounding the toroidal core with r , θ and z in the presence of the top plate: $z = z_1 = 13$ mm, $r = 134$ (r_6), 140 (r_7), 150 (r_8), 170 (r_9) mm, $\theta = 0 - 360^\circ$ (Fig. 4.13)
- Fig. 4.26 Variation of the vertical of flux density B surrounding the toroidal core with r , θ and z in the presence of the top plate: $z = z_2 = 41$ mm, $r = 134$ (r_6), 140 (r_7), 150 (r_8), 170 (r_9) mm, $\theta = 0 - 360^\circ$ (Fig. 4.13).
- Fig. 4.27 Variation of the vertical of flux density B surrounding the toroidal core with r , θ and z in the presence of the top plate: $z = z_3 = 70$ mm, $r = 134$ (r_6), 140 (r_7), 150 (r_8), 170 (r_9) mm, $\theta = 0 - 360^\circ$ (Fig. 4.13)
- Fig. 4.28 Variation of circumferential magnetic field B surrounding the toroidal core with r , θ and z in the presence of the top plate: $z = z_2 = 41$ mm, $r = 134$ (r_6), 140 (r_7), 150 (r_8), 170 (r_9) mm, $\theta = 0 - 360^\circ$ (Fig. 4.13).

- Fig. 4.29 Variation of flux density B surrounding the toroidal core with r , θ , z and brush positions in the absence of the top plate: $z = z_2 = 41$ mm, $r = 134$ (r_6) mm, $\theta = 0 - 360^\circ$, brush positions T_{b1} , T_{b2} and T_{b3} are at turn 100, 154 and 207 respectively.
- Fig. 4.30 Variation of flux density Bz above the toroidal core with r , θ , z and brush positions in the absence of the top plate: $z = 84$ mm, $r = 87$ (r_2) mm, $\theta = 0 - 360^\circ$, brush positions T_{b1} , T_{b2} and T_{b3} are at turn 100, 154 and 207 respectively.
- Fig. 4.31 TS1225 toroidal core (in the absence of top and bottom plate shown Schematically)
- Fig. 4.32 Validation of FE modelling comparison of vertical component of flux density values (Bz) obtained from modelling with corresponding to experimental data, measured in air above the toroidal core (in the absence of top and bottom plate shown schematically in Fig. 4.31); $z = z_4 = 91$ mm, (a) $r = r_2 = 87$ mm, (b) $r = r_3 = 110$ mm and (c) $r = r_5 = 130$ mm; other parameters: $I_1 = 12$ A, $I_2 = 12$ A; total number of turns $N=296$; taps T_1 at turn number 1; T_5 at turn number 296 and T_3 the brush position (T_b) at turn number 148 ($\theta \cong 180^\circ$).
- Fig. 4.33 Validation of FE modelling comparison of vertical component of flux density values (Bz) obtained from modelling with corresponding to experimental data, measured in air above the toroidal core (in the absence of top and bottom plate shown schematically in Fig. 4.31); $z = z_6 = 117$ mm, (a) $r = r_2 = 87$ mm, (b) $r = r_3 = 110$ mm and (c) $r = r_5 = 130$ mm; other parameters: $I_1 = 12$ A, $I_2 = 12$ A; total number of turns $N=296$; taps T_1 at turn number 1; T_5 at turn number 296 and T_3 the brush position (T_b) at turn number 148 ($\theta \cong 180^\circ$).
- Fig. 4.34 Validation of FE modelling comparison of vertical component of flux density values B obtained from modelling with corresponding to experimental data, measured in air around the toroidal core (in the absence of top and bottom plate shown schematically in Fig. 4.31); $r = r_6 = 150$ mm, (a) $z = z_1 = 13$ mm, (b) $z = z_2 = 41$ mm and (c) $z = z_3 = 70$ mm; other parameters: $I_1 = 12$ A, $I_2 = 12$ A; total number of turns $N=296$; taps T_1 at turn number 1; T_5 at turn number 296 and T_3 the brush position (T_b) at turn number 148 ($\theta \cong 180^\circ$).
- Fig. 4.35 TS1225 toroidal core (in the presence of top plate and absence of bottom plate shown Schematically)
- Fig. 4.36 Validation of FE modelling comparison of vertical component of flux density values (Bz) obtained from modelling with corresponding to experimental data, measured in air above the toroidal core (in the presence of top plate and absence of bottom plate shown schematically in Fig. 4.35); $z = z_6 = 117$ mm, (a) $r = r_2 = 87$ mm, (b) $r = r_3 = 110$ mm and (c) $r = r_5 = 130$ mm; other parameters: $I_1 = 12$ A, $I_2 = 12$ A; total number of turns $N=296$; taps

T_1 at turn number 1; T_5 at turn number 296 and T_3 the brush position (T_b) at turn number 148 ($\theta \cong 180^\circ$).

- Fig. 4.37 Validation of FE modelling comparison of vertical component of flux density values B obtained from modelling with corresponding to experimental data, measured in air around the toroidal core (in the presence of top and absence of bottom plate shown schematically in Fig. 4.35); $r = r_6 = 150\text{mm}$, (a) $z = z_1 = 13\text{mm}$, and (b) $z = z_3 = 70\text{mm}$; other parameters: $I_1 = 12\text{A}$, $I_2 = 12\text{A}$; total number of turns $N=296$; taps T_1 at turn number 1; T_5 at turn number 296 and T_3 the brush position (T_b) at turn number 148 ($\theta \cong 180^\circ$).
- Fig. 4.38 Validation of FE modelling comparison of vertical component of flux density values (Bz) obtained from modelling with corresponding to experimental data, measured in air above the toroidal core (in the absence of top and bottom plate shown schematically in (b)); $z = z_4 = 91\text{mm}$, $r = r_2 = 87\text{mm}$; other parameters: $I_1 = 15.9\text{A}$, $I_2 = 9.1\text{A}$; total number of turns $N=257$; taps T_1 at turn number 1; T_4 at turn number 257 and T_3 the brush position (T_{b1}) at turn number 100.
- Fig. 4.39 Validation of FE modelling comparison of vertical component of flux density values (Bz) obtained from modelling with corresponding to experimental data, measured in air above the toroidal core (in the absence of top and bottom plate shown schematically in (b)); $z = z_4 = 91\text{mm}$, $r = r_2 = 87\text{mm}$; other parameters: $I_1 = 9.5\text{A}$, $I_2 = 15.5\text{A}$; total number of turns $N=257$; taps T_1 at turn number 1; T_4 at turn number 257 and T_3 the brush position (T_{b2}) at turn number 154.
- Fig. 4.40 Validation of FE modelling comparison of vertical component of flux density values (Bz) obtained from modelling with corresponding to experimental data, measured in air above the toroidal core (in the absence of top and bottom plate shown schematically in (b)); $z = z_4 = 91\text{mm}$, $r = r_2 = 87\text{mm}$; other parameters: $I_1 = 4.7\text{A}$, $I_2 = 20.3\text{A}$; total number of turns $N=257$; taps T_1 at turn number 1; T_4 at turn number 257 and T_3 the brush position (T_{b3}) at turn number 207.
- Fig. 4.41 Validation of FE modelling comparison of vertical component of flux density values B obtained from modelling with corresponding to experimental data, measured in air around the toroidal core (in the absence of top and bottom plate shown schematically in (b)); $r = r_6 = 150\text{mm}$, $z = z_2 = 41\text{mm}$; other parameters: $I_1 = 15.9\text{A}$, $I_2 = 9.1\text{A}$; total number of turns $N=257$; taps T_1 at turn number 1; T_4 at turn number 257 and T_3 the brush position (T_{b1}) at turn number 100.
- Fig. 4.42 Validation of FE modelling: comparison of vertical component of flux density values B obtained from modelling with corresponding to experimental data, measured in air around the toroidal core (in the absence of top and bottom plate shown schematically in (b)); $r = r_6 = 150\text{mm}$, $z = z_2 = 41\text{mm}$; other parameters: $I_1 = 9.5\text{A}$, $I_2 =$

15.5A; total number of turns $N=257$; taps T_1 at turn number 1; T_4 at turn number 257 and T_3 the brush position (T_{b2}) at turn number 154.

- Fig. 4.43 Validation of FE modelling: comparison of vertical component of flux density values (B_z) obtained from modelling with corresponding to experimental data, measured in air around the toroidal core (in the absence of top and bottom plate shown schematically in (b); $z = z_4 = 91\text{mm}$, $r = r_2 = 87\text{mm}$; other parameters: $I_1 = 4.7\text{A}$, $I_2 = 20.3\text{A}$; total number of turns $N=257$; taps T_1 at turn number 1; T_4 at turn number 257 and T_3 the brush position (T_{b3}) at turn number 207.
- Fig. 5.1 Longitudinal section of the toroidal core showing the main geometric parameters investigated.
- Fig. 5.2 Longitudinal section of the core showing its original geometric dimensions (in mm) for one of the variable transformers investigated (not drawn to scale); area of the core $A_c = 2451 \text{ mm}^2$.
- Fig. 5.3 Transformer core showing various geometric dimensions (in mm) including the variable height h reduced by 25% (not drawn to scale); $A_c = 1838.25 \text{ mm}^2$.
- Fig. 5.4 Transformer core showing various geometric dimensions (in mm) including the variable width w reduced by 25% (not drawn to scale); $A_c = 1838.25 \text{ mm}^2$.
- Fig. 5.5 Transformer core showing various geometric dimensions (in mm) including the variable height h and width w both reduced by 25% (not drawn to scale); $A_c = 1378.7 \text{ mm}^2$.
- Fig. 5.6 Schematic diagrams of conductor turns showing the original dimensions (in mm): (a) smaller odd turn T_1 , (b) large overlapping even turn T_2 ; not drawn to scale.
- Fig. 5.7 Schematic of the toroidal core the outer diameter D_o of which is increased by increasing the inner diameter by w (not drawn to scale).
- Fig. 5.8 single layer winding turns (no overlapping) wound around large diameter transformer core.
- Fig. 5.9 Schematic diagram of the core showing circular contours one close to inner radius r_1 and the other to outer radius r_2 along which flux density values were calculated for comparing modelling results.
- Fig. 5.10 Variation of magnitude and distribution of flux density, B in the toroidal core (b) for various changes in geometric parameters h and w . The graphs show the distribution of B along a circular contour r_1 (shown in Fig. 5.9) for brush (T_b) and tap position (T_1 , T_4) shown in (a).
- Fig. 5.11 Variation of magnitude and distribution of flux density, B in the toroidal core (b) for changes in geometric parameters D_i and D_o . The graphs show the distribution of B along two circular contours

r_1 and r_2 (shown in Fig. 5.9) for brush (T_b) and tap position (T_1, T_4) shown in (a).

- Fig. 5.12 Contour plot of flux density B distribution in large core $R_i = 130\text{mm}$ i.e. no winding overlap and the brush track is on the inner surface of the toroidal core ($B_{\max} = 0.439\text{ T}$).
- Fig. 5.13 Variation of magnitude and distribution of flux density, B in the toroidal core (b) for various changes in geometric parameters h and w . The graphs show the distribution of B along a circular contour r_1 (shown in Fig. 5.9) for brush (T_b) and tap position (T_1, T_4) shown in (a).
- Fig. 5.14 Variation of magnitude and distribution of flux density, B in the toroidal core (b) for various changes in geometric parameters h and w . The graphs show the distribution of B along a circular contour r_1 (shown in Fig. 5.9) for brush (T_b) and tap position (T_1, T_4) shown in (a).
- Fig. 5.15 Effects of operational regime 1 determined by brush (T_b) and tap positions (T_1, T_4) shown in (a) on saturation level and distribution of core flux density (B) in one of the designs of commercial voltage stabilisers investigated. Total number of turns $N = 288$, maximum flux density 0.5T .
- Fig. 5.16 Effects of operational regime 2 determined by brush (T_b) and tap positions (T_1, T_4) shown in (a) on saturation level and distribution of core flux density (B) in one of the designs of commercial voltage stabilisers investigated. Total number of turns $N = 257$, maximum flux density 1.3T
- Fig. 5.17 Effects of operational regime 3 determined by brush (T_b) and tap positions (T_1, T_4) shown in (a) on saturation level and distribution of core flux density (B) in one of the designs of commercial voltage stabilisers investigated. Total number of turns $N = 288$, maximum flux density 0.22T .
- Fig. 5.18 Effects of operational regime 4 determined by brush (T_b) and tap positions (T_1, T_4) shown in (a) on saturation level and distribution of core flux density (B) in one of the designs of commercial voltage stabilisers investigated. Total number of turns $N = 257$, maximum flux density 1.5T .
- Fig. 5.19 Effects of operational regime 5 determined by brush (T_b) and tap positions (T_1, T_4) shown in (a) on saturation level and distribution of core flux density (B) in one of the designs of commercial voltage stabilisers investigated. Total number of turns $N = 285$, maximum flux density 0.9T .
- Fig. 5.20 Effects of operational regime 6 determined by brush (T_b) and tap positions (T_1, T_4) shown in (a) on saturation level and distribution of core flux density (B) in one of the designs of commercial voltage stabilisers investigated. Total number of turns $N = 257$, maximum flux density 0.4T .

- Fig. 5.21 Effects of operational regimes determined by brush (T_b) and tap positions (T_1, T_4 at turn 257, etc.) shown in (a) and (c) on the saturation level and distribution of core flux density in the TS 1225 variable transformer. The graphs in (b) and (d) show flux densities along three circular contours inside the core (near the inner (1) and outer (3) radii and in the middle (2) of the core) on xy-plane (z at the mid height of the core).
- Fig. 5.22 Effects of core saturation and eddy currents in the top plate on the magnitude and distribution of magnetic field in air above the core (30 mm above the core) in the presence (a) and absence (b) of the top plate. Total number of turns $N = 296$ and brush position at turn 148 ($\theta = 180^\circ$)
- Fig. 5.23 Effects of core saturation and brush position on the magnitude and distribution of magnetic field in air above the core (5 mm above the core) in the absence of the top plate: (a) Brush position at turn 100 ($T_{b1}, \theta = 135^\circ$). (b) Brush position at turn 207 $T_{b3}, \theta = 240^\circ$. Total number of turns $N = 296$.
- Fig. 5.24 Effects of core saturation and eddy currents in the top plate on magnetic field distribution in air above the core: (a) with top plate, $N=296$, brush position at $\theta=180^\circ$, (b) without top plate, $N=258$, brush position at $\theta=240^\circ$. The graphs show flux densities along three circular contours (with radius $r = 40$ (1), 80 (2), and 110 (3) mm) on xy-plane above the core ($z = 65.5$ mm).
- Fig. 5.25 Schematic diagram of part of the top plate showing various sections through the plate thickness used for calculating eddy currents (J).
- Fig. 5.26 Distribution of eddy current on the bottom surface of the top plate ($J_{\max} = 29 \text{ A/mm}^2, f = 50 \text{ Hz}$).
- Fig. 5.27 Distribution of eddy current on the section through 0.5 mm from bottom surface of the plate ($J_{\max} = 18 \text{ A/mm}^2, f = 50 \text{ Hz}$).
- Fig. 5.28 Distribution of eddy current on the section through 1.0 mm from bottom surface of the plate ($J_{\max} = 8.4 \text{ A/mm}^2, f = 50 \text{ Hz}$).
- Fig. 5.29 Distribution of eddy current on the section through 2.5 mm from bottom surface of the plate ($J_{\max} = 15.7 \text{ A/mm}^2, f = 50 \text{ Hz}$).
- Fig. 5.30 Colour contour of current density at bottom surface of the top plate ($J_{\max} = 29 \text{ A/mm}^2$ at $f = 50 \text{ Hz}$).
- Fig. 5.31 Colour contour of current density at top surface of the top plate $J_{\max} = 19 \text{ A/mm}^2$ at $f = 50 \text{ Hz}$
- Fig. 5.32 Colour contour of current density at bottom surface of the top plate $J_{\max} = 47 \text{ A/mm}^2$ at $f = 350 \text{ Hz}$.
- Fig. 5.33 Colour contour of current density at top surface of the top plate $J_{\max} = 33 \text{ A/mm}^2$ at $f = 350 \text{ Hz}$

Symbols and Abbreviations

Unless otherwise stated in this text, the general symbols used in this thesis have the following meanings;

- V_P Primary voltage of a typical two-winding single phase conventional transformer.
- V_S Secondary voltage of a typical two-winding single phase conventional transformer.
- I_P Primary current of a typical two-winding single phase conventional transformer.
- I_S Secondary current of a typical two-winding single phase conventional transformer.
- N_P Number of turns in primary winding of a typical two-winding single phase conventional transformer.
- N_S Number of turns in secondary winding of a typical two-winding single phase conventional transformer.
- r.m.s* Root mean square value.
- R Resistance [Ω].
- H Magnetic field [henry]
- Φ Magnetic flux [wb]
- B Magnetic flux density [T].
- V r.m.s. voltage to the winding [V].
- A_c Cross section area of the core [m^2].
- f Frequency of V [Hz].
- N Number of winding turns to which V is applied.
- I_o No-load current in a typical single phase conventional transformer (also referred to as the magnetising current, I_μ)
- $I_{o\mu}$ A reactive or magnetising component of I_o , producing the flux Φ and thereby in phase with it.
- I_{oa} An active component of I_o , (in phase with the applied primary voltage.

K	Coefficient of transformation (transformer ratio, ratio of the number of turns).
F_p	Primary magnetic motive force (m.m.f).
F_s	Secondary magnetic motive force (m.m.f).
P_c	Power loss in the core.
P_e	Power loss due to eddy current.
P_h	Power loss due to hysteresis.
P_b	Power loss in the brush.
FE	Finite element.
3D	Three dimensions.
A	Magnetic vector potential.
J	Current density
Al	Aluminium material.
J_s	source current density.
J_e	eddy current density.
V	Electric scalar potential.
ϕ	Reduced magnetic scalar potential.
ψ	Total magnetic scalar potential.

Acknowledgements

I would like to express my sincere appreciation and thanks to my supervisor Dr S H Khan for his encouragement and guidance at every stage of this work. Particularly I would like to thank him for his patience and painstaking and long effort in proofreading this thesis a number of times. I would also like to thank my co-supervisor Professor k Grattan for his guidance and encouragement. My sincere acknowledgement also goes to my previous co-supervisor Professor L Finkelstein for his guidance and support throughout the duration of my research.

The author would like to thank Messrs. William Lyons at Claude Lyons Limited (CL) and Derek Maule (previously at CL), UK for active collaboration over the years and for providing us with experimental facilities. The author would also like to thank Messrs. Nigel Lee (previously at CL) and Niall Gray at Claude Lyons Limited for many useful discussions and assistance with the experimental work.

I wish to acknowledge the support of the Libyan Secretary of Higher Education whose financial support provided me with the opportunity to study. Their financial support is highly appreciated.

Throughout this work, I much appreciate the help of the departmental secretaries Mrs. Joan Rivellini; and Mrs. Linda Carr.

I am grateful to my wife for her enduring patience and her support without which I could not achieve this goal.

Finally, I would like to pay a special tribute to my parents, sisters and brothers who have supported me in many ways throughout the course of my studies and to whom this thesis is dedicated.

Declaration

I hereby grant powers of discretion to the University Librarian to allow this thesis to be copied in whole or in part without further reference to me. This permission covers only single copies made for study purposes, subject to normal conditions of acknowledgement.

Abstract

The prime topic of research presented in this thesis is the development and use of computer-based modelling methodologies for design and performance modelling of key industrial components in the electrical industry, exemplified in variable transformers used in voltage regulation and control. Despite the recent introduction of the solid-state devices variable transformers, which are adjustable autotransformers, are still widely used as voltage regulators in many applications. Although originally developed as voltage regulating and testing devices for use in the laboratory, variable transformers have since found countless applications in many key industries with significant importance in UK exports.

Although conventional transformers are well covered in the literature, very few studies have been carried out so far that concern variable transformer and, to our knowledge, none concerning the modelling, design and validation of variable transformers. This research addresses these issues.

Detailed methodologies for mathematical modelling and performance-analysis of variable transformers have been developed. These have been realised in detailed 3D finite element (FE) models of commercial variable transformers using a general-purpose electromagnetic (EM) FE package Opera-3d running under Unix on Sun workstations. The core activities have included the accurate modelling and computation of magnetic field in the complex topology in and around the transformer core taking into account various nonlinearities (e.g. saturation, eddy currents, etc.).

Validation of modelling results constitutes an essential and integral part of any modelling work. In order to validate the above modelling methodologies and refine the FE models developed, experimental investigations of one of the designs of commercial variable transformers TS1225 were carried out in industry. The experimental results obtained in terms of flux density values were compared with corresponding data obtained from FE modelling. This showed good agreement which validated the modelling methodologies developed and

established confidence in the results of further more extensive modelling investigations.

Having validated the modelling methodologies, investigations were carried out to quantify and evaluate the effects of various design and operational regimes on magnetic field distribution in commercial variable transformers. This included the detailed investigation of field distribution in air above the transformer core which contributes to eddy current losses in the transformer top plate. This was also investigated to quantify the effects of higher harmonics. The results of the modelling studies to establish the effects of operational regimes determined by various brush and tap positions gave a vital insight into the design of the transformer core for a given output power. The detailed investigation of flux density distribution in the core and its variation with its geometric parameters quantified the effects of these parameters on the core design.

The modelling methodologies developed and the investigations carried out using the FE models developed constitute an integral part of computer aided design (CAD) and analysis of variable transformers. The same modelling strategies could be equally used for the design and analysis of similar electromagnetic devices.

Chapter 1.

Introduction and Background

1.1. Introduction

Despite the recent introduction of solid-state devices, Variable transformers are still widely used as voltage regulators in many applications. A variable transformer is adjustable autotransformer which differs from conventional transformers in that there is an electrical contact between the primary and secondary windings. Unlike conventional transformers which have two or more windings, an autotransformer has a single winding, all or part of which is common to both the primary and secondary circuits. Compared to conventional transformers, autotransformers may have lower leakage reactance and losses, smaller magnetizing current and usually lower cost. Variable transformers are widely used in many applications and experimental work, testing of electrical and electronic equipment, testing and calibration of electrical measuring instruments (e.g. voltmeters, ammeters, etc.), speed control of electrical motors, etc [40].

A basic variable transformer consists of a single layer of winding, wound on a toroidal core, and an electro-graphitic (carbon) brush which traverses this winding. The brush track (commutator) is made by removing a portion of the insulation from each turn of the winding, thus forming a series of commutator elements. The basic principle is that of a tap-changing transformer. The brush is always in contact with one or more wires, and continuously taps off any desired fraction of the winding voltage. It is possible, therefore, to move the contact under load without interrupting the circuit.

Variable transformers, are used to control voltage and thus to regulate other quantities such as current, power, light, and heat, which are sensitive to voltage change. Most type may be connected to provide voltage control from zero to 17 percent above line voltage or to line voltage only. Models are available in various ampere sizes. The rated current (which may be drawn at any brush setting) is specified for each model. A maximum current rating is also given which is the current that may be drawn at or near line or zero voltage.

The variable autotransformers investigated in this research are 'REGAVOLT®' transformers manufactured by Claude Lyons Limited, UK. Originally designed, patented, and manufactured by General Radio Company [11], USA (now known as GenRad Corporation) who patented the variable transformer in 1933. Covered by patents under which other manufacturers were licensed, this invention now embodies many electrical and mechanical improvements in the original design, the result of a continuous development program carried on since 1933. Among these is the patented [14] Duratrak® contact surface, an improvement that makes the variable transformers as reliable as a fixed-ratio transformer.

1.2. Review of Previous Work on the topic

Although conventional transformers are well covered in literature [3], [4], [8], [12], [13], [17], [21], [22], [29], [31], [32], [38], [39], [46], and [48], very few studies have been carried out so far that concern autotransformers and, to our knowledge none concerning modelling, design and validation of variable transformers. Most of the published literature in this area concerns analytical and experimental studies of large and specialised tapped autotransformers [6];[16], [22], [23], [27], and [45]. In [27] the transmission-line model is used to study specialised autotransformers widely used for impedance matching of two single-ended circuits, and in [51] the non-linear electrical circuit model is used to analyse short-circuit transients in large power autotransformers. Attempts have been made in [16] to take into account the effects of tertiary winding parameters and in [23] the effects of higher harmonics on autotransformer performance using analytical techniques is considered. Extensive experimental studies are carried out in [22] and [45] to investigate and understand the mechanisms of

mechanical and thermal effects of short-circuit faults in large power autotransformers. A major deficiency is that none of the work concerns variable transformers and hardly addresses the critical design issues mentioned below in relation to them. The analytical techniques used are unsuitable for tackling the complicated non-linear problems involved. Although experimental techniques are important, their use is extremely expensive, very time consuming and thus best used for the validation of initial simulation results.

1.3. The Need for Design Methodologies for Variable Transformers

Despite the fact that variable transformers described above are generally simple and robust electrical devices, they rely on complex nonlinear electromagnetic, thermal and electromechanical processes that underlie their efficient, reliable and safe operation. These usually interrelated processes need to be understood and quantified in order to optimise their design and ensure long-term safe and reliable performance. In some large commercial variable transformers there are reports of large circulating and eddy currents in various constructive parts of these transformers resulting in temperature rise and the creation of local 'hot spots'. The mechanical damage to the insulation in variable transformers has been suggested as being attributed to the long-term accumulated effects of such electromagnetic and mechanical factors as switch-ON voltage (up to 6KV) and switch-ON current surges (up to 500A) producing high transient magnetic forces on the winding, increased copper loss, and vibration of the winding at frequencies higher than the normal 50 Hz in the presence of harmonics. Magnetic flux density in the transformer core needs to be limited to avoid saturation and excessive core losses due to hysteresis and possible eddy currents (especially, the case of loss of insulation of the laminated core). Saturation may cause increased leakage flux and the induction of large eddy and circulating currents in the nearby constructive parts of the transformer. These effects need to be understood and investigated for the effective design of variable transformers that would ensure their long-term reliability and optimum performance.

In order to understand the basic electromagnetic processes and other effects on the design and performance of a variable transformer a detailed study of its

magnetic field distribution is needed. For this the development of appropriate methodologies for mathematical modelling and computation of the 3D nonlinear magnetic field distribution in variable transformers using the FE technique. This would involve the steady-state and transient of nonlinear Poisson's equation in the complex geometry of such transformers for which there are no analytical solution. The 3D FE models and the software design tools that has been developed would be used to investigate the magnetic field distribution in and around the transformer core taking into account saturation and eddy-current effects for various design parameters (e.g. geometric, material and electrical) and brush and tap positions under no-load and full-load operational conditions. The modelling results could be used to calculate the copper and iron losses in the transformer which include hysteresis, eddy-current and circulating-current losses primarily in the transformer core and in short-circuited winding turns (top and base plates, brush gear, etc.). In addition, the results would be essential in the investigation of the nature and magnitude of the magnetic force acting on the transformer for various tap and brush positions. This force causes the tightly wound turns to vibrate (at power and higher frequencies in the presence of harmonics) which may result in insulation damage and ultimately lead to shorted turns. The FE models could also be used to study and quantify the effects of harmonics of primary and secondary (load) currents on magnetic field distribution and losses in the transformer. An important aspect of any modelling work is the validation of the simulation results and this is of fundamental importance to the applicability and possible refinement of FE modelling methodologies proposed above. This has been done by comparing simulation results with existing experimental data, also using data obtained from linked experimental studies to be conducted at Claude Lyons, the industrial collaborator of the work, with commercial variable transformers.

In the absence of any existing methodologies for mathematical modelling and CAD of variable transformers that tackle the problems discussed above, the academic and industrial context of the research under taken in this study is clear. The modelling methodologies that need to be developed should give a fundamental insight into the physical nature and extent of these problems and solve them for CAD, performance evaluation and the prediction of variable

transformers. The CAD techniques to be developed should lead to significant improvements to the design and performance of variable transformers. By their generic nature, the methodologies would be applicable to tackle similar problems in many other related areas.

1.4. Aims and Objectives of the Work

The above discussion set out the academic and industrial context and establishes the scope of the work that needs to be undertaken for investigation of variable transformers by mathematical modelling. This also leads to the following aims of the work:

- (a) Development of appropriate methodologies for mathematical modelling and computation of 3D magnetic field distribution in variable transformers using finite element method (FEM)
- (b) Experimental investigation of magnetic field distribution in variable transformers.
- (c) Validation of FE models developed in (a) by comparing modelling result with experimental data obtained in (b).
- (d) Investigation of commercial variable transformers using the modelling methodologies developed in (a).

Based on the above aims the primary aim of the work is to develop and validate a modelling and design capability combining all major aspects of electromagnetic processes in variable transformers that would help design safe; efficient and robust variable transformers.

1.5. Structure of the Thesis

This thesis presents the basic operational principles of the variable transformer, the methodologies, the aims of the work and the comparison between the experimental and simulation results of the transformer under investigation. The modelling is achieved by using Finite Element (FE) modelling and computation of 3D magnetic field distribution in commercial variable transformers used as voltage stabilisers.

Chapter one provides a general introduction to variable transformer theory and its applications. It provides a detailed description and analyses of the basic principle of the variable transformer and its operation, describing the main construction features and an analysis of its magnetic circuit; the commutation of the winding and the brushes.

A review of previous work on the topic and the aims and objectives of this work is discussed.

Chapter two is devoted to the Finite Element (FE) modelling of magnetic fields; introduction of Finite Element method followed by a study of mathematical formulation of 3D magnetic field distribution; fields in non-conducting media; fields in conducting media; the considered assumptions related to this type of modelling; boundary conditions and the estimated errors in Finite Element (FE) modelling.

Chapter three concerning with the realisation of 3D Finite Element models of the commercial variable transformer under investigation, it begins with the development of the basic Finite Element model of the constructive features of the single-phase commercial variable transformer, and defining of its winding.

Chapter four focuses on experimental investigations carried out to measure the magnetic field in air above and around the core for various operational regimes and configurations of TS1225 variable transformers. A description of the construction of the experimental models is provided. The setup of non-magnetic

experimental apparatus is provided, a detailed description of the experimental measurements of the magnetic flux density for the three classified models.

In chapter five the validation of Finite Element models is explained by comparison of modelling results with the experimental data for the three specified experimental models. Also the investigation of commercial variable transformers by finite Element modelling is given in chapter five, such as investigation of the core for various design parameters by variation of outer diameter of the core and the calculations of the winding turns, the effects of design parameters on field distribution in the core, the effects of core saturation on the top plate and a study of the effects of higher harmonics are examined.

Chapter six discuss the conclusions and the possible future work of this type of modelling and investigation for any electrical devices.

This thesis presents the basic operational principle; methodologies and some of the results of performance modelling of variable transformers. This is done by finite element (FE) modelling and computation of 3D magnetic field distribution in commercial variable transformers used as voltage stabilizers

1.6. The Basic Principle of an Autotransformer

An autotransformer shown schematically in Fig. 1.1 serves as a common magnetic circuit to link two or more electrical circuits. When the primary winding is connected to an alternating-voltage source, an alternating magnetic flux will be produced. The magnitude of this flux, which is analogous to electrical current, depends on the voltage applied to the primary turns. All the turns on the transformer are linked by the same magnetic field by mutual inductance. This field induces the same voltage per turn throughout the winding. The magnitude of the voltage induced in the secondary portion of the winding depends, therefore, on the number of the turns in the secondary circuit [15].

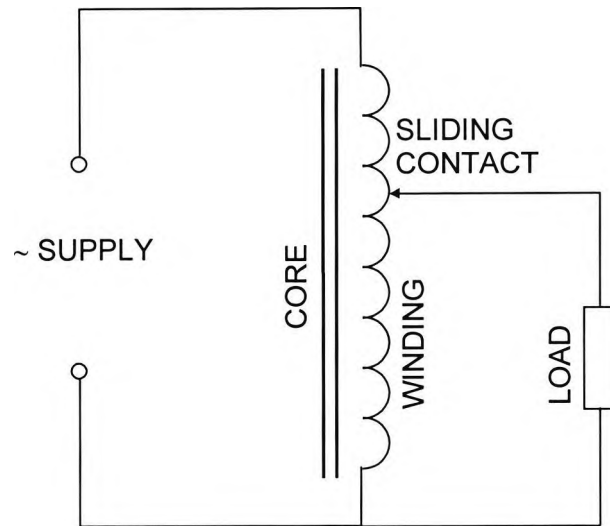
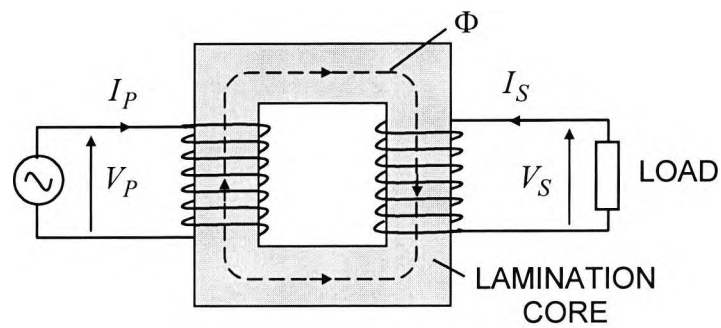
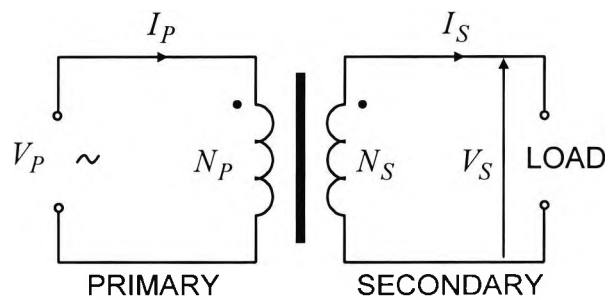


Fig. 1.1 Basic arrangement of an autotransformer



(a)



(b)

Fig. 1.2 Typical two-winding single phase conventional transformer: (a) core and electrically isolated windings, (b) simplified schematic of the electrical circuit.

In order to make the transformer action most effective, all of the flux should be confined to a definite path linking all turns in the winding. This is approximated

by the use of a core of iron or other ferromagnetic material which has a much higher permeability than air. Variable transformers use spirally wound cores of strip stock, grain-oriented, so that the flux path is along the axis of maximum permeability.

In an ideal core where all flux lines produced by the current winding link with all the winding turns, and there is no leakage flux and saturation of the core, the maximum magnetic flux density in the transformer may then be calculated by the following equation:

$$B_{\max} = \frac{V}{4.44 N f A_c} \quad (1.1)$$

Where:

B_{\max} = flux density [T]

V = r.m.s. voltage to the winding [V]

A_c = cross section area of the core [m²]

f = frequency of V [Hz]

N = number of winding turns to which V is applied

From (1.1) it can be seen that the flux density, B_{\max} is directly proportional to V and inversely proportional to A_c , f and N . Here the maximum flux density B_{\max} is used because of the non-linearity of iron-core materials and because factors such as core loss and magnetising current are more dependent upon maximum than upon average or r.m.s. values.

In a typical single phase conventional transformer on no load, the no-load current I_o (also referred to as the magnetising current, I_μ) taken by the primary winding consists of two components (see Fig. 1.3):

- (a) A reactive or magnetising component $I_{o\mu}$ producing the flux, Φ and thereby in phase with it.
- (b) An active component I_{oa} (in phase with the applied primary voltage) which supplies the core losses (eddy current and hysteresis losses) and the negligible I^2R loss in the primary winding. This component is very small

compared to $I_{o\mu}$ so that the no-load power factor is very small. It is clear from Fig. 1.3 that $I_{\mu} = \sqrt{I_{o\mu}^2 + I_{oa}^2}$.

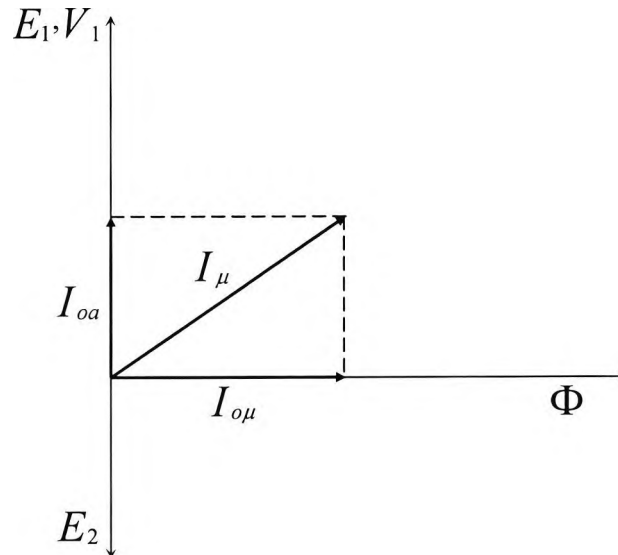


Fig. 1.3 Phase diagram of transformer on no-load

Fig. 1.2 shows a typical two-winding single phase conventional transformer in which the secondary voltage V_s is a multiple of the primary voltage V_p in accordance with ratio of the number of turns called the transformer ratio (or coefficient of transformation) K :

$$\frac{V_s}{V_p} = \frac{E_s}{E_p} = \frac{N_s}{N_p} = K \quad (1.2)$$

Here E_p and E_s are respectively r.m.s. values of electro motive force (e.m.f.) induced in the primary and secondary windings.

At full load the efficiency of such a transformer is almost 100% (97-98%, input power (primary power) P_p out put power (secondary power) P_s) and the primary and secondary power factors are nearly equal ($\phi_p = \phi_s$). Further more, the demagnetising effect of the secondary current (magneto motive force, $F_s = I_s N_s$) on full load is almost totally balanced by the primary magneto motive force (m.m.f.) $F_p = I_p N_p$. Any variation of current in the secondary winding changes the flux Φ and hence the e.m.f. E_p induced by this flux in the primary

winding, thereby enabling the primary current I_P to vary nearly proportionally to the secondary current I_S . Thus there exists a balance of primary and secondary m.m.f. $F_P \approx F_S$. Based on what has been said above, it can be deduced that:

$$P_P \approx P_S \Rightarrow I_P V_P \cos \phi_P \approx I_S V_S \cos \phi_S \Rightarrow \frac{I_P}{I_S} = \frac{V_S}{V_P} \quad (1.3)$$

$$F_P \approx F_S \Rightarrow I_P N_P \approx I_S N_S \Rightarrow \frac{I_P}{I_S} = \frac{N_S}{N_P} \quad (1.4)$$

Combining (1.3) and (1.4) the following important relationship is obtained

$$\frac{I_P}{I_S} \approx \frac{N_S}{N_P} \approx \frac{V_S}{V_P} \quad (1.5)$$

To see the formation of an autotransformer in which, unlike a conventional transformer, there is an electric connection between primary and secondary windings, let us consider that for the transformer in Fig. 1.2 the transformer ratio $K = 3$ ($N_S = 3N_P$), $V_P = 120\text{v}$. This means $V_S = 3V_P = 360\text{v}$ and $I_P = 3I_S$.

If this transformer delivers a current of 1A to this load ($I_S = 1\text{A}$) for a rating of 360VA ($P_S = 360\text{VA}$) then a primary current of $I_P = 3\text{A}$ will be needed.

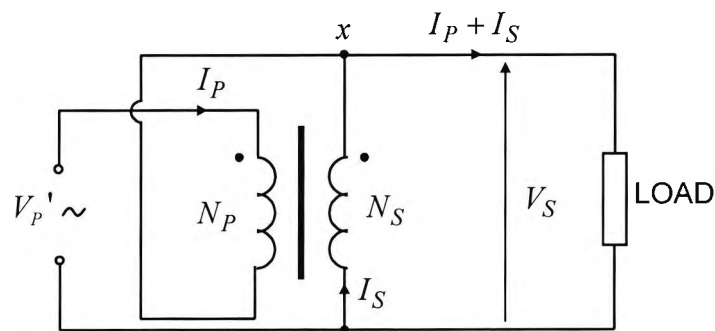


Fig. 1.4 Primary and secondary windings of conventional transformer connected in series.

1.6.1. Principle of a variable transformer

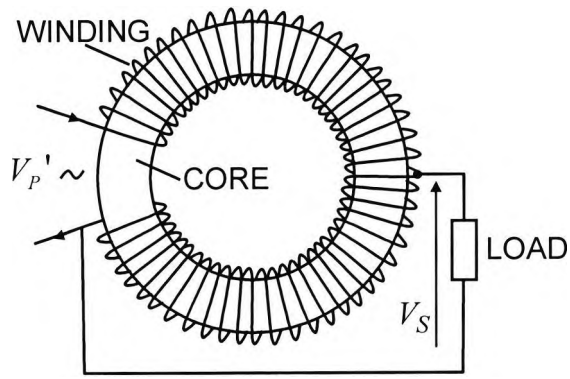
If the primary and the secondary windings in Fig. 1.2 (b) are now connected in series as shown in Fig. 1.4 the new primary voltage (line voltage) V_P' will be the

sum of V_P and V_S : $V_P' = V_P + V_S = 480\text{v}$. The load voltage (secondary voltage, $V_S = 360\text{v}$) will remain the same but the load current will increase to $I_P + I_S = 4\text{A}$ by adding the primary and the secondary currents at node x . This will result in the increase in the volt-ampere rating of $P_S = V_S I_S = 1440\text{VA}$.

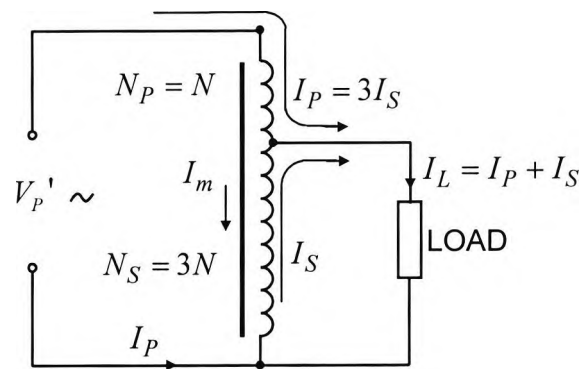
As can be seen this simple connection of primary and secondary windings has converted the conventional transformer in Fig. 1.2 into an autotransformer in which the volt-ampere rating has been quadrupled without any change in the windings or the core. However, the magnetising current, I_μ will now traverse both primary and secondary windings and since the number of the turns has now been increased by a factor of four, I_μ will be one-fourth as large. But with the line voltage now four times as great, $480/120$, the magnetising m.m.f. will remain unchanged, as expected, since the core is being excited by the same number of volts per turn.

The conventional autotransformer diagram, with the current paths, is shown in Fig. 1.5. Note that I_μ adds vectorially to I_P and subtracts vectorially from I_S . Also I_P and I_S are opposing, and $N_P I_P = NI_P = 3NI_S = N_S I_S$.

Let us now consider the continuously adjustable autotransformer (variable transformer). The circuit of Fig. 1.6 differs from the transformer and autotransformer circuits shown in Figs. 1.1, 1.3 and 1.4 in that the number of turns in the primary and in the secondary may be continuously adjusted by means of a sliding brush [11]. Also, the winding usually consists of a single conductor size from beginning to end, where as, in a fixed autotransformer (Fig. 1.5), the two sections often employ different conductor sizes to minimise copper losses [15].



(a)



(b)

Fig. 1.5 Circuit diagram of fixed tap autotransformer (a) core and electrically connected windings, (b) simplified schematic of the electrical circuit.

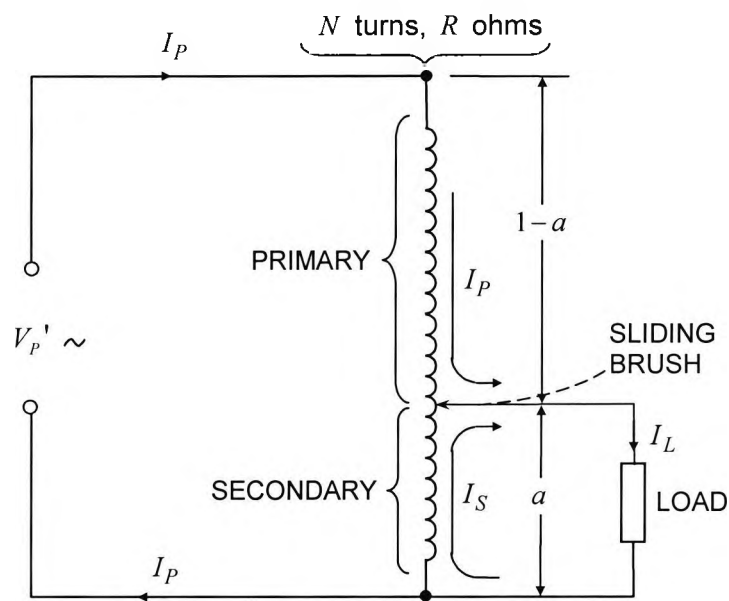


Fig. 1.6 Circuit of basic variable transformer

1.6.2. Operation of a Variable Transformer

In Fig. 1.6, let a represent any number between zero and unity. Thus with the brush as shown, there will be aN turns and aR ohms in the secondary winding, and $(1-a)N$ turns and $(1-a)R$ ohms in the primary winding.

Then the load voltage is

$$V_L = aV_p \quad (1.6)$$

Volt-amperes of the load

$$(VA)_L = aV_p I_L \quad (1.7)$$

$$I_p = \frac{(VA)_L}{V_p} = \frac{aV_p I_L}{V_p} = aI_L \quad (1.8)$$

Primary m.m.f. F_p

$$I_p N_p = aI_L (1-a)N = (a-a^2)NI_L \quad (1.9)$$

$$I_s = I_p \frac{N_p}{N_s} = aI_L (1-a) \frac{N}{aN} = (1-a)I_L \quad (1.10)$$

Secondary m.m.f. F_s

$$I_s N_s = (1-a)I_L aN = (a-a^2)NI_L \quad (1.11)$$

From (1.9) and (1.11), $I_s N_s = I_p N_p$

Copper loss P_{cu}

$$\begin{aligned} \sum W &= I_p^2 R_p + I_s^2 R_s = a^2 I_L^2 (1-a)R + (1-a)^2 I_L^2 aR \\ &= I_L^2 R (a^2 - a^3 + a - 2a^2 + a^3) = I_L^2 R (a - a^2) \end{aligned} \quad (1.12)$$

Differentiating,

$$\frac{d}{da}(a - a^2) = 1 - 2a = 0 \quad \Rightarrow \quad a = \frac{1}{2} \quad (1.13)$$

Maximum copper loss $P_{cu \text{ max}}$

$$\sum W = I_L^2 R \left(\frac{1}{2} - \frac{1}{4} \right) = \frac{I_L^2 R}{4} \quad (1.14)$$

Therefore the maximum copper loss for a constant-current load occurs when the brush is at the midpoint. The rated current can be determined by assigning a value to I_L that will keep the mid-point-brush-setting temperature rise below the permissible limit.

At any other brush setting, the constant-current copper loss is less, which means the current can be increased while the copper loss remains constant.

Let the current at the mid-point setting be I_R .

Then

$$I_L^2 R (a - a^2) = I_R^2 (R/4) \Rightarrow I_L^2 = I_R^2 / 4(a - a^2) \quad (1.15)$$

$$I_L = I_R / 2\sqrt{a - a^2} \quad (1.16)$$

The solution of this equation gives the curve of Fig. 1.7. As a approaches zero or unity, I_L approaches infinity. Problems of thermal conductivity and brush heating make the usual limit of I_L either 1.3 or 1.5 times I_R .

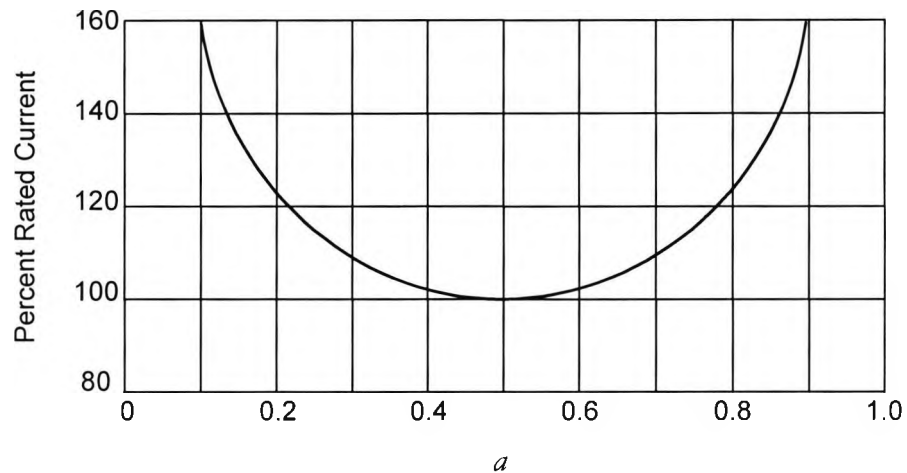


Fig. 1.7 Constant copper-loss current versus output voltage ('a' represent any number between zero and unity).

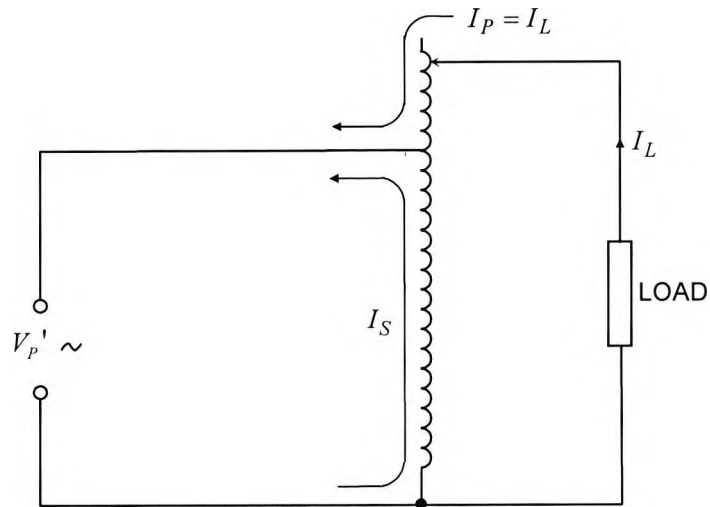


Fig. 1.8 Autotransformer step-up connections

In Fig. 1.8, the roles of the line and load, as shown in Fig. 1.6, have been reversed. The line current is now equal to the original load current, etc.

In equation (1.8), $I_P = aI_L$

$$I_P = aI_R \frac{1}{2\sqrt{a-a^2}} = \frac{I_R}{2\sqrt{\frac{1}{a}-1}} \quad (1.17)$$

which yields the curve of Fig. 1.9. Combining the curves of Fig. 1.7 and Fig. 1.9, we obtain the familiar form shown in Fig. 1.10.

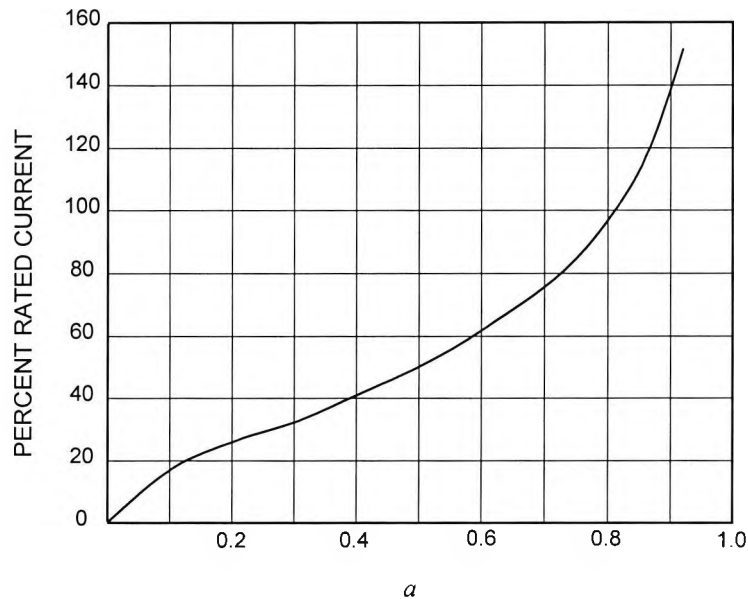


Fig. 1.9 Load current versus ratio of input to output voltage (a represent any number between zero and unity).

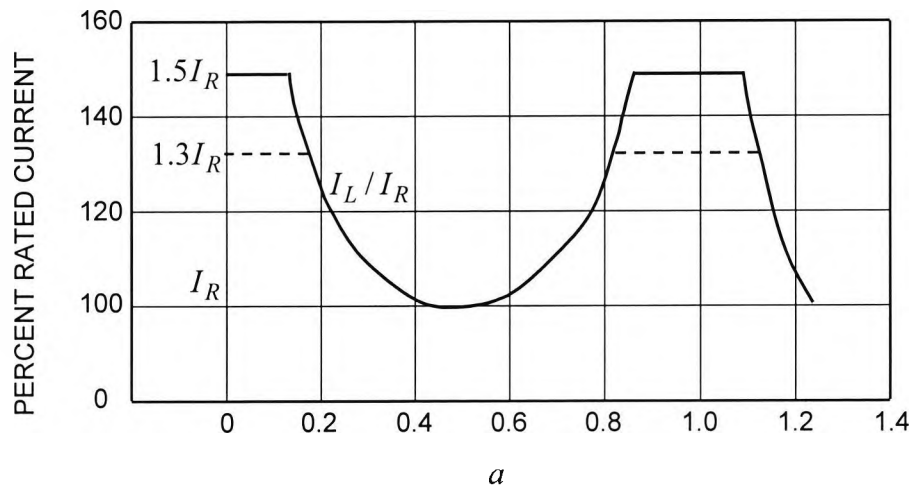


Fig. 1.10 Output current versus transformation ratio.

1.7. The Basic Construction Features and Physical Processes in Variable Transformers

1.7.1. The magnetic circuit

The magnetic circuit of a variable transformer consists of a closed toroidal core usually of rectangular or circular cross-section and made of laminated ferromagnetic iron. The toroidal core used in, for example, Variac autotransformers investigated in this work, is formed by winding grain-oriented strip steel, much as one would spool ribbon. It is then goes through careful thermal annealing in a protective atmosphere to improve its magnetic properties. Because the flux paths are always parallel to the preferred longitudinal grain orientation, wound cores of this construction have inherently lower losses than cores formed from stacked washers stamped from sheet stock, in which the flux paths cannot everywhere parallel the grain of the material. Wound cores also permit closer packing of the magnetic material into the available space, with a corresponding gain in the stacking factor (ratio of useful magnetic material volume to total available volume).

The losses in the core P_c of a variable transformer, as in the core of any other transformer, consist of the eddy current loss P_e and hysteresis loss P_h ;

$P_c = P_e + P_h$. For a given volume of the core the eddy current loss P_e is a function of core flux density B , frequency f and lamination thickness t ; $P_e = K_e f^2 B^2 t^2$, where K_e is a constant. The hysteresis loss is attributed to the loss associated with cyclic magnetisation and demagnetisation of the core as the core magnetic field (B, Φ) changes with time and frequency f . For a given core volume \forall the hysteresis loss $P_h = f \forall A_h$ where A_h is the area of the hysteresis loop of the core material. The above simple relationships show that core loss in a variable transformer is a complex function of flux density in the core and other design parameters of the core. The core magnetic flux B_{max} , is limited to avoid excessive core loss and excitation. The limit for Variac type autotransformers is approximately 1.8 Tesla at low power frequencies (25, 50, and 60Hz). This limit is based on a magnetizing current not to exceed 10% of the rated current, (that may be drawn at any brush setting,) based on temperature rise with the unit operating at the lowest recommended frequency. Most of variable autotransformers are normally designed for flux densities of between 1.4 and 1.5 Tesla.

It is clear that the core loss for a given flux density decreases with decreasing frequency although, for a given winding; core and voltage, the flux density is inversely proportional to the frequency. All these factors need to be taken into account in order to be able to optimise the design of variable transformers and predict their performance.

1.7.2. The winding

The winding of variable transformers are made from single-turn an insulated wire that surrounds the core. Most commonly, it is a toroid, which permits brush to traverse the winding on specially prepared brush track. The wire size is closely fixed by the current rating and the maximum allowable temperature rise. A very high grade of insulation is required to withstand high operating temperatures. The brush track is by removing enough insulation and wire from the brush track to offer an adequately large contact surface to the brush. The number of turns in the winding is determined by the operating voltage,

frequency, brush loss, required resolution, most favourable copper-to-core ratio, and wire size.

Because of its superior conductivity and reasonable price, copper is usually employed in transformer windings. However, bare copper tends to oxidize when heated and below 150 C, this oxidation is gradual and is limited to a relatively thin, medium-conductivity film of cuprous oxide. Above 150 C, (which the brush contact may reach due to abnormal thermal regions) however, a thick, black, poorly conductive film of cupric oxide forms rapidly. The cupric film interposed between brush and winding, causes severe heating under load, initiating a vicious cycle of temperature rise and oxidation.

This difficulty is avoided, for example, in Duratrak® [14] contact surface by coating the brush track with a precious-metal alloy (gold or silver-based). The coating resists oxidation and does not corrode easily. The contact resistance between brush and track is greatly influenced by the coating material, and optimum brush parameters will differ for different coatings if the optimum no-load-to-full-load brush-loss compromise is to be realized.

The copper loss (I^2R) in the winding is one of the main losses in variable transformers, and also a dominant design factor. Conductor size is closely fixed by the current rating and the maximum allowable temperature rise. Small transformers cannot be operated at a flux density sufficiently high to equalise core and copper losses (condition for maximum efficiency) without excessive magnetising current. In a variable transformer, with the input voltage applied across the entire winding, copper loss at a constant output current varies with brush setting from a maximum at mid-point, decreasing gradually, and then abruptly, to zero at the winding end. Were it not for the poor thermal conductivity of the necessary insulation, the load could be increased as the brush approached the end of the winding, and, theoretically, could reach infinity if the brush and thermal limitations, the current increase must be held to a modest 30 to 50 percent. A constant impedance load that draws maximum current at line voltage may be controlled downward to zero without exceeding a safe temperature rise. The rated current is based on the temperature rise at the mid-point brush setting but the maximum current can be drawn only at or near line or zero voltage.

1.7.3. The brushes and commutation

The commutation (the process of current transfer from the brush track to the brushes as they transverse the winding turns) in variable transformers is facilitated by carbon brushes which transverse the brush track that acts as the commutator. Brushes in variable transformers are often made of electro-graphite. The properties of the brushes material; resistance characteristics; mechanical design and thermal properties of the contact are most important for proper operation of variable transformers. The contact resistance between an electro-graphitic brush and a metallic surface varies with the current passing through the surface, and the resistance of the brush itself depends to a large degree on the current density. The resistance of the brush varies with the current passing through it in a manner that maintains a substantially constant voltage drop. This voltage drop varies with the composition of the brush and with the pressure applied, and is used by brush manufacturers in the rating of their product [33]. A definite relation between this voltage drop and the volts-per-turn of the unit must be maintained to prevent excessive heating of the short-circuited turn and of the contact [15].

In traversing the track, the brush often bridges more than one turn. As the brush loses contact with one turn and makes contact with another, a voltage-dividing action occurs which allows the selection of voltage increments less than the voltage difference between turns. As a result, the resolution or incremental adjustment of variable transformers is actually better than would be indicated by the number of turns alone.

Fig. 1.11 shows a simplified diagram of 'commutation' in variable transformers. The resistances R_1 and R_2 represent the brush-to-winding interface resistances. For approximate calculations the brush-to-body, brush-to-holder, and turn resistances can be considered negligible in a properly designed variable transformer. The load current, I_L is the algebraic sum of the currents, I_1 and I_2 , traversing R_1 and R_2 , respectively; V_T is the voltage induced in the short-circuited turn. As the brush traverses the winding, R_1 and R_2 vary inversely as their respective areas of contact. The maximum loss, for a given

brush and load current, occurs at the midpoint of the traverse [15], where $R_1 = R_2$. Furthermore, at this maximum-loss point, the loss will be a minimum when

$$R_1 = R_2 = \frac{V_T}{I_L}$$

Under these conditions $I_L = I_1$, $I_2 = 0$

and the brush-loss $P_b = V_T I_L$.

If the load current is reduced to zero, the bridging brush-loss

$$P_b = \frac{V_T I_L}{2}$$

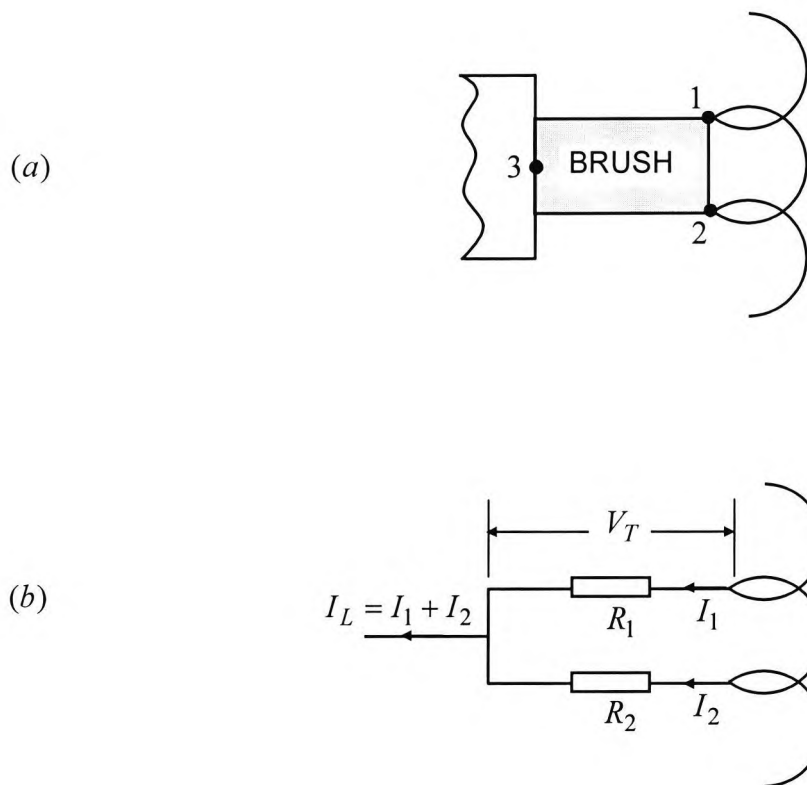


Fig. 1.11 commutation in variable transformers: (a) one turn is short-circuited (bridged) by the brush, (b) equivalent circuit of the brush arrangement.

Chapter 2.

Finite Element Modelling of Variable Transformers

2.1. Introduction

This chapter presents the use of finite elements method and the mathematical formulation of magnetic fields; it focuses on static magnetic fields, as well as on eddy current, in variable transformers. It attempts to summarise the magnetic field computations as used by OPERA-3d package, but it does not claim to present the computing method with full mathematical rigor.

In general, the objective of finite element analysis is to approximate with a sufficient degree of accuracy the values of the unknowns of a governing differential equation at selected points on the domain of a continuous physical system or structure. A mathematical model of the physical system or structure, divided into *nodes* and finite *elements*, is created, and the governing equations are applied to it and solved for each node.

The main function of the finite element program is to reduce the differential equation to a set of simultaneous algebraic equations, which can be readily solved by a computer. The solution of these equations yields directly, or by means of minor additional computation, the desired unknown quantities

The main step involved in a finite element analysis is to create the finite element model. The finite element model is a geometrical representation of the actual physical structure or body being analysed. Dividing the structure into a number of sub regions called "elements" creates the model. The values of the unknown

quantities are to be computed at selected points in the elements, usually at the corners. These points are called "nodes."

The process of dividing up the body is often called "discretisation" and is normally performed by the user. As we shall see in later chapters, discretisation of the body or structure is the most important phase of the analysis and greatly affects the accuracy of the results.

It is important to emphasize that the finite element model is a mathematical simulation of the actual physical structure or body that it represents. The physical properties must be specified. If the body is made of iron, the material properties of iron must be assigned to the elements of the body

2.2. Mathematical Formulation of 3D Magnetic Field Distribution in Variable Transformers

2.2.1. Basic equations

The governing laws of electromagnetic field problems can be expressed very concisely by a single set of equations, namely those associated with the name of Maxwell [64]. The basic variables are the following set of five vectors and one scalar:

Electric field intensity	E volt/metre
Magnetic field intensity	H ampere/metre
Electric flux density	D coulomb/metre ²
Magnetic flux density	B Tesla
Electric current density	J ampere/meter ²
Electric charge density	ρ coulomb/metre ²

The field equations can be written in the form

$$\nabla \cdot \bar{D} = \rho \quad (\text{Gauss's law})$$

$$\nabla \cdot \bar{B} = 0$$

$$\nabla \times \mathbf{E} = -\frac{d\mathbf{B}}{dt} \quad (\text{Faraday's Law})$$

$$\nabla \times \mathbf{H} = \mathbf{J} + \frac{d\mathbf{D}}{dt} \quad (\text{Ampere's Law}) \quad (2.1)$$

The field vectors are related by the material property equations

$$\mathbf{D} = \epsilon \mathbf{E}$$

$$\mathbf{B} = \mu \mathbf{H}$$

$$\mathbf{J} = \sigma \mathbf{E} \quad (\text{Ohm's Law}) \quad (2.2)$$

It should be noted that the equation

$$\nabla \cdot \mathbf{J} = -\frac{d\mathbf{B}}{dt} = 0 \quad (2.3)$$

is an immediate consequence of (2.6).

Describing the properties of the medium being dealt with in terms of permittivity ϵ , permeability μ and conductivity σ are not necessarily simple constants, a notable exception being the case of ferromagnetic materials for which the B-H relationship may be a highly complicated nonlinear law [64]. Furthermore, ϵ and μ may represent anisotropic materials. With flux densities differing in direction from corresponding field intensities. In such cases the constitutive constants have to be written as tensors. For free space, using the SI system of units, $\epsilon_0 = 8.854 \times 10^{-12}$ Farad/metre and $\mu_0 = 4\pi \times 10^{-7}$ henry/metre.

2.2.2. Fields in non-conducting media

Three-dimensional stationary electromagnetic fields can be represented as the sum of a solenoidal field and a rotational field. In electrostatic fields, there is never a rotational component; the field can therefore always be defined using the electrostatic potential (ψ). The electric field intensity (E) is given by:

$$\bar{\mathbf{E}} = -\nabla\psi \quad (2.4)$$

The divergence of the electric flux density ($\bar{\mathbf{D}}$) is related to the charge density (ρ):

$$\nabla \cdot \bar{\mathbf{D}} = \rho \quad (2.5)$$

Combining equations 1.19 and 1.20 and introducing the dielectric permittivity tensor (ϵ) gives the usual Poisson's equation description of the electrostatic potential:

$$\nabla \cdot \epsilon \nabla \psi = -\rho \quad (2.6)$$

where

$$\bar{\mathbf{D}} = \epsilon \bar{\mathbf{E}}$$

Magnetic fields on the other hand in general consist of both solenoidal and rotational components [68]. The field produced by electric currents has a rotational component inside the volumes where the currents flow. In the exterior space, the field is solenoidal but the scalar potential is multi-valued. The field produced by magnetised volumes is solenoidal. It is convenient to use a splitting of the total field into two parts in order to obtain a description of the field in terms of a simple scalar potential. The total field intensity $\bar{\mathbf{H}}$ is defined using the reduced field intensity ($\bar{\mathbf{H}}_m$) and the conductor field intensity

$$\bar{\mathbf{H}} = \bar{\mathbf{H}}_m + \bar{\mathbf{H}}_s \quad (2.7)$$

the reduced field intensity can now be represented using the reduced scalar potential (ϕ):

$$\bar{\mathbf{H}}_m = -\nabla\phi \quad (2.8)$$

and in the case of stationary magnetic fields where the exciting currents are prescribed, the conductor field intensity may always be directly evaluated by integration [68]:

$$\bar{\mathbf{H}}_s = \int_{\Omega_j} \frac{\bar{\mathbf{J}} \times \bar{\mathbf{R}}}{|\bar{\mathbf{R}}|^3} d\Omega_j \quad (2.9)$$

The divergence of the flux density is always zero. Introducing the permeability tensor (μ) and combining equations 2.22 to 2.24 gives the partial differential equation for the reduced scalar potential (ϕ)[68]:

$$\nabla \cdot \mu \nabla \phi - \nabla \cdot \mu \left(\int_{\Omega_J} \frac{\bar{\mathbf{J}} \times \bar{\mathbf{R}}}{|\bar{\mathbf{R}}|^3} d\Omega_J \right) = 0 \quad (2.10)$$

This equation, like the Poisson's equation for electrostatic fields, can easily be solved using the finite element method. However, the reduced potential formulation for magnetic fields is not acceptable. Large errors are found in the total fields computed by this method. The errors arise because the space variation of $\bar{\mathbf{H}}_m$ and $\bar{\mathbf{H}}_s$ will be quite different if one is represented using derivatives of the finite element shape functions (a low order polynomial in \mathbf{x}) and the other using direct evaluation of the integral in equation 1.23. This effect combined with the possibility that $\bar{\mathbf{H}}_m$ and $\bar{\mathbf{H}}_s$ will strongly cancel in some volumes of the space leads to magnification of the errors in the approximate solution for $\bar{\mathbf{H}}_m$. The cancellation problem is particularly critical in the interior of non-linear magnetic materials, where the magnified errors destroy the accuracy of the Jacobean matrix used for Newton iterations. It is also very undesirable when magnetic shielding is being designed since the largest errors will occur in volumes where the shield is most effective.

The above difficulty can be completely avoided when currents are not flowing in the magnetic materials. Exterior to the volumes where currents flow, the total field can be represented using the total magnetic scalar potential (ϕ):

$$\bar{\mathbf{H}} = -\nabla \phi \quad (2.11)$$

where the total magnetic scalar potential satisfies:

$$\nabla \cdot \mu \nabla \phi = 0 \quad (2.12)$$

By combining the two representations (the total and reduced scalar potentials) cancellation difficulties can be completely avoided. The minimal combination consists of using the reduced potential only inside volumes where currents flow and the total potential everywhere else. This has practical limitations in that the

reduced potential volume may have a complicated shape and cutting surfaces would need to be specified in the total potential space to maintain a single valued potential. For these reasons, simple singly connected spaces are generally used for the reduced potential volumes.

In exceptional circumstances, where it is impossible to create singly connected total scalar potential volumes, it is possible to use reduced scalar potential within magnetic materials. Because of the cancellation problems described above, such reduced scalar potential volumes should be as small as possible and away from regions where accuracy is critical. Reduced scalar potential must be used in magnetic material carrying source currents.

On the interface between the total and reduced potential spaces, the two potentials can be exactly linked together by applying the conditions of normal B and tangential H continuity. This involves evaluation of the normal field produced by the conductors and the scalar potential that could be used to represent the conductor field on the interface surface. Practically, this also makes the method more attractive than the straightforward reduced potential formulation. Evaluating the fields from conductors although well defined is expensive. The reduced potential formulation requires that the conductor fields be evaluated throughout the non-linear magnetic material volumes. The total potential on the other hand only requires the conductor field to be evaluated on the interface surface between the reduced and total potential volumes for the solution of the equations. However, the current field is needed throughout the reduced potential volumes to obtain the total field during post processing.

2.2.3. Field in conducting media

In time varying fields, the currents that are induced in conducting volumes are part of unknowns in the system. Their fields cannot therefore be evaluated by simply performing integration. Inside the conducting volumes, the field representation must include a rotational component. The most elegant approach is to combine the efficient total and reduced scalar potential method for non-conducting volumes with an algorithm that uses a vector potential (\vec{A}) in the conducting volumes [68].

In a low frequency time varying magnetic field when the dimensions of the objects in the space are small compared to the wavelengths of the fields, the magnetic and electric fields are related by the low frequency limit of Maxwell's equations:

$$\nabla \times \bar{H} = \bar{J} \quad (2.13)$$

where

$$\nabla \times \bar{E} = -\frac{\partial \bar{B}}{\partial t} \quad (2.14)$$

$$\bar{J} = \sigma(\bar{E} + \bar{u} \times \bar{B}) \quad (2.15)$$

and σ is the electrical conductivity and u the velocity. At this point we assume that the velocity is zero.

The flux density \bar{B} can be represented using a vector potential \bar{A} where:

$$\bar{B} = \nabla \times \bar{A} \quad (2.16)$$

Using vector potential and combining equations 1.28 to 1.31 gives the following equation for \bar{A} :

$$\nabla \times \frac{1}{\mu} \nabla \times \bar{A} = -\sigma \frac{\partial \bar{A}}{\partial t} - \sigma \nabla V \quad (2.17)$$

The gauge used in ELEKTRA is the Coulomb gauge

$$\nabla \cdot \bar{A} = 0 \quad (2.18)$$

and after including it into equation 2.23 the new governing equation is

$$\nabla \times \frac{1}{\mu} \nabla \times \bar{A} - \nabla \frac{1}{\mu} \nabla \cdot \bar{A} + \sigma \left(\frac{\partial \bar{A}}{\partial t} + \nabla V \right) = 0 \quad (2.19)$$

It is also necessary to solve the secondary equation

$$\nabla \cdot \sigma \nabla V + \nabla \cdot \sigma \frac{\partial \bar{A}}{\partial t} = 0 \quad (2.20)$$

This vector potential description of fields inside conducting volumes can be directly combined with the total and reduced potential description in non-conducting spaces. The normal flux and tangential field intensity interface conditions are used to exactly couple the two field descriptions.

2.2.4. "Cuts" in total and vector potential regions

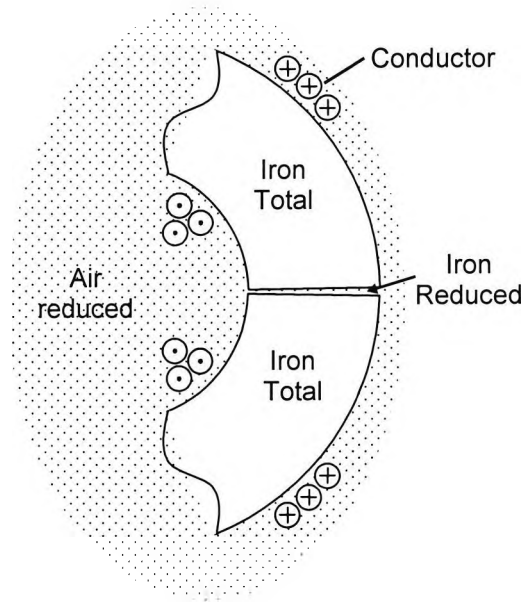


Fig. 2.1 Schematic diagram shows the cut in total potential region.

When a current, I , passes through the centre of a continuous magnetic ring (e.g. toroidal core), a multiply connected problem exists if the ring defined as total or vector potential. The reduced potential hole in a total potential space must have a current sum of zero; otherwise the scalar potential in the total space is multi-valued [35].

This can be seen from Ampere's Law

$$\nabla \times H = J = 0 \quad (2.21)$$

or in integral form:

$$\oint H \cdot dl = I = 0 \quad (2.22)$$

The definition of total magnetic scalar potential requires J to be zero, implying the net current enclosed by the contour integral to be zero. This is violated in the above, as the contour integral (within total potential region) is non-zero.

To correct this, a cut surface must be introduced to make the reduced potential space simply connected, as shown in Fig. 2.1.

2.3. The finite element method (FEM) and its basic procedures

The 3D finite element (FE) modelling of variable transformers is mainly based on the mathematical modelling and computation of magnetic field distributions in the 3D problem domain $\Omega(r, \theta, z)$ by solving appropriate field equations. This leads, in general, to the solution of the following non-linear Poisson's equation in terms of magnetic vector potential A and current density J [52]; [60] and [66]:

$$\nabla \times \frac{1}{\mu} \nabla \times A = J \text{ in } \Omega(r; \theta; z) \quad (2.23)$$

In the conducting sub-domains of Ω where eddy currents can flow (e.g. AI top and base plates, iron core, etc.) the current density consists of the source

$$J = J_e + J_s = -\sigma \left(\frac{\partial A}{\partial t} + \nabla V \right) \quad (2.24)$$

current density J_s and eddy current density J_e . In Eq. (2.2) V is the electric scalar potential. Considering this and the necessary current continuity condition $\nabla \cdot J = 0$, the vector potential formulation (A-V) of fields in the conducting sub-domains given by the following two equations [52]:

$$\nabla \times \frac{1}{\mu} \nabla \times A + \sigma \left(\frac{\partial A}{\partial t} + \nabla V \right) = 0 \quad (2.25)$$

$$\nabla \cdot \sigma \left(\frac{\partial A}{\partial t} + \nabla V \right) = 0 \quad (2.26)$$

Since Eq. (2.4) is essentially the result of taking the divergence of Eq. (2.3), they are not independent. However, the uniqueness of their solutions is ensured by explicitly applying Coulomb gauge condition $\nabla \cdot A = 0$ to these coupled equations (together with the condition $A \cdot n = 0$ imposed on the external boundaries to conductors). This results in the governing equations of Eq. (2.19) and Eq. (2.20), which describe the magnetic fields in the conducting sub-domains of the 3D problem domain Ω . This vector potential formulation of fields is directly combined with the reduced (ϕ) and total (ψ , $\nabla \cdot \mu \nabla \psi = 0$) magnetic scalar potential formulations of fields in the non-conducting sub-domains [60]. To exactly couple these field descriptions the equality of the normal flux and tangential field intensity interface conditions ($B_{n1} = B_{n2}$, $H_{\tau1} = H_{\tau2}$) are also imposed.

Under appropriate boundary conditions on external boundaries of the problem domain the solution of the field equation was obtained by numerical FE technique [62]. For this various 3d FE models of the commercial variable transformer shown in figures from Fig. 3.7 to Fig. 3.23 were developed using the commercial FE package OPERA-3d [63]. Description of the systematic model-building strategy used for this purpose will be given in chapter 3.

2.4. Assumptions

The magnetic field distribution in the variable transformer shown in Fig. 2.2 is given, in general by the non-linear Poisson's equation described by equation (2.3). It is solved by numerical FE method under appropriate assumptions, which are commonly used in most cases of magnetic field modelling using FEM:

- (i) The displacement current, giving rise to capacitance effects is negligible for this kind of device modelled in this investigation.
- (ii) With non-linear permeability, the B-H curve is normally assumed to be single valued, i.e. there is no hysteresis effect. For the ferromagnetic materials used

for simulation in this work the area of the hysteresis loop is 'very small' so are any hysteresis effects. For this reason this assumption is justified.

- (iii) The continuous N-turn toroidal winding of the variable transformer under investigation is replaced by N single-turn coils tightly placed winding around the toroidal core. This is justified given the closely wound toroidal winding and it simplifies the definition of FE model.
- (iv) The materials in various FE regions are piece-wise homogeneous and isotropic. This significantly simplifies FE modelling, especially as the materials used are homogeneous and isotropic.

2.5. Boundary Conditions

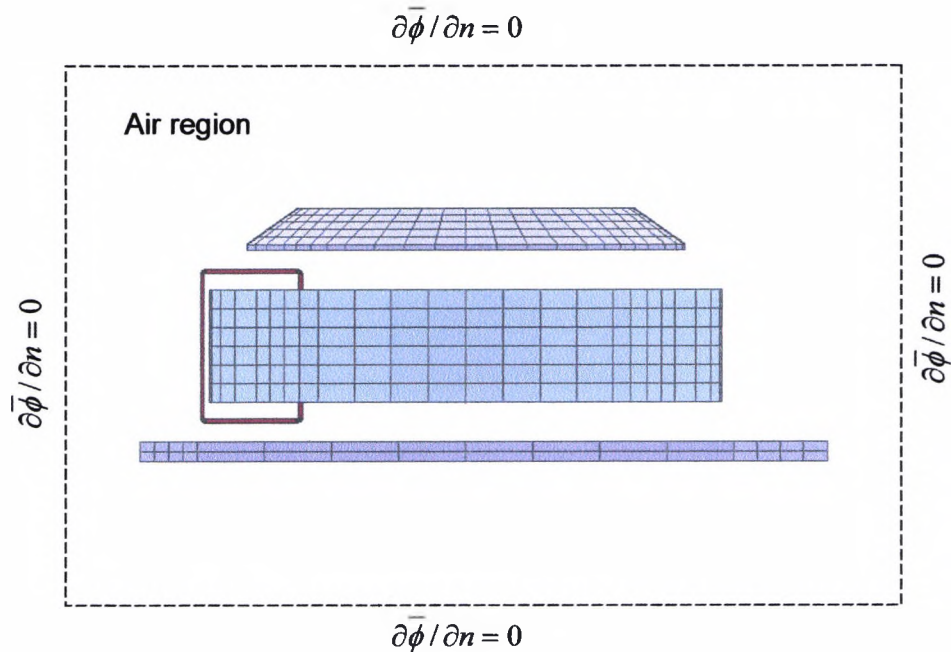


Fig. 2.2 Longitudinal view of the FE model showing the boundary condition.

In general, the essential boundary conditions are prescribed values of potential or field, valid on the boundary surfaces. In this case the tangential magnetic field (i.e. $\partial\phi/\partial n = 0$) is specified.

This is justified if the outer boundary of the problem domain around the transformer is chosen sufficiently far apart so that any further repositioning of the boundary surfaces away from the transformer does not appreciably change the FE solution.

2.6. Estimation of Errors in Finite Element Modelling

The local error at a point within a finite element model is strongly linked to the size of the elements surrounding the point and weakly linked to the average element size over the whole space, although this second source of error becomes more important and less easily estimated in non-linear solutions. The relationship between the local error in the solution and the surrounding elements size is given by:

For linear shape functions

$$E(\Phi) = O(h^2) \quad (2.27)$$

and for quadratic shape functions

$$E(\Phi) = O(h^3) \quad (2.28)$$

Where E is the error, O means "of the order" and h is the linear dimension of the elements. This simple analysis is only true for square elements, but it is reasonable to assume the worst case and use the largest dimension for h unfortunately, these formulas only give the order of the error, the actual error is dependent on the solution, or more precisely the geometry of the model in the vicinity of the point. As an example, consider a point close to the corner of a magnetised steel cube, the field will be weakly singular at the corner. Given the same size discretisation over the whole space, the errors will be far larger close to the edges and corners of the cube. This is because the low order polynomials used in the finite elements are not good at approximating the singularity. Calculating the magnetic field from the potential solution generally results in larger errors in the field than there were in the potential.

Differentiation of the finite element shape functions to determine the field gives an error in the field that is worse by $O(h^{-1})$. In the case of linear shape

functions, this results in an error in the field $O(h)$. In the ELEKTRA program special facilities have been included in order to reduce the errors in the fields that are computed from potential solutions. Two methods are available that increase the field precision; the best method depends on the problem being solved. Nodal weighted averaging improves the field accuracy to $O(h^2)$. The volume integration technique does not improve the order of the error, but it enables the variation of the field to be calculated very accurately remote from steel or dielectric regions.

It is essential that the user of a finite element program carry out a number of analyses to examine the effect of element size on the solution. Using the ideas introduced above it is clear that the best approach is to solve the same model with two levels of finite element discretisation or with the same discretisation but using linear elements in one case and quadratic elements in the other. Taking as an example the use of two levels of discretisation, such that the element dimensions are halved in the second case, the case with the larger number of elements will have solution errors that are 4 times smaller (the errors in the fields evaluated by differentiation of the shape functions will be halved). Examination of the changes between the two solutions will give a good estimate of the discretisation errors, but not, as pointed out in the previous section any indication of the accuracy of the model.

This approach is very good for two-dimensional discretisation, but in three dimensions, the 8 fold increase in the number of nodes quickly becomes prohibitive for all but the simplest geometries. When increasing the overall discretisation becomes too expensive, it is necessary to carry out more trial analyses, in each case choosing particular regions of increased discretisation to determine the sensitivity of the solution to the change in element size. An experienced user will have learnt how to minimise the number of trials as a result of carrying out this type of experiment on a number of different geometries.

Chapter 3.

Realisation of 3D Finite Element Models of Commercial Variable Transformers

3.1. Introduction

For the purpose of developing modelling methodologies and 3D FE models of variable transformers a single-phase commercial variable transformer type TS 1225 mentioned earlier was considered. It consists of a single-layer toroidal winding tightly and closely wound on the toroidal core. The core is made of spirally wound grain-oriented silicon steel. The winding turns lie side by side on the outer surface but overlap on the inner surface because of the significant difference in circumferential lengths of the inner and outer surface of the core especially for large transformers. The out-put voltage is varied by rotating the aluminium top plate which holds one or multiple segmented brushes attached to the brush gear not shown in Fig. 3.1b) that traverse the winding turns on the outer surface of the core. The brush track, which acts as the commutator, is made by stripping off insulation from the outer surface of each of the winding turns. In large variable transformers the commutator surface is coated with gold to increase the reliability and effectiveness of commutation. The segmented brushes made of electro-graphite are always in contact with the commutator and overlap one or more turns and continuously tap off the desired fraction of the winding output voltage. Fig. 3.1 shows such a transformer.

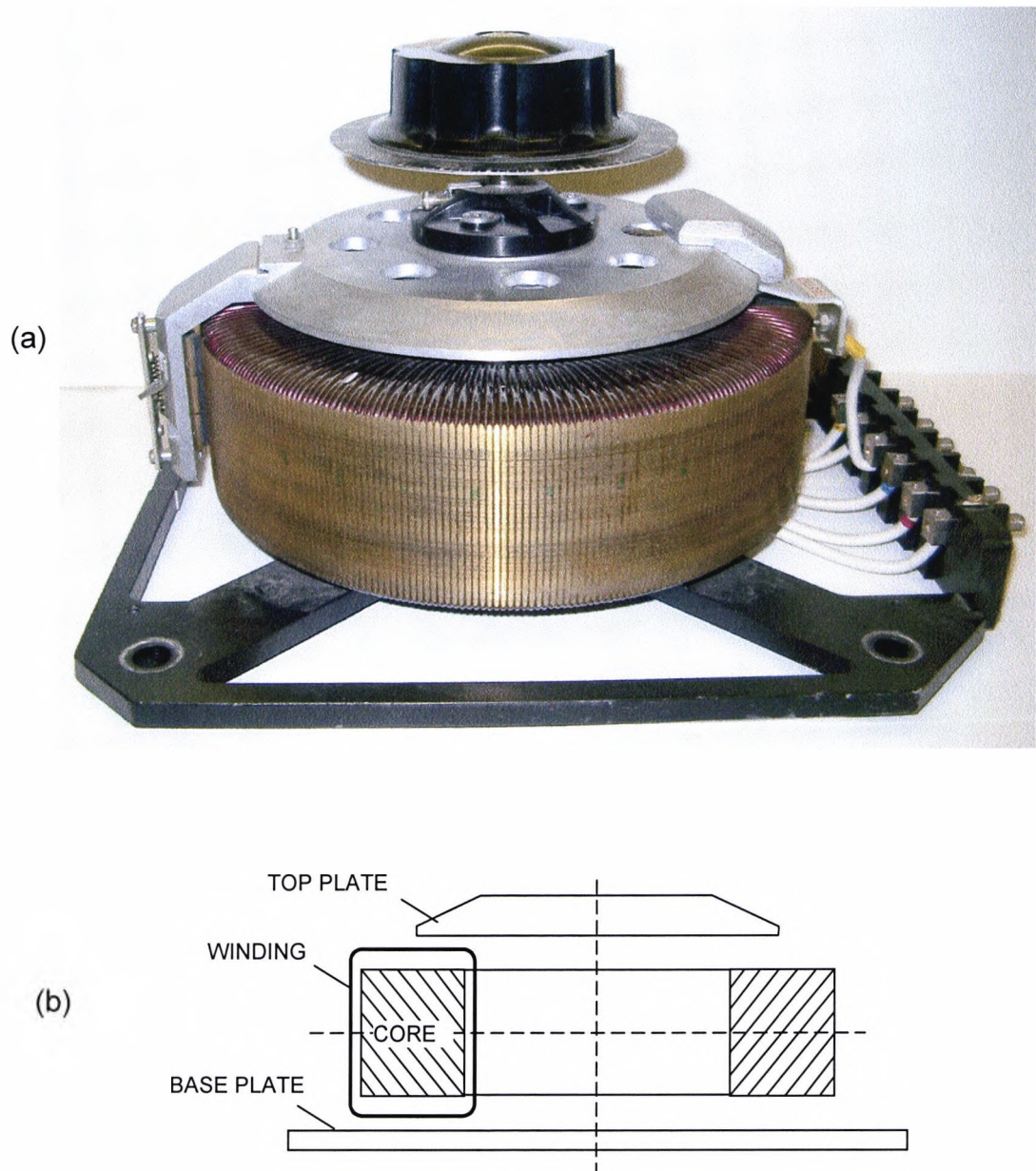


Fig. 3.1 Typical commercial variable transformers investigated: (a) transformer type TS1225; (b) it's simplified longitudinal section showing main constructive elements (not drawn to scale).

Because of the asymmetry in both the geometry and field distribution in the variable transformer shown in Fig. 3.1, the Poisson's equation must be solved in 3D taking into account saturation nonlinearities and eddy-current effects. For this various 3D FE models of the transformer have been developed using the commercial software packages OPERA-3d, TOSCA and ELECTRA. Despite the flexibility and user-friendliness of the software package, the complex geometry

and the need for incorporating detail geometric features make the 3D-model definition of the transformer quite complicated and time consuming. For effective and efficient model definition, a systematic modelling approach was adopted to set up the basic 3D model. During the course of model development substantial effort was put into the FE realisation of the N single-turn coils because of the way the original toroidal winding, which they replace, is wound. The single-turn coils, although lie side by side on the outer surface of the core, overlap on its other surfaces because of the difference in circumferential lengths between the inner and outer surfaces. The complex geometric features of the base and top plates also posed many challenges for model building.

Fig. 3.2 shows the BH curve of the type used magnetic material used for simulation (Unisil 35M5).

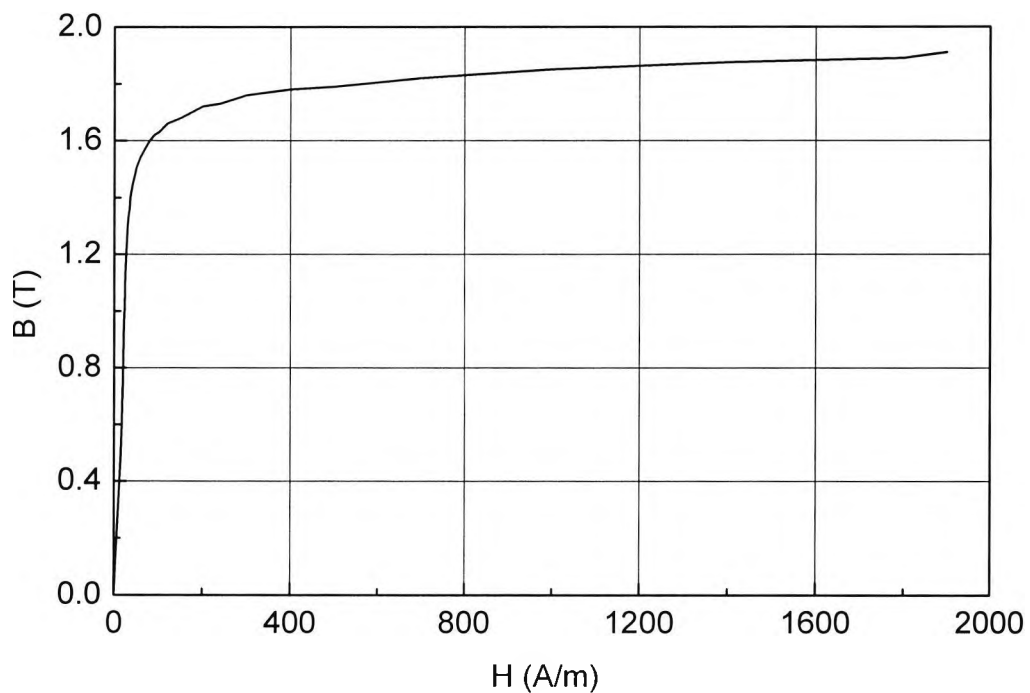


Fig. 3.2 Magnetization curve of Unisil 30M5 grain-oriented silicon steel used in TS 1225 transformer core.

Details of some of the main geometric dimensions of variable transformer (TS1225) are shown in Fig. 3.3.

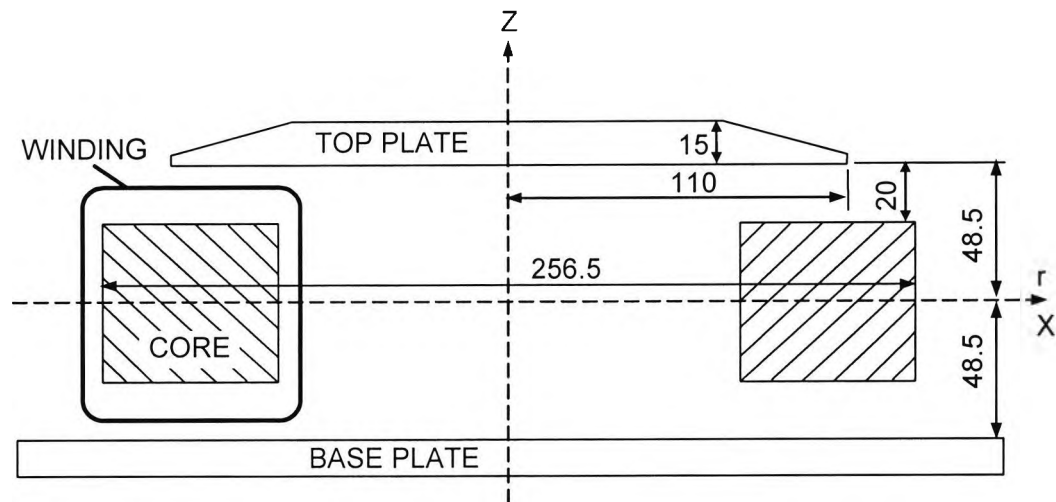


Fig. 3.3 Schematic diagram of the TS1225 transformer showing some of the main geometric parameters (dimension in mm, not drawn to scale)

Details of the geometric dimensions of the top plate, the toroidal core and the base plate of the transformer are shown in; Fig. 3.4, Fig. 3.5 and Fig. 3.6 respectively.

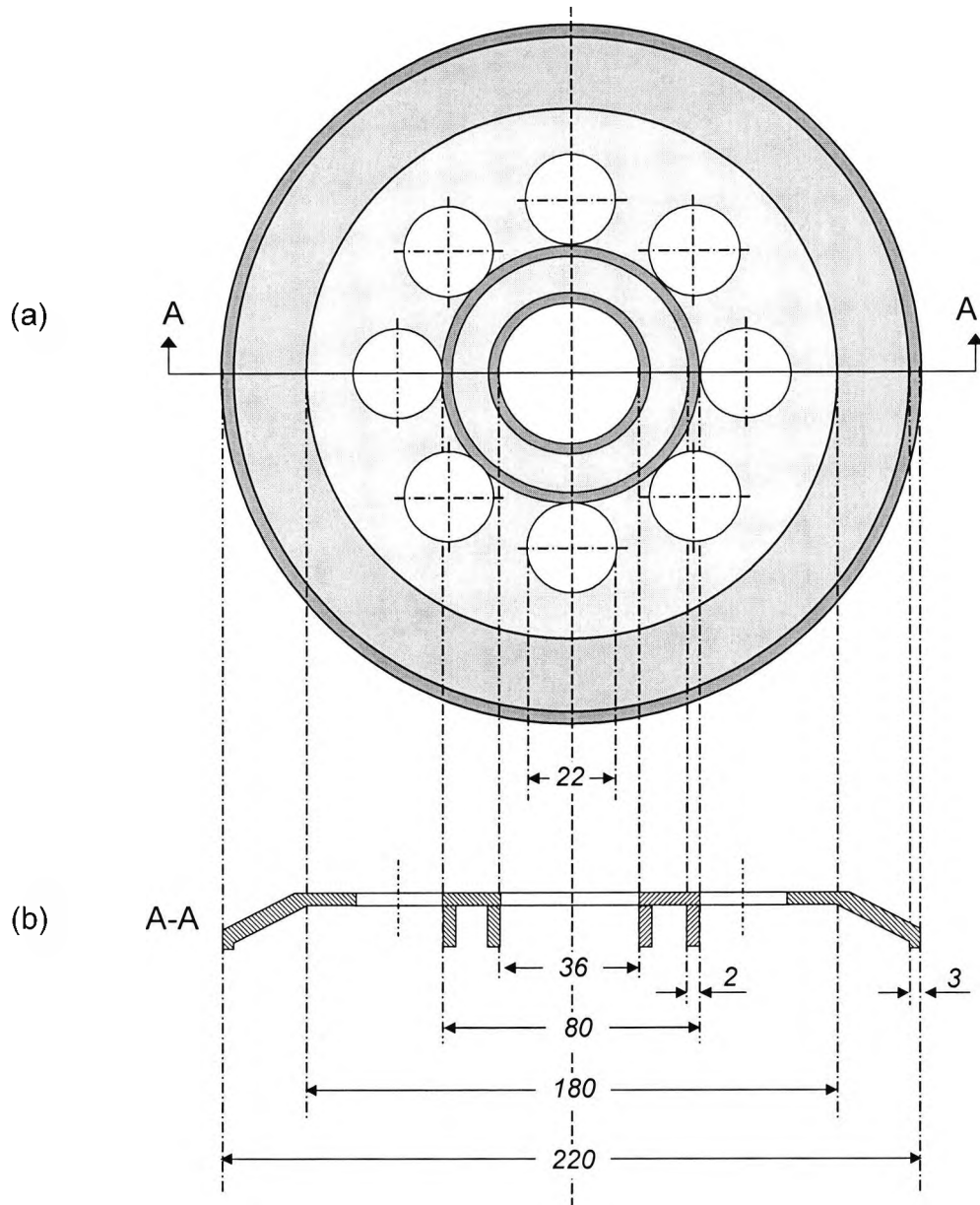


Fig. 3.4 Schematic diagram of the top plate: (a) bottom view and (b) longitudinal section through A-A; (dimensions in mm, not drawn to scale).

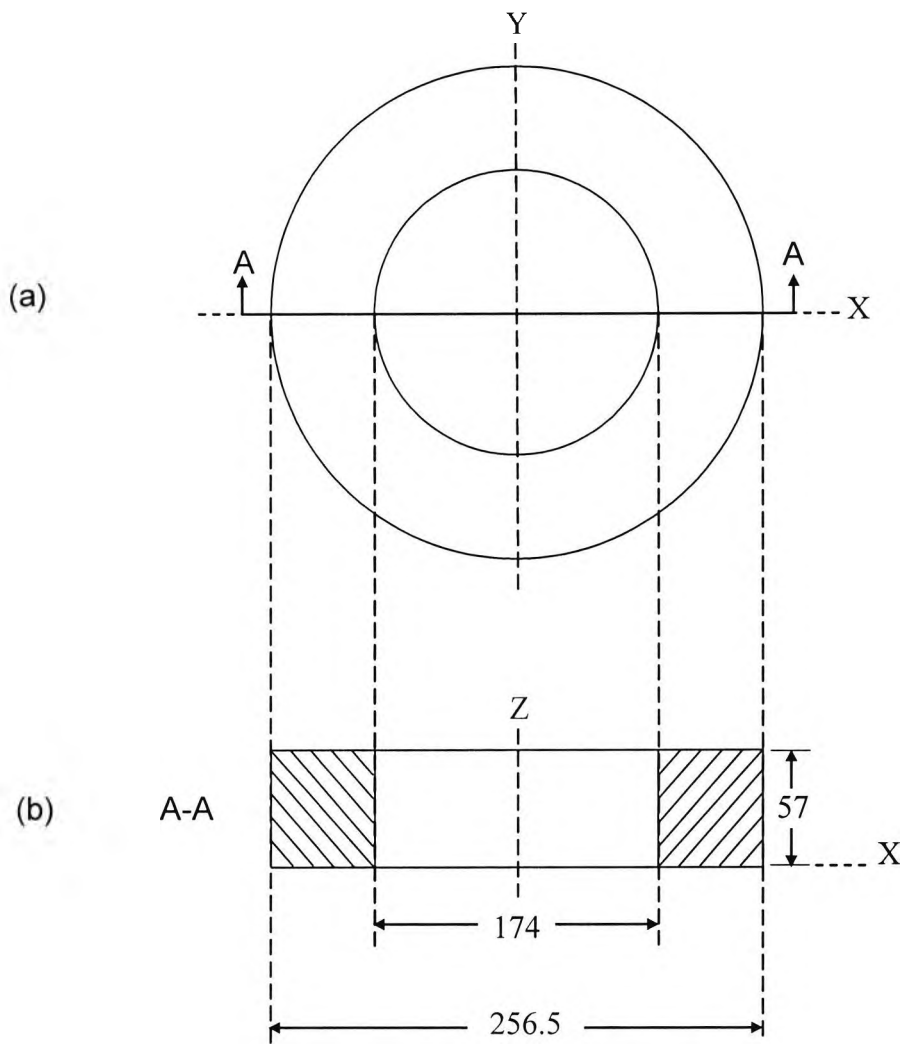


Fig. 3.5 Schematic diagram of the toroidal core: (a) top view, (b) longitudinal section through A-A (dimensions in mm, not drawn to scale)

The toroidal construction of the core shown in Fig. 3.5 is advantageous in facilitating brush contact with every turn of a winding. If the rectangular form is used, a simple slider can operate on only one leg, and even a double slider can utilise only two of the four legs. The use of a slider operating directly on the turns of the winding provides a simple and inexpensive means of obtaining the low voltage between adjacent contact points which is necessary to secure efficient operation.

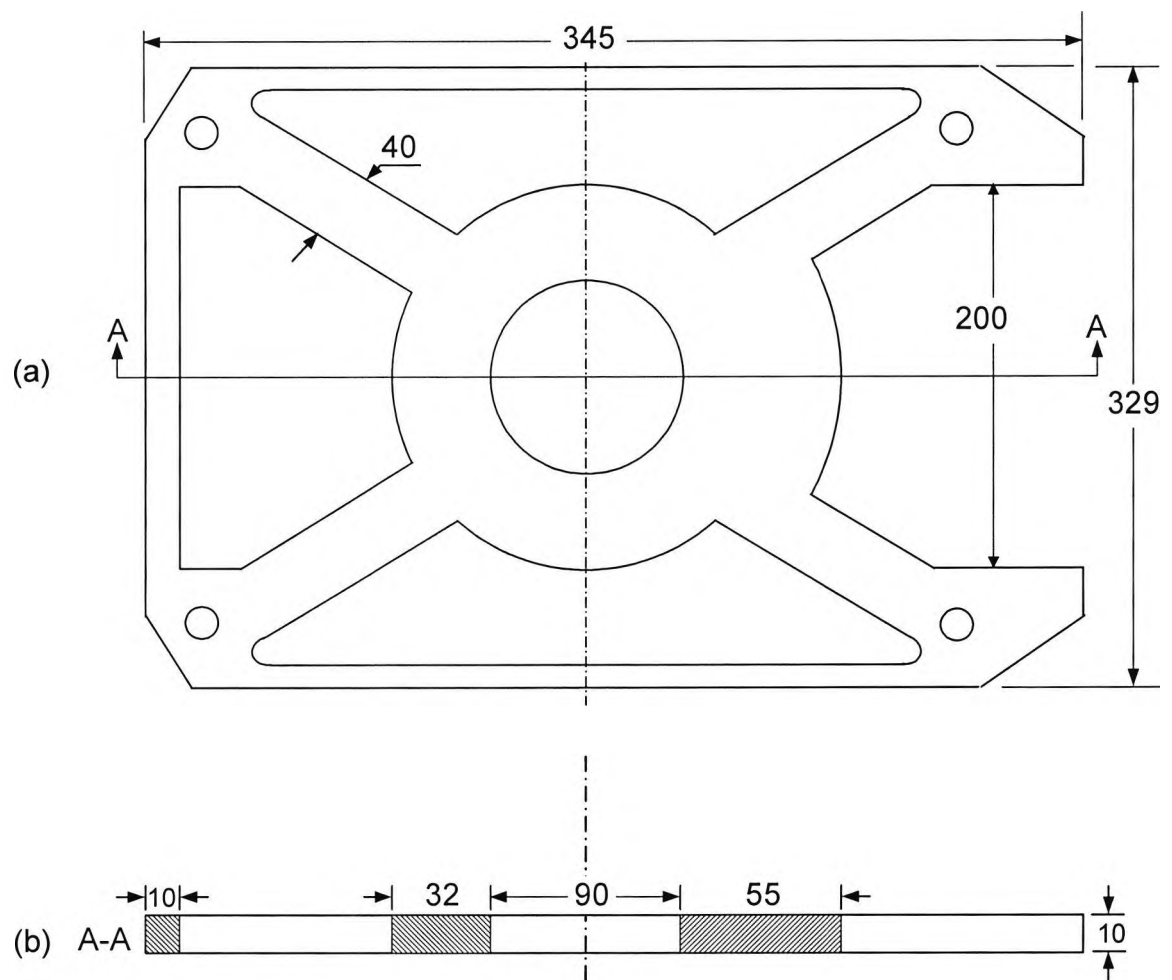


Fig. 3.6 Schematic diagram of the base plate: (a) top view and (b) longitudinal section through A-A, (dimensions in mm and not drawn to scale).

3.2. Development of basic finite element model of single-phase commercial variable transformer

Figures from Fig. 3.7 to Fig. 3.13 show various stages of 3D FE model development of variable transformer type TS1225. The basic model-building strategy for 3D models in OPERA-3d involves the definition of a 2D base plane, which contains the 'foot prints' of all the geometric features of the device being modelled. The base plane is then extruded or swept through space in the third dimension to create the volume discretisation. The typical model shown in Fig. 3.23 contains over 400k 8-noded hexahedral elements including the air regions

surrounding the transformer. It has been used to calculate the magnetic field distribution in the transformer for various linear and non-linear magneto static cases with and without eddy current effects using ELEKTRA and TOSCA, the analysis models for OPERA-3d.

As mentioned earlier the 3D FE model of the transformer was built by defining all the geometric features of the transformer on a 2D 'base plane' in X-Y coordinates, and extruding it in the third Z direction. For this, various modelling tool 'commands' provided by OPERA-3D were used.

3.2.1. Finite Element Model Definition

The FE modelling of variable transformers starts with the definition and realization of its 3D FE models. For this various model definition commands provided by the Opera-3d pre-processor module were used. The following section describe some of the main commands that were used both in the keyboard and batch command (through 'command input files') modes.

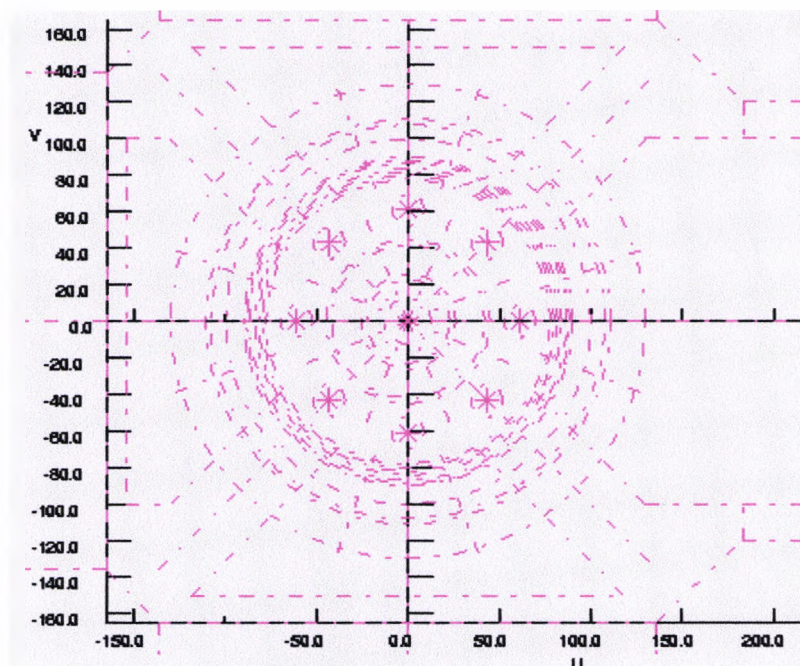


Fig. 3.7 Definition of construction lines outlining all major geometric features on the base plane.

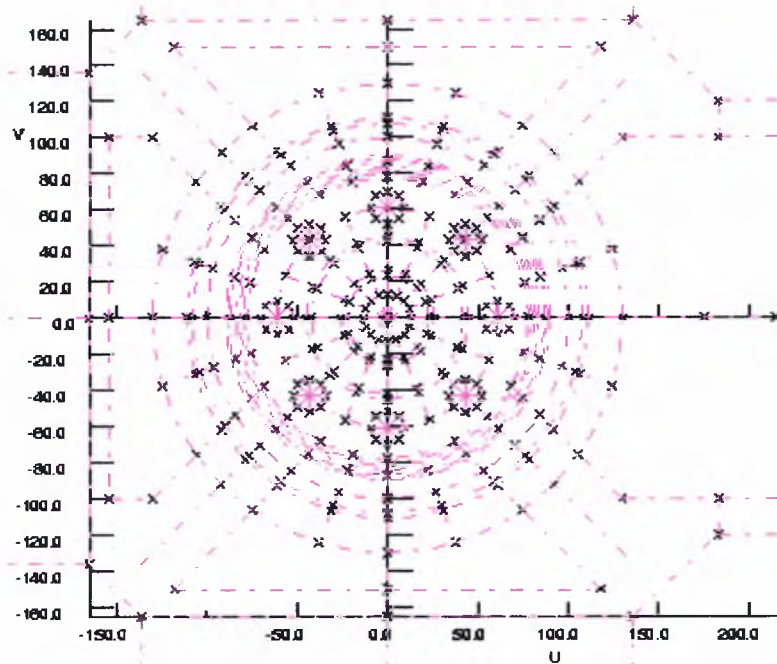


Fig. 3.8 Use of construction lines to define points giving the geometric features of the transformer.

Points to define the corners and mid-side points of the facets in the base plane Fig. 3.7 and Fig. 3.8 are defined by using the graphics cursor or the keyboard.

(f) Facet definition mode: Facets (Fig. 3.9) are defined by connecting the points on the base plane. Facets can be triangles or quadrilaterals with straight or curved edges. Points are selected in sequence as corners (with menu item Corner or cursor hit C) or mid-side points (with menu item Mid-side or cursor hit M). For triangles or quadrilaterals with no mid-point on the fourth side, menu item Close or cursor hit F can be used to close the facet. Sides with mid-side points are quadratic. The mid-side points must be between the $\frac{1}{4}$ and $\frac{3}{4}$ points along the length of the side (this is verified by the 'Check' command. If the mid-side point is not half way along the side the discretisation will also vary quadratically, with smaller elements near the corner which is closer to the mid-side point. This can be used to grade the mesh even for straight-sided facets. Points, which have been used as corners, cannot subsequently be used as mid-side points, and vice-versa.

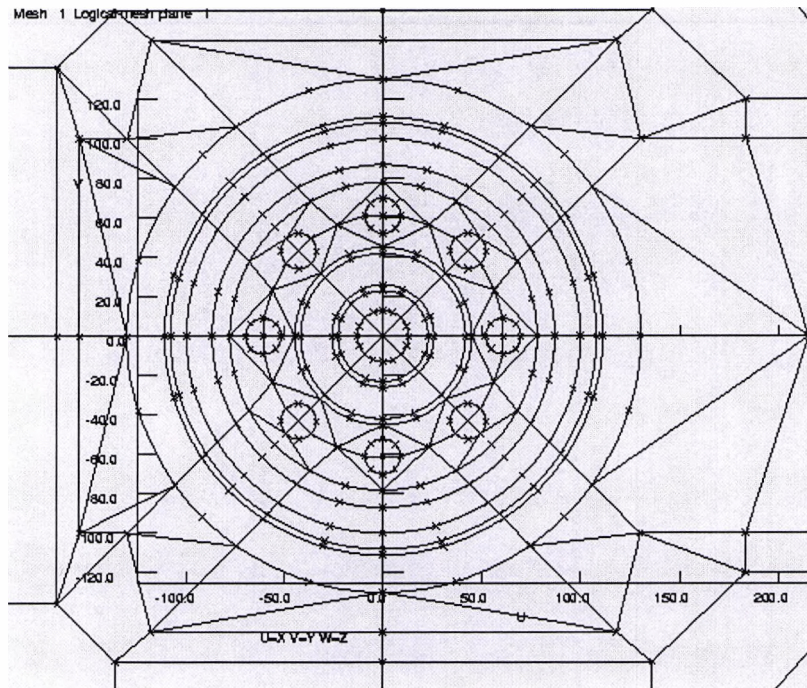


Fig. 3.9 Definition of 2D surfaces (facets) on the base plane by connecting predefined points.

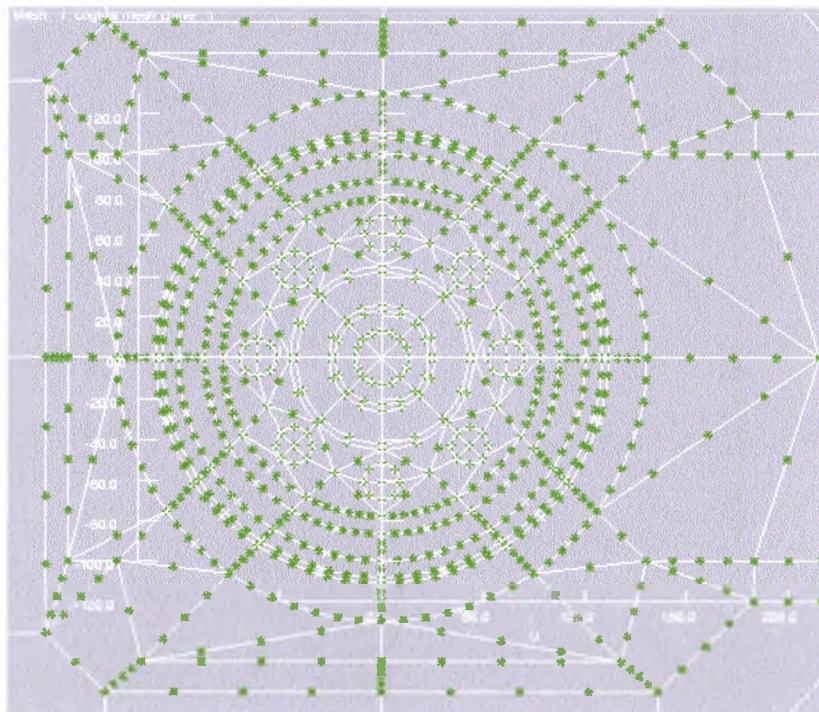


Fig. 3.10 Subdivision of facets on the base plane.

(g) Base plane subdivision mode: The volumes created by extruding the initial surface plane (base plane) are treated as super-elements. They are normally divided into smaller elements that are used for the actual finite element approximation. The division of the volume into elements is determined by the subdivision defined for the facet edges and the subdivision specified for each layer of mesh created by an extrusion operation Fig. 3.10.

A default subdivision of 1 is initially set for all facet edges. When all the edges have been updated, the program will reply that the subdivision is complete. Only regular subdivision is supported by the analysis programs; opposite faces of the volumes must have equal numbers of divisions. The subdivision defined for an edge is therefore carried through and displayed for all adjoining facets.

Triangular facets are meshed by mapping onto a quadrilateral with 2 corners coincident therefore triangles must have 2 sides with the same number of subdivisions. It is not possible to leave the subdivision phase until this condition is satisfied.

The subdivision of each edge is uniform, unless the edge is a quadratic line with the mid-point not at the geometric mid-point of the line. In that case the elements at the end of the edge closer to the mid-point will be smaller than those at the other end.

(h) Extrusions mode: Once the initial surface set of facets has been defined and subdivisions assigned to the edges, the program moves on to applying extrusion operations to the set of facets Fig. 3.11— Fig. 3.14. There must be at least one extrusion operation applied to the set of facets, but many others may be needed to define the complete problem. It is also possible to add more extrusions to a completed mesh using the Extend command. The Extend command must be used to add the second and subsequent extrusions if the data is defined in menu mode.

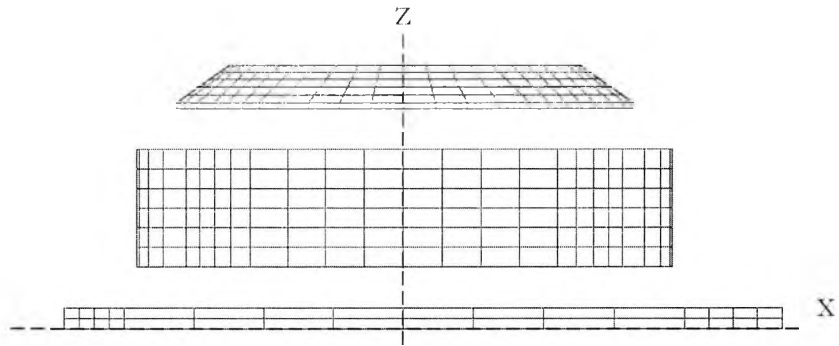


Fig. 3.11 2D wire-frame representation of the extruded 3D finite element model of the variable transformer TS 1225, showing the main constructive features.

Subdivision: This specifies the number of layers of elements there will be between the two planes. The subdivision is ignored when define is being used for conductor elements.

Linear or Quadratic: The W-directed lines can be linear or quadratic. The lines are created initially linear, i.e. straight, but if quadratic is selected, a mid-extrusion plane of points is also created, at the geometric mid-points of the lines. This means that quadratic lines can be changed to be curved, or to have non-uniform subdivision by moving the points on the mid-extrusion plane away from the geometric mid-points of the lines. The mid-points should be between the $\frac{1}{4}$ and $\frac{3}{4}$ points along the length of the extrusion.

(i) Material definition mode: The extrusion operations create a discretisation of space. It is now necessary to set the material and mesh properties within each volume.

The first compulsory keyword is the material name. The second compulsory keyword is the potential type. These are 'Reduced'; 'Total' and 'Vector'. The Reduced scalar potential can be used for any material and must be applied to volumes, which will contain source conductors. It should only be used in non-AIR materials if the source conductor and material geometry would make a total scalar potential volume multiply connected, or if source currents flow in the iron. The Total scalar potential should be used for electrostatics problems; in magnetic problems; it can also be used for AIR and any non-conducting and

non-linear permeable material. The Vector potential is for conducting material carrying eddy currents in time-dependent analyses.

Optional keywords defining properties are linear, quadratic, scalar, vector and the packing factor.

Linear and quadratic define the element types to be used. Linear elements are 8-noded; quadratic elements are 20-noded isoperimetric. TOSCA allows both element types to be used in one problem. For ELEKTRA all elements must be the same type.

In electrostatic problems (TOSCA), the volume electric charge density is specified by scalar followed by one numeric value.

In magnetostatic problems (TOSCA) with anisotropic materials the local coordinate system for the material is defined by vector followed by 3 Euler angles. If the material is laminated, the packing factor is specified by pack followed by one numeric value which multiplies the permeability in the direction parallel to the laminations (the local XY plane). If the material is to be specified by multiple BH curves, only the vector property is required here to define the local coordinate system for the material. In either case, anisotropy must be switched on in the TOSCA command.

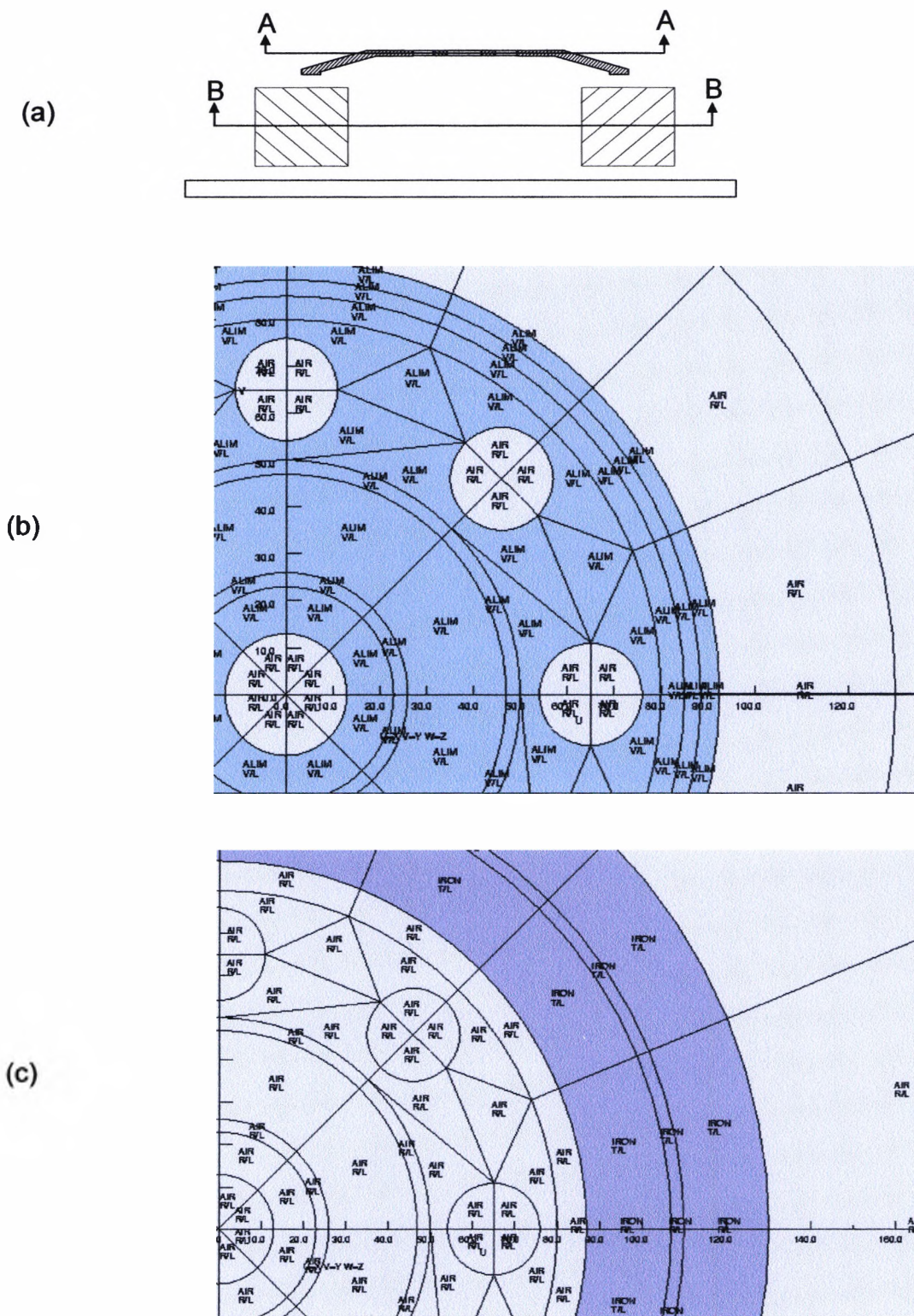


Fig. 3.12 Schematic diagram of the transformer (a); part of the cross-section A-A (b) and part of the cross-section B-B (c).

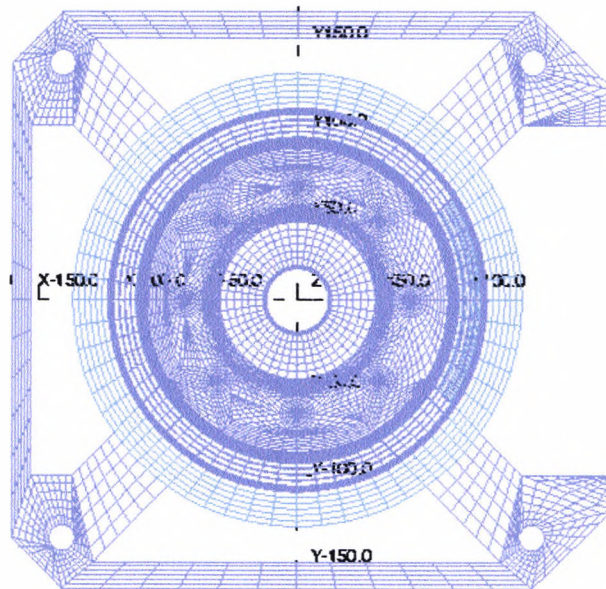


Fig. 3.13 Top view of the FE model showing mesh subdivision.

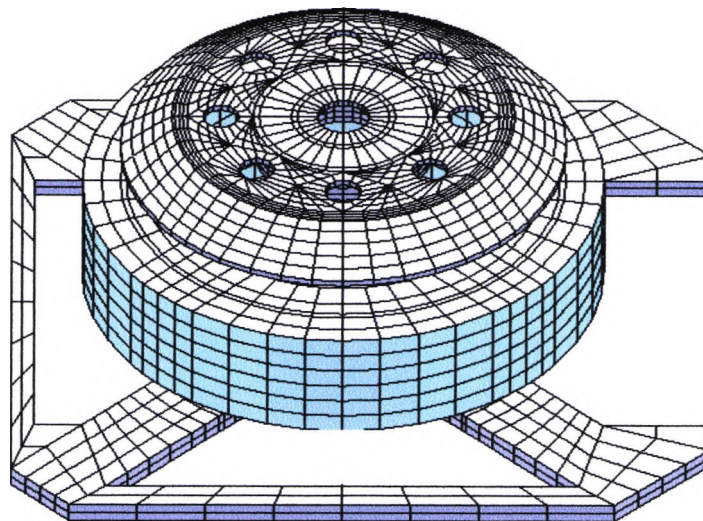


Fig. 3.14 The 3D model is obtained by extrusion of the base plane in the third, Z direction by moving points on mesh planes and transforming sets of points on mesh planes (winding not shown).

(j) Boundary Condition Definition Mode: Boundary conditions can be set on any surface of any volume in the mesh.

i- By restricting the Magnetic field to be 'NORMAL' or 'TANGENTIAL'. This sets combinations of the potentials and derivatives as appropriate for the type of problem and volume concerned shown in Table 3.1.

Table 3.1 Types of normal and tangential boundary conditions used by the software.

	Field Symmetry	Scalar Potential	Vector Potential
Tangential Magnetic or Normal Elec.	$H \cdot n = 0$	$\frac{\partial \phi}{\partial n} = 0$	$A \times n = 0$ $V = 0$
Normal Magnetic or Tangential Elec.	$H \times n = 0$	$\phi = \text{constant}$	$(\nabla \times A) \times n = 0$ $A \cdot n = 0$ $\frac{\partial V}{\partial n} = 0$

n is the normal unit vector to the surface being considered.

ϕ refers to either the Reduced or Total scalar potential.

A vector potential

at the far-field boundary the choice of boundary condition should not influence the accuracy of the solution if the boundary is sufficiently removed from the area of interest.

If there were no symmetry, some (or all) of the far-field boundary would need to be given a Normal magnetic condition to "gauge" the problem.

The default boundary condition at far-field boundary $\frac{\partial \phi}{\partial n} = 0$ (tangential magnetic) will impose this condition.

When the default condition is used in a region of reduced potential (ϕ) only the magnetisation field H_m is tangential.

The field from coils, H_s must also reflect this by correct definition of the complete coil set.

Far field boundary: The solution of a magnetic field model must be truncated artificially at the boundary of the finite element mesh. This leads to errors

because the boundary conditions imposed imply images of the model in the far field boundary.

One simple test that can be used to test the significance of this error is to solve the problem with first zero potential (tangential magnetic $\phi = 0$) assigned at the far field and then with zero normal derivative (normal magnetic $\frac{\partial \phi}{\partial n} = 0$), the true solution will lie between the two.

An alternative faster approach is to calculate the field on the far field boundary, the images will be providing approximately half the field. If the image field is too large the outer boundary must be moved further away.

If the stray field is of primary concern it may be useful to consider the magnetization integral field calculation method available in OPERA. This is weakly affected by the position of the far field boundary.

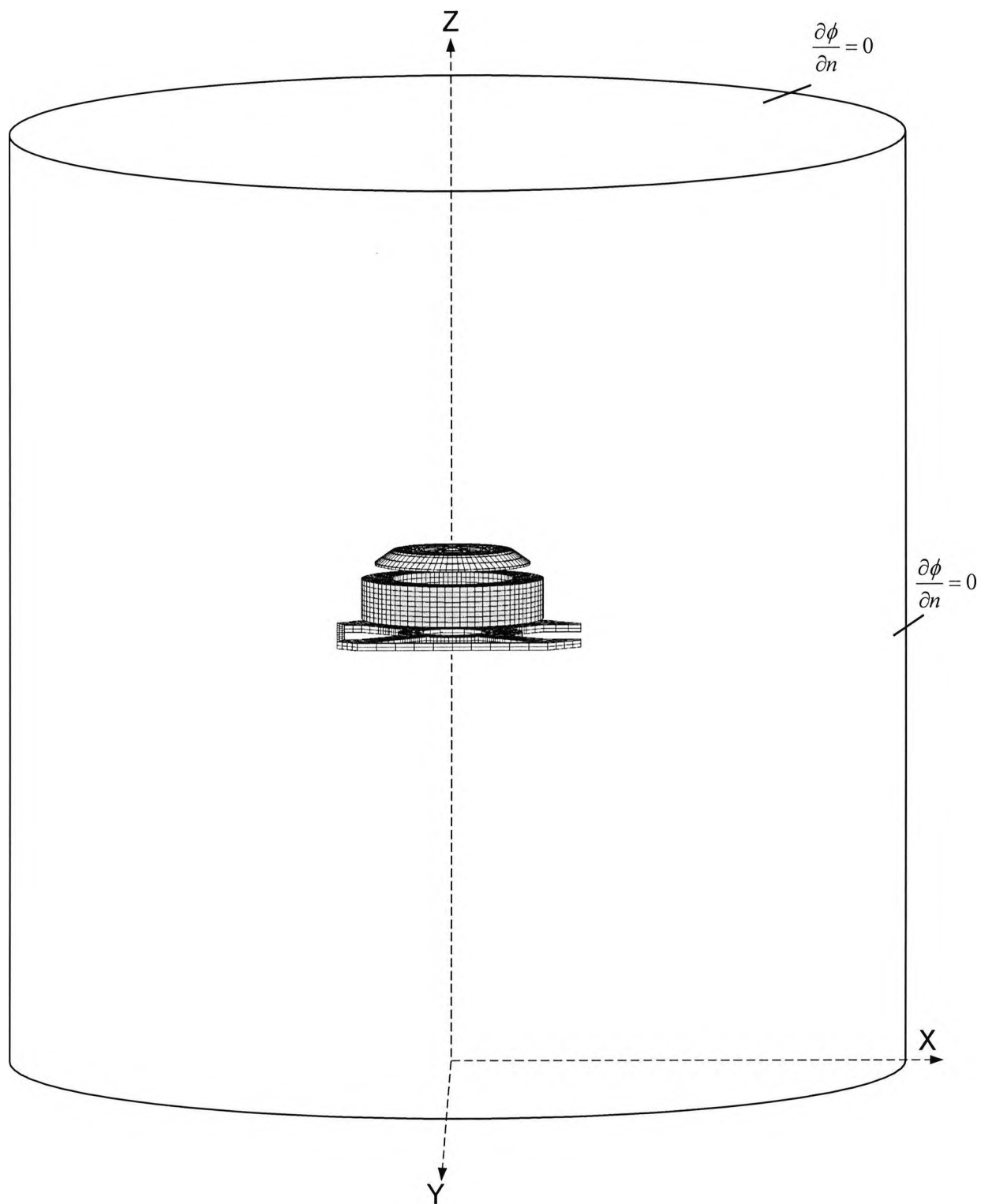


Fig. 3.15 The actual boundary conditions used for the 3D model.

If necessary a potential boundary condition can be assigned in addition to the normal or tangential conditions in order to override the zero values of scalar potential.

ii- By setting values of potential or the normal derivative of scalar potential or components of vector potential.

If potential or derivative boundary conditions are used, a facet can have up to 4 potential boundary conditions, one for the scalar potential and one for each component of the vector potential. Thus, for example, defining a condition on the normal derivative of the X component of the vector potential would overwrite any previously defined condition on the A_x , but would not affect any conditions on A_y , A_z or the scalar potential.

In scalar potential regions, setting a constant potential condition specifies that the tangential components of the field are to be zero and constant derivative specifies the value of the normal field. Non-zero total scalar potential conditions can be used to impose an external field (i.e. a potential difference or m.m.f. across the problem) or to balance enclosed currents in multiply connected geometries. Reduced scalar potential boundary conditions can only have the value zero. The zero derivative condition is the natural condition of the finite element mesh and need not be assigned explicitly.

In vector potential regions, setting A_x , A_y or A_z to zero implies that the current density in that direction is also zero. The constant electric scalar potential boundary condition should also be set on surfaces where the tangential components of current density are zero. This constant should in general be zero, unless the voltage is driving the problem. The boundary condition names are stored as labels on each facet and can be used to select parts to the model in the Display command.

3.3. Definition of conductors

As mentioned earlier, for 3D modelling purpose the continuous N-turn helical winding of the variable transformer was replaced by N single-turn coil, tightly and compactly wound around its toroidal core. As mentioned earlier in section 3.1, even with this simple function, definition of conductors in such variable transformers poses a substantial challenge because of its geometric configuration.

In OPERA-3d conductors are defined using the conductor command which enters the various conductor sub-command modes. In this mode new conductors may be defined, existing conductors edited or erased, the parameters of the current set of conductors may be listed or they may be stored in a conductor data file. The following sub-commands are used:

Sub-command	Function
Define	Define a new conductor
Erase	Erase one or several conductors
Modify	Modify one or several conductors
Print	Print details of one or several conductors to the terminal and the log file
Quit	Leave the conductor command
Write	Write a data file with commands to define all the conductors

The package provides 'templates' for a wide range of pre-defined conductor geometries, such as solenoid, racetrack, bedstead, etc. With the availability of flexible and user definable local and global coordinate systems Fig. 3.16, the software allows to define accurately virtually any configurations of these conductor geometries.

To enable conductors to be oriented in space correctly, local coordinate systems can be defined, and to reduce the amount of data necessary symmetry and reflection codes can be used to replicate a basic shape.

Parameters common to all conductors including the local coordinate systems and replication parameters are described first, before details of the conductor shapes are given and, lastly, the parameters of the sub-commands are listed.

In order to define the single-turn coils of the variable transformer, the template for the generally oriented racetrack Fig. 3.17 was used. Table 3.2 shows various coordinate systems and geometric parameters used for this purpose.

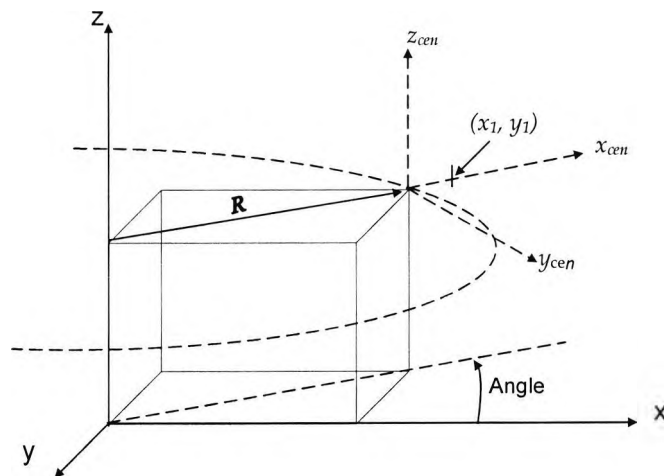


Fig. 3.16 Global and local coordinate systems used for definition of conductors.

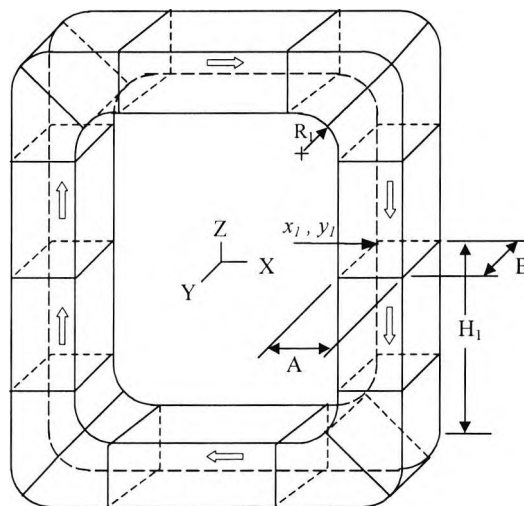


Fig. 3.17 Wire frame representation of the generally oriented racetrack conductor showing the local and global coordinate systems and defining conductor geometric parameters.

Table 3.2 Various coordinate system, and geometric parameters used to define a general racetrack conductor.

Local coordinate system 1	$X_{CEN}, Y_{CEN}, Z_{CEN}, ANGL$
Local coordinate system 2 (origin)	X_0, Y_0, Z_0
Local coordinate system 2 (Euler angles)	T, P, S
Conductor cross section	A, B
Local coordinates of bottom inside corner	X_1, Y_1
Half length and corner radius	H_1, R_1
Current density, symmetry and phase angle	CURD, SYMM, PHAS
Reflections in local coordinate system 1 coordinate planes	IRXY, IRYZ, IRZX
TOLE	TOLE

The continuous winding of one of the designs of variable transformer modelled comprised of 296 turns each of which were represented by single-turn coil. Because these turns, lying side by side on the outer surface, overlapped on other surfaces (due to the significant difference in circumferential lengths of the inner and outer surfaces of the toroidal core), the outer side of to the winding is wound through a serrated moulding with a total number of 325 displacements (d) along the outer surface 2π (track line), i.e. each turn is displaced circumferentially by an amount $d = 2\pi/325$ radians, To make the single turns wound similar to the real winding the turns were divided into two groups one slightly bigger in size than the other to allow the overlapping. The smaller sized turns (odd turns) were placed at odd-number positions (e.g., 15, 17, 19,,309) as shown in Fig. 3.18 and the large ones (even turns) were placed at even-number positions (e.g., 16, 18, 20,,310) as shown in Fig. 3.19.

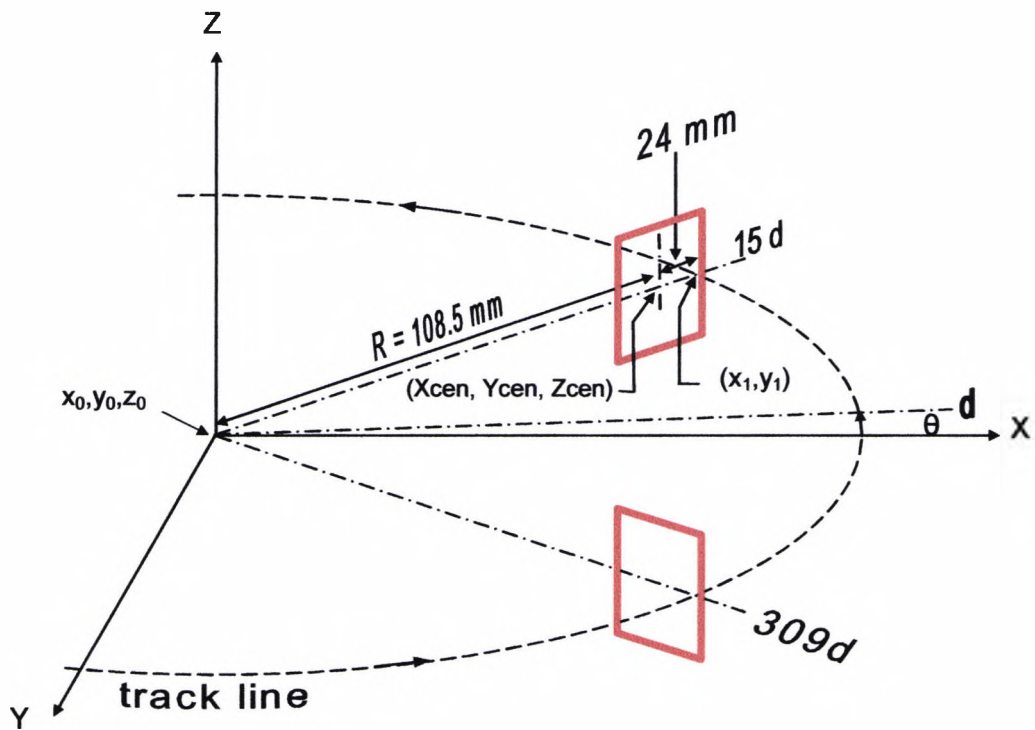


Fig. 3.18 Schematic diagram showing the positions of odd turns from 15 to 309; total number of turns 148 (not drawn to scale).

Thus:

$$\text{Displacement } (d) = (2\pi / 325) \text{ radian,}$$

$$\theta = d * (180 / \pi) \text{ degrees}$$

$$X_{cen} = R \cos i \theta$$

$$Y_{cen} = R \sin i \theta,$$

$$Z_{cen} = H_1 + Z$$

$$\text{Angle position of } i\text{-th turn} = i * \theta$$

$$\text{For odd turns } i = (15, 17, 19, \dots, 309)$$

$$\text{For even turns } i = (16, 18, 20, \dots, 310)$$

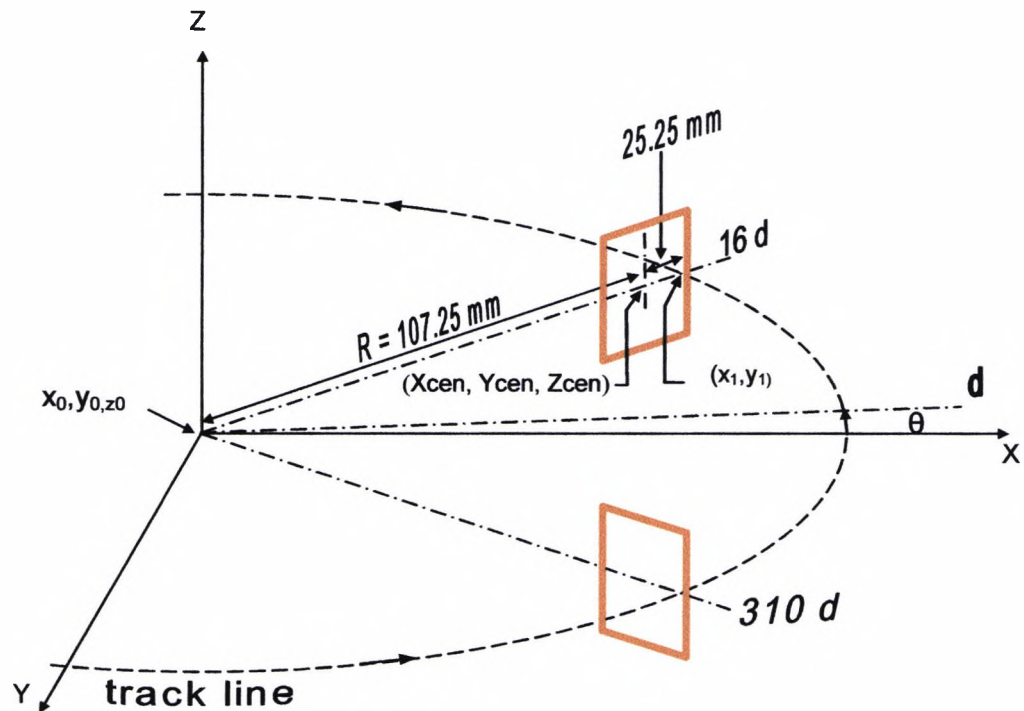
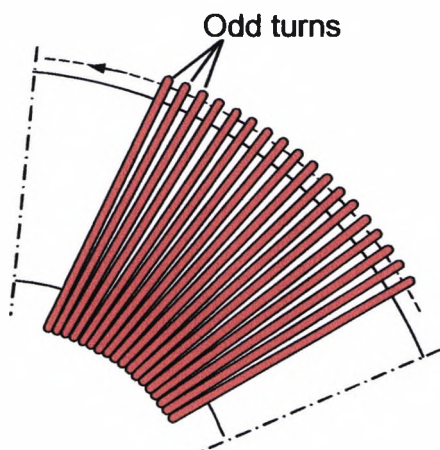


Fig. 3.19 Schematic diagram showing the positions of even turns from 16 to 310; total number of turns 148 (not drawn to scale).

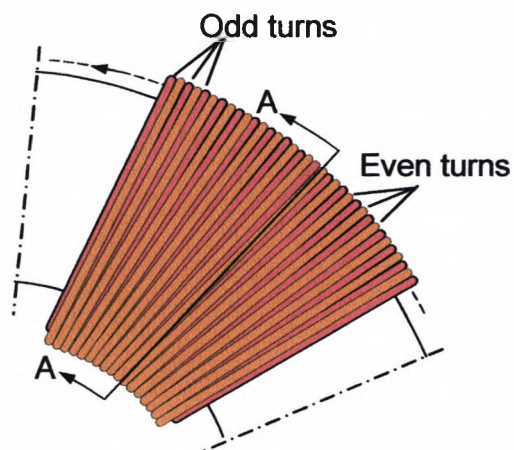
In order to automatically calculate the positions and generate the odd and even turns a two command input files developed, one for the odd turns and the other for the even turns see appendix 2.

The generation processes of the turns are shown in Fig. 3.18 and Fig. 3.19.

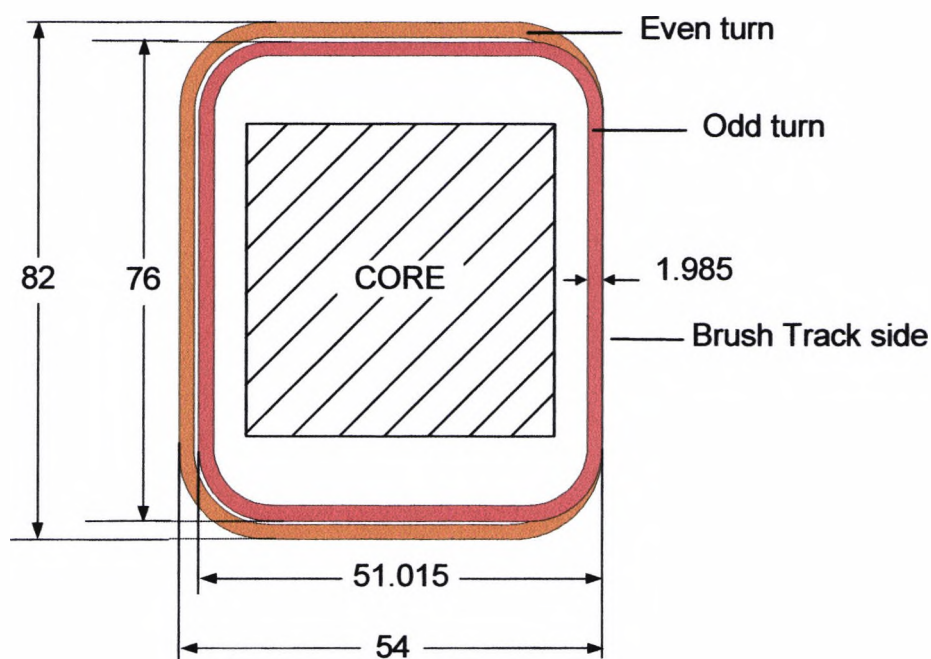
Fig. 3.20 shows compact arrangement of these overlapping turns around the toroidal core.



(a)



(b)



(c)

(d)

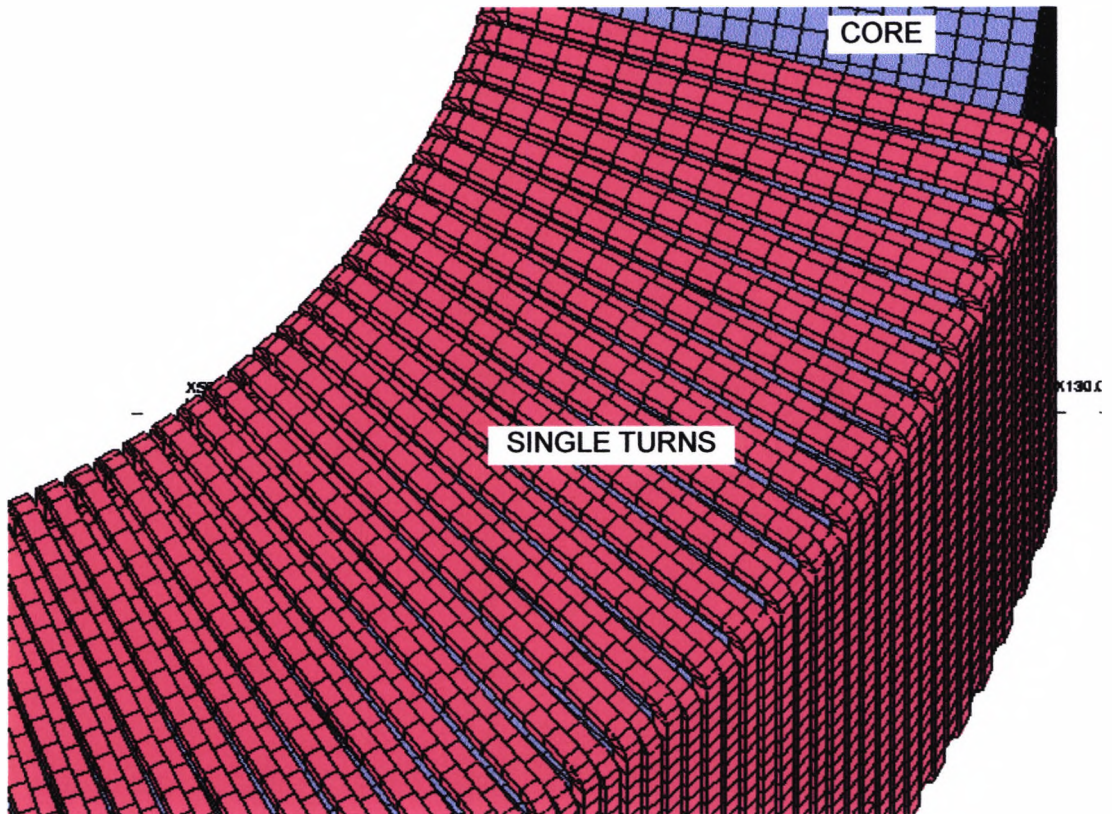


Fig. 3.20 Schematic diagram showing the generation of single-turn coils on the toroidal core; (a) odd turns, (b) odd and even turns, (c) longitudinal section through A-A showing the over-lapping of turns, (d) 3D view of the overlapping turns (dimensions in mm not drawn to scale).

The current flowing in the conductors is defined by the current density. For conductors with changing cross section the current density applies to the first face of the conductor. For steady state alternating current problems the phase angle of the current density can also be set. The phase angle is the angle in degrees around the ac cycle at which the current density is maximum.

The fields from conductors are calculated using an adaptive integration method, which requires supplying a tolerance. This specifies the error tolerance on the flux density in the units system being used. The field from conductors without a tolerance parameter, or with tolerance set equal to zero is calculated to a tolerance of 10^{-3} Tesla.

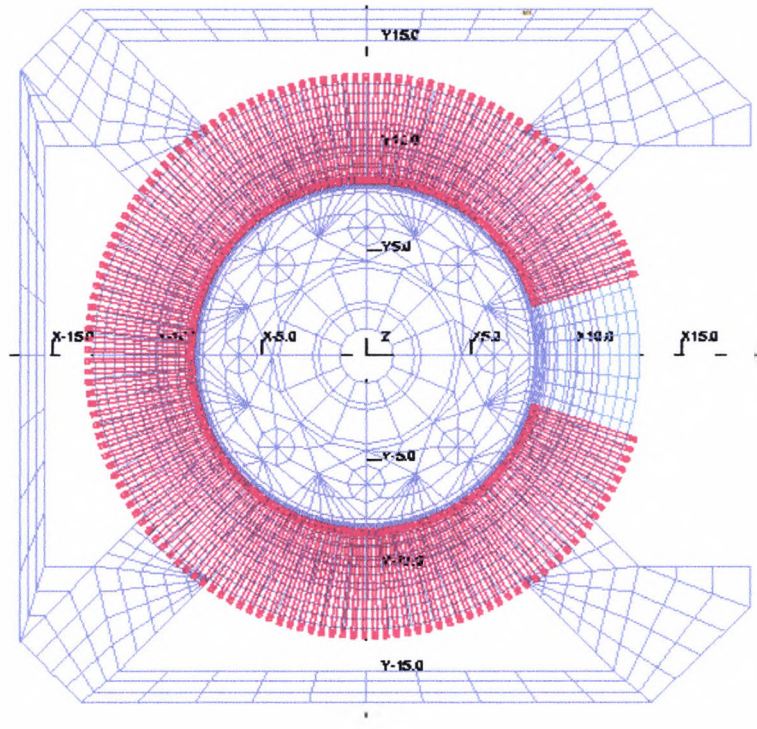


Fig. 3.21 Top view of the 3D FE model of the variable transformer showing half of the conductor turns.

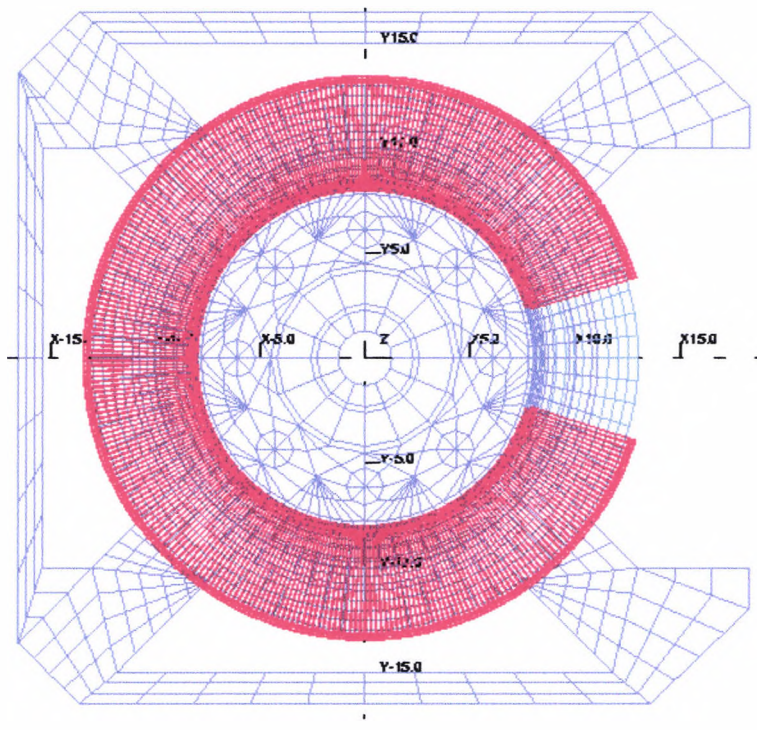


Fig. 3.22 Top view of the 3D FE model of the variable transformer showing all the conductor turns.

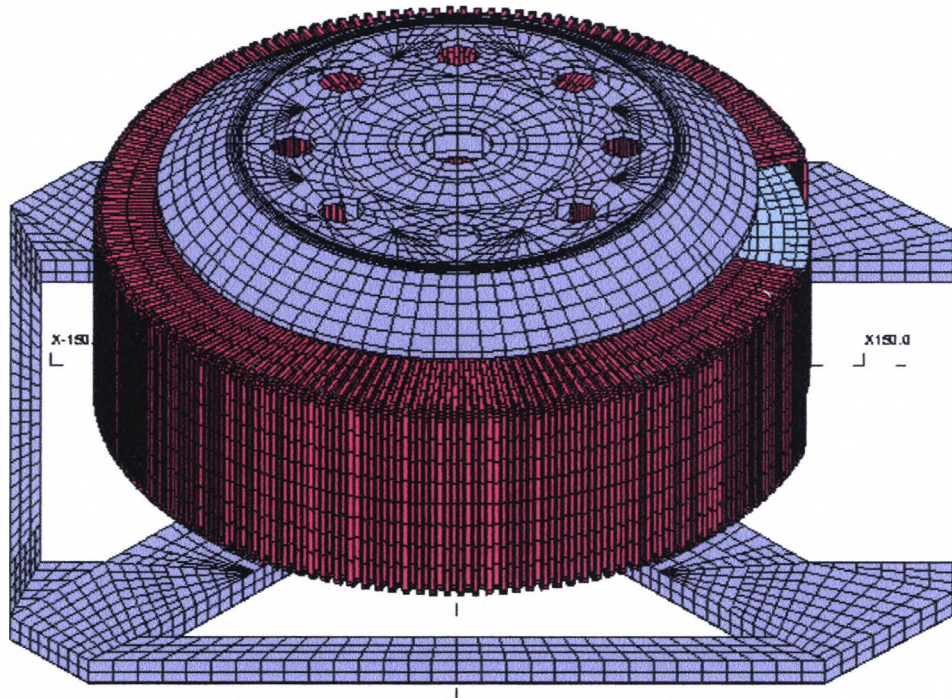


Fig. 3.23 Full 3D FE model of the commercial variable transformer type TS1225 used for modelling investigations.

Using the modelling methodologies described earlier a full 3D model of the commercial variable transformer shown in Fig. 3.23 was developed. This basic model was used to obtain the steady state and transient solutions of field equations by which the magnetic field distributions in the 3D problem domain of the transformer were obtained. Such simulations allow the investigation of magnetic field distribution in and around the transformer core taking into account saturation and eddy-current effects for various design parameters (e.g. geometric, material and electrical) and brush and tap positions under no-load and full-load operational conditions. The modelling results may be used to calculate the copper and iron losses in the transformer which include hysteresis, eddy-current and circulating-current losses primarily in the transformer core and in any short-circuited winding turns (caused, for example by insulation damage and brush position) and in other constructive elements (top and base plates, brush gear, etc.). In addition, such modelling results are essential in the investigation of the nature and magnitude of any magnetic forces acting on the winding for various taps and brush positions. This forces may cause the tightly wound turns to vibrate (at power and at higher frequencies in the presence of

harmonics) which may result in insulation damage and ultimately lead to shorted turns. The FE models may also be used to study and quantify the effects of harmonics of primary and secondary (load) currents on magnetic field distribution and losses in the transformer. The validation of modelling results against experimental data is of fundamental importance in the applicability and possible refinement of FE modelling methodologies described above.

Chapter 4.

Experimental Investigation of Magnetic Fields in Variable Transformers and Validation of Finite Element models

4.1. Introduction

Experimental investigations of one of the designs of commercial variable transformers TS1225 were carried out to validate and refine the FE models described in the previous chapter. The main aim was to measure the magnetic field distribution in air around the toroidal core for various operational regimes and configurations of the transformer.

This was needed to refine and validate the FE models, and to develop confidence in subsequent modelling experiments carried out for more complex operational regimes and various design variables. For experimental investigations, a number of different experimental models of the TS1225 variable transformer were used. A special experimental apparatus was constructed to measure reliably and accurately various components of magnetic flux density values at numerous points in the 3D space around the toroidal core. The apparatus shown in Fig. 4.1 was made entirely from non-magnetic material, especially designed to hold the Gauss meter (GM05) and fix the position of the Hall probe in the cylindrical system of coordinates r , θ , z . It allowed the Hall probe to be placed at various positions of interest in the 3D space around the core easily and accurately. The technical specifications of the Gauss meter used are given in Appendix A. The experimental investigations were carried out at Claude Lyons Limited, UK who provided the necessary experimental facilities, various equipment and local supervision.

The experimental work was carried out in the following stages:

- (a) Building of the appropriate apparatus for measurement.
- (b) Set-up of the experimental models.
- (c) Taking measurement of flux densities using the above models.
- (d) Analysis of experimental results.

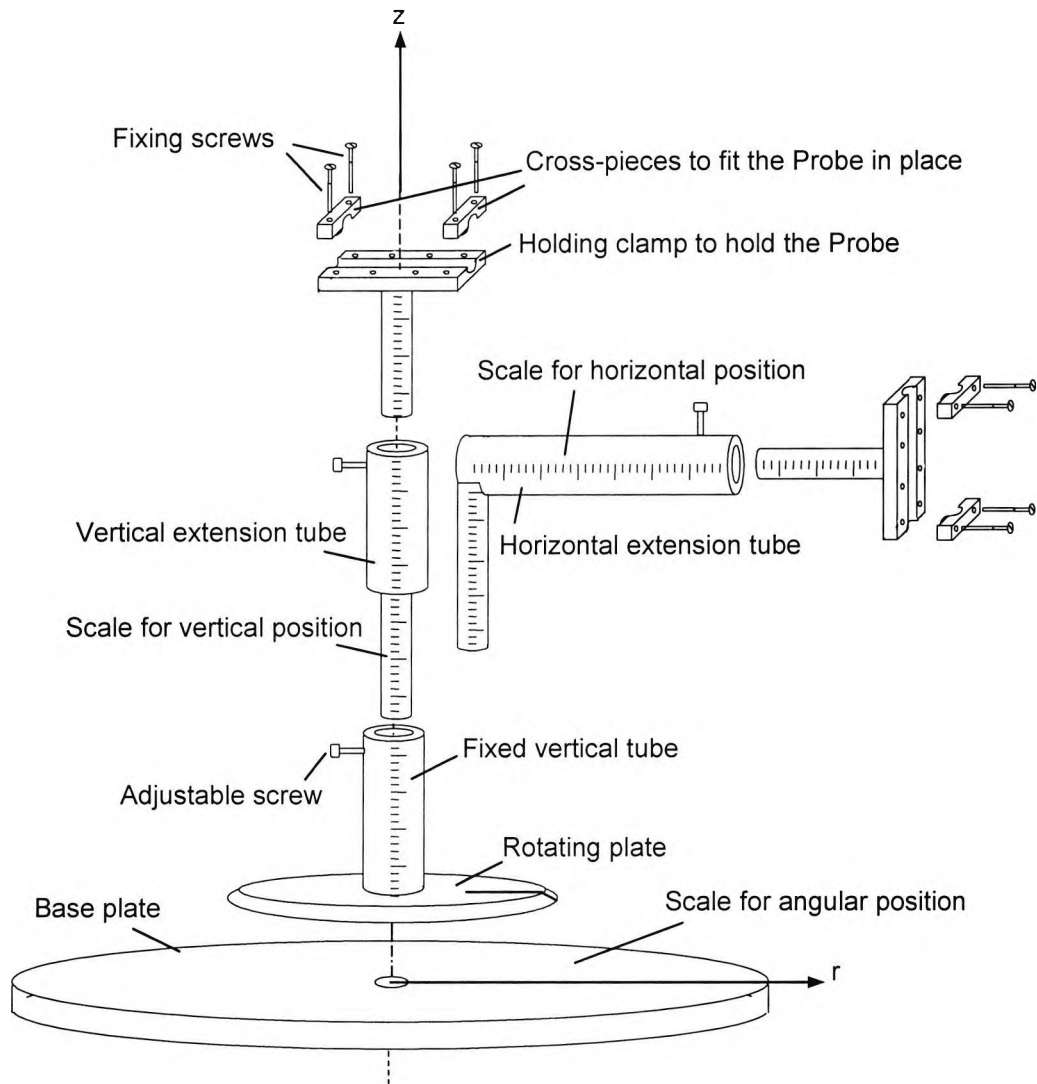


Fig. 4.1 Simplified diagram of the experimental apparatus (made of non-magnetic material) used for experimental investigation of variable transformers (not drawn to scale).

4.2. Experimental Models for Investigations

4.2.1. Experimental apparatus

As mentioned earlier the experimental apparatus shown in Fig. 4.1 was designed specially for the measurement of field distribution around a variable transformer (type TS1225) using a Gauss-meter (GM05). The apparatus was entirely made from non-magnetic material. It comprises a simple construction which consists of the following component parts; the base and rotating plates, vertical and horizontal extension tubes, and the holding clamp to hold the Gauss-meter Probe. The apparatus provides three degree of freedom and allows varying the position of the Hall probe in the r , θ , z spatial co-ordinates around the transformer core. The core of the transformer under investigation is placed concentrically on the stationery base plate (Fig. 4.2) and the rotating plate, mounted on it rotates on a 360-degree scale allowing angular positioning of the Hall probe. The Gauss-meter with the Hall probe is held in position on the holding clamp by means of screws.

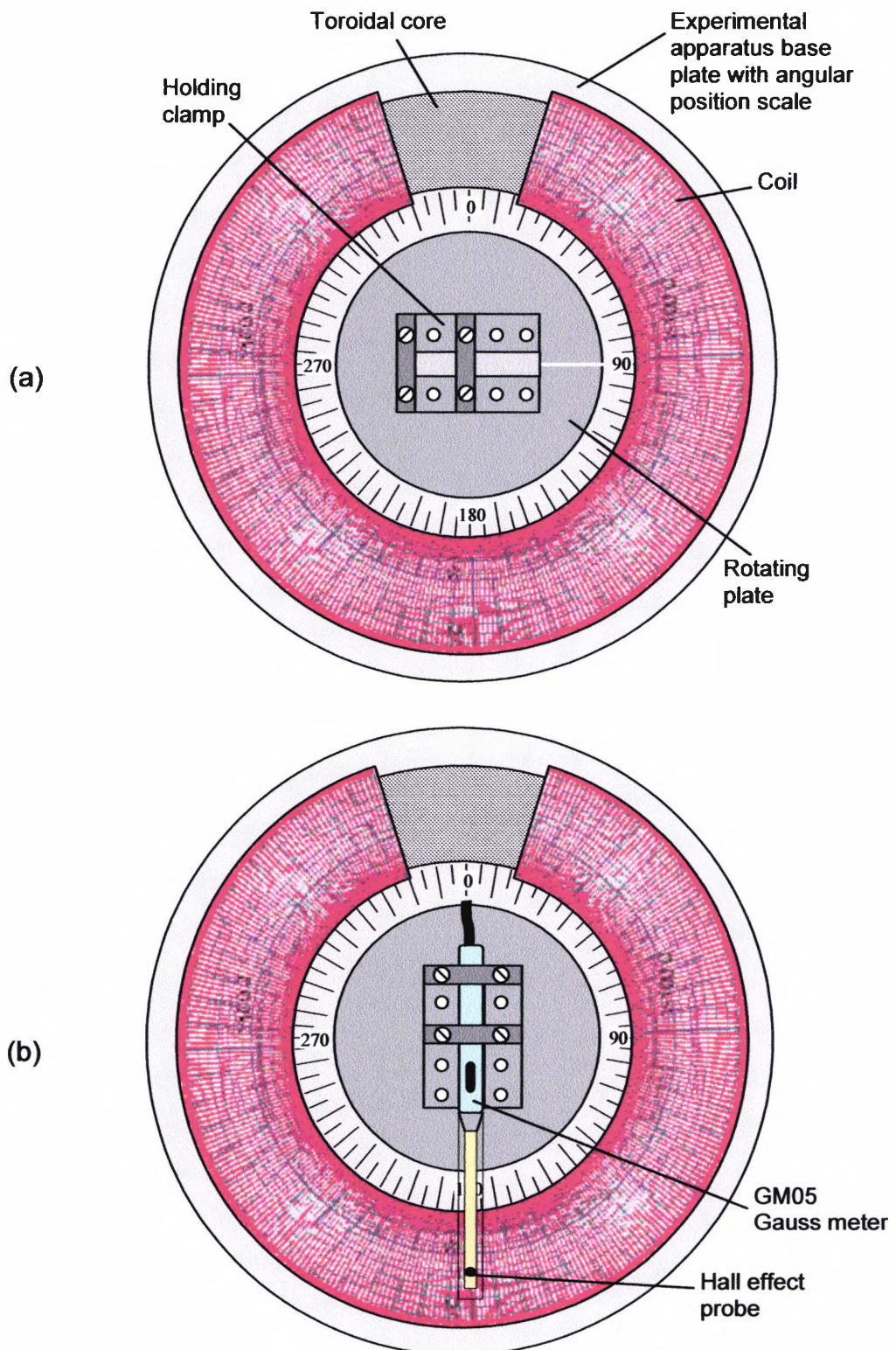


Fig. 4.2 Top view of the transformer core (without top plate) placed concentrically on the experimental apparatus: (a) without Gauss-meter, (b) with Gauss-meter.

Thus the vertical and horizontal positions of the Hall sensor are valued and measured on the mm scales drawn on the vertical and horizontal tubes.

For measurement purposes, the angular position θ of the hall probe was valued from 0 to 360° by an angular of 5° for each horizontal and vertical position r and z . Fig. 4.2 (a) and (b) show the experimental apparatus with angular positions marked on its base plate. Fig. 4.3 and Fig. 4.4 show the basic placements of the Gauss-meter for the measurement of magnetic field component above and around the transformer core.

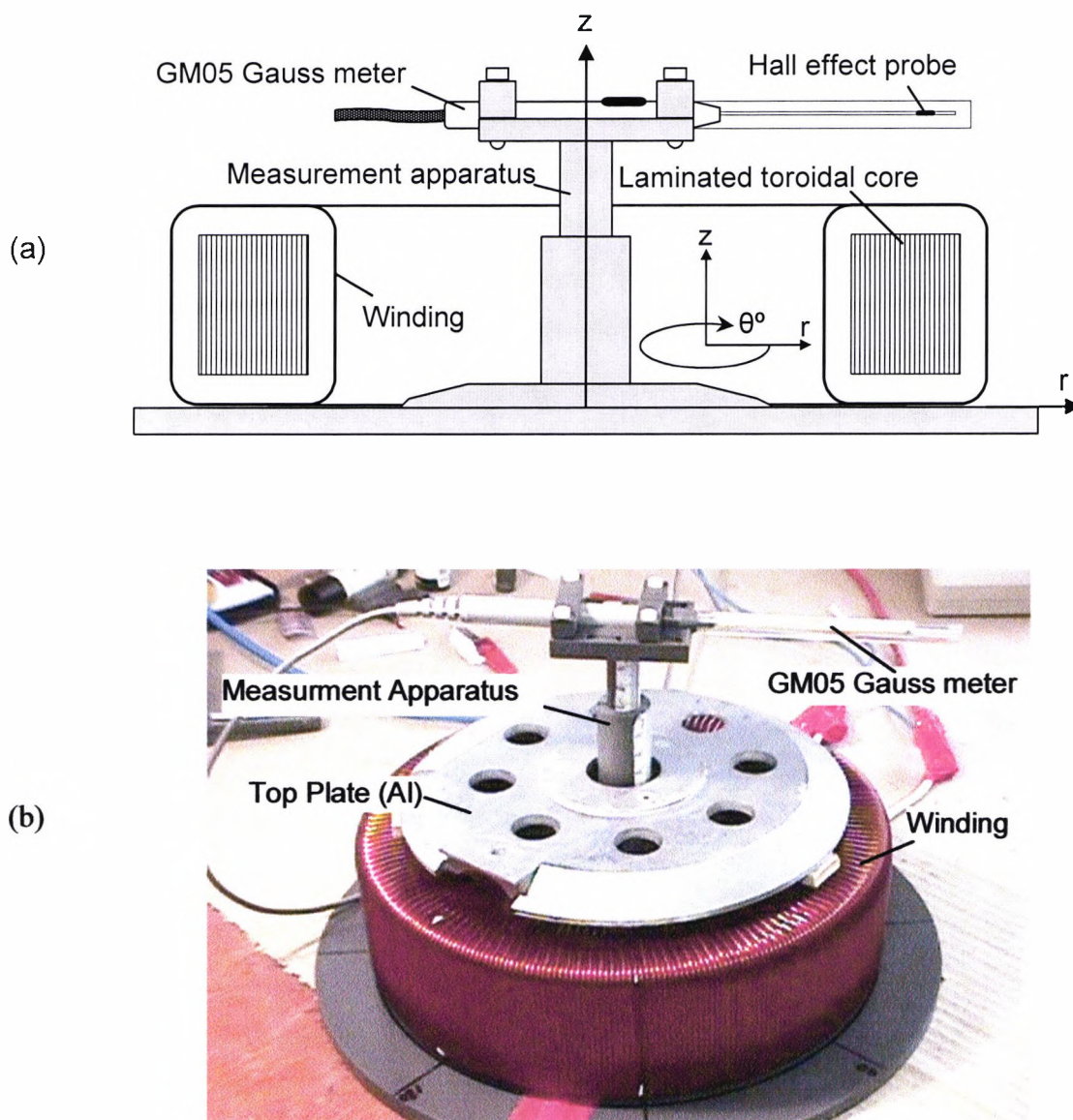


Fig. 4.3 Arrangement of experimental apparatus for the measurement of magnetic field above the toroidal core of the transformer: (a) schematic diagram, (b) photograph showing the actual transformer used (brush gear not shown).

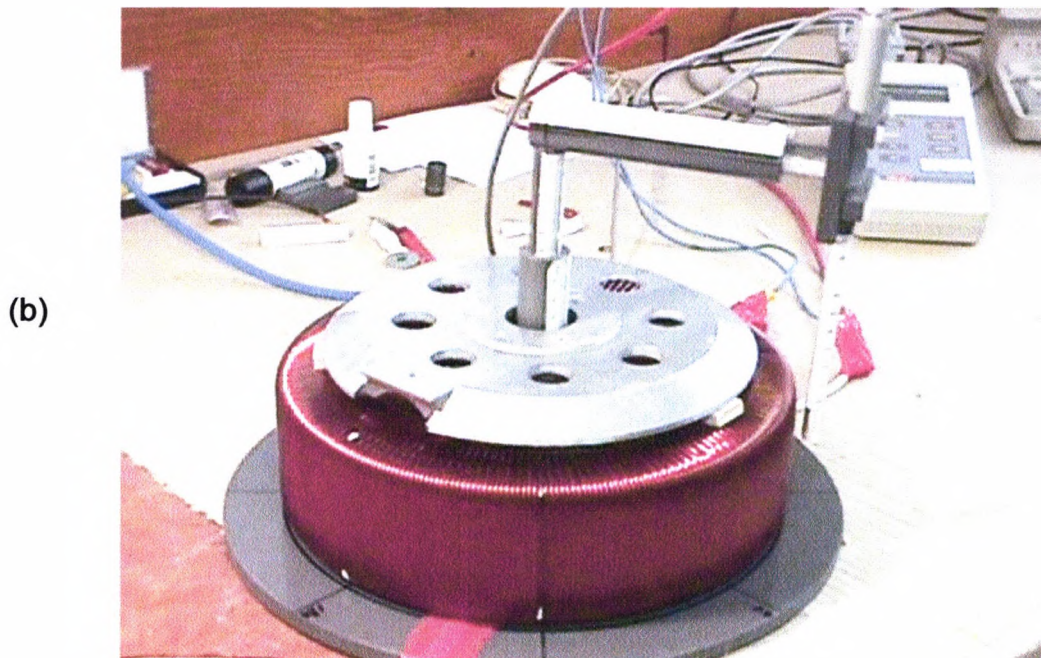
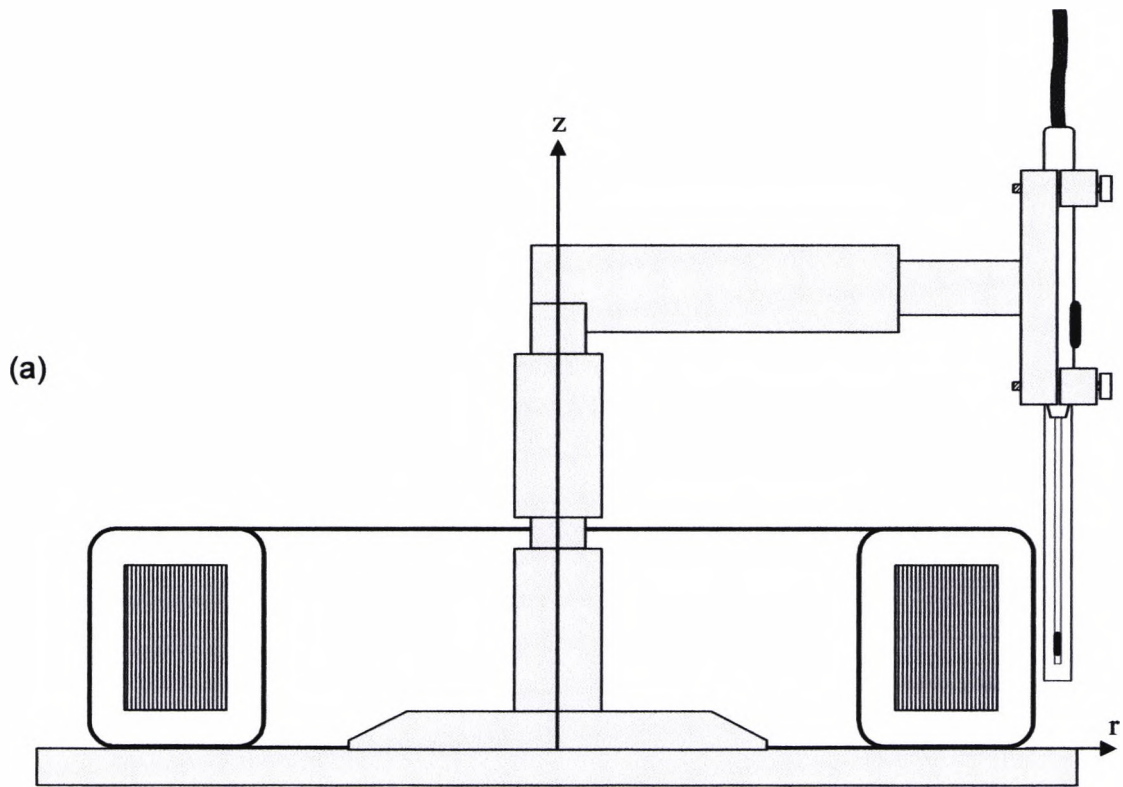


Fig. 4.4 Arrangement of experimental apparatus for the measurement of magnetic field around the toroidal core of the transformer: (a) schematic diagram, (b) photograph showing the actual transformer used (brush gear not shown).

4.2.2. The experimental models

As mentioned in the introduction the main aim of the experimental investigation was to measure magnetic field distribution for various operational regimes and configuration of one of the commercial variable transformers. For this, a number of different experimental models described below were used with extreme brush positions which represented extreme cases. These were done for two different total transformer turns.

Model 1:

Primarily consists of the transformer without its top and bottom plates. Measurement data were taken for various tap and brush positions shown in Fig. 4.5 as shown

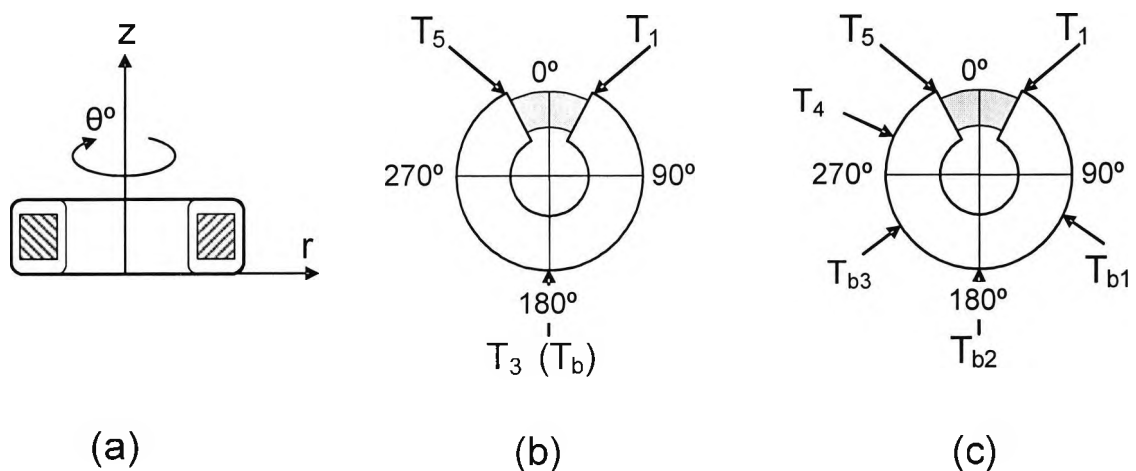


Fig. 4.5 Schematic diagram of the transformer for various models: (a) without top and bottom plates for various tap and brush positions. (b) taps T_1 at turn no. 1, T_5 at turn no. 296 and brush position T_3 (T_b) at turn no. 149 (Models 1, 2 case 1); (c) taps T_1 , T_4 and T_5 – at turns 1, 257 and 296 respectively, and brush positions T_{b1} , T_{b2} and T_{b3} – at turns 100, 154 and 207 respectively (Model 3 case 2).

In Fig. 4.5 two different cases of brush and tap position are used. In case 1 (Fig. 4.5(b)) the three taps are connected as follows: tap T_1 – is connected to transformer turn number 1, tap T_5 – to turn number 296 and T_3 – to turn number 148 (brush position T_b). In case 2 (Fig. 4.5(c)) the taps are connected as follows: tap T_1 – to turn 1, tap T_4 to turn 257 and tap T_5 – to turn 296. Brush positions T_{b1} , T_{b2} and T_{b3} are at turns 100, 154 and 207 respectively. The circuit

diagram for transformer windings corresponding to these cases are shown in Fig. 4.6.

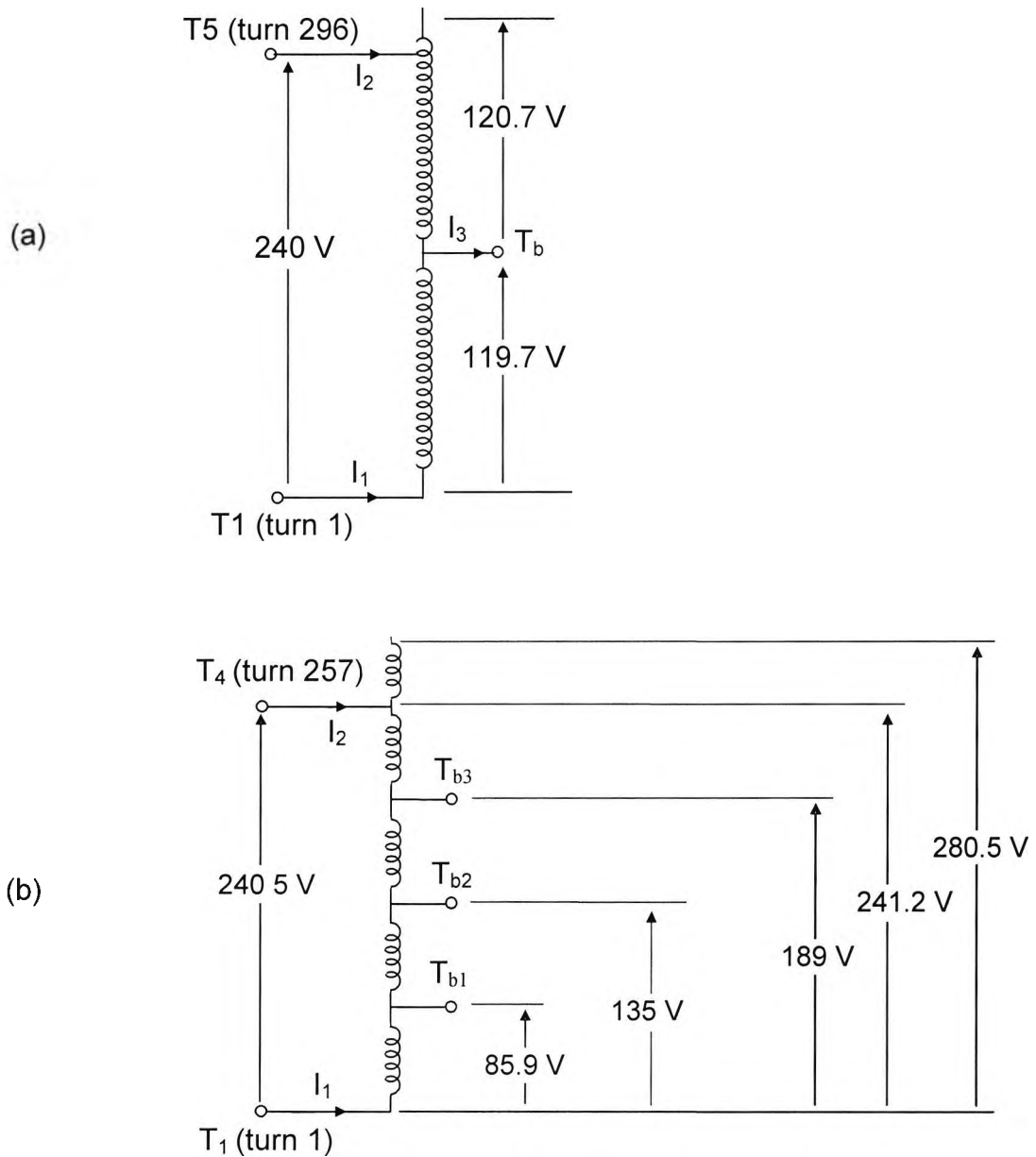


Fig. 4.6 Schematic diagram showing various tap and brush positions on the winding for experimental cases 1 (a) and 2 (b).

Fig. 4.7 and Fig. 4.8 show the full circuit diagrams corresponding to these experimental cases. Here the experimental autotransformer AT_2 is fed through a supply autotransformer AT_1 whose output voltage can be varied. The supply transformer AT_1 acts both as a power supply and load for experimental transformer AT_2 .

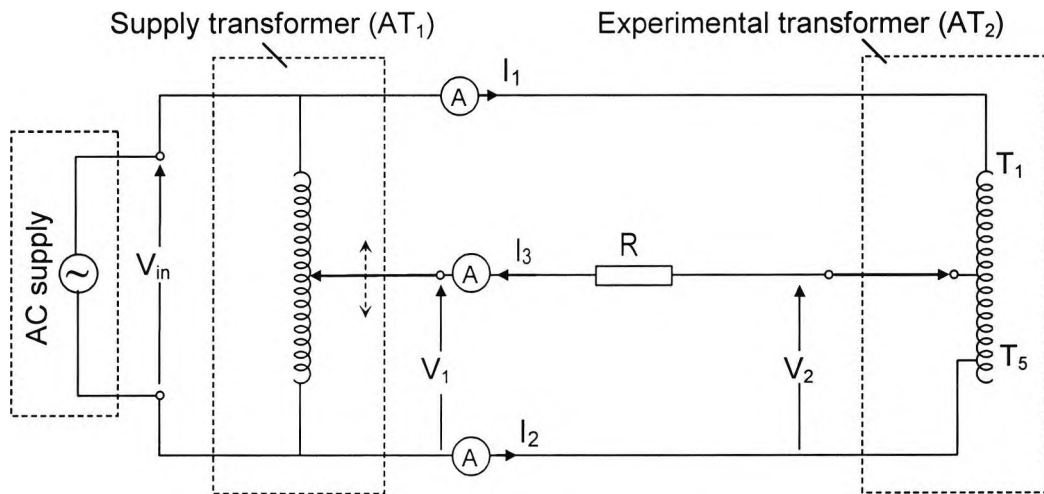


Fig. 4.7 Full circuit diagram for experimental investigation of autotransformer (experimental case 1).

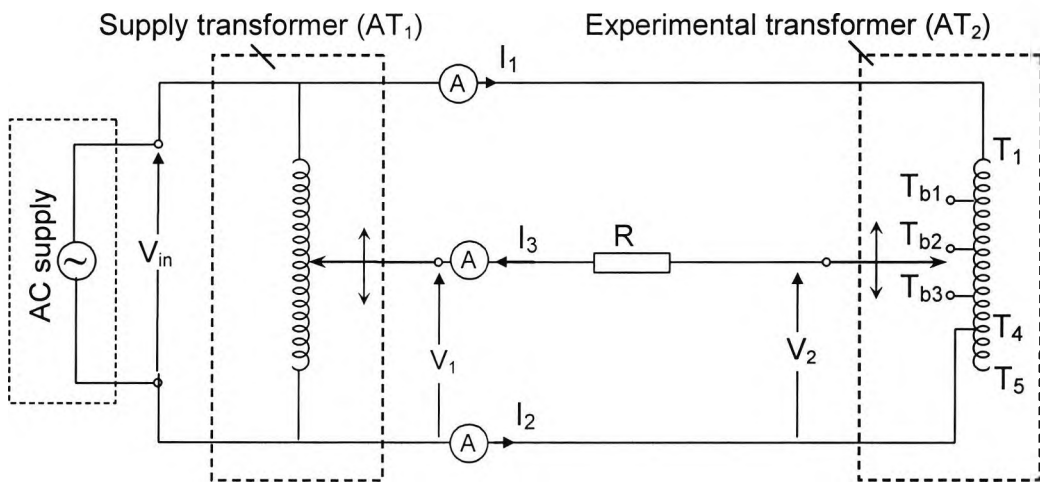


Fig. 4.8 Full circuit diagram for experimental investigation of autotransformer (experimental case 2).

The current distributions in the experimental transformer AT₂ for the two experimental cases are given in Table 4.1 and Table 4.2.

Table 4.1 Current distribution in transformer for experimental case-1.

Brush position	Turn number	I ₁ (A)	I ₂ (A)	I ₃ (A)
T _b	148	12.22	12.11	24.68

Table 4.2 Current distribution in the transformer for experimental case-2.

Brush position	Turn number	I1 (A)	I2 (A)	I3 (A)
Tb1	100	15.71	9.05	24.88
Tb2	154	9.42	15.32	24.81
Tb3	207	4.66	20.34	24.97

In Fig. 4.7 and Fig. 4.8, the following parameters apply:

$$V = V_{in} = 240V, \quad R = 0.5 \Omega$$

$$I_3 = I_1 + I_2 = 25A, \quad I_3 = \frac{V_2 - V_1}{R}$$

For case 1 the resistance between tap positions T_1 and T_5 , $R_5 = 0.5 \Omega$; for case 2 the resistances between T_1 and T_4 , $R_4 = 0.4 \Omega$, between T_1 and T_{b3} , $R_3 = 0.35 \Omega$, between T_1 and T_{b2} , $R_2 = 0.3 \Omega$, and between T_1 and T_{b1} , $R_1 = 0.2 \Omega$.

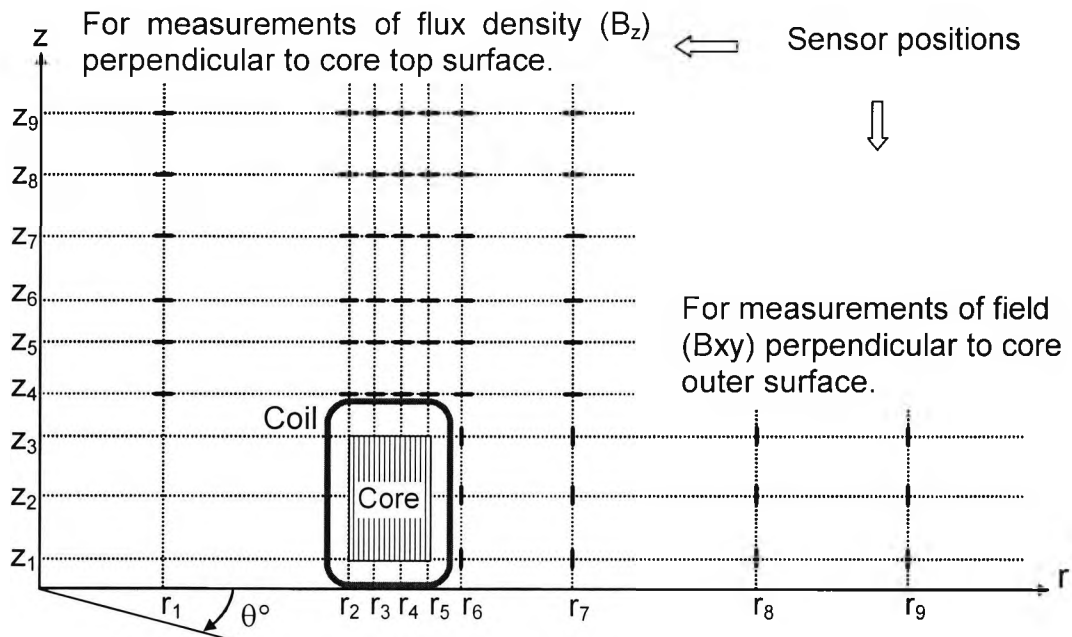


Fig. 4.9 Schematic diagram showing sensor positions in r , θ , z for experimental Model 1.

For taking field measurements above and around the toroidal core of the experimental transformer the Hall-effect sensor described earlier was placed at various positions by varying spatial coordinates r , θ and z . The r , z positions are shown in Fig. 4.9 and given in Table 4.3. For each combination of r , z the sensor position was rotated through 360° by an interval of 5° (72 positions).

Table 4.3 The sensor positions (in mm) for magnetic field measurements surrounding the toroidal core (Fig. 4.9).

z_3 (70)	134	140	150	170
z_2 (41)	134	140	150	170
z_1 (13)	134	140	150	170
	r_6	r_7	r_8	r_9

Fig. 4.10 and Fig. 4.11 show the dimensions involved along spatial coordinates r and z .

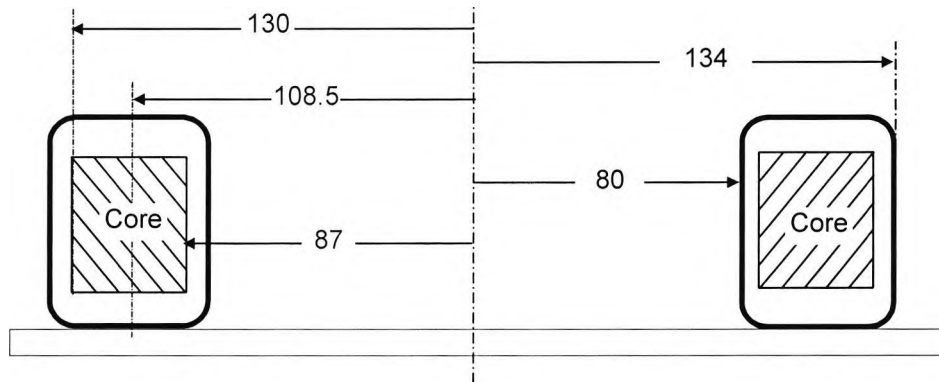


Fig. 4.10 Schematic diagram showing dimensions along r (mm) direction (not drawn to scale).

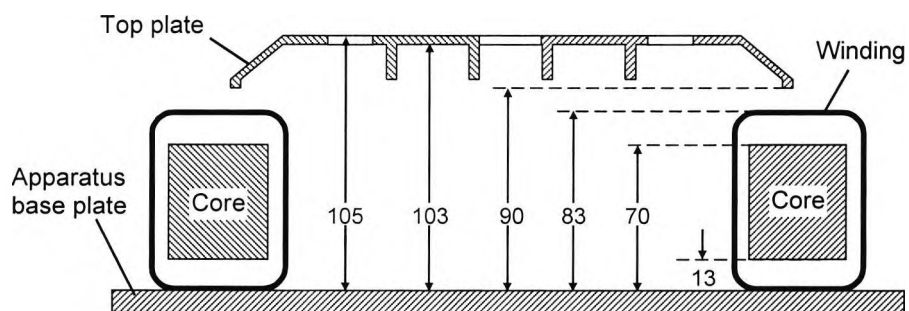


Fig. 4.11 Schematic diagram showing dimensions along z direction.

Model 2:

In the experimental Model 2 field measurements were taken in the presence of the transformer top plate for various tap and brush positions shown in Fig. 4.12.

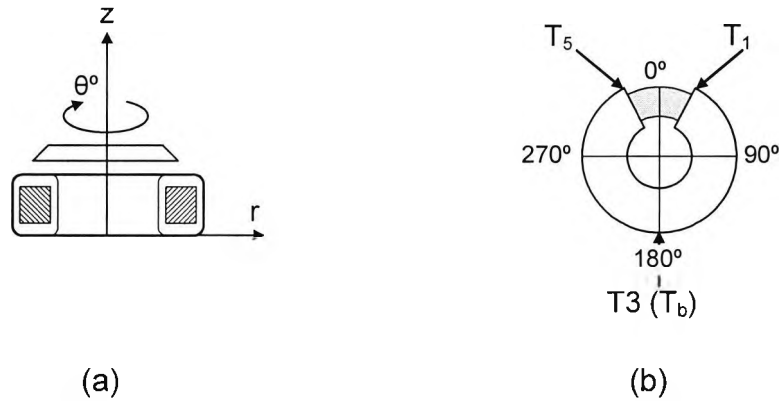


Fig. 4.12 Schematic diagram of the transformer for Model 2 (a) with top plate, (b) taps T_1 at turn no. 1, T_5 at turn no. 296 and T_3 at turn no. 148 (brush position T_b).

The sensor positions used for this experimental model are given in Fig. 4.13 and Table 4.4.

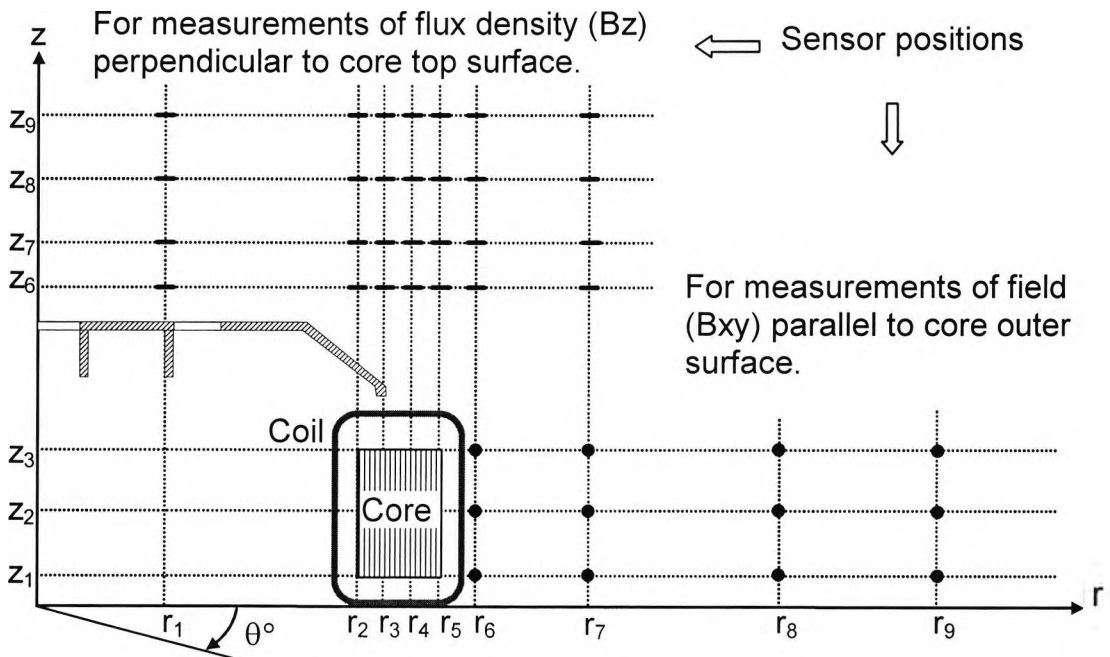


Fig. 4.13 Schematic diagram showing sensor positions in r , θ , z for experimental Model 2.

Table 4.4 The sensor positions (in mm) for magnetic field measurements above the toroidal core (Fig. 4.9 and Fig. 4.13).

Without top plate	With top plate	z_9 (230)	35	87	110	120	130	140
		z_8 (200)	35	87	110	120	130	140
		z_7 (170)	35	87	110	120	130	140
		z_6 (117)	35	87	110	120	130	140
	z_5 (103)	35	87	110	120	130	140	
	z_4 (091)	35	87	110	120	130	140	
			r_1	r_2	r_3	r_4	r_5	r_7

Model 3:

The experimental Model 3 involved the autotransformer without the top plate as for Model 1. These different fixed tap positions on the winding were used for brush positions shown in Fig. 4.5(c).

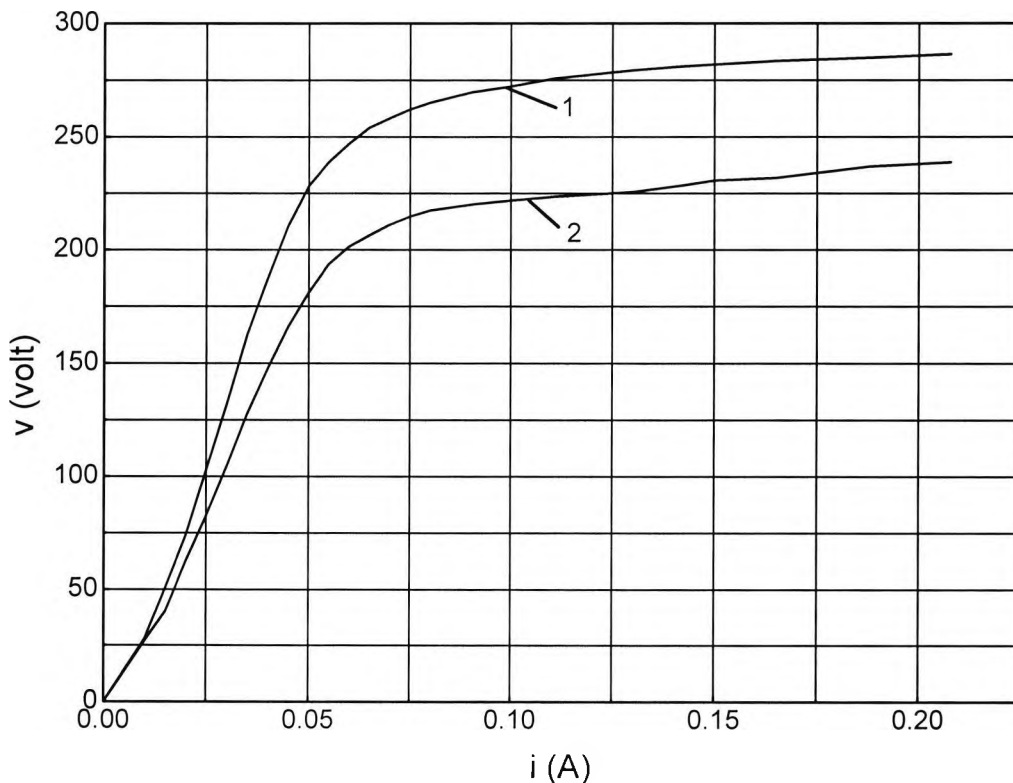


Fig. 4.14 No load v - i characteristics of TS1225 autotransformer for tap positions corresponding to experimental cases 1 (graph 1) and 2 (graph 2).

4.3. Results of Flux Density Measurements

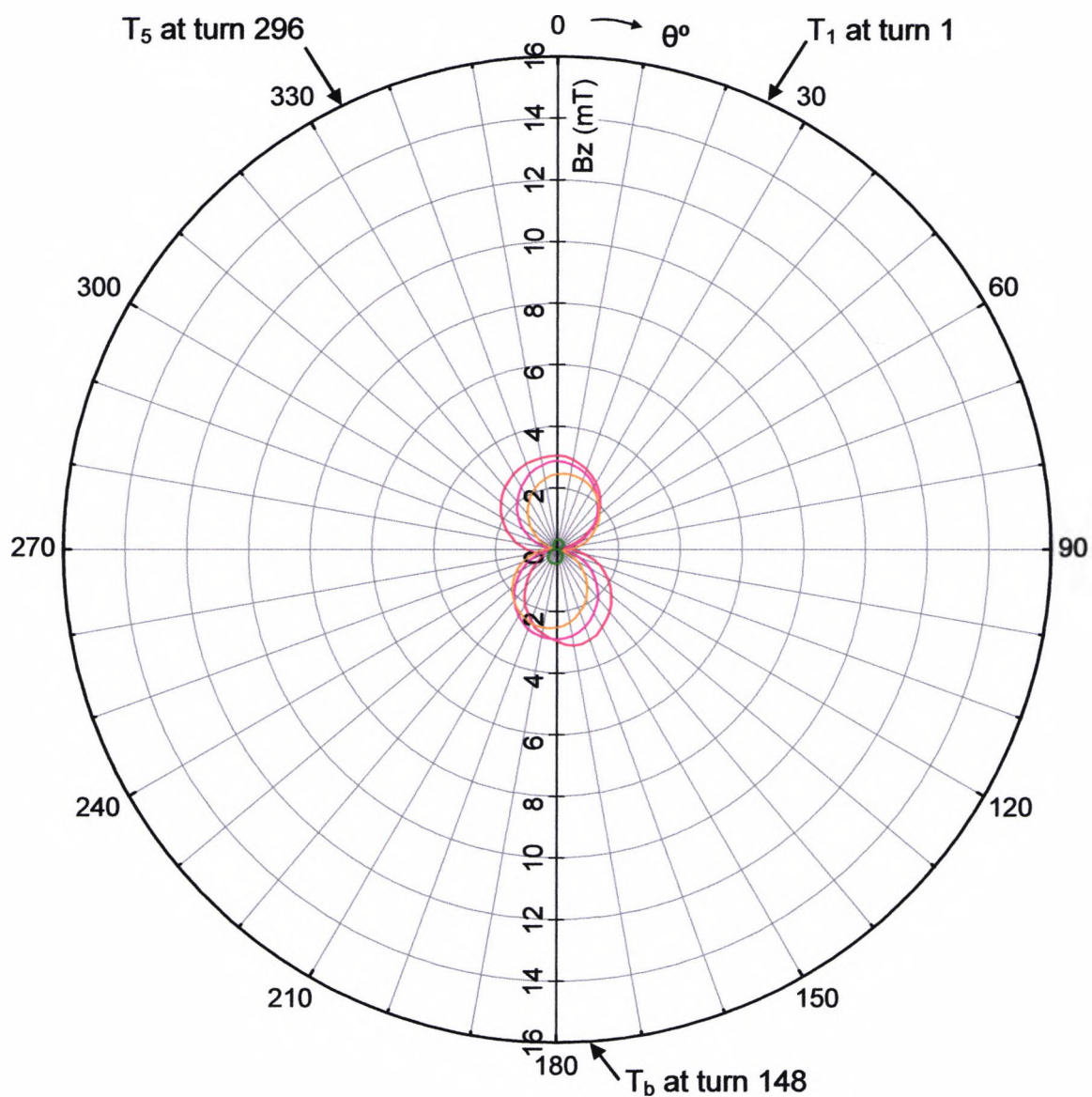
Some of the results of experimental investigation of the TS1225 Variable Transformer in terms of flux density distributions are described in the following section. The full set of experimental data can be found in the Appendix. Fig. 4.14 shows the no-load v-i characteristics of the TS1225 Variable Transformer for tap positions corresponding to experimental cases 1 and 2 described earlier.

4.3.1. Results for Model 1:

Figures (Fig. 4.15 – Fig. 4.18) show the variation of the vertical component of flux density B_z above the toroidal core with r , θ , and z in the absence of the top plate. These data were obtained for tap positions T1, T5 and T3 (brush position T_b) at turns 1, 296 and 148 respectively. The other parameters included the following: $I_1 = 12A$; $I_3 = 25A$; $V = 240v$ and $f = 50$ Hz.

All these experimental results are obtained to validate some of the initial modelling results and refine the 3D FE models used for more complex investigations. Figures Fig. 4.15-Fig. 4.21 and the other results presented in this Chapter show a wide variation in both magnitude and distribution of magnetic field in air around the toroidal core. It can be seen from these figures that maximum flux density follows the brush and tap positions for a given operational regime. This factor needs to be taken into account for the evaluation of stray fields in air for design purposes. Further more, high flux density values can also be seen to be prevalent in air in the regions close proximity (e.g. Fig. 4.16) to the unwound part of the core.

All these factors contribute to a highly non-uniform magnetic field distribution in air around the core which is very much dependent upon the operational regime.



- $z_4 = 91$ mm
- $z_5 = 103$ mm
- $z_6 = 117$ mm
- $z_9 = 230$ mm

Fig. 4.15 Variation of the vertical component of flux density B_z above the toroidal core with r , θ and z in the absence of the top plate: $r = r_1 = 35$ mm, $z = 91$ (z_4), 103 (z_5), 117 (z_6), 230 (z_9) mm, $\theta = 0 - 360^\circ$ (Fig. 4.9)

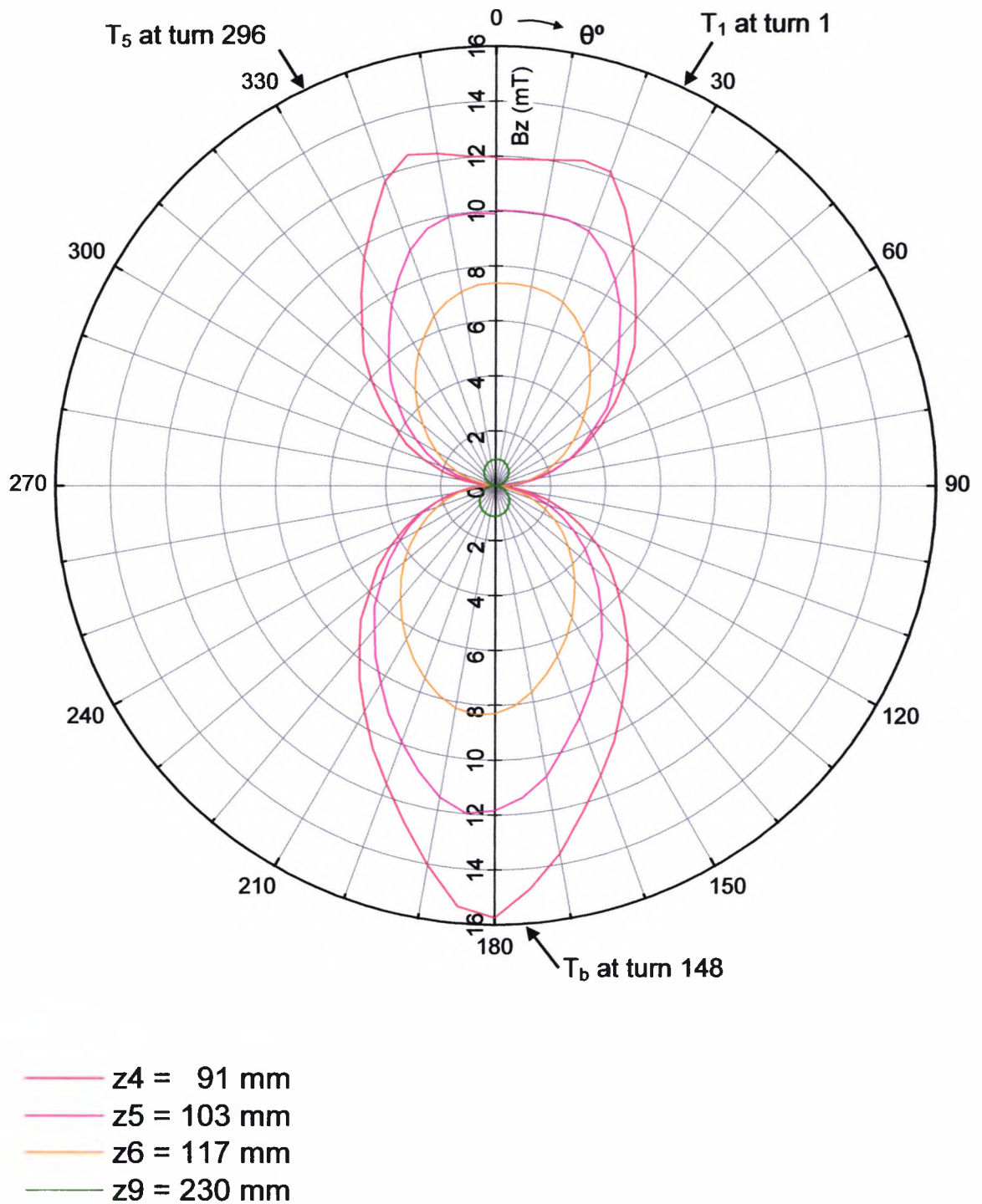


Fig. 4.16 Variation of the vertical component of flux density B_z above the toroidal core with r , θ and z in the absence of the top plate: $r = r_3 = 110$ mm, $z = 91$ (z_4), 103 (z_5), 117 (z_6), 230 (z_9) mm, $\theta = 0 - 360^\circ$ (Fig. 4.9).

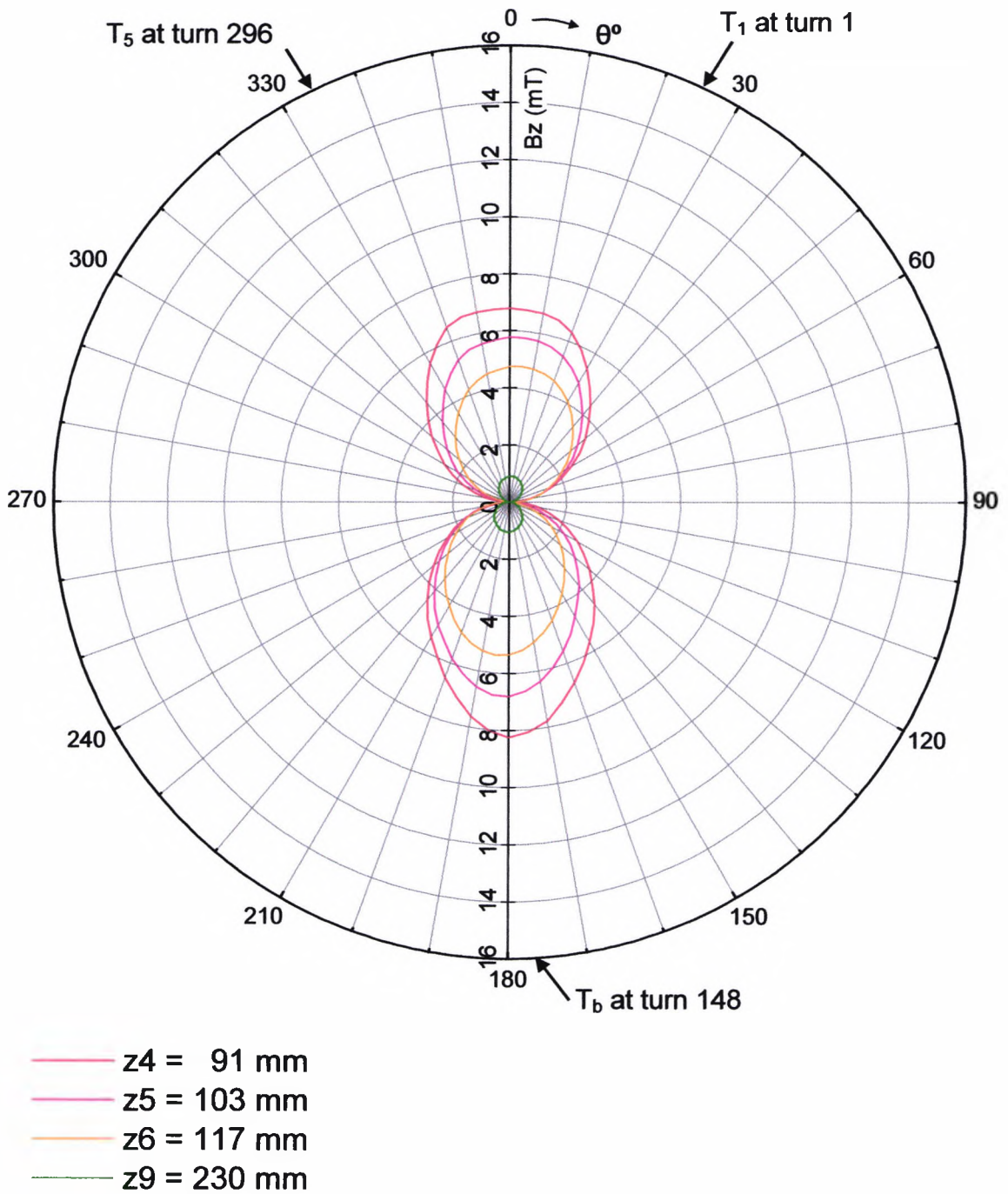


Fig. 4.17 Variation of the vertical component of flux density B_z above the toroidal core with r , θ and z in the absence of the top plate: $r = r_7 = 140$ mm, $z = 91$ (z_4), 103 (z_5), 117 (z_6), 230 (z_9) mm, $\theta = 0 - 360^\circ$ (Fig. 4.9).

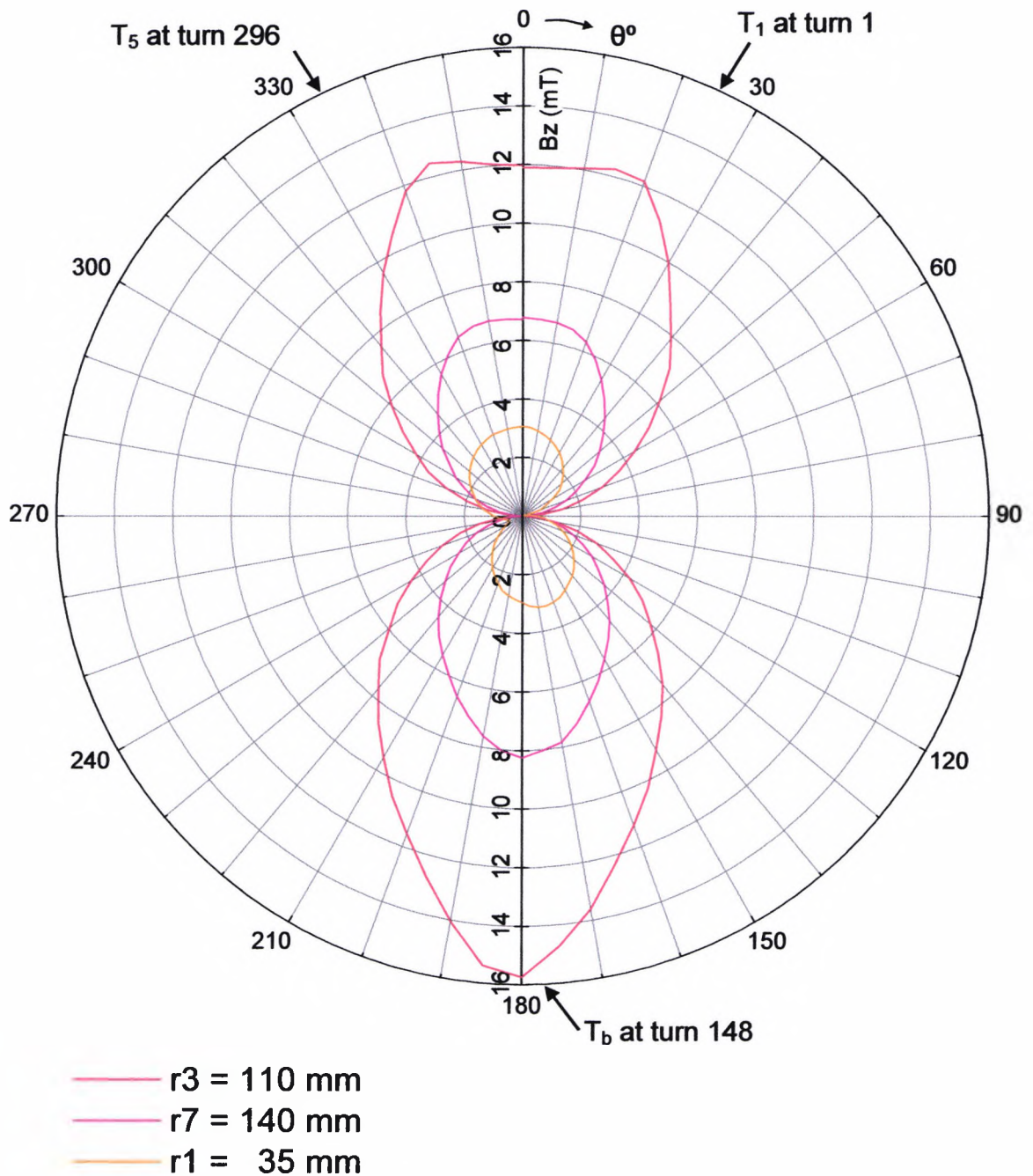


Fig. 4.18 Variation of the vertical component of flux density B_z above the toroidal core with r , θ and z in the absence of the top plate: $z = z_4 = 91 \text{ mm}$, $r = 35$ (r_1), 110 (r_3), 140 (r_7) mm , $\theta = 0 - 360^\circ$ (Fig. 4.9).

Some of the results of field measurement at various positions surrounding the toroidal core in the absence of the top plate are shown in Figures (Fig. 4.19 – Fig. 4.21) The measurements were taken for tap positions T_1 , T_5 and T_3 (brush position T_b) at turns 1, 296 and 148 respectively. The electrical parameters were as following: $I_1 = 12\text{A}$, $I_3 = 25\text{A}$, $V = 240\text{v}$ and $f = 50 \text{ Hz}$.

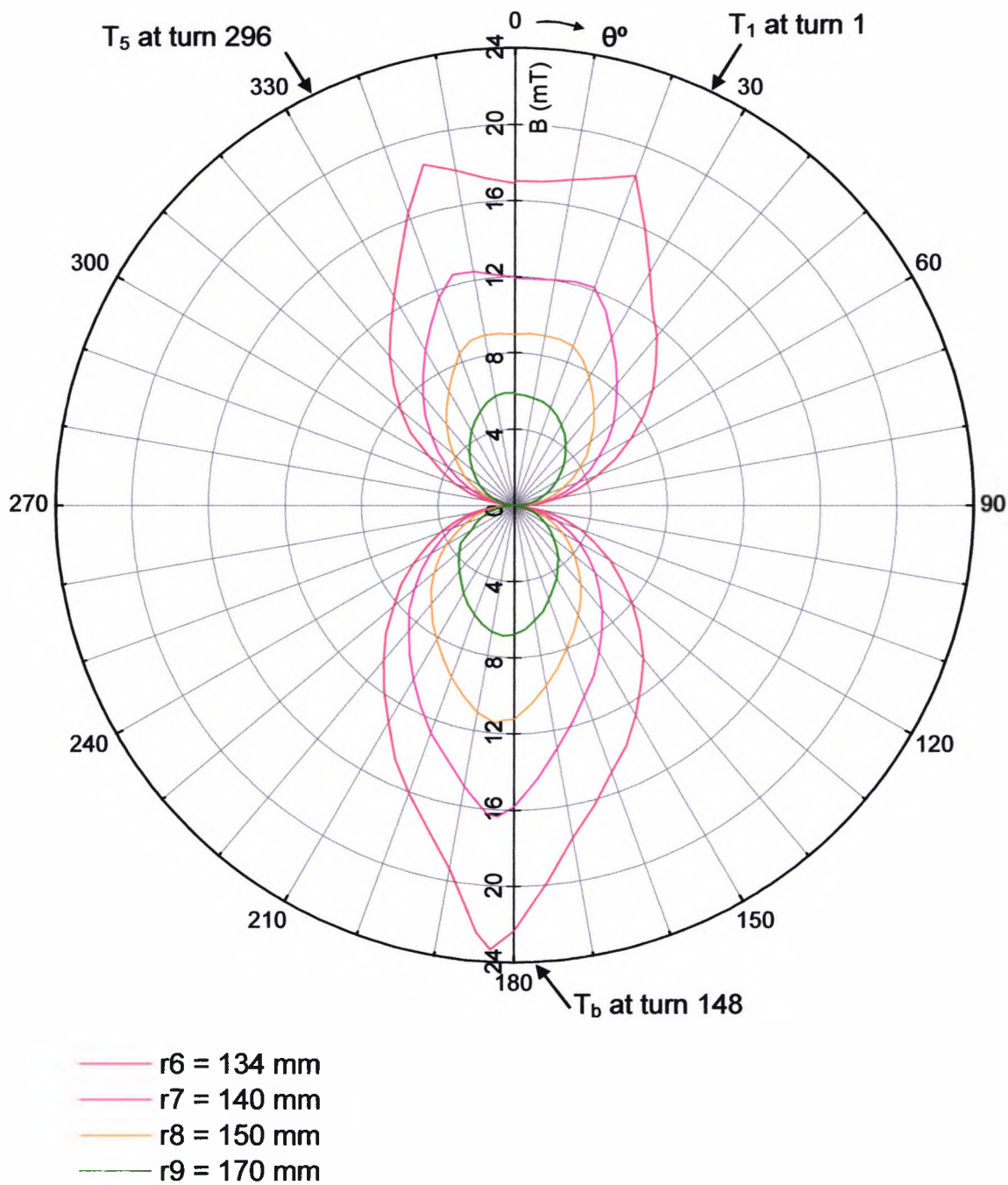


Fig. 4.19 Variation of flux density B surrounding the toroidal core with r , θ and z in the absence of the top plate: $z = z_1 = 13 \text{ mm}$, $r = 134$ (r_6), 140 (r_7), 150 (r_8), 170 (r_9) mm , $\theta = 0 - 360^\circ$ (Fig. 4.9).

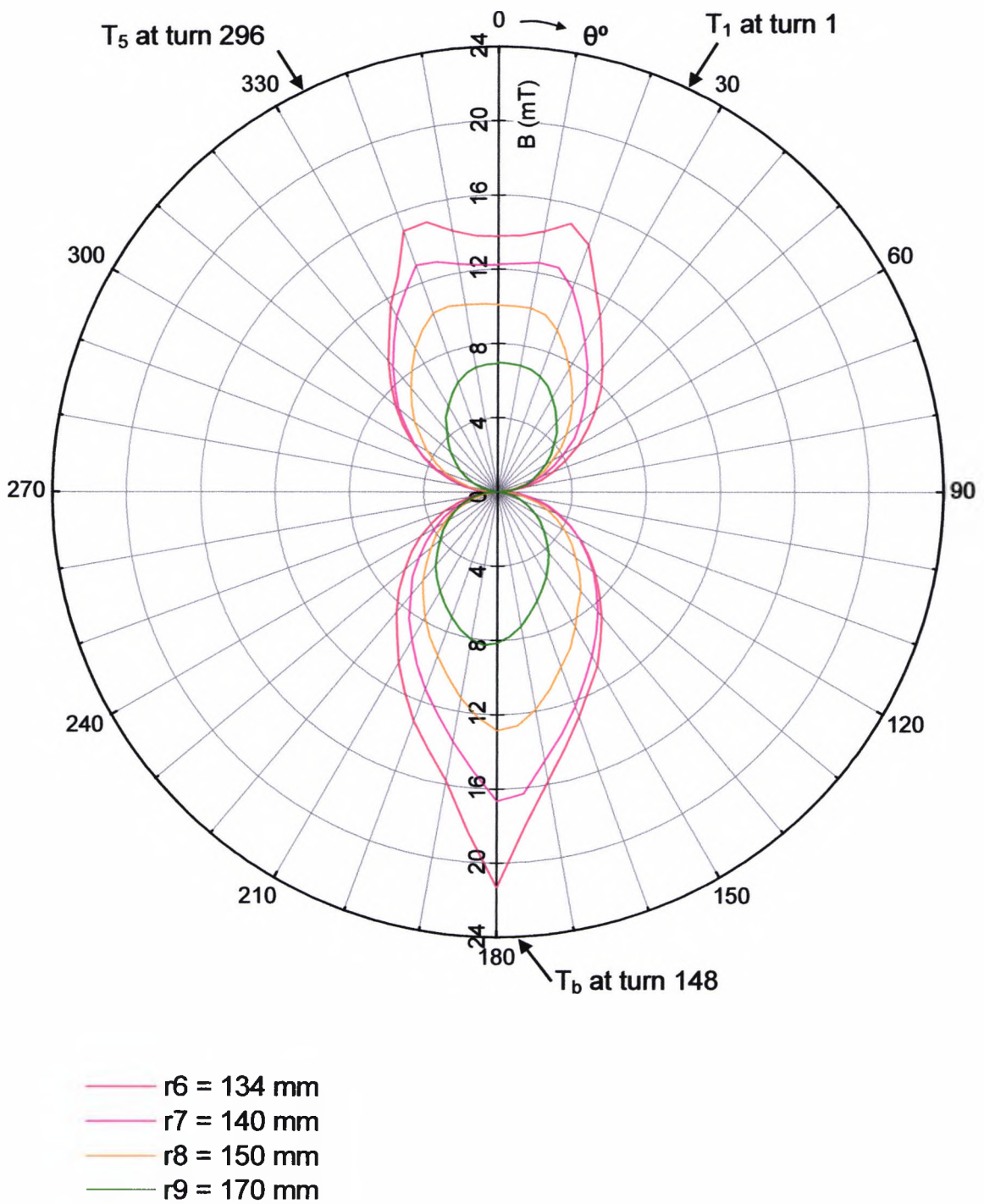


Fig. 4.20 Variation of flux density B surrounding the toroidal core with r , θ and z in the absence of the top plate: $z = z_2 = 41 \text{ mm}$, $r = 134$ (r_6), 140 (r_7), 150 (r_8), 170 (r_9) mm, $\theta = 0 - 360^\circ$ (Fig. 4.9).

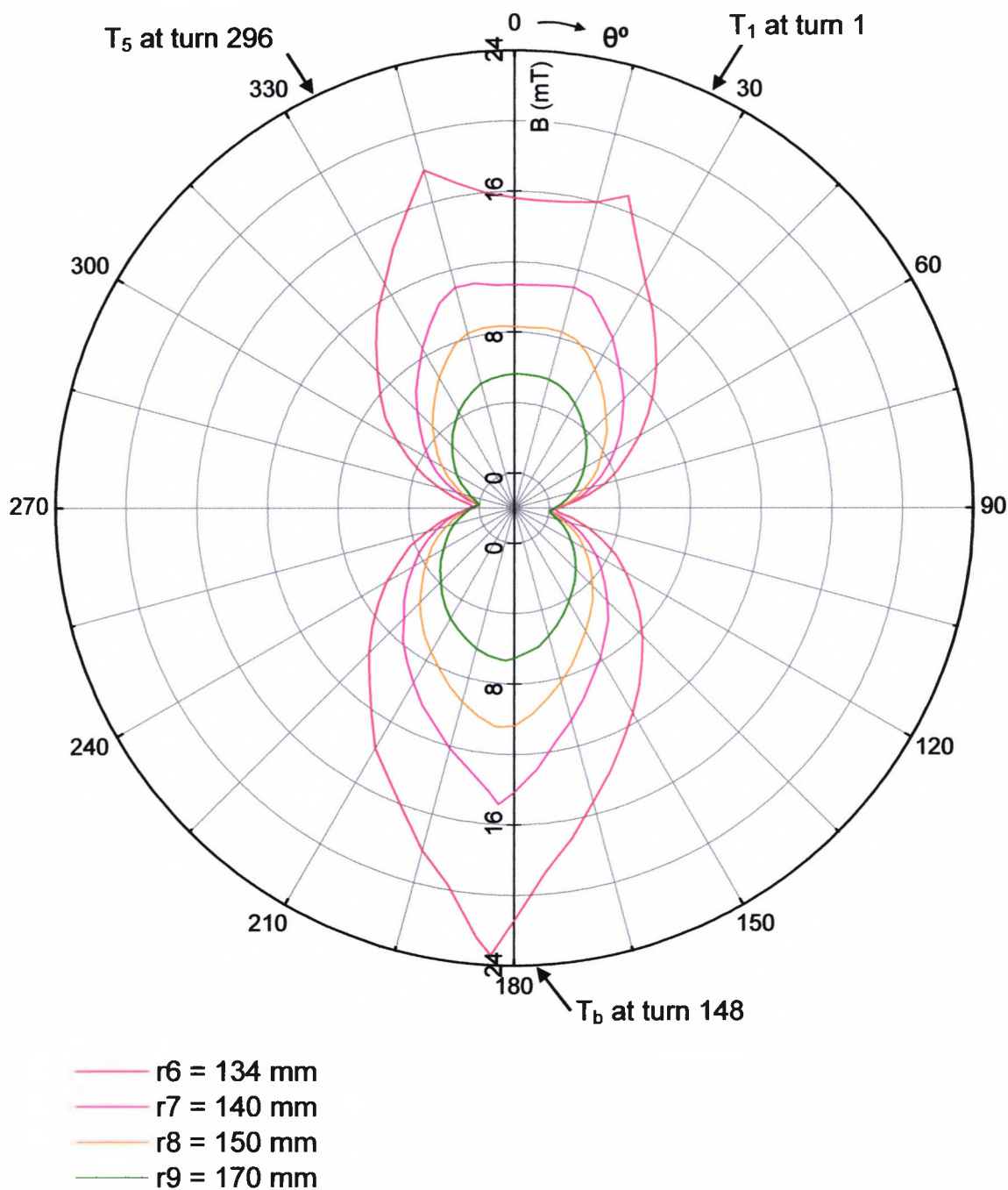


Fig. 4.21 Variation of flux density B surrounding the toroidal core with r , θ and z in the absence of the top plate: $z = z_3 = 70 \text{ mm}$, $r = 134$ (r_6), 140 (r_7), 150 (r_8), 170 (r_9) mm, $\theta = 0 - 360^\circ$ (Fig. 4.9).

The effects of the top plate on magnetic field distribution above the toroidal core can be seen by comparing Figures (Fig. 4.15–Fig. 4.18) with Figs. (Fig. 4.22–Fig. 4.24). Figures Fig. 4.22–Fig. 4.24 show the variation of the vertical component of flux density B_z above the toroidal core with r , θ , z in presence of

the top plate. Comparison of these figures shows the screening effect of the top plate.

4.3.2. Results for model 2:

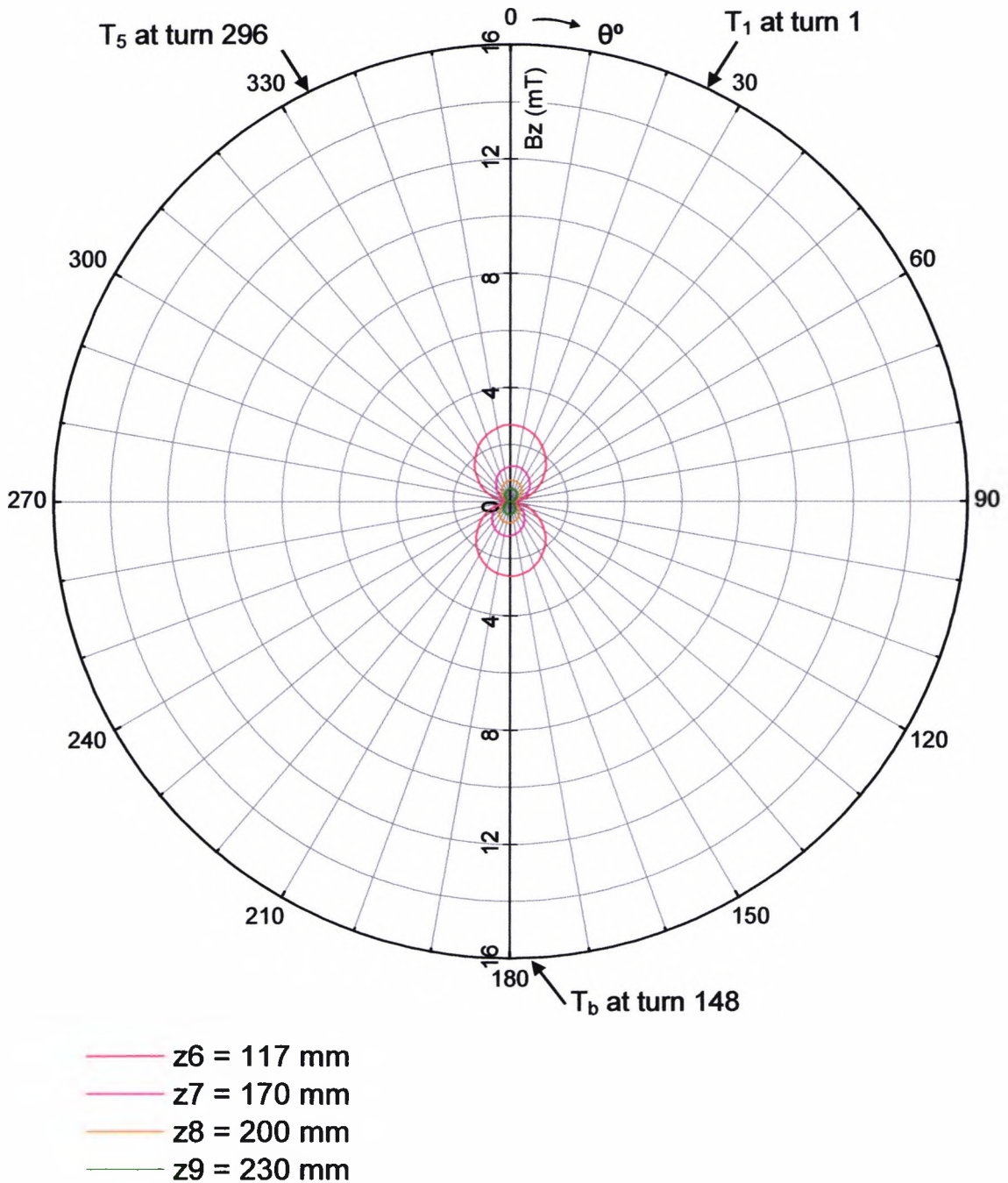


Fig. 4.22 Variation of the vertical component of flux density B_z above the toroidal core with r , θ and z in the presence of the top plate: $r = r_1 = 35$ mm, $z = 117$ (z_6), 170 (z_7), 200 (z_8), 230 (z_9) mm, $\theta = 0 - 360^\circ$ (Fig. 4.13).

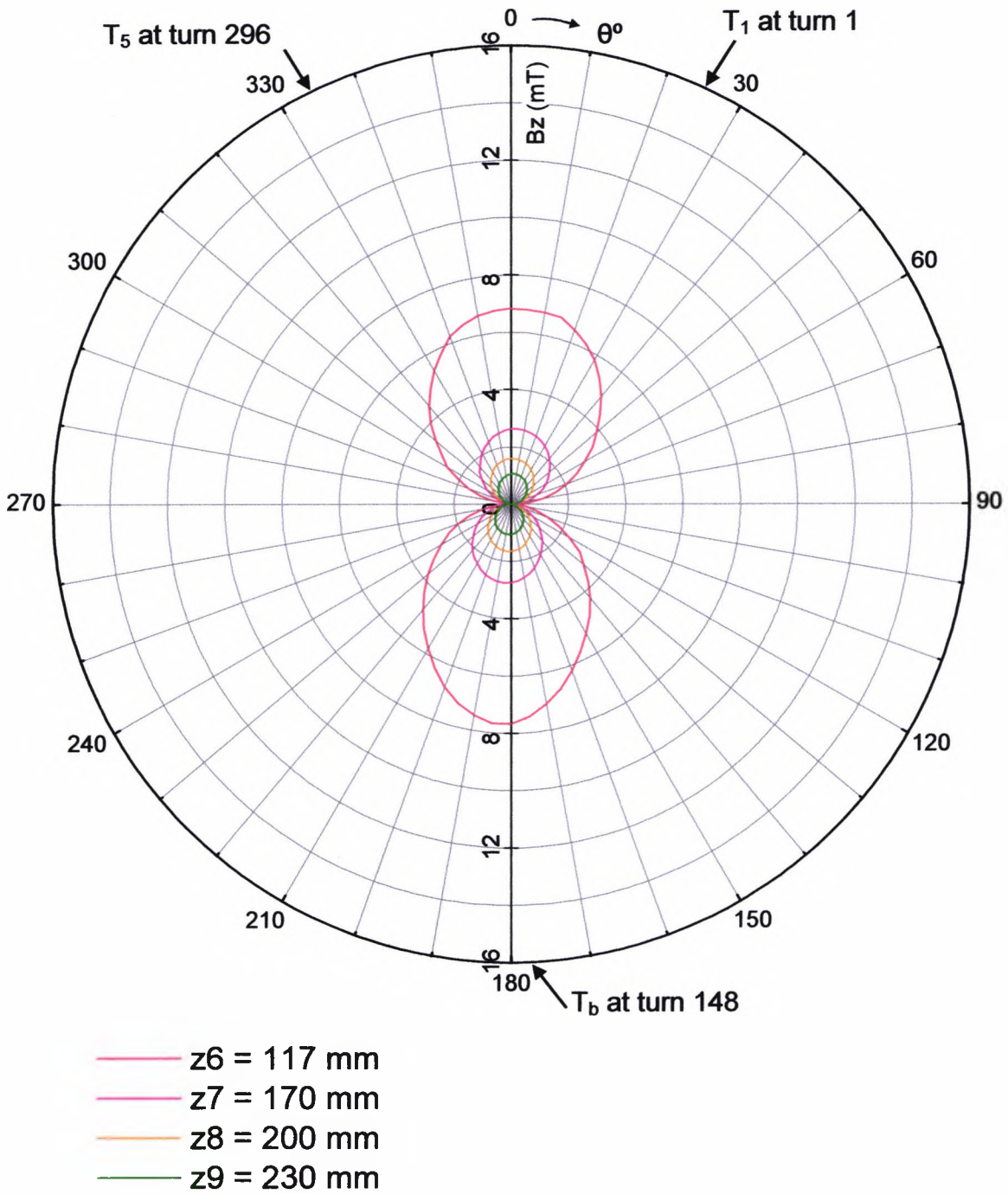


Fig. 4.23 Variation of the vertical component of flux density B_z above the toroidal core with r , θ and z in the presence of the top plate: $r = r_3 = 110$ mm, $z = 117$ (z_6), 170 (z_7), 200 (z_8), 230 (z_9) mm, $\theta = 0 - 360^\circ$ (Fig. 4.13).

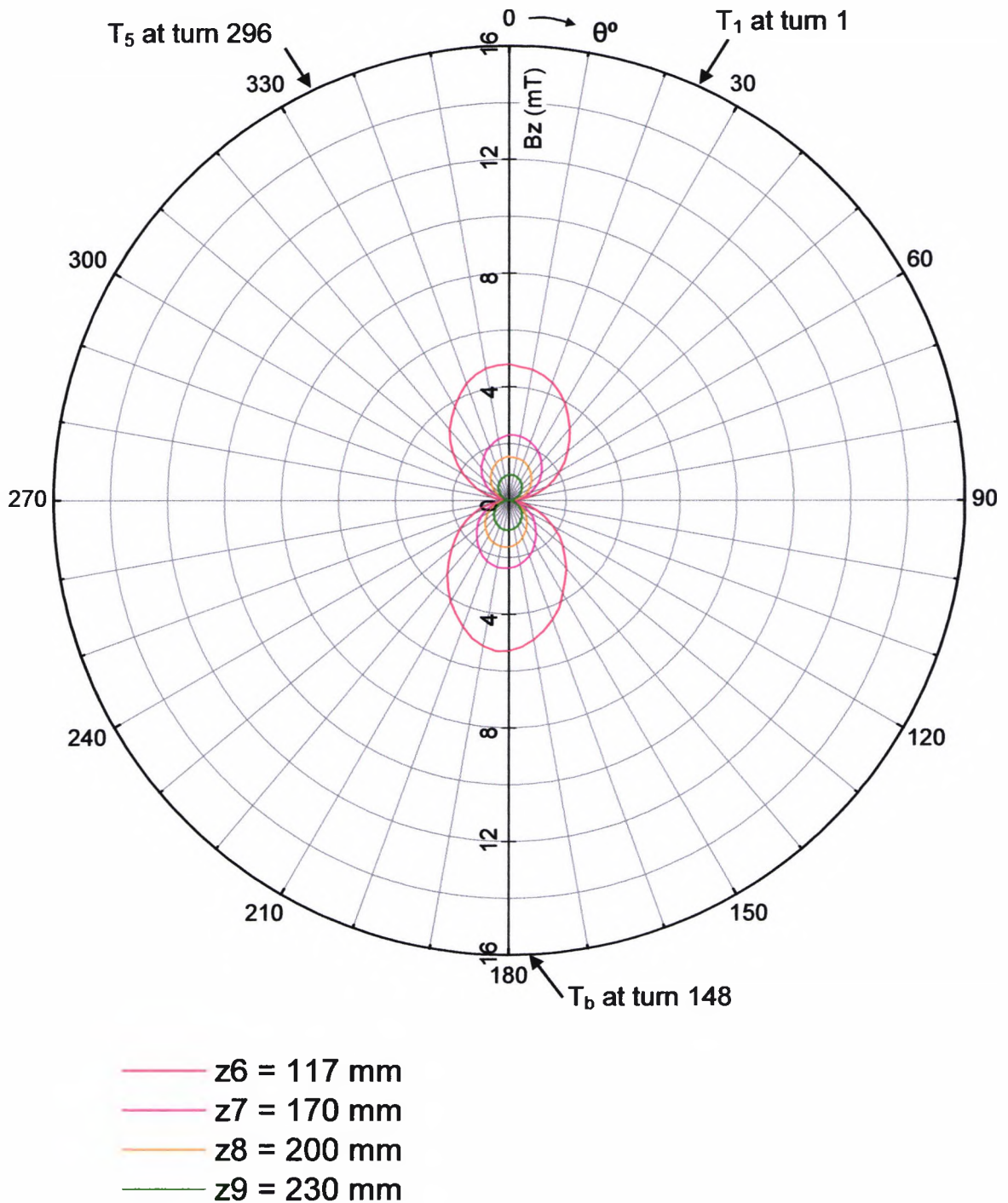


Fig. 4.24 Variation of the vertical component of flux density B_z above the toroidal core with r , θ and z in the presence of the top plate: $r = r_7 = 140 \text{ mm}$, $z = 117 (z_6)$, $170 (z_7)$, $200 (z_8)$, $230 (z_9) \text{ mm}$, $\theta = 0 - 360^\circ$ (Fig. 4.13).

The effect of the top plate on field distribution surrounding the toroidal core can be seen by comparing figures Fig. 4.19-Fig. 4.21 with figures Fig. 4.25 – Fig. 4.27. It shows that the top plate has marginal effect on this field, especially

further away from the core where the end-effect of the top plate is smaller. The variation of the circumferential field around the core is shown in Fig. 4.28.

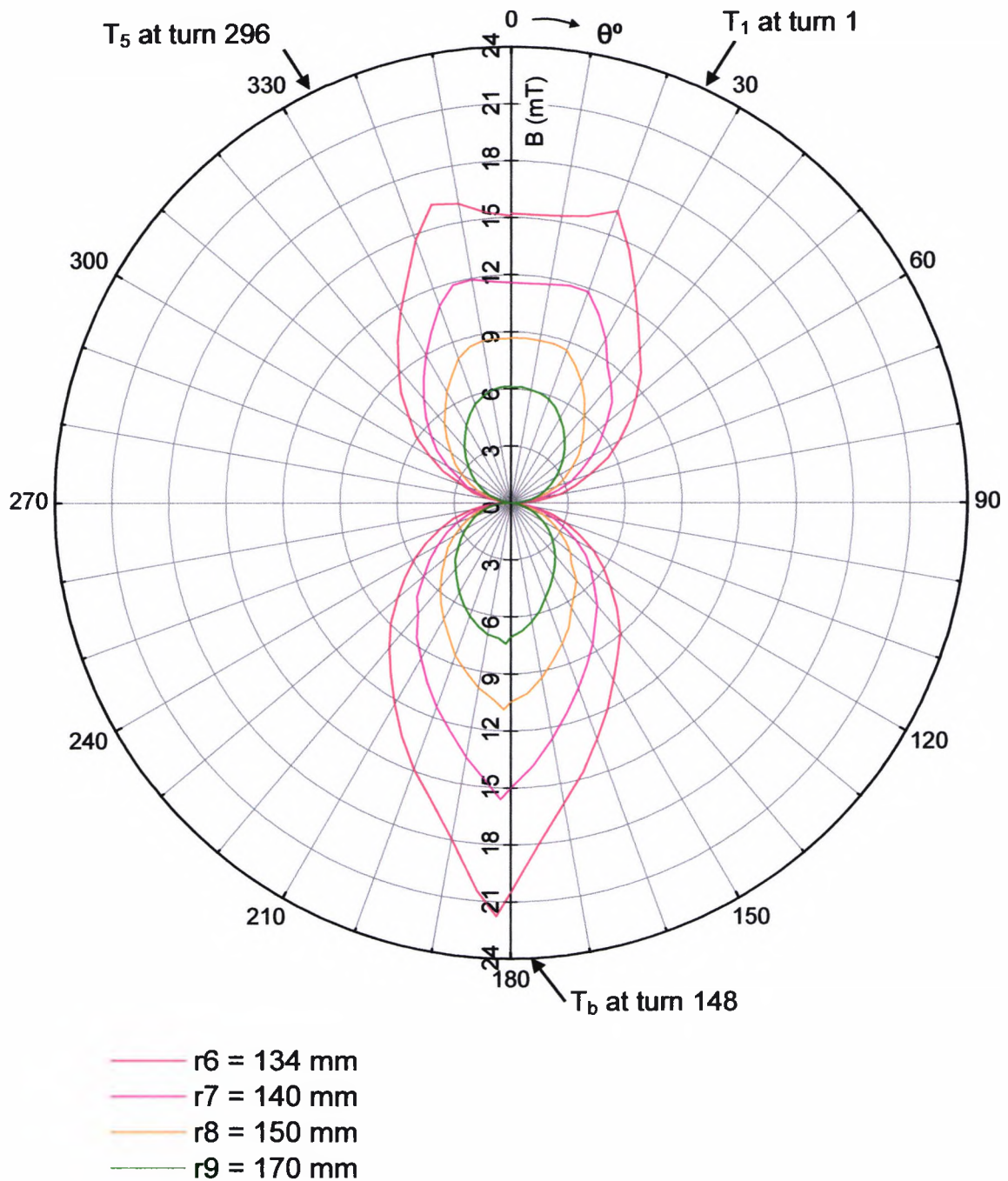


Fig. 4.25 Variation of the flux density B surrounding the toroidal core with r , θ and z in the presence of the top plate: $z = z_1 = 13$ mm, $r = 134$ (r_6), 140 (r_7), 150 (r_8), 170 (r_9) mm, $\theta = 0 - 360^\circ$ (Fig. 4.13)

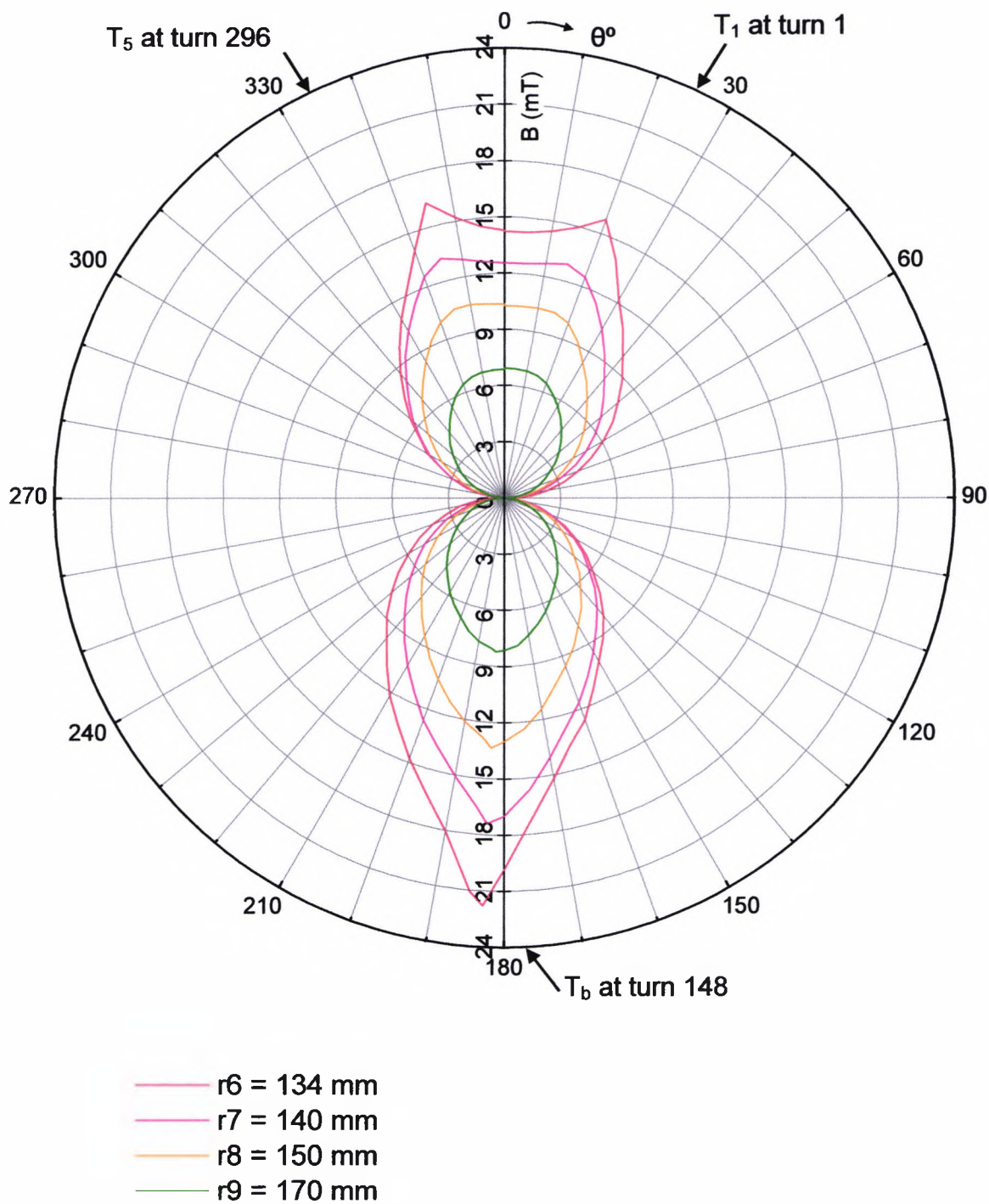


Fig. 4.26 Variation of the vertical of flux density B surrounding the toroidal core with r , θ and z in the presence of the top plate: $z = z_2 = 41 \text{ mm}$, $r = 134 (r_6)$, $140 (r_7)$, $150 (r_8)$, $170 (r_9) \text{ mm}$, $\theta = 0 - 360^\circ$ (Fig. 4.13).

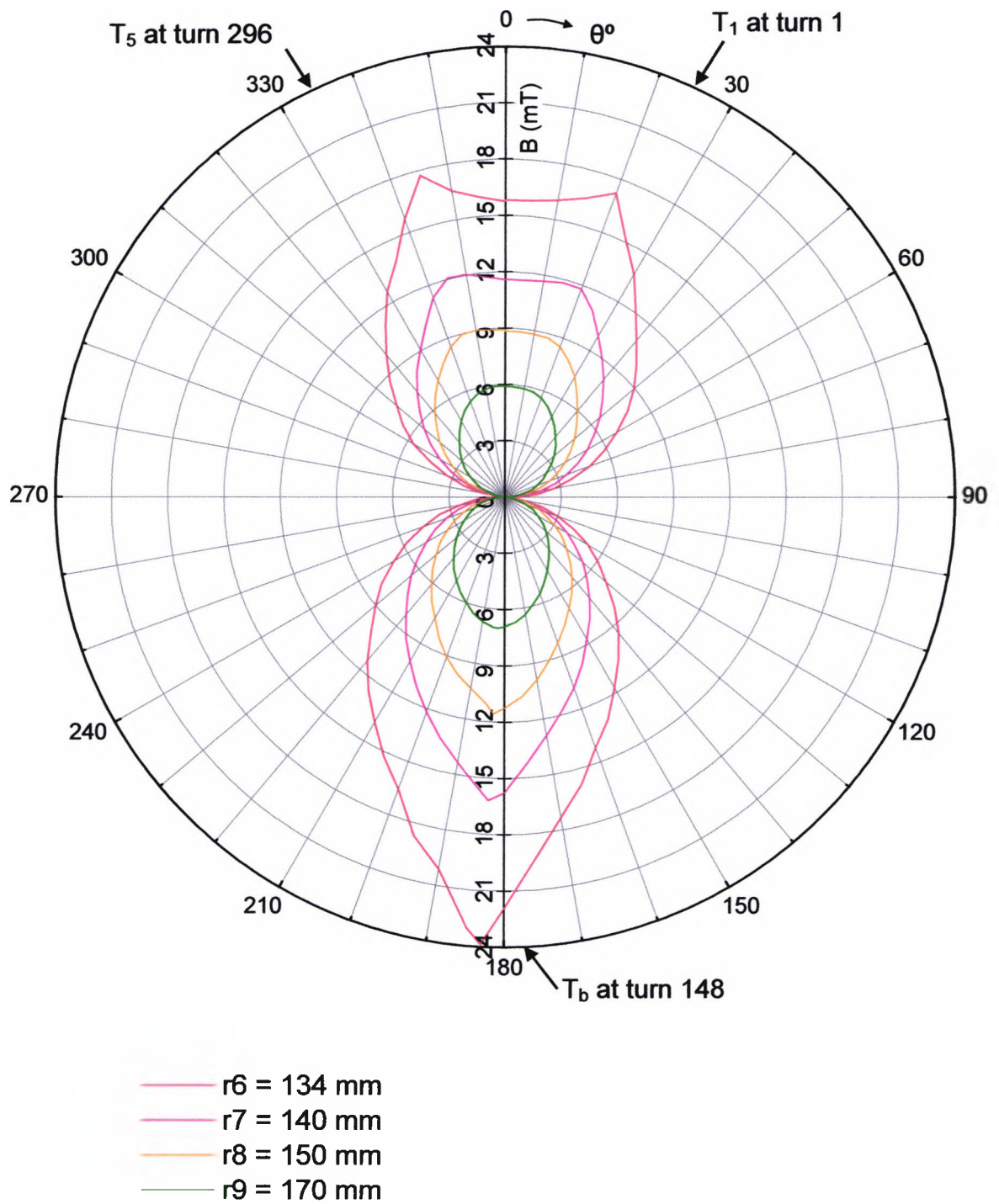


Fig. 4.27 Variation of the vertical of flux density B surrounding the toroidal core with r , θ and z in the presence of the top plate: $z = z_3 = 70 \text{ mm}$, $r = 134 (r_6)$, $140 (r_7)$, $150 (r_8)$, $170 (r_9) \text{ mm}$, $\theta = 0 - 360^\circ$ (Fig. 4.13)

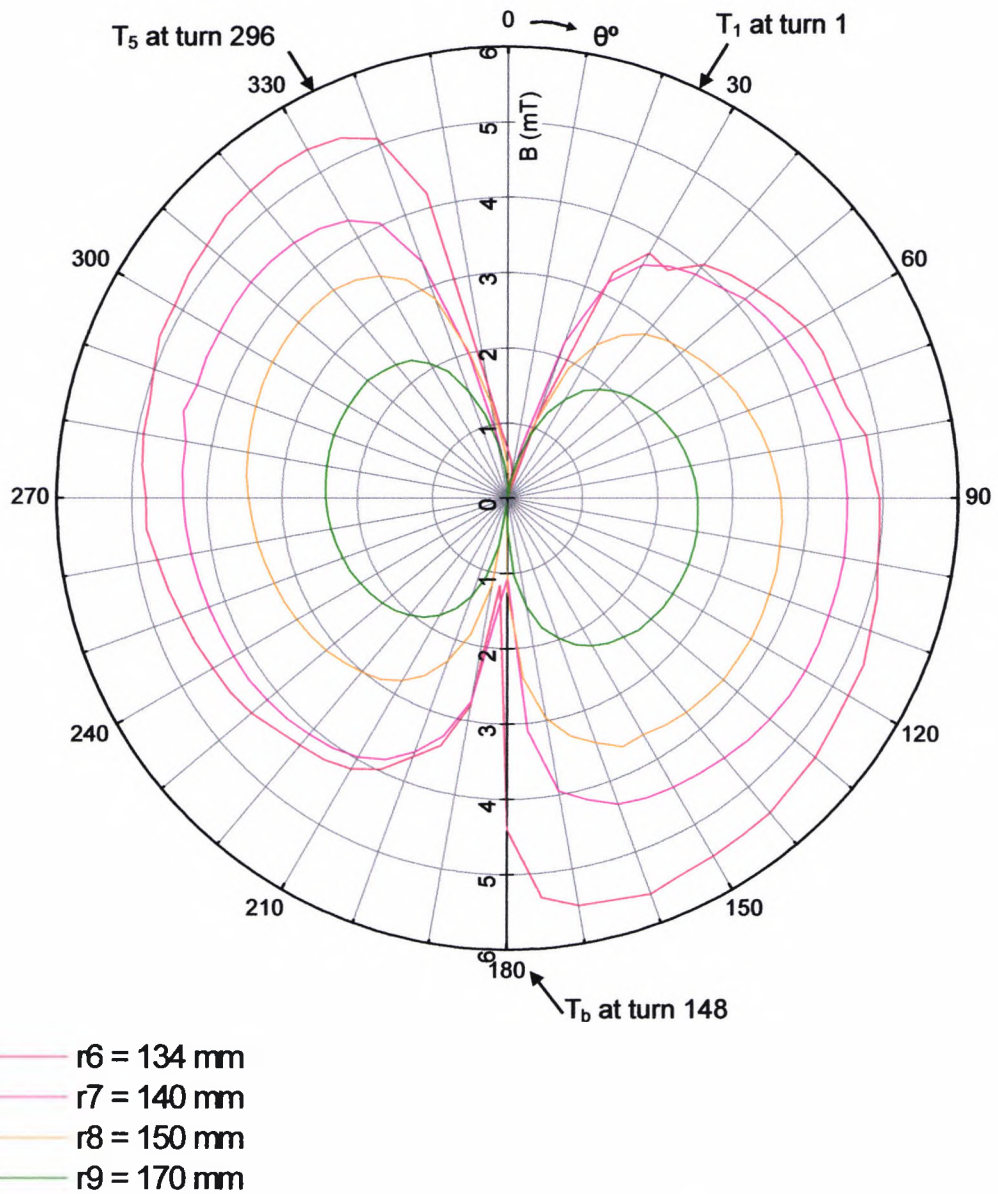


Fig. 4.28 Variation of circumferential magnetic field B surrounding the toroidal core with r , θ and z in the presence of the top plate: $z = z_2 = 41 \text{ mm}$, $r = 134$ (r_6), 140 (r_7), 150 (r_8), 170 (r_9) mm, $\theta = 0 - 360^\circ$ (Fig. 4.13).

The effects of brush and tap positions on magnetic field distribution above and surrounding the transformer core can be seen from figures Fig. 4.29 and Fig. 4.30. It is evident that the spatial distribution of peak flux density corresponds to the brush position and the distribution of this field is highly non-uniform in nature. For Fig. 4.28, the following electrical parameters apply:

$I_1 = 12 \text{ A}$, $I_3 = 25 \text{ A}$, $V = 240\text{v}$, and $f = 50 \text{ Hz}$. Taps T_1 and T_4 are at turns 1 and 257 respectively. For Fig. 4.29 and Fig. 4.30 currents are: $I_1 = 15.9$; 9.5 and 4.7 A . $I_2 = 9.1$; 15.5 and 20.3 A .

4.3.3. Results for Model 3:

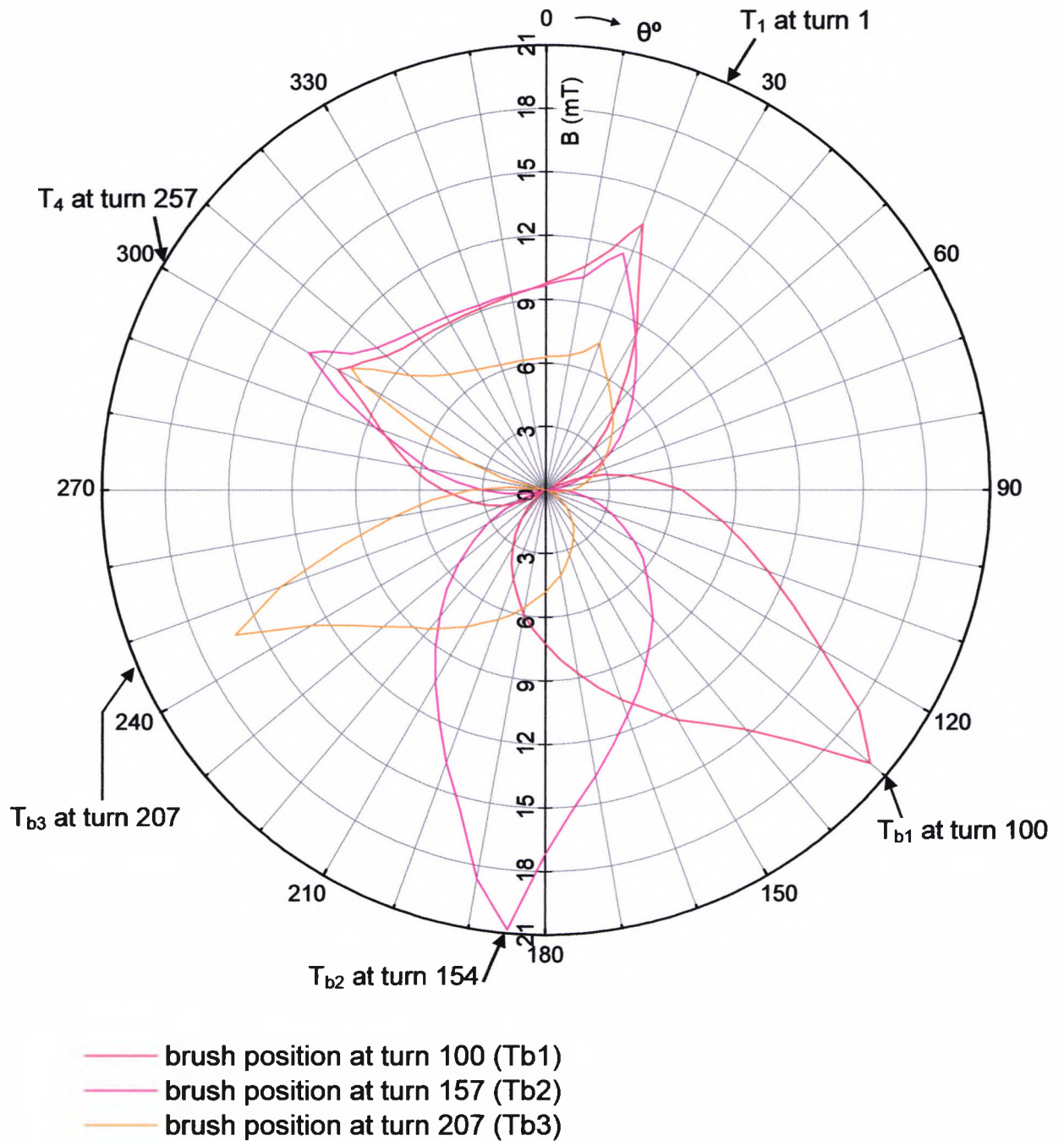


Fig. 4.29 Variation of flux density B surrounding the toroidal core with r , θ , z and brush positions in the absence of the top plate: $z = z_2 = 41$ mm, $r = 134$ (r_6) mm, $\theta = 0 - 360^\circ$, brush positions T_{b1} , T_{b2} and T_{b3} are at turn 100, 154 and 207 respectively.

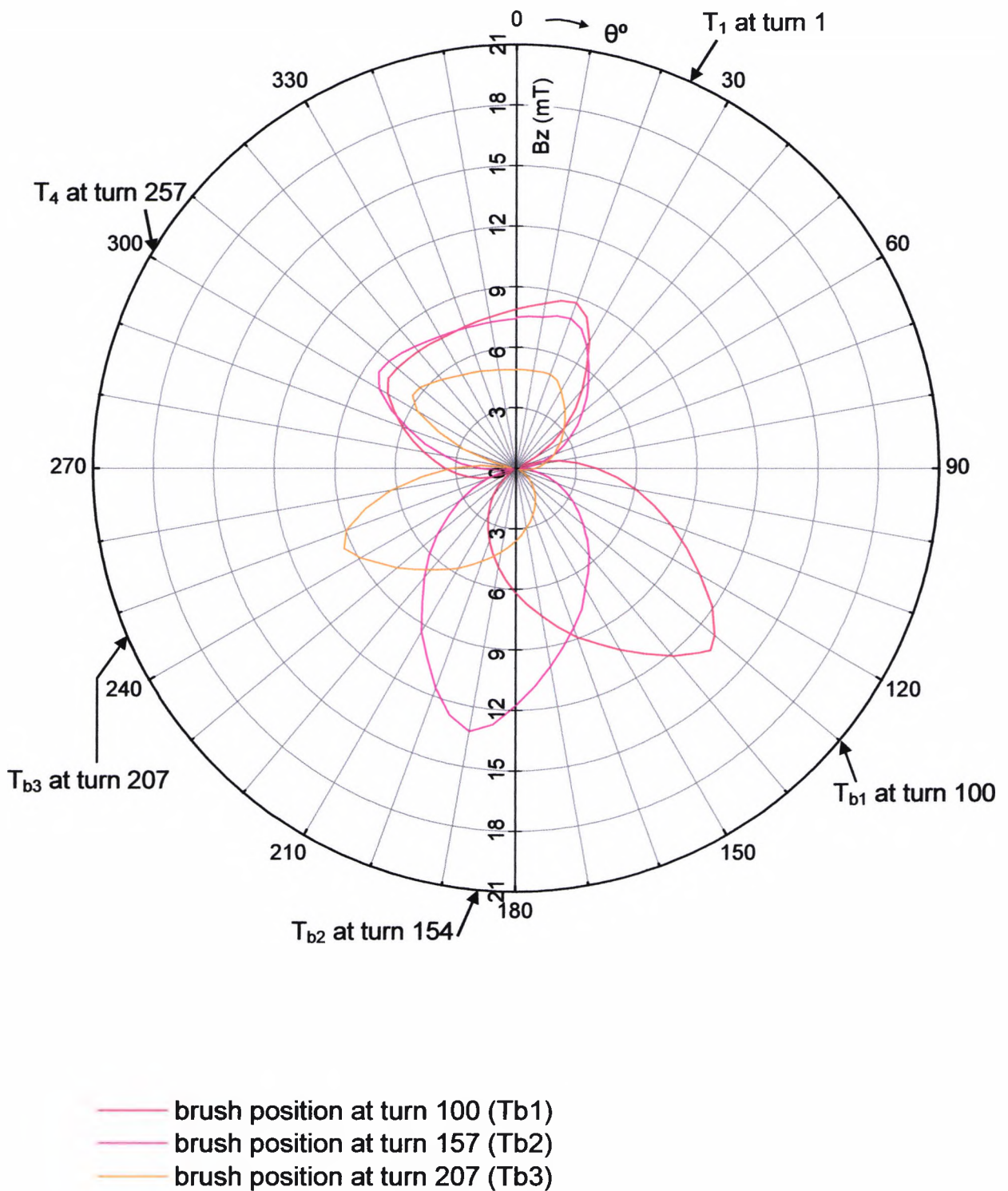


Fig. 4.30 Variation of flux density B_z above the toroidal core with r , θ , z and brush positions in the absence of the top plate: $z = 84$ mm, $r = 87$ (r_2) mm, $\theta = 0 - 360^\circ$, brush positions T_{b1} , T_{b2} and T_{b3} are at turn 100, 154 and 207 respectively.

4.4. Validation of Finite Element Models

This section presents some of the results of modelling investigation of the TS1225 commercial variable transformer described earlier. The results are compared with corresponding experimental data obtained in the previous chapter. This is to validate the modelling methodologies developed and establish confidence in the results of Sub-sequent modelling studies. Results are presented in terms of magnetic field distribution in air over and around the toroidal core of the transformer for various brush and tap positions. Some of the results compared also show the effects of the top plate on field distribution over the core. It is shown that the magnitude and distribution of this field is affected by operational regimes characterized by brush and tap positions which determine the current distribution in the winding. As shown below in this chapter the modelling results are in good agreement with the experimental data which validates the FE modelling strategies used.

4.4.1. Comparison of modelling Results with Experimental Data for Model 1.

Comparison of some of the FE results with the corresponding experimental data, obtained for experimental Model 1 described in the previous chapter are shown in Figures Fig. 4.31-Fig. 4.34. These are for flux density values above and around the toroidal core for various r and z values. The parameters like currents I_1 and I_2 , and brush/tap positions are also varied. It can be said from these figures that, overall the modelling results are in good agreement with the experimental ones. This validates the modelling methodologies and the FE models developed in this work. However, these are further refined for more detail modelling investigations described in the subsequent chapters.

From the figures presented here it can be seen that this good agreement is especially true for flux density values nearer to the core in terms of distances r and z . The difference between modelling and experimental results in these figures for values of r , z farther from the core are mainly attributable to FE modelling and experimental errors which can only be minimised but never completely eliminated. These include discretisation errors due to finite number and size of volume elements used in FE modelling, various measurements

errors associated with the Gauss-meter used, its precise positioning, some variations in input currents over the period of a given cycle of measurement, etc. the main discrepancies between modelling and experimental results can be seen for xy component of flux density, B_{xy} (for example, in Fig. 4.42 and Fig. 4.43). This is attributed to the fact that while the simulation results can accurately represent the resultant of x and y components of flux density (B_x , B_y), this cannot be done so by experiment. This is due to both positional and orientational inaccuracies of the Hall probe used for measurements. Considering this, the maximum accuracy is obtained for the measurement of the three main components (e.g. B_z) of the flux density vector \vec{B} .

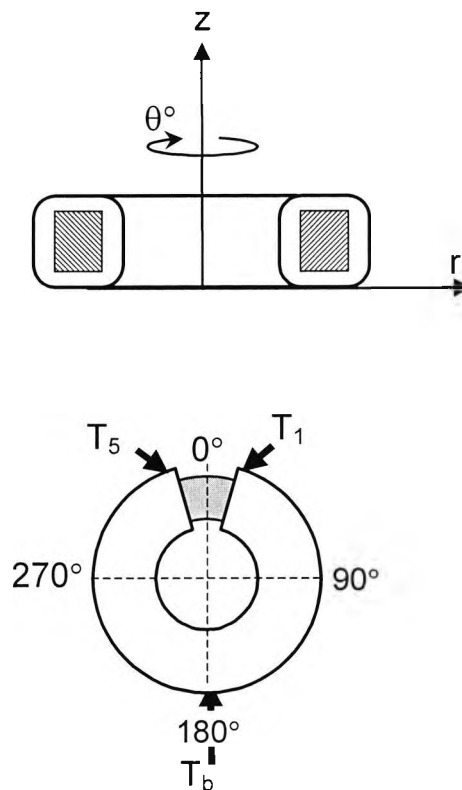
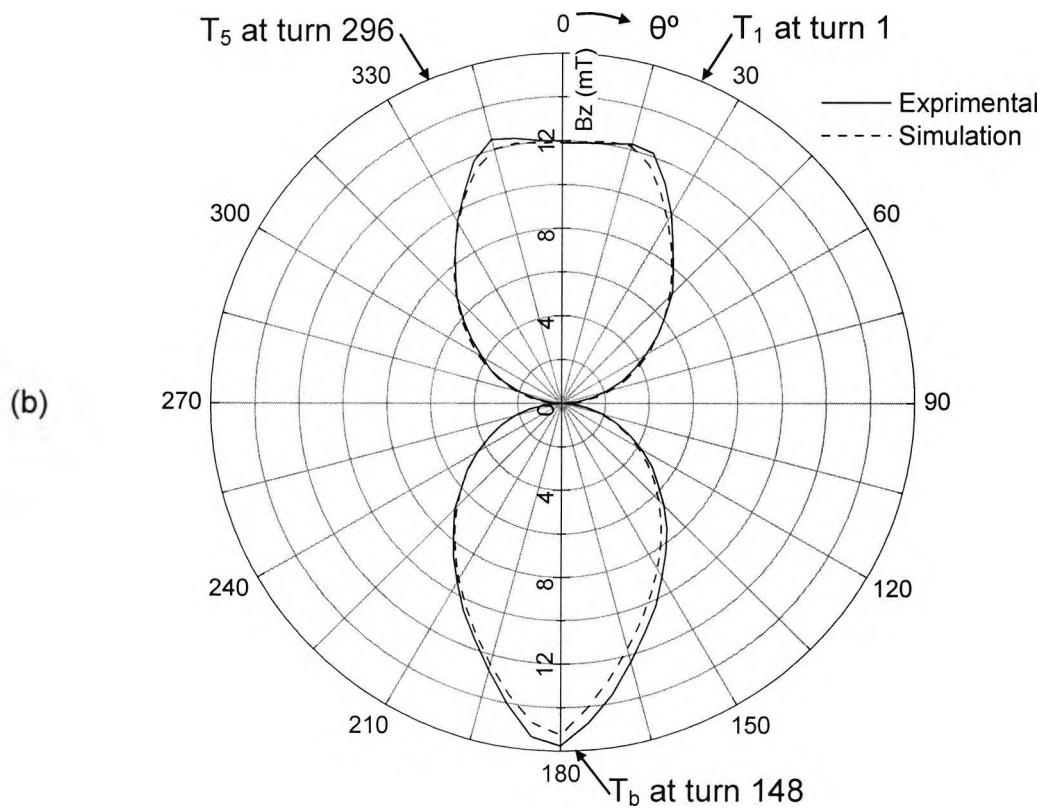
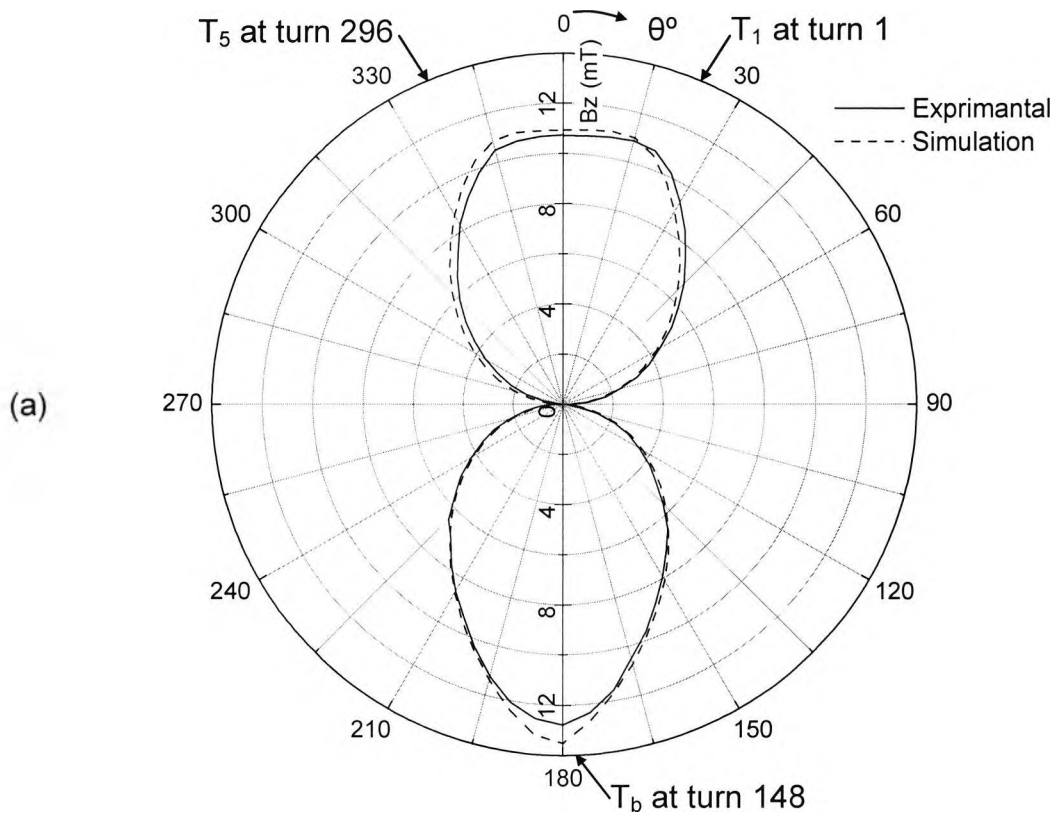


Fig. 4.31 TS1225 toroidal core (in the absence of top and bottom plate shown Schematically)



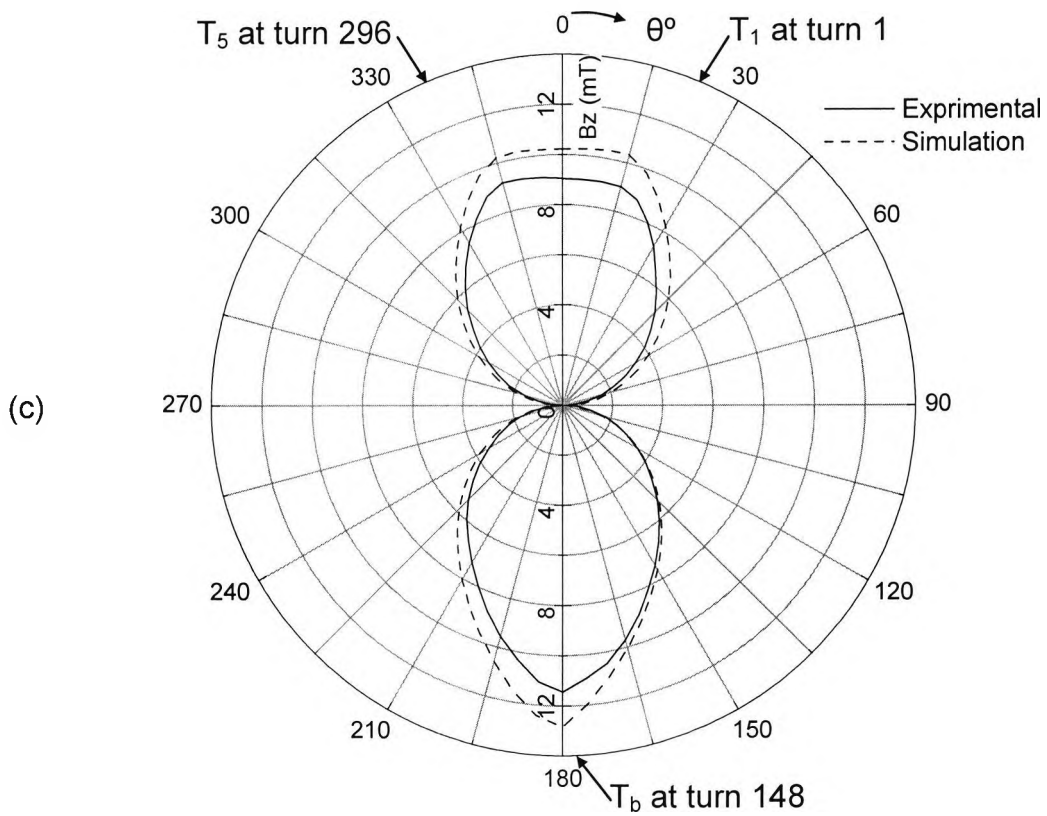
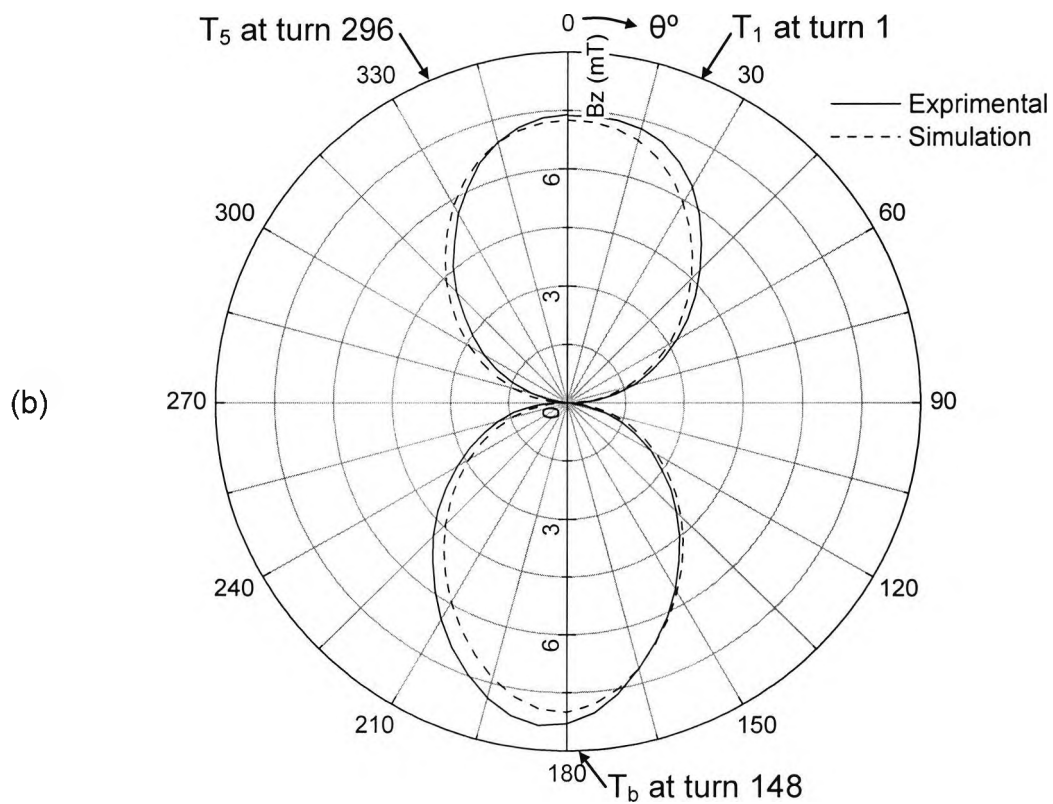
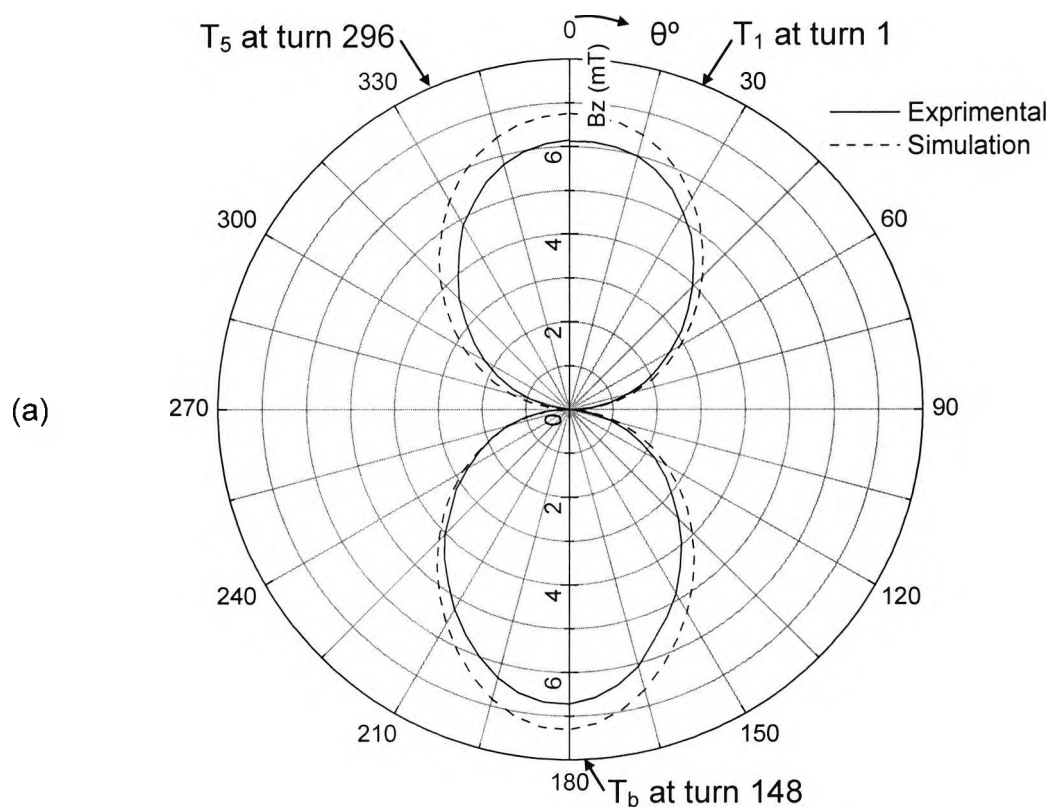


Fig. 4.32 Validation of FE modelling comparison of vertical component of flux density values (B_z) obtained from modelling with corresponding to experimental data, measured in air above the toroidal core (in the absence of top and bottom plate shown schematically in Fig. 4.31); $z = z_4 = 91\text{mm}$, (a) $r = r_2 = 87\text{mm}$, (b) $r = r_3 = 110\text{mm}$ and (c) $r = r_5 = 130\text{mm}$; other parameters: $I_1 = 12\text{A}$, $I_2 = 12\text{A}$; total number of turns $N=296$; taps T_1 at turn number 1; T_5 at turn number 296 and T_3 the brush position (T_b) at turn number 148 ($\theta \cong 180^\circ$).



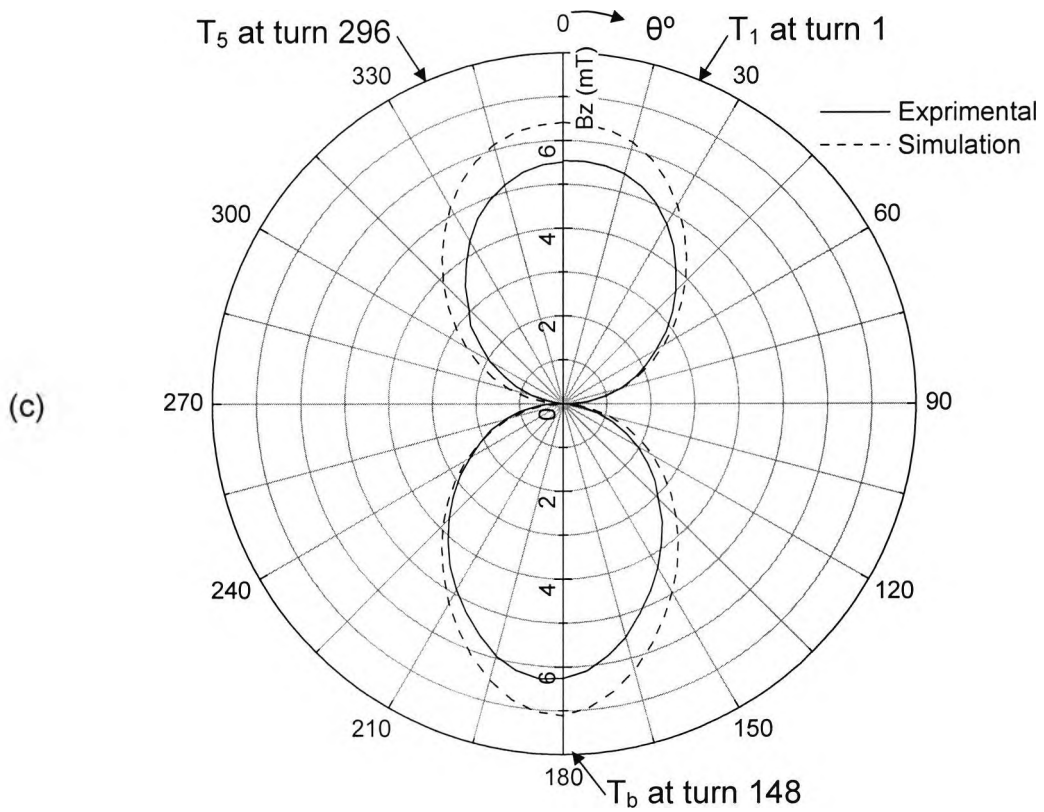
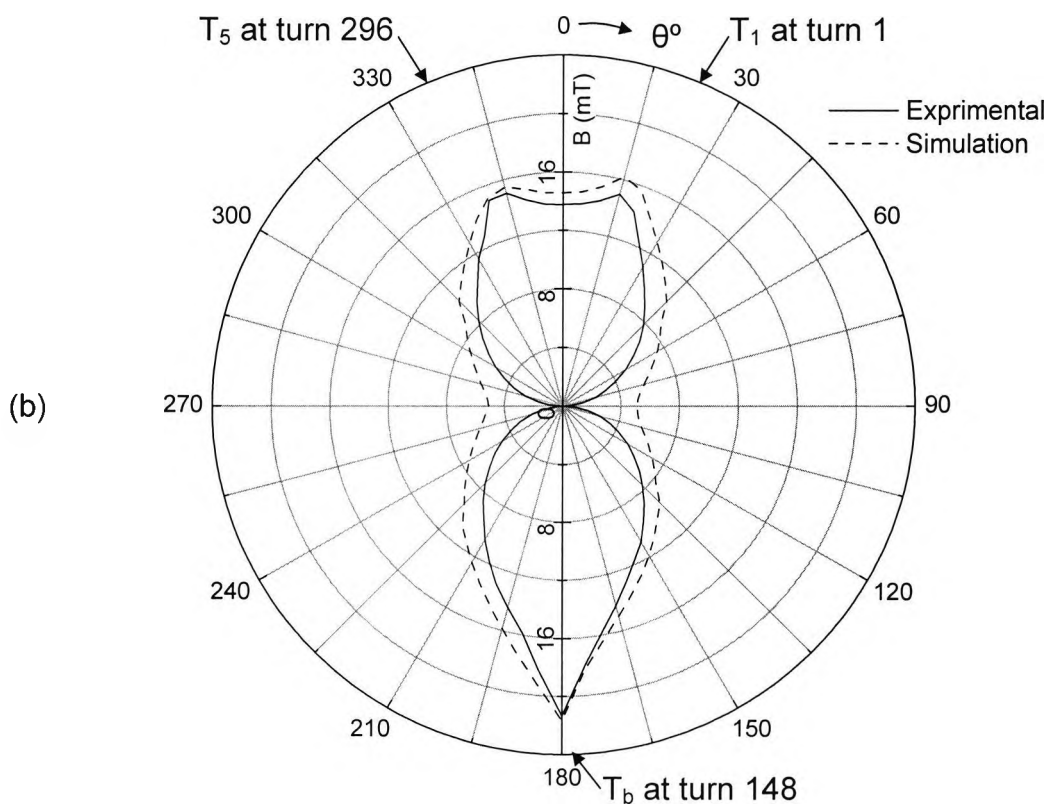
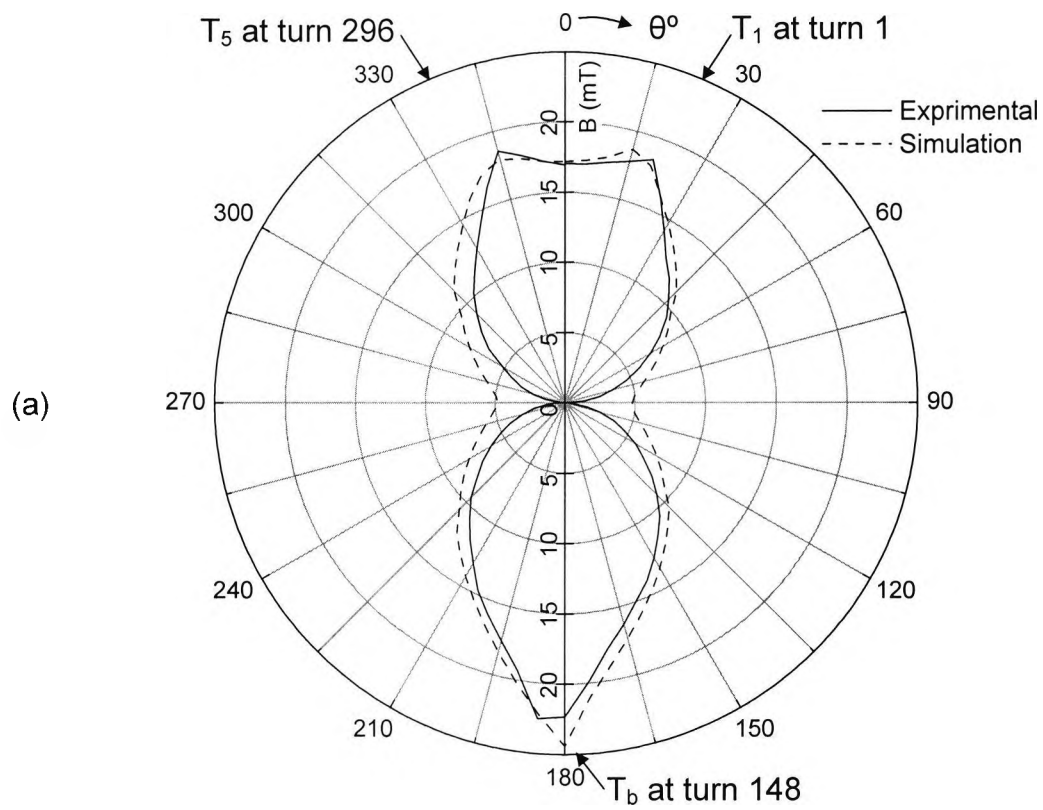


Fig. 4.33 Validation of FE modelling comparison of vertical component of flux density values (B_z) obtained from modelling with corresponding to experimental data, measured in air above the toroidal core (in the absence of top and bottom plate shown schematically in Fig. 4.31); $z = z_6 = 117\text{mm}$, (a) $r = r_2 = 87\text{mm}$, (b) $r = r_3 = 110\text{mm}$ and (c) $r = r_5 = 130\text{mm}$; other parameters: $I_1 = 12\text{A}$, $I_2 = 12\text{A}$; total number of turns $N=296$; taps T_1 at turn number 1; T_5 at turn number 296 and T_3 the brush position (T_b) at turn number 148 ($\theta \cong 180^\circ$).



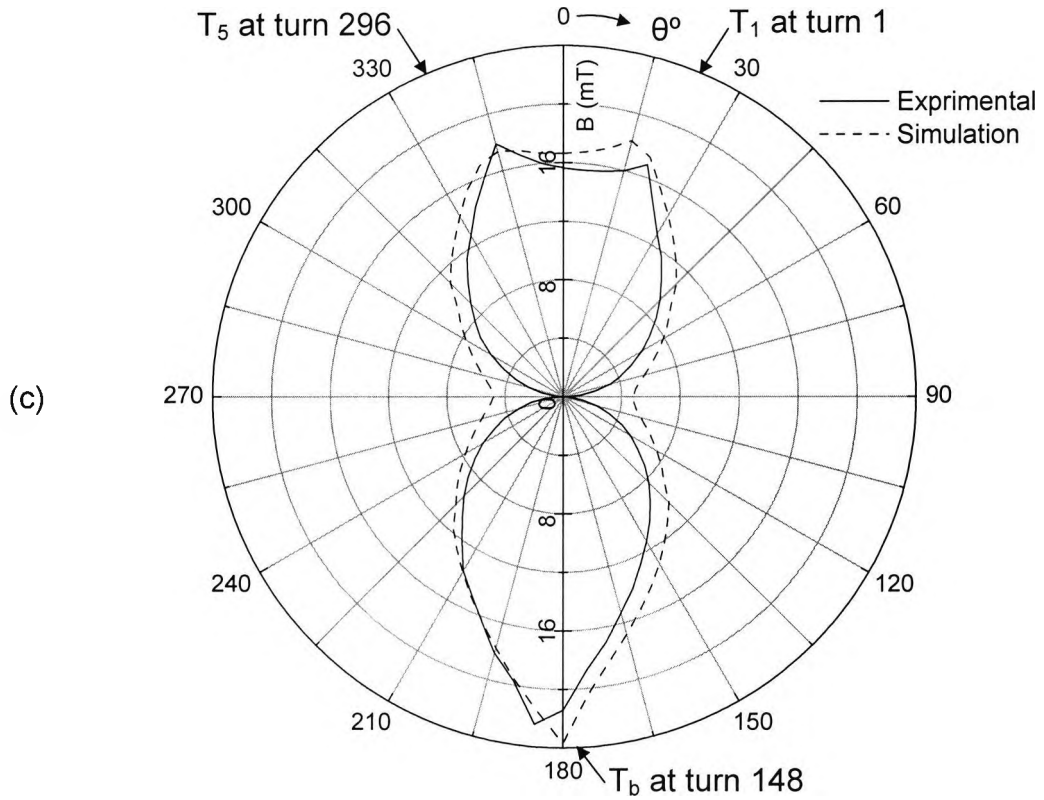


Fig. 4.34 Validation of FE modelling comparison of vertical component of flux density values B obtained from modelling with corresponding to experimental data, measured in air around the toroidal core (in the absence of top and bottom plate shown schematically in Fig. 4.31); $r = r_6 = 150\text{mm}$, (a) $z = z_1 = 13\text{mm}$, (b) $z = z_2 = 41\text{mm}$ and (c) $z = z_3 = 70\text{mm}$; other parameters: $I_1 = 12\text{A}$, $I_2 = 12\text{A}$; total number of turns $N=296$; taps T_1 at turn number 1; T_5 at turn number 296 and T_3 the brush position (T_b) at turn number 148 ($\theta \cong 180^\circ$).

4.4.2. Comparison of modelling Results with Experimental Data for Model 2.

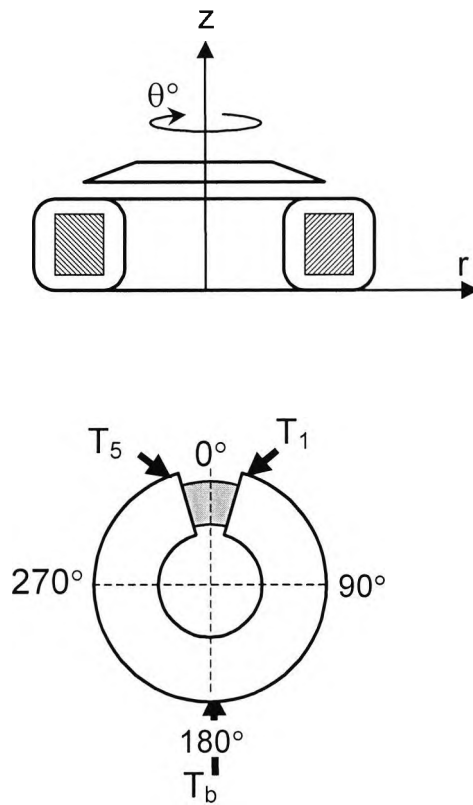
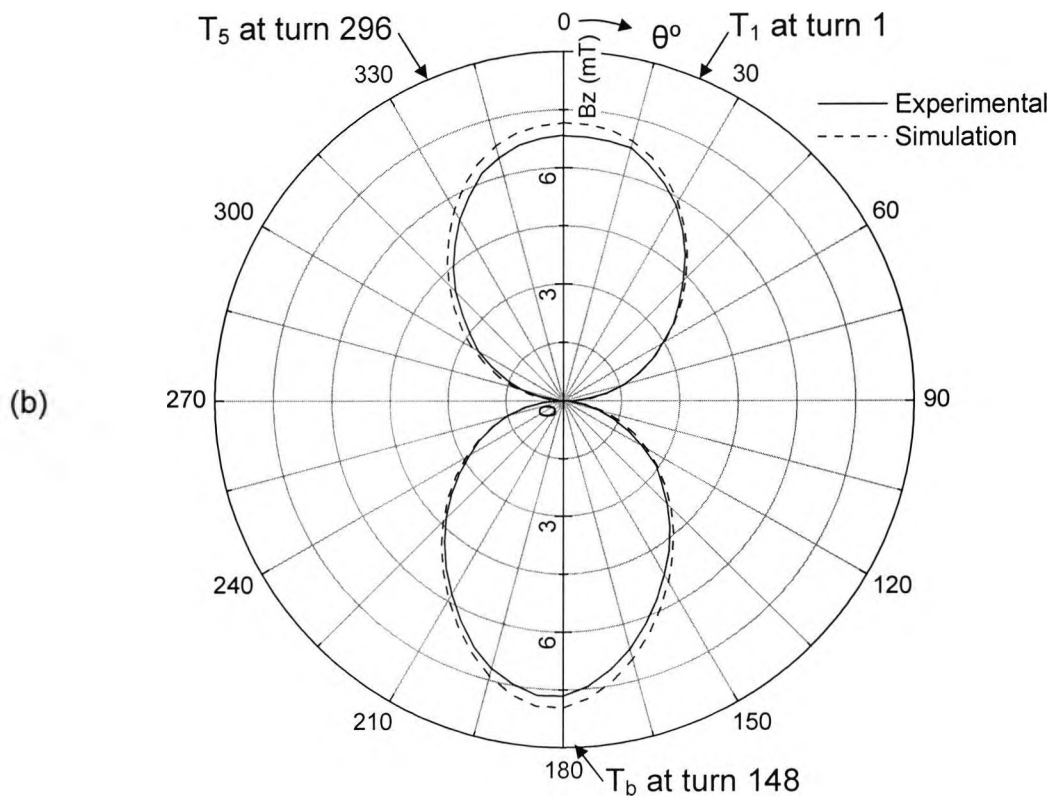
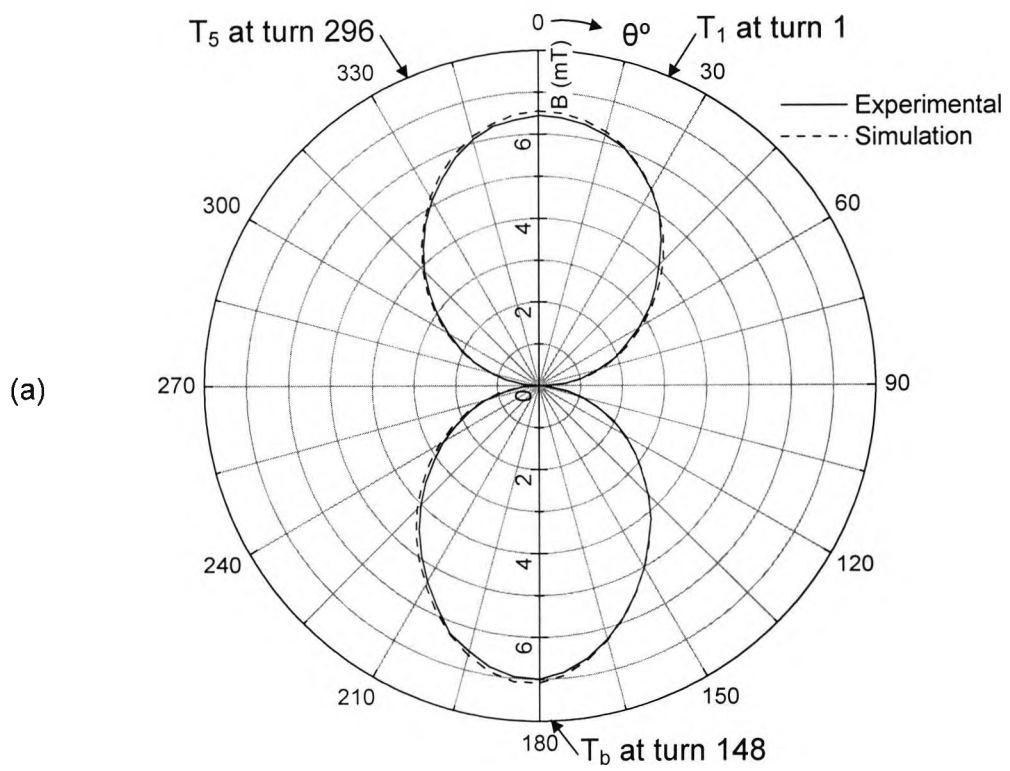


Fig. 4.35 TS1225 toroidal core (in the presence of top plate and absence of bottom plate shown Schematically)



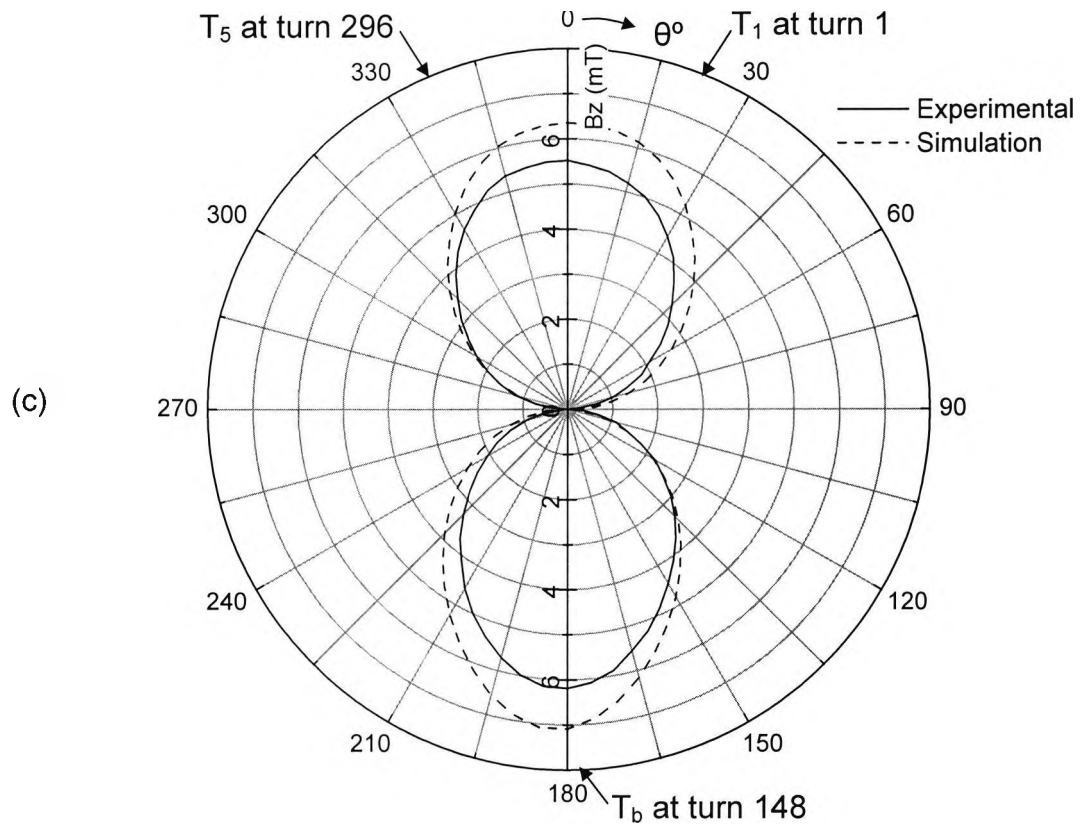


Fig. 4.36 Validation of FE modelling comparison of vertical component of flux density values (B_z) obtained from modelling with corresponding to experimental data, measured in air above the toroidal core (in the presence of top plate and absence of bottom plate shown schematically in Fig. 4.35); $z = z_6 = 117\text{mm}$, (a) $r = r_2 = 87\text{mm}$, (b) $r = r_3 = 110\text{mm}$ and (c) $r = r_5 = 130\text{mm}$; other parameters: $I_1 = 12\text{A}$, $I_2 = 12\text{A}$; total number of turns $N=296$; taps T_1 at turn number 1; T_5 at turn number 296 and T_3 the brush position (T_b) at turn number 148 ($\theta \cong 180^\circ$).

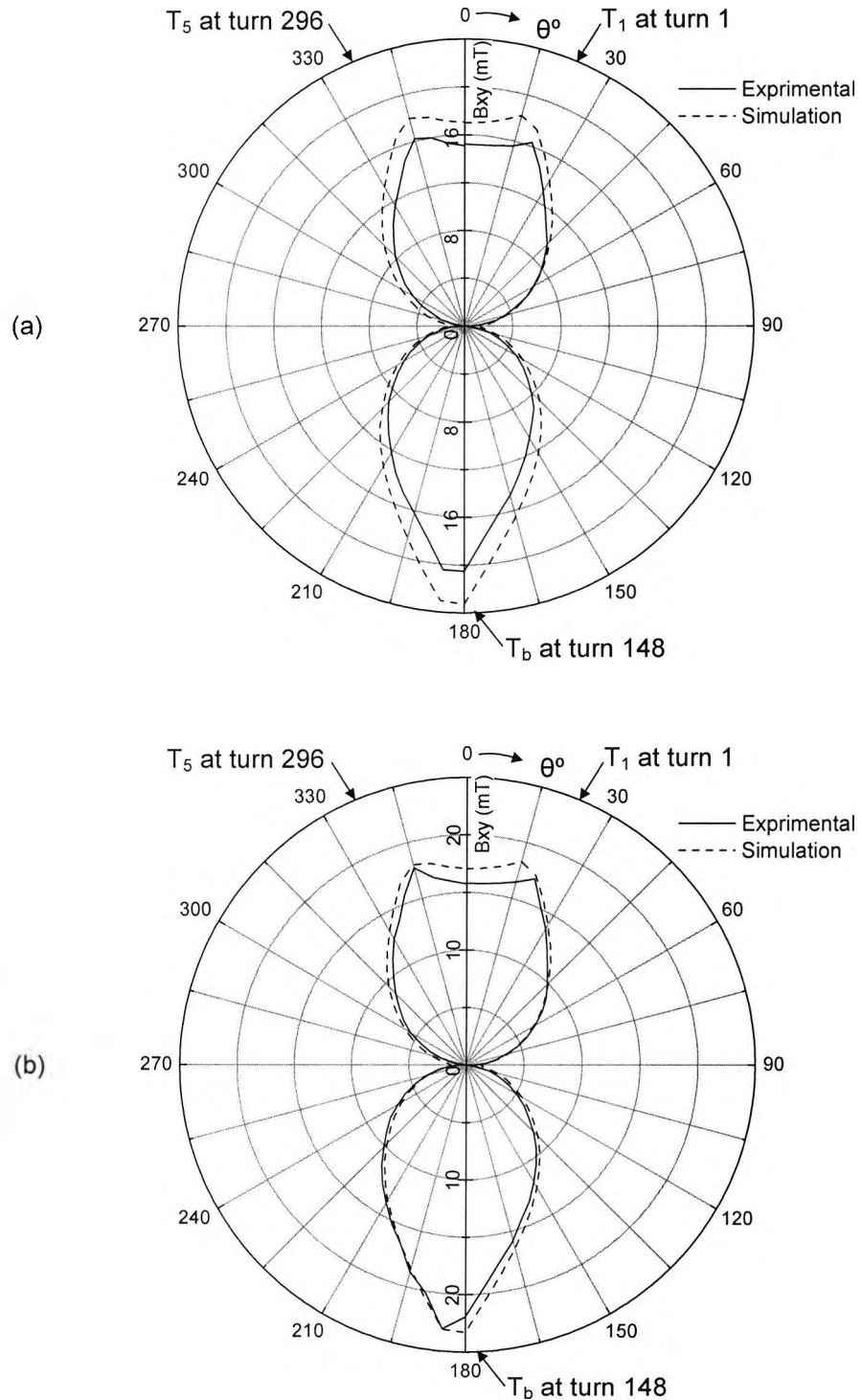


Fig. 4.37 Validation of FE modelling comparison of vertical component of flux density values B obtained from modelling with corresponding to experimental data, measured in air around the toroidal core (in the presence of top and absence of bottom plate shown schematically in Fig. 4.35); $r = r_6 = 150\text{mm}$, (a) $z = z_1 = 13\text{mm}$, and (b) $z = z_3 = 70\text{mm}$; other parameters: $I_1 = 12\text{A}$, $I_2 = 12\text{A}$; total number of turns $N=296$; taps T_1 at turn number 1; T_5 at turn number 296 and T_3 the brush position (T_b) at turn number 148 ($\theta \cong 180^\circ$).

4.4.3. Comparison of modelling Results with Experimental Data for Model 3.

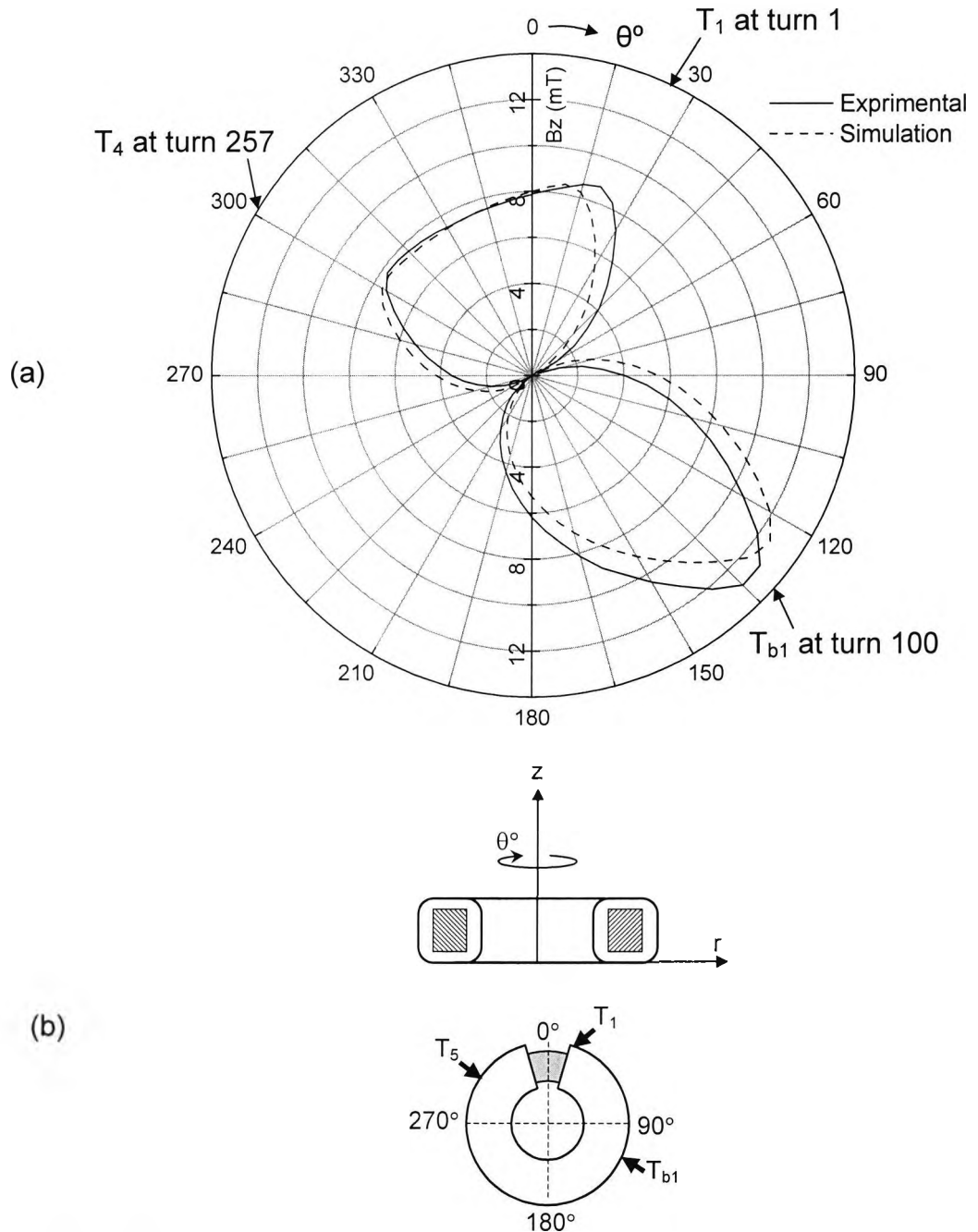


Fig. 4.38 Validation of FE modelling comparison of vertical component of flux density values (B_z) obtained from modelling with corresponding to experimental data, measured in air above the toroidal core (in the absence of top and bottom plate shown schematically in (b)); $z = z_4 = 91\text{mm}$, $r = r_2 = 87\text{mm}$; other parameters: $I_1 = 15.9\text{A}$, $I_2 = 9.1\text{A}$; total number of turns $N=257$; taps T_1 at turn number 1; T_4 at turn number 257 and T_3 the brush position (T_{b1}) at turn number 100.

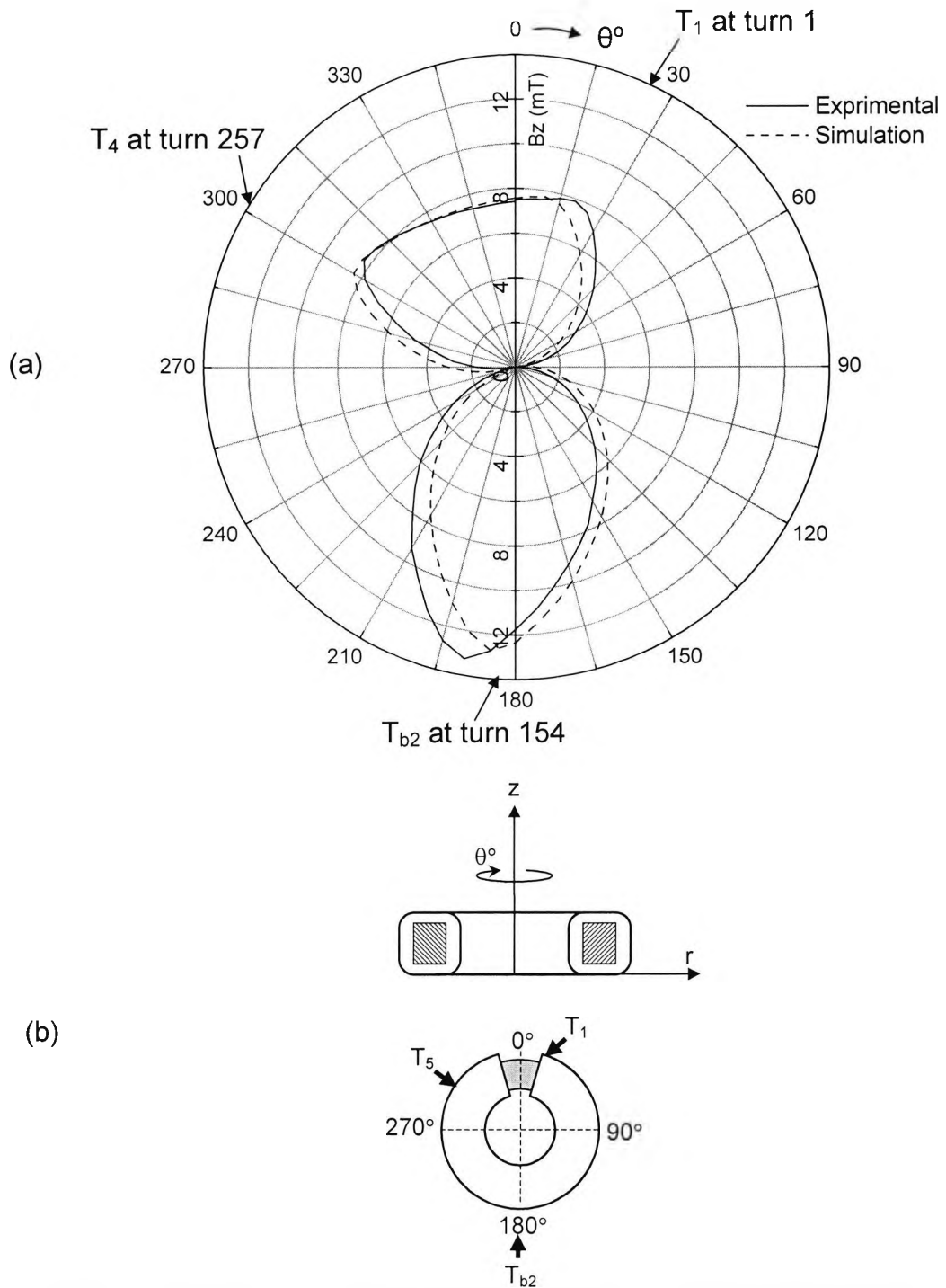


Fig. 4.39 Validation of FE modelling comparison of vertical component of flux density values (B_z) obtained from modelling with corresponding to experimental data, measured in air above the toroidal core (in the absence of top and bottom plate shown schematically in (b); $z = z_4 = 91\text{mm}$, $r = r_2 = 87\text{mm}$; other parameters: $I_1 = 9.5\text{A}$, $I_2 = 15.5\text{A}$; total number of turns $N=257$; taps T_1 at turn number 1; T_4 at turn number 257 and T_3 the brush position (T_{b2}) at turn number 154.

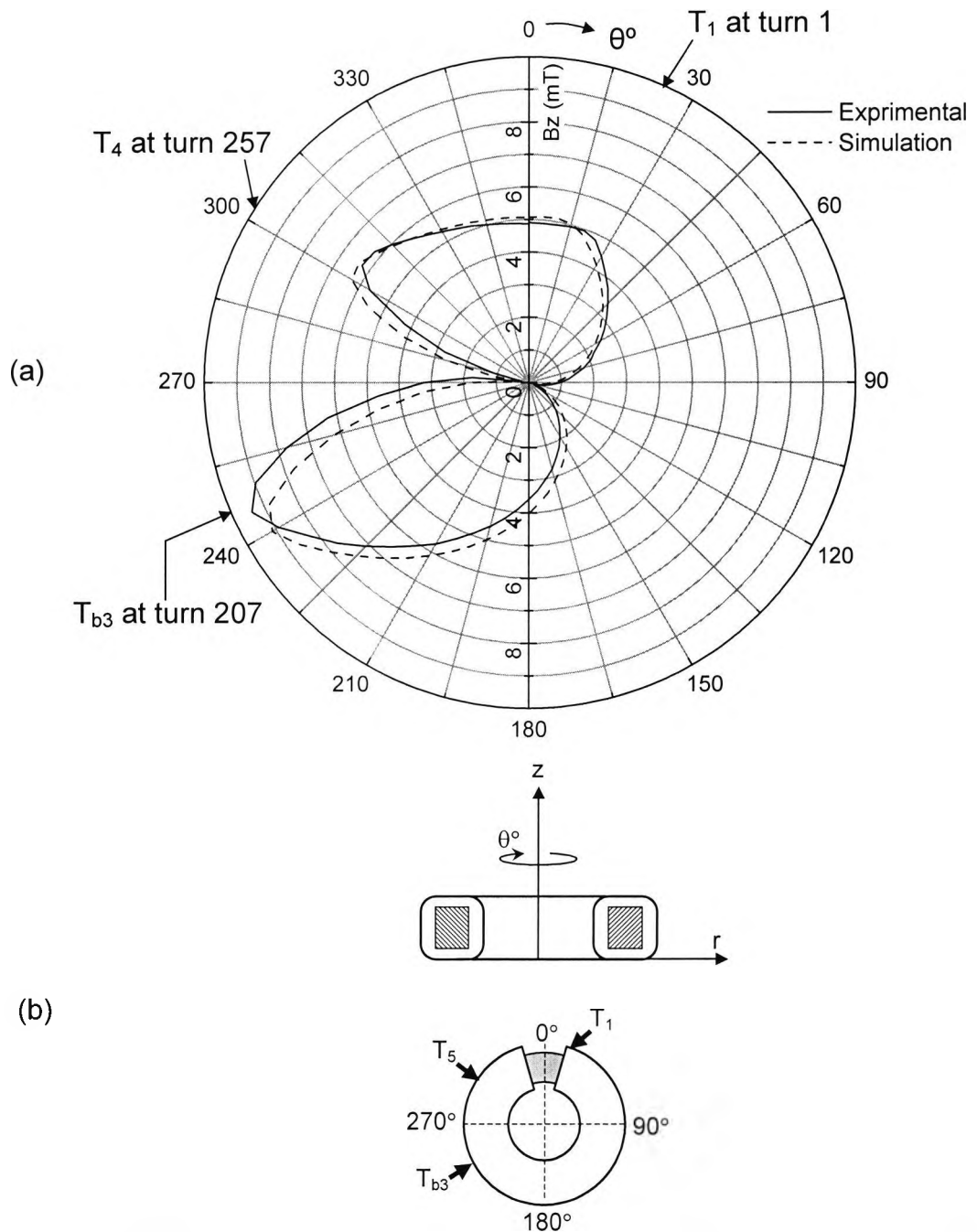


Fig. 4.40 Validation of FE modelling comparison of vertical component of flux density values (B_z) obtained from modelling with corresponding to experimental data, measured in air above the toroidal core (in the absence of top and bottom plate shown schematically in (b)); $z = z_4 = 91\text{mm}$, $r = r_2 = 87\text{mm}$; other parameters: $I_1 = 4.7\text{A}$, $I_2 = 20.3\text{A}$; total number of turns $N=257$; taps T_1 at turn number 1; T_4 at turn number 257 and T_3 the brush position (T_{b3}) at turn number 207.

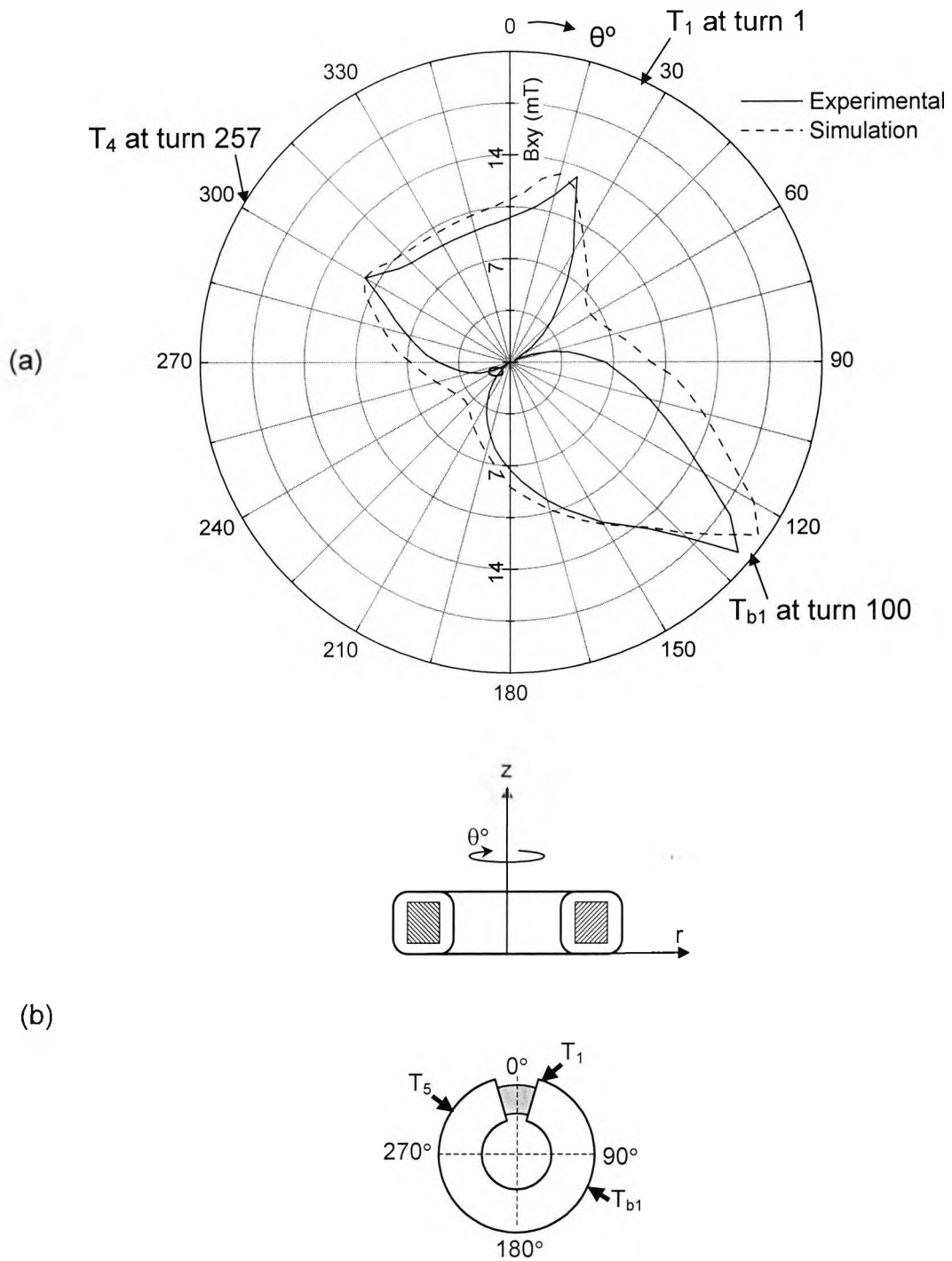


Fig. 4.41 Validation of FE modelling comparison of vertical component of flux density values B obtained from modelling with corresponding to experimental data, measured in air around the toroidal core (in the absence of top and bottom plate shown schematically in (b)); $r = r_6 = 150\text{mm}$, $z = z_2 = 41\text{mm}$; other parameters: $I_1 = 15.9\text{A}$, $I_2 = 9.1\text{A}$; total number of turns $N=257$; taps T_1 at turn number 1; T_4 at turn number 257 and T_3 the brush position (T_{b1}) at turn number 100.

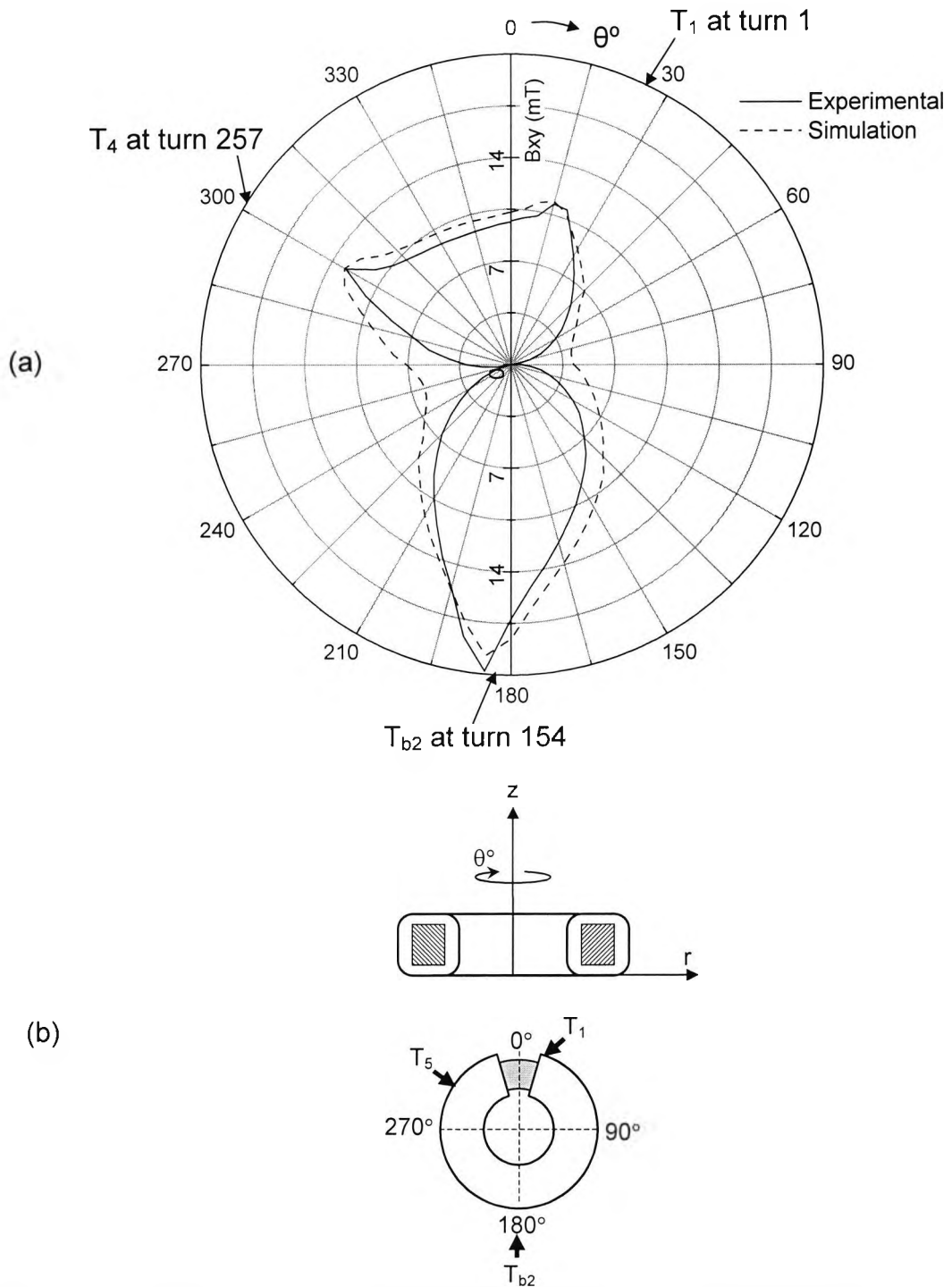


Fig. 4.42 Validation of FE modelling: comparison of vertical component of flux density values B obtained from modelling with corresponding to experimental data, measured in air around the toroidal core (in the absence of top and bottom plate shown schematically in(b)); $r = r_6 = 150\text{mm}$, $z = z_2 = 41\text{mm}$; other parameters: $I_1 = 9.5\text{A}$, $I_2 = 15.5\text{A}$; total number of turns $N=257$; taps T_1 at turn number 1; T_4 at turn number 257 and T_3 the brush position (T_{b2}) at turn number 154.

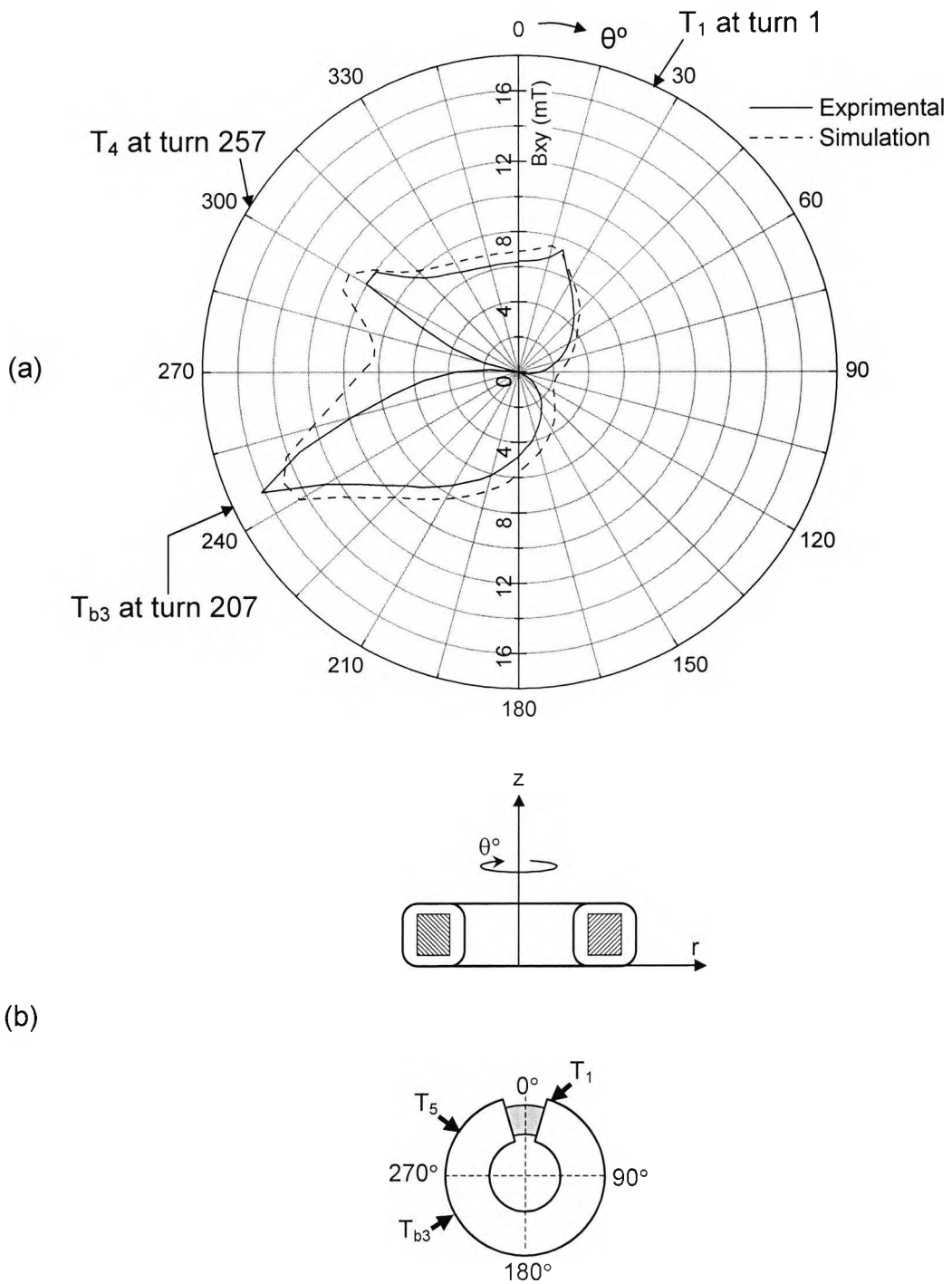


Fig. 4.43 Validation of FE modelling: comparison of vertical component of flux density values (B_z) obtained from modelling with corresponding to experimental data, measured in air around the toroidal core (in the absence of top and bottom plate shown schematically in (b)); $z = z_4 = 91\text{mm}$, $r = r_2 = 87\text{mm}$; other parameters: $I_1 = 4.7\text{A}$, $I_2 = 20.3\text{A}$; total number of turns $N=257$; taps T_1 at turn number 1; T_4 at turn number 257 and T_3 the brush position (T_{b3}) at turn number 207.

Chapter 5.

Investigation of Commercial Variable Transformers by Finite Element Modelling

5.1. Introduction

Having developed the methodologies for finite element (FE) modelling of variable transformers and validated some of the modelling results corresponding experimental data, this chapter presents the results of further investigation of various designs of commercial variable transformers used as voltage stabilisers. The investigation is carried out by 3D FE modelling and computation of non-linear magnetic field distribution in various designs of such transformers. The effects of electromagnetic and geometric parameters, and various operational regimes (brush and tap positions) on the distribution of magnetic field and saturation level in the core are calculated and discussed. Their effects on magnetic field distribution in the air above the core are also discussed. These factors ultimately define the overall size and performance of the voltage stabilisers investigated in this chapter. Results are presented in terms of flux plots and design curves.

5.2. Investigation of the core for various Design Parameters

It is obvious that, the core of a variable transformer plays a vital role in its effective performance. It also comprises one of its major constructive features that ultimately determine its overall size. One of the main optimisation problems in variable transformers is to find the minimum core size that, would ensure an acceptable level of core saturation for various geometric parameters and

operational regimes given by, for example, brush and tap positions. Fig. 5.1 shows the longitudinal section of a typical core of such a transformer.

The inner and outer radii R_i and R_o determine the core width and hence, the overall 'footprint' of a transformer. The outer radius R_o also determines the total length of the brush track and so the total number of winding turns N that can be placed side by side on the track for a given conductor size used for the winding. This means that the value of R_o cannot be taken less than a given lower threshold since the number of winding turns N , constituting the brush track, directly determines the range and the resolution of variability of voltage that can be achieved by a given transformer design.

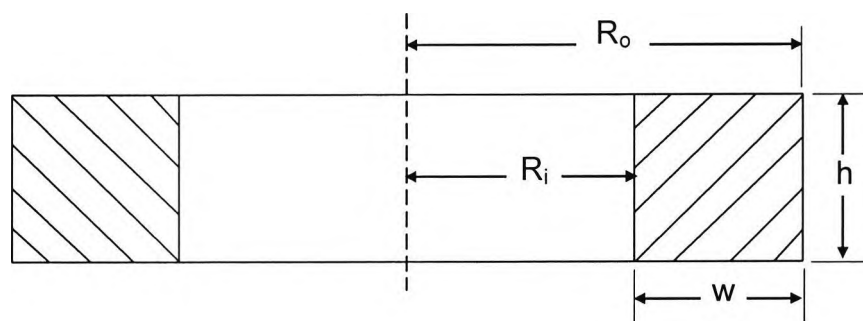


Fig. 5.1 Longitudinal section of the toroidal core showing the main geometric parameters investigated.

The lower threshold for the height of the core h is determined by the minimum surface area of the brush track that is needed to accommodate an adequate number and size of segmented brushes that traverse the track. This section investigates a typical transformer core (e.g. TS1225) to evaluate the effects of various design parameters. Fig. 5.2 – Fig. 5.5 show the various geometric parameters of the core which were varied to investigate their effects on the core in terms of magnitude and distribution of flux density in the core.

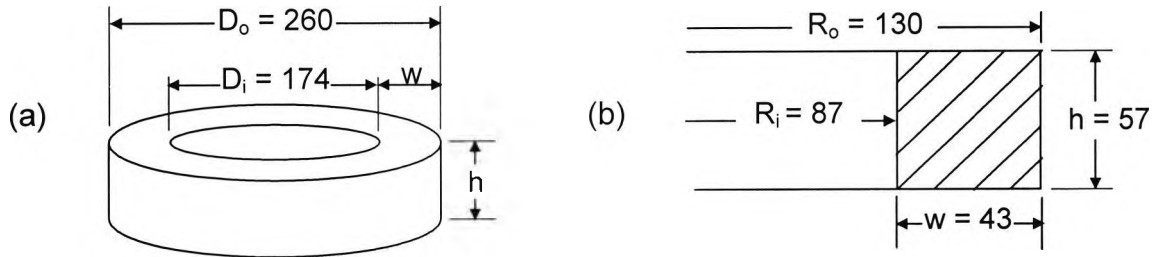


Fig. 5.2 Longitudinal section of the core showing its original geometric dimensions (in mm) for one of the variable transformers investigated (not drawn to scale); area of the core $A_c = 2451 \text{ mm}^2$.

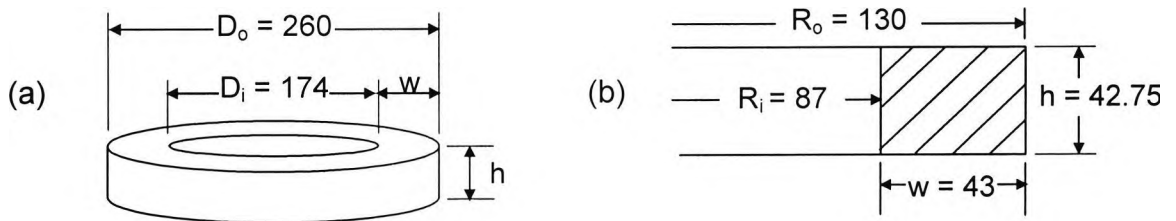


Fig. 5.3 Transformer core showing various geometric dimensions (in mm) including the variable height h reduced by 25% (not drawn to scale); $A_c = 1838.25 \text{ mm}^2$.

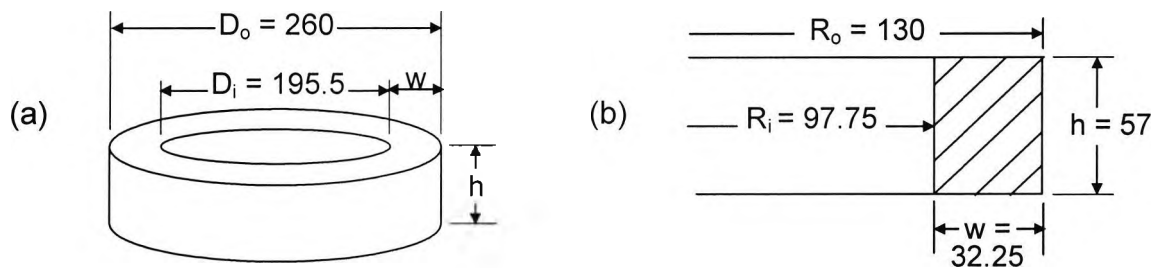


Fig. 5.4 Transformer core showing various geometric dimensions (in mm) including the variable width w reduced by 25% (not drawn to scale); $A_c = 1838.25 \text{ mm}^2$.

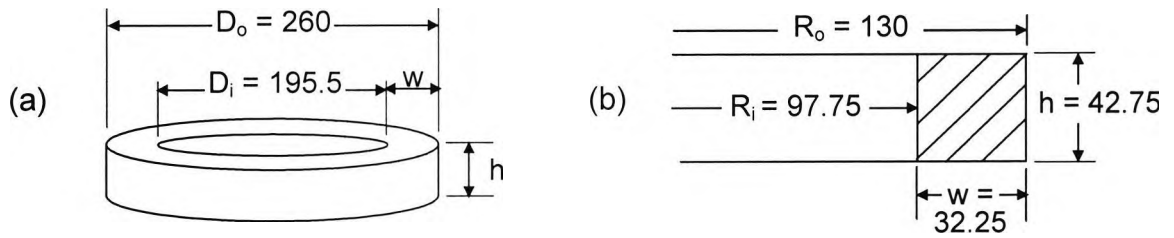


Fig. 5.5 Transformer core showing various geometric dimensions (in mm) including the variable height h and width w both reduced by 25% (not drawn to scale); $A_c = 1378.7 \text{ mm}^2$.

Table 5.1 summarizes the various cases of modelling investigation based on the combination of core parameters shown in Figs, Fig. 5.2 – Fig. 5.5.

Throughout these modelling investigations, the total magneto-motive force (m.m.f) of the winding was kept constant and was equal to that of the original configuration of the transformer modelled (Table 5.1, raw 3). The outer diameter of the core D_o was also kept constant for these investigations. However, variations in core dimensions meant that relevant dimensions of the winding turns made up of generally oriented race track (Fig. 3.16; Fig. 3.17 and Table 3.2) also needed to be adjusted. This is done in the following section.

Table 5.1 combination of core parameters used for various cases of modelling investigation; L_w – total winding length, R_w – winding resistance.

Modelling Cases	D_i	D_o	h	w	A_c	L_w	R_w
	mm	mm	mm	mm	mm^2	m	Ω
CASE 1 (original parameters)	174	260	57	43	2451	75.4	0.36
CASE 2	174	260	42.75	43	1838.25	64.75	0.31
CASE 3	195.5	260	57	32.25	1838.25	68.30	0.33
CASE 4	195.5	260	42.75	32.25	1378.7	57.70	0.28

5.2.1. Calculation of winding parameters

As mentioned in the previous chapters for all modelling investigations the continuous helical winding of variable transformers was replaced with equivalent single turn conductors producing the same m.m.f. As mentioned in

section 3.3, because of the overlapping of turns, these turns were divided into two layers (groups) – one slightly bigger in size than the other. Fig. 5.6 shows the odd, T_1 (smaller) and even T_2 (larger) turns.

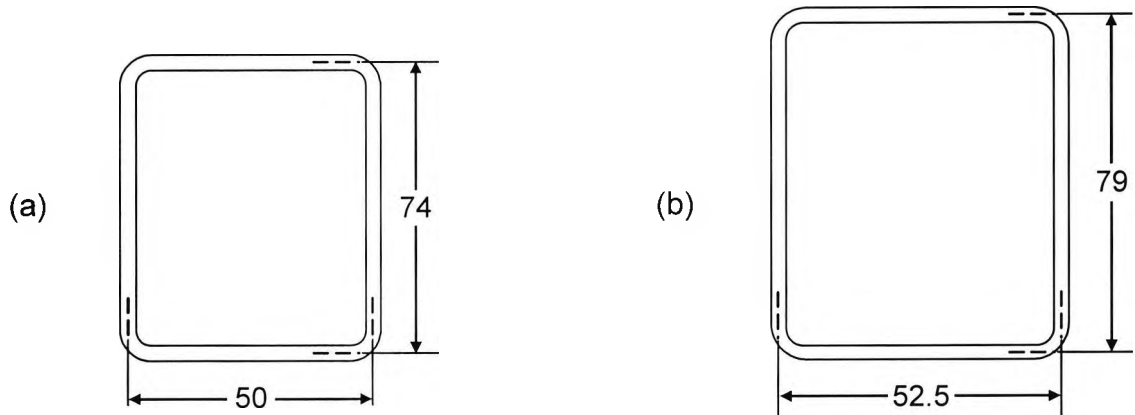


Fig. 5.6 Schematic diagrams of conductor turns showing the original dimensions (in mm): (a) smaller odd turn T_1 , (b) large overlapping even turn T_2 ; not drawn to scale.

The original Parameters for the first layer of winding turns consisting of smaller odd number turns T_1 are as followings Fig. 3.17 and Table 3.2:

$$(X_0, Y_0, Z_0) = (0, 0, 0)$$

$$X_{CEN} = 108.5 * \cos(\theta),$$

$$Y_{CEN} = 108.5 * \sin(\theta),$$

$$Z_{CEN} = 28.5 (h/2) + H_C \text{ (height of the core from the base plane).}$$

$$\theta = \text{from } 17 * (2 * \pi / 325) \text{ to } 311 * (2 * \pi / 325) \text{ increased by } 2 * (2 * \pi / 325)$$

$$A = B = 1.897 \text{ mm}$$

$$X_1 = 24 \text{ mm}, Y_1 = 0$$

$$H_1 = 36 \text{ mm}, R_1 = 1 \text{ mm}$$

For the second layer of winding turns consisting of larger even number of turns T_2 , the following parameters apply

$$(X_0, Y_0, Z_0) = (0, 0, 0)$$

$$X_{CEN} = 107.5 * \cos(\theta),$$

$$Y_{CEN} = 107.5 * \sin(\theta),$$

$$Z_{CEN} = 28.5 (h/2) + H_C \text{ (height of the core above the base plane).}$$

$$\theta = \text{from } 16 * (2 * \pi / 325) \text{ to } 310 * (2 * \pi / 325) \text{ increased by } 2 * (2 * \pi / 325)$$

$$A = B = 1.897 \text{ mm}; X_1 = 25.25 \text{ mm}; Y_1 = 0; H_1 = 38.5 \text{ mm and } R_1 = 1 \text{ mm}$$

The following two tables give these parameters for reduced core dimensions w and h :

Table 5.2 Conductor parameters for first layer of winding turns for reduced core dimensions w and h .

Parameters (mm)	25% reduction in h	25% reduction in w	25% reduction in both h, w
X_{CEN}	$108.5 \cdot \cos(\theta)$	$113.875 \cdot \cos(\theta)$	$113.875 \cdot \cos(\theta)$
Y_{CEN}	$108.5 \cdot \sin(\theta)$	$113.875 \cdot \sin(\theta)$	$113.875 \cdot \sin(\theta)$
Z_{CEN}	$21.375 + H_C$	$28.5 + H_C$	$21.375 + H_C$
X_I	24	18	18
H_I	27	36	27

Table 5.3 Conductor parameters for second layer of winding turns for reduced core dimensions w and h .

Parameters (mm)	25% reduction in h	25% reduction in w	25% reduction in both h, w
X_{CEN}	$107.25 \cdot \cos(\theta)$	$112.625 \cdot \cos(\theta)$	$112.625 \cdot \cos(\theta)$
Y_{CEN}	$107.25 \cdot \sin(\theta)$	$112.625 \cdot \sin(\theta)$	$112.625 \cdot \sin(\theta)$
Z_{CEN}	$21.375 + H_C$	$28.5 + H_C$	$21.375 + H_C$
X_I	25.25	19.25	19.25
H_I	29.5	38.5	39.5

The resistance R of the original winding consisting of N turns is calculated using conductor parameters:

$$L_{T1} \text{ (length of single turn T1)} = (50 + 74) \cdot 2 = 248 \text{ mm}$$

$$L_{T2} \text{ (length of single turn T2)} = (52.5 + 79) \cdot 2 = 263 \text{ mm}$$

$$N \text{ (total number of turns)} = 295$$

$$\text{The length of the winding } L_w = N/2 (L_{T1} + L_{T2}) = (295)/2 \cdot (248 + 263) = 75.373 \text{ m}$$

$$A_T \text{ (single turn cross-section area)} = 3.6 \times 10^{-6} \text{ m}^2$$

$$\text{Copper conductivity } (\sigma) = 5.8 \times 10^7 \text{ siemens}$$

$$\text{The winding resistance } R = N/2 (L_{T1} + L_{T2}) / \sigma A_T = 75.373 / (5.8 \times 10^7 \cdot 3.6 \times 10^{-6}) = 75.373 / 208.8 = 0.361 \Omega$$

Similarly winding resistance for other conductor sizes are calculated (see Appendix C)

5.2.2. Variation of outer diameter of the core

Modelling investigations were carried out to investigate the effects of the outer diameter D_o of the core. This was achieved by increasing the inner diameter D_i by w (Fig. 5.7), the cross-section area of the core A_c was kept constant.

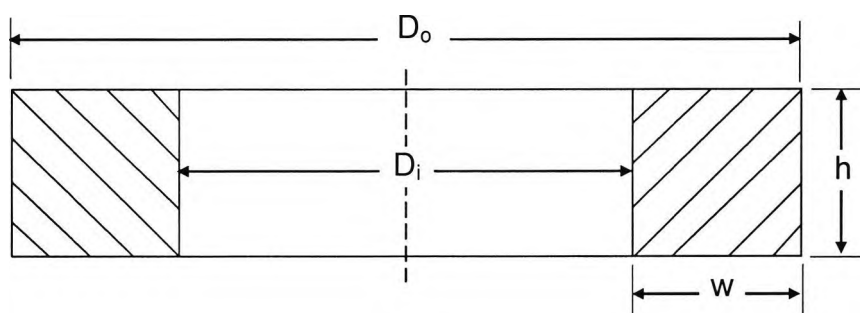


Fig. 5.7 Schematic of the toroidal core the outer diameter D_o of which is increased by increasing the inner diameter by w (not drawn to scale).

The main dimensions of the core in this case are as follows:

$$h = 57 \text{ mm}, w = 43 \text{ mm}$$

$$D_i = 260 \text{ mm}, D_o = 346 \text{ mm}$$

$$A_c = 2451 \text{ mm}^2$$

One of the advantages of increasing the outer diameter of the core is to increase the length of the brush track that allows the core to be wound without having to overlap turns (Fig. 5.8). Further more, by increasing the outer diameter and decreasing the inner diameter it is possible to obtain a large and thinner core without reducing its area. With no overlapping of turns the commutator could be put on the inner surface of the wound core.

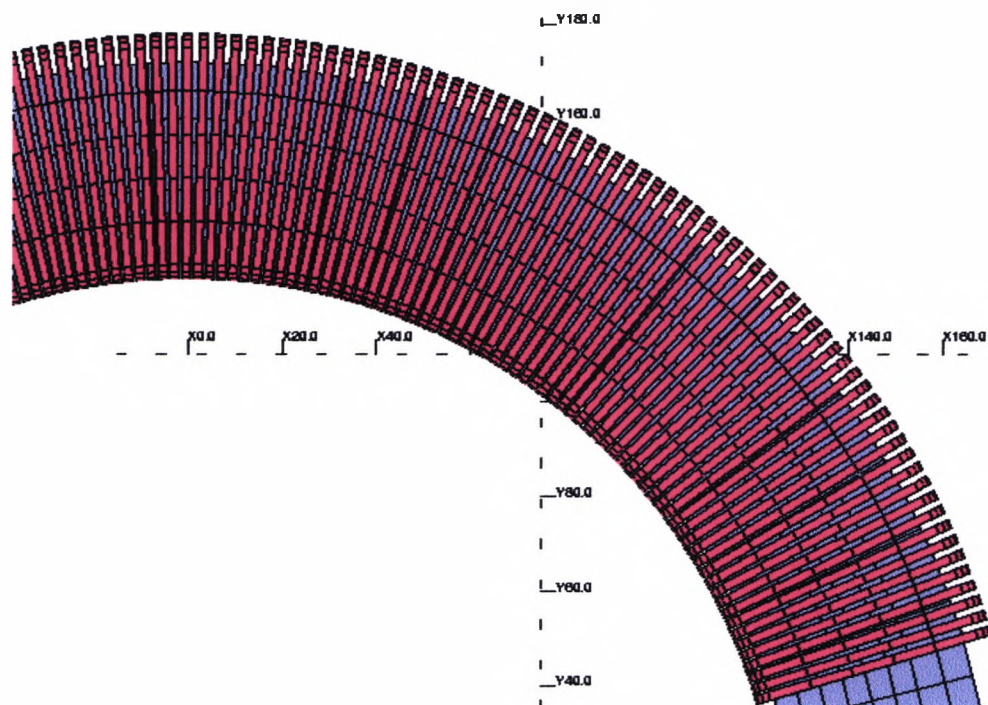


Fig. 5.8 single layer winding turns (no overlapping) wound around large diameter transformer core.

Having defined the core dimensions, the calculate and realise the correct winding turns around the core is define by the developed executable command 'macros' (command input file) see appendix 2.

5.2.3. Effects of design parameters on field distribution in the core

As mentioned earlier various investigations were carried out to quantify the effect of geometric parameters on magnetic field distribution in the core. (B along a circular contour near the inner r_1 or outer r_2 radius in the cross section on the xy-plane at the mid-height of the core Fig. 5.9). Fig. 5.10 - Fig. 5.14 show some of these results. The graphs in these figures show the distribution of flux density. As can be seen from these graphs, the design parameters have significant effects on the magnetic field distribution and local and overall saturation level in the core [41]. Although these graphs represent the magnetic field distribution in the core along a closed contour near the inner radius of the core, further investigations suggest that the pattern of distribution remains the same over the entire section of the core. The 'dip' in the graphs shown in Figs. Fig. 5.13 and Fig. 5.14 correspond to brush or tap positions. It is clear from

these graphs that the distribution of flux density inside the core is predominantly non-uniform and, for given brush and tap positions, the degree of this non-uniformity increases with the reduction in core size. By comparing the graphs in these figures it can be seen that with the reduction in core size the overall saturation level in the core is reduced. However this does not seem to affect the maximum value of the flux density which is more localised in Fig. 5.10 and Fig. 5.14 than that in Fig. 5.13. This means, although the maximum saturation level at localised areas inside the core is not largely affected by core size, the overall saturation level is reduced because of the redistribution of flux over the effective section of the core. This should lead to the reduction in core losses for various operational regimes of these voltage stabilisers.

As mentioned, modelling results show that the overall saturation level in the core is reduced with the reduction in core size mainly because of more uniform distribution of flux in the core. However, as the core size decreases there needs to be a trade-off between this overall saturation (which should not exceed the saturation flux density permitted by the core material used) and the total circumferential length of the core which is needed to place the required number of turns of a given conductor size.

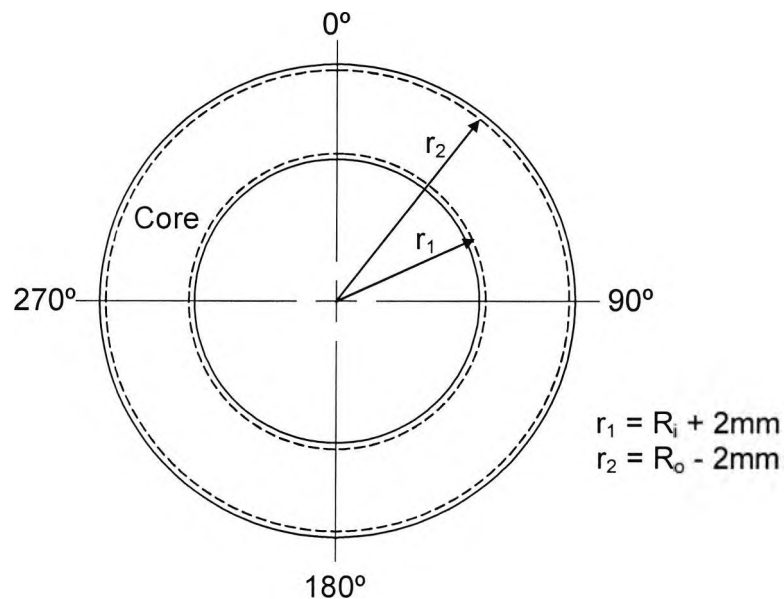


Fig. 5.9 Schematic diagram of the core showing circular contours one close to inner radius r_1 and the other to outer radius r_2 along which flux density values were calculated for comparing modelling results.

Comparing modelling results of different core sizes:

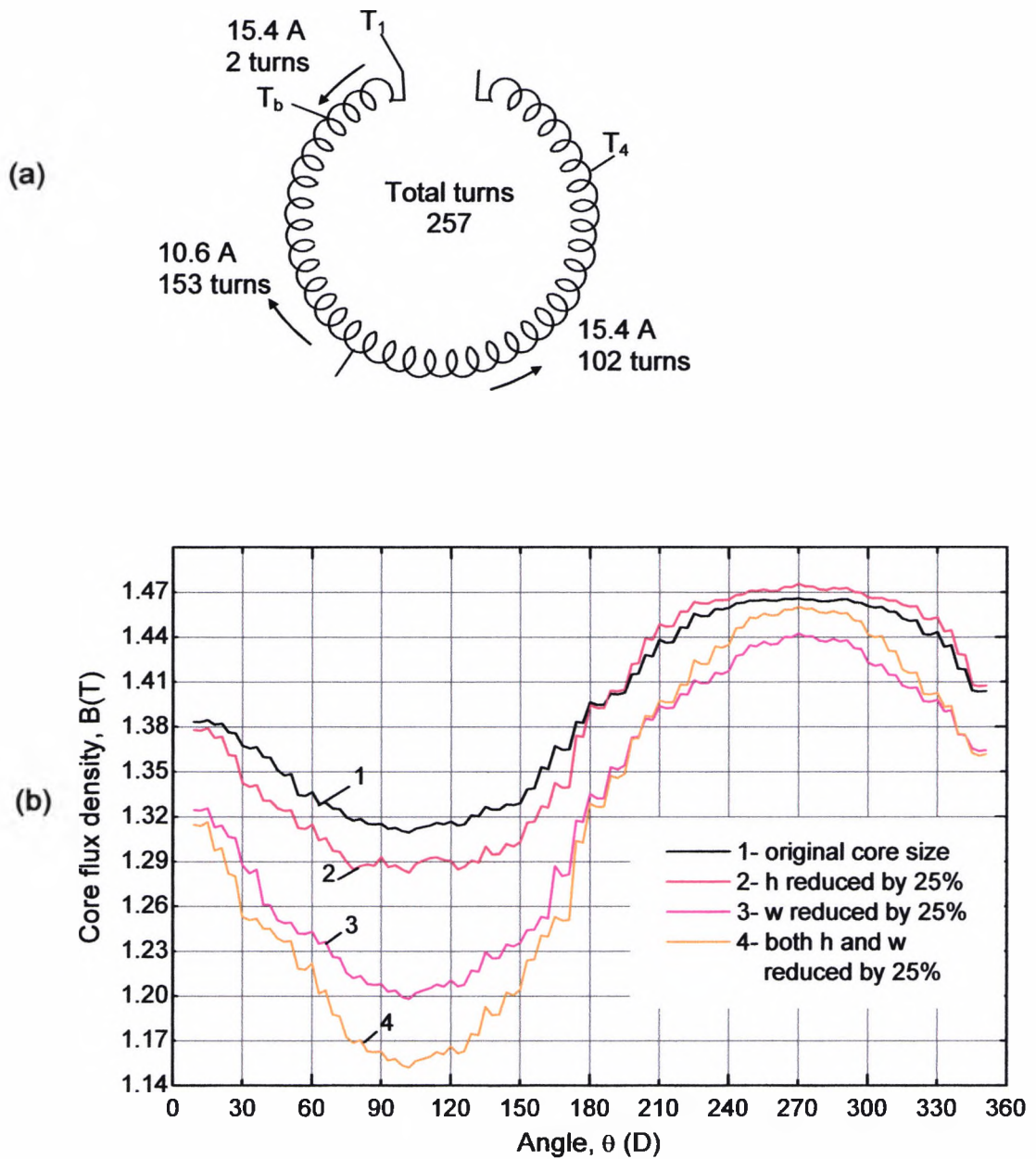


Fig. 5.10 Variation of magnitude and distribution of flux density, B in the toroidal core (b) for various changes in geometric parameters h and w . The graphs show the distribution of B along a circular contour r_1 (shown in Fig. 5.9) for brush (T_b) and tap position (T_1, T_4) shown in (a).

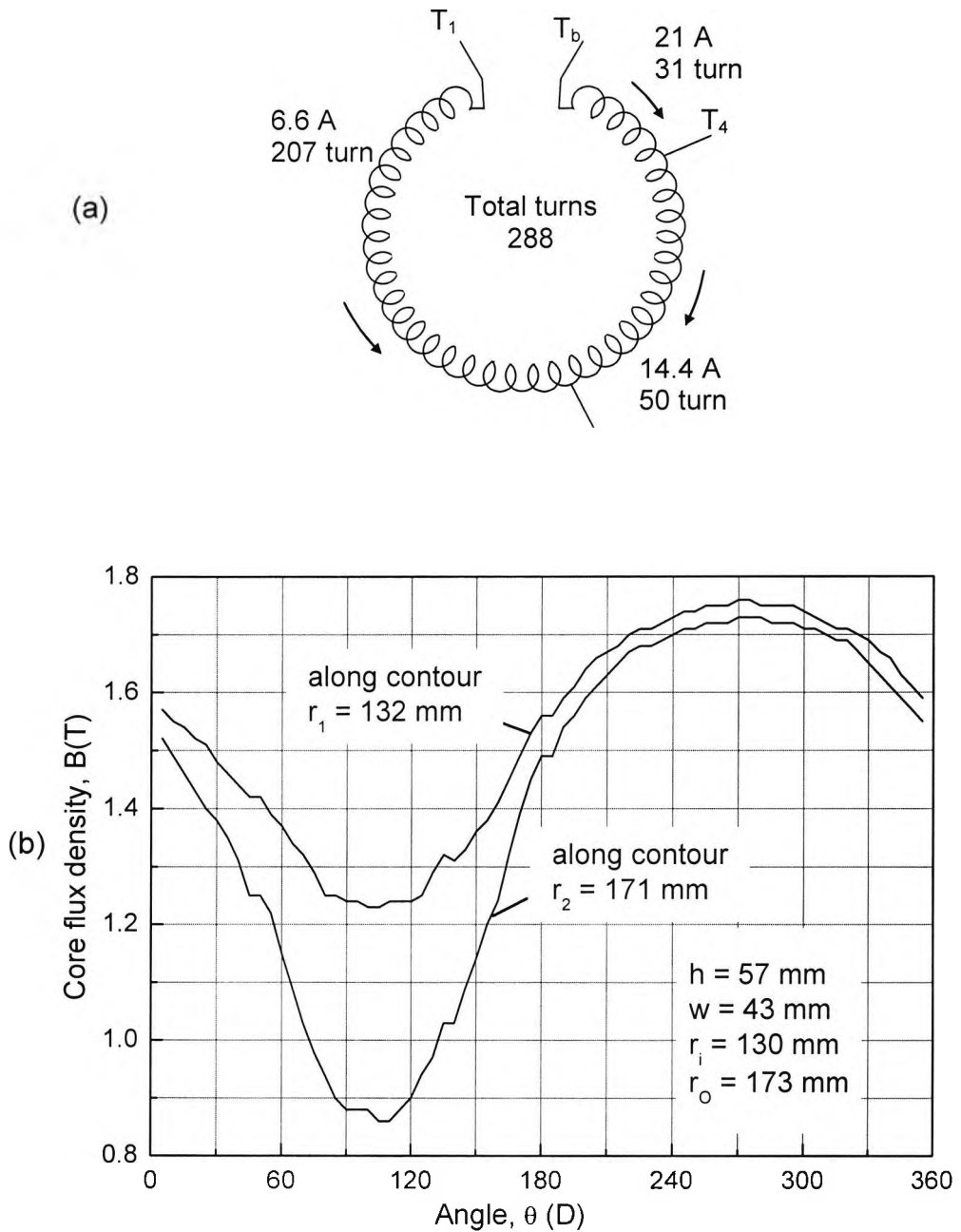


Fig. 5.11 Variation of magnitude and distribution of flux density, B in the toroidal core (b) for changes in geometric parameters D_i and D_o . The graphs show the distribution of B along two circular contours r_1 and r_2 (shown in Fig. 5.9) for brush (T_b) and tap position (T_1 , T_4) shown in (a).

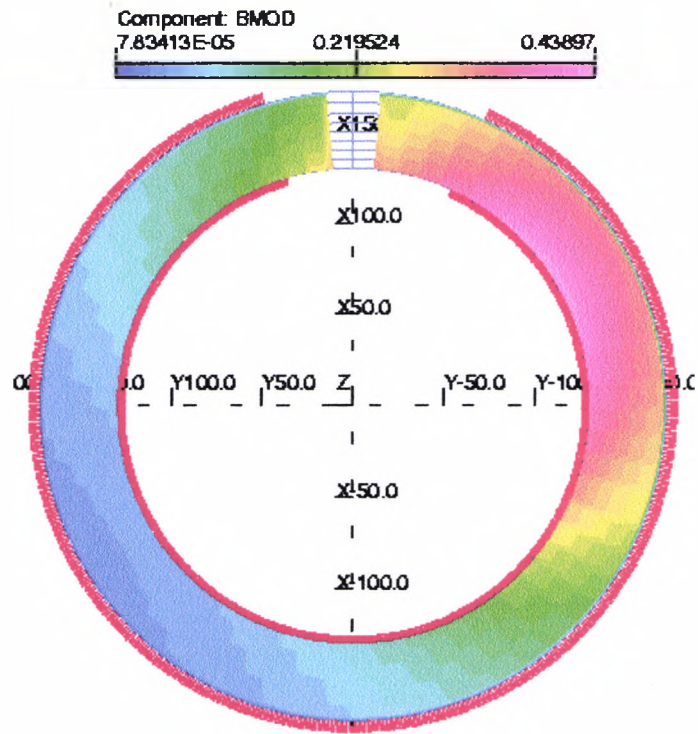


Fig. 5.12 Contour plot of flux density B distribution in large core $R_i = 130\text{mm}$ i.e. no winding overlap and the brush track is on the inner surface of the toroidal core ($B_{\text{max}} = 0.439\text{ T}$).

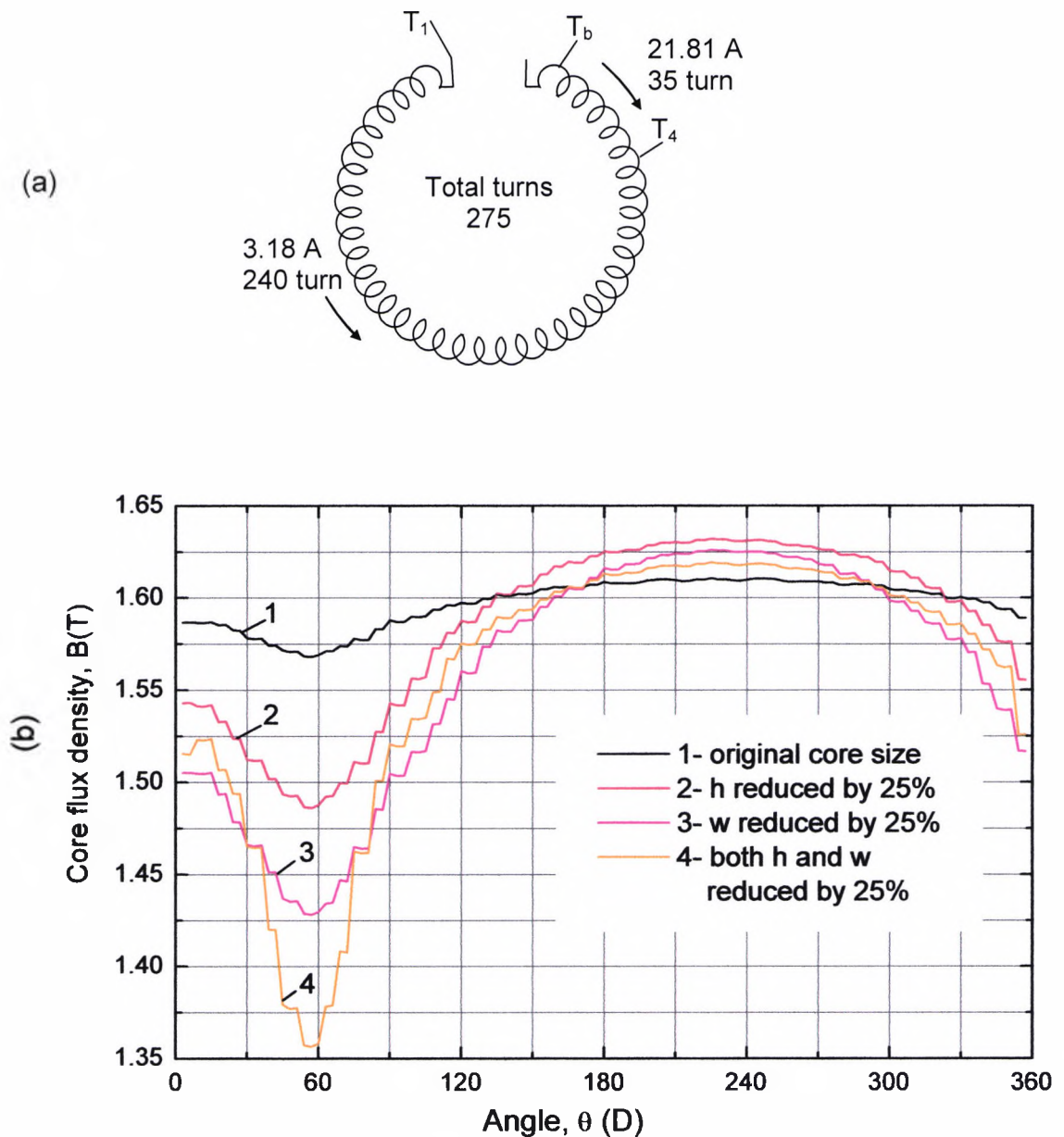


Fig. 5.13 Variation of magnitude and distribution of flux density, B in the toroidal core (b) for various changes in geometric parameters h and w . The graphs show the distribution of B along a circular contour r_1 (shown in Fig. 5.9) for brush (T_b) and tap position (T_1, T_4) shown in (a).

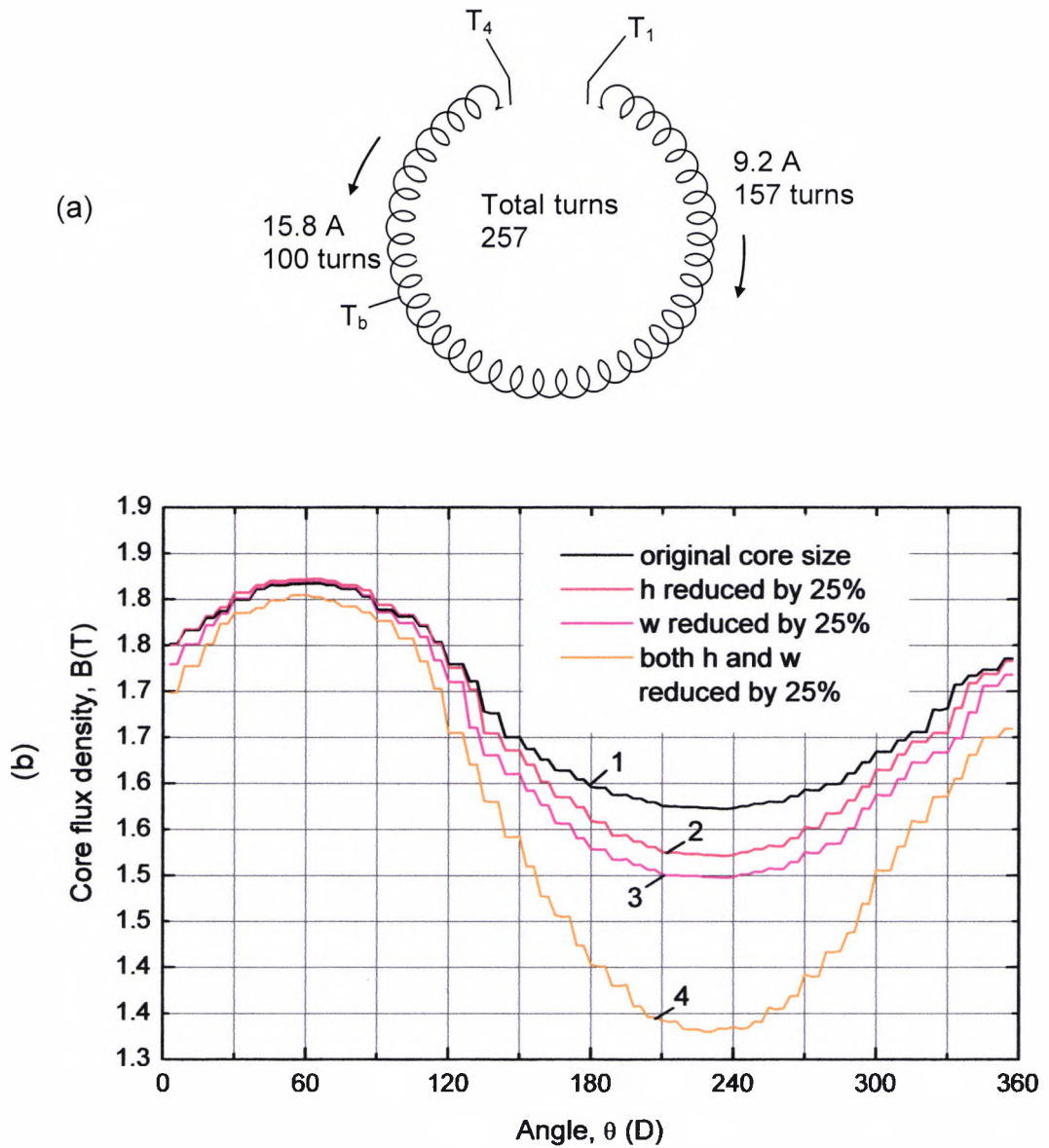


Fig. 5.14 Variation of magnitude and distribution of flux density, B in the toroidal core (b) for various changes in geometric parameters h and w . The graphs show the distribution of B along a circular contour r_1 (shown in Fig. 5.9) for brush (T_b) and tap position (T_1, T_4) shown in (a).

5.2.4. Effects of brush and tap positions

Fig. 5.15 – Fig. 5.20 show the results of investigations of the effects of various operational regimes characterised by brush and tap positions on the magnitude and distribution of magnetic field in the core. These mainly reflected on the saturation of the core. Fig. 5.15 – Fig. 5.20 show the effects of brush (T_b) and tap positions (T_1, T_4) alone on the level of saturation and magnetic field distribution in the core. In all cases the geometric parameters of the core are kept constant. The distribution of current in various sections of the winding, which is determined by brush (T_b) and tap positions (T_1, T_4), also determines the distribution of magnetic flux in the core. Consequently, this determines the saturation level and distribution of flux density in the core. For example, comparison of flux density distributions shows that the particular brush and tap positions shown in Fig. 5.18 results in higher level of saturation (maximum flux density 1.51 T) and more uniform flux distribution in the core than that obtained from Fig. 5.20 which gives higher non-uniformity and lower level of saturation (maximum flux density 0.4 T) [41].

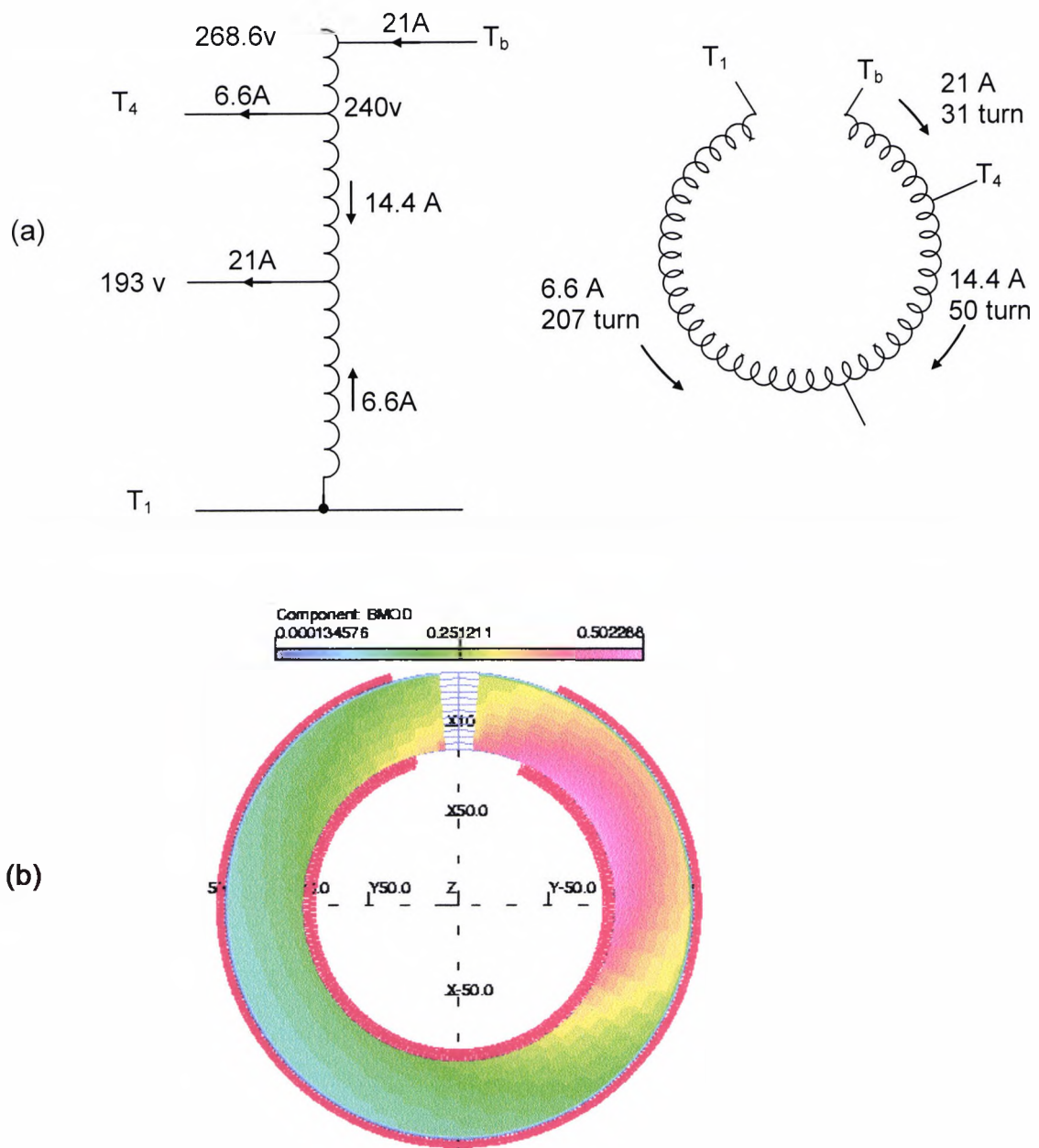


Fig. 5.15 Effects of operational regime 1 determined by brush (T_b) and tap positions (T_1 , T_4) shown in (a) on saturation level and distribution of core flux density (B) in one of the designs of commercial voltage stabilisers investigated. Total number of turns $N = 288$, maximum flux density $0.5T$.

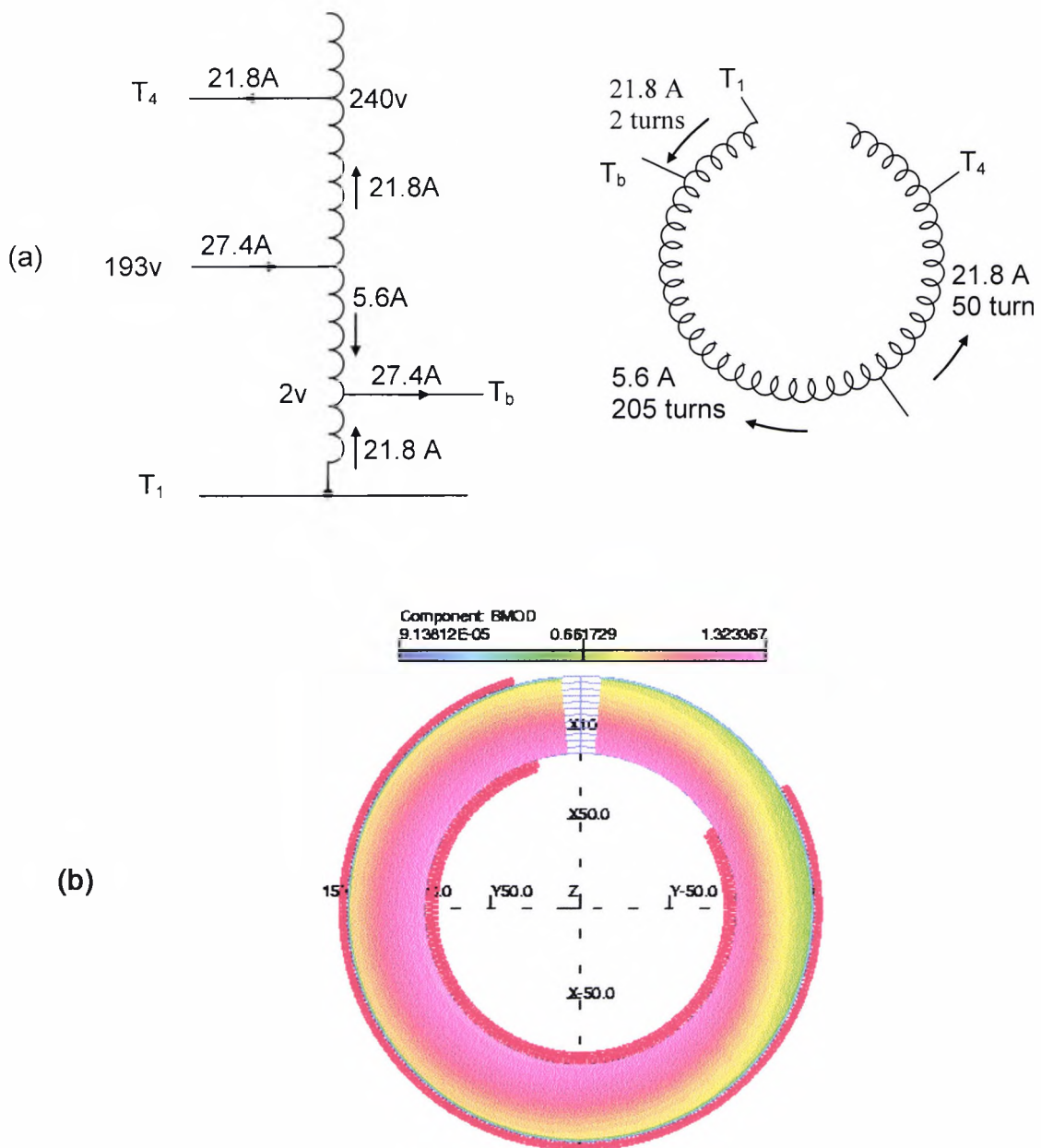


Fig. 5.16 Effects of operational regime 2 determined by brush (T_b) and tap positions (T_1 , T_4) shown in (a) on saturation level and distribution of core flux density (B) in one of the designs of commercial voltage stabilisers investigated. Total number of turns $N = 257$, maximum flux density 1.3T

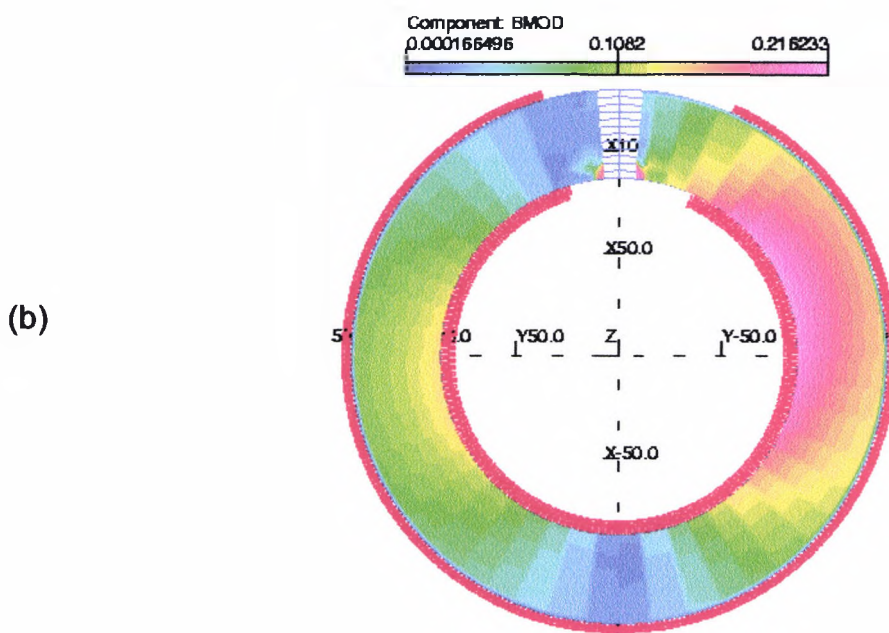
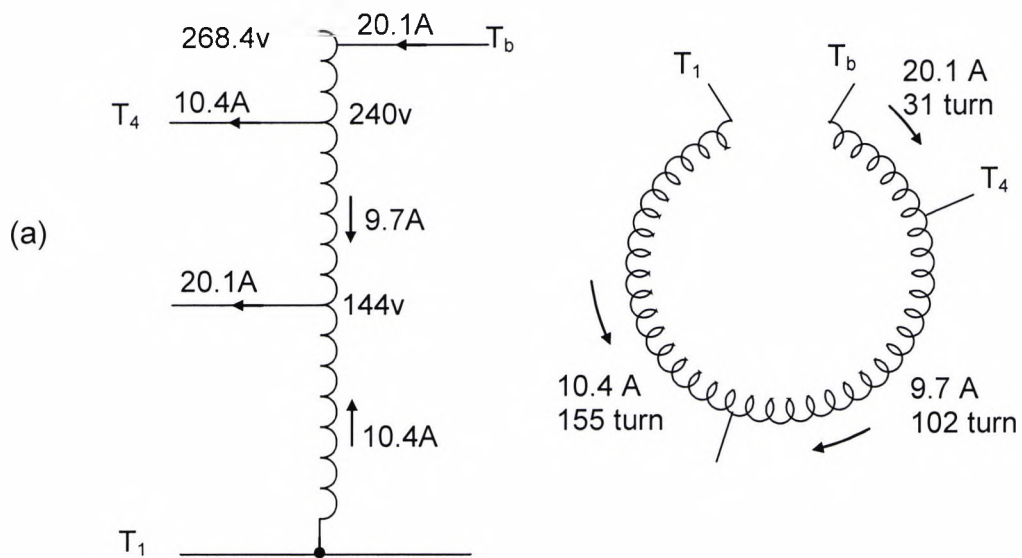


Fig. 5.17 Effects of operational regime 3 determined by brush (T_b) and tap positions (T_1 , T_4) shown in (a) on saturation level and distribution of core flux density (B) in one of the designs of commercial voltage stabilisers investigated. Total number of turns $N = 288$, maximum flux density $0.22T$.

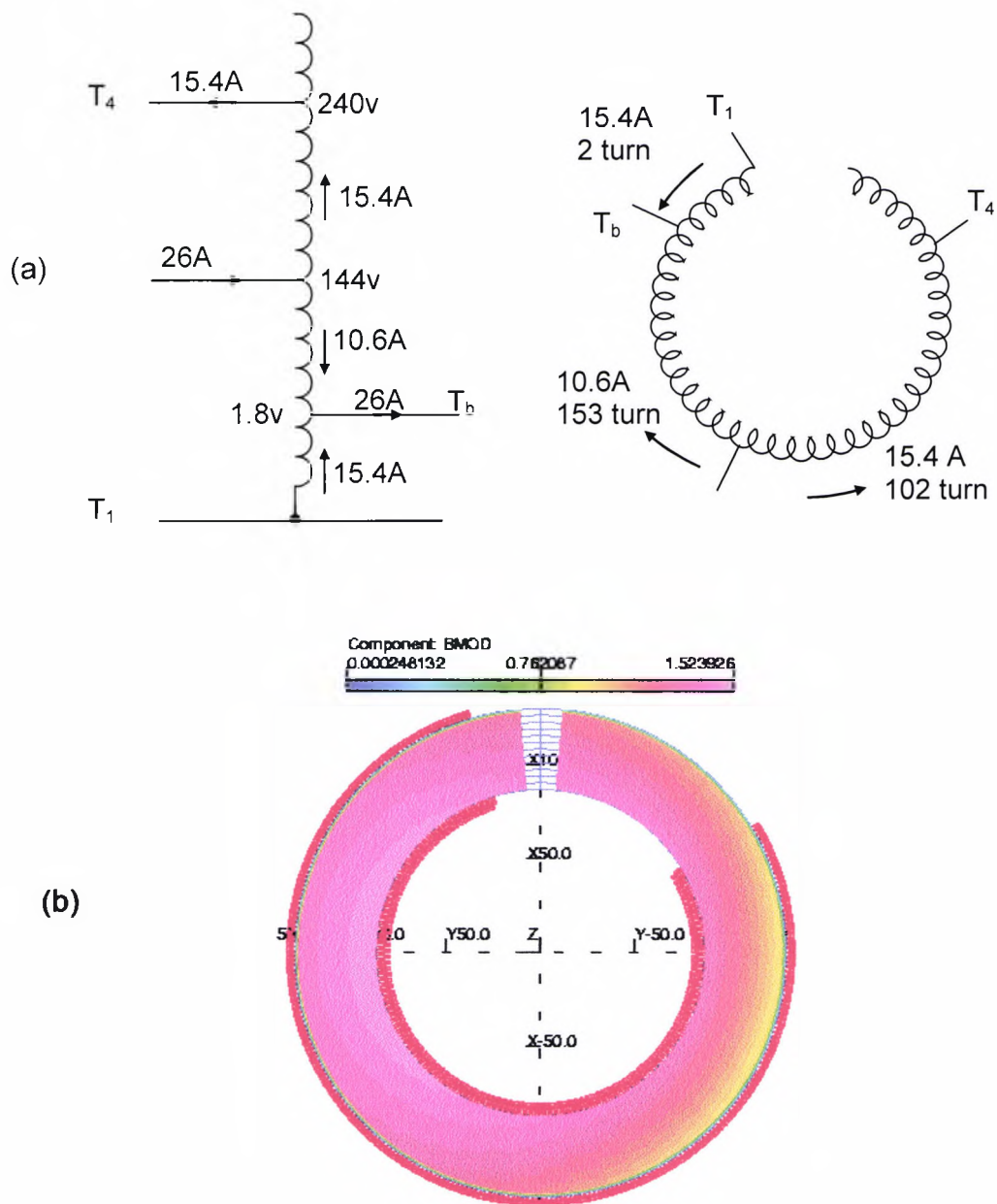


Fig. 5.18 Effects of operational regime 4 determined by brush (T_b) and tap positions (T_1 , T_4) shown in (a) on saturation level and distribution of core flux density (B) in one of the designs of commercial voltage stabilisers investigated. Total number of turns $N = 257$, maximum flux density 1.5T.

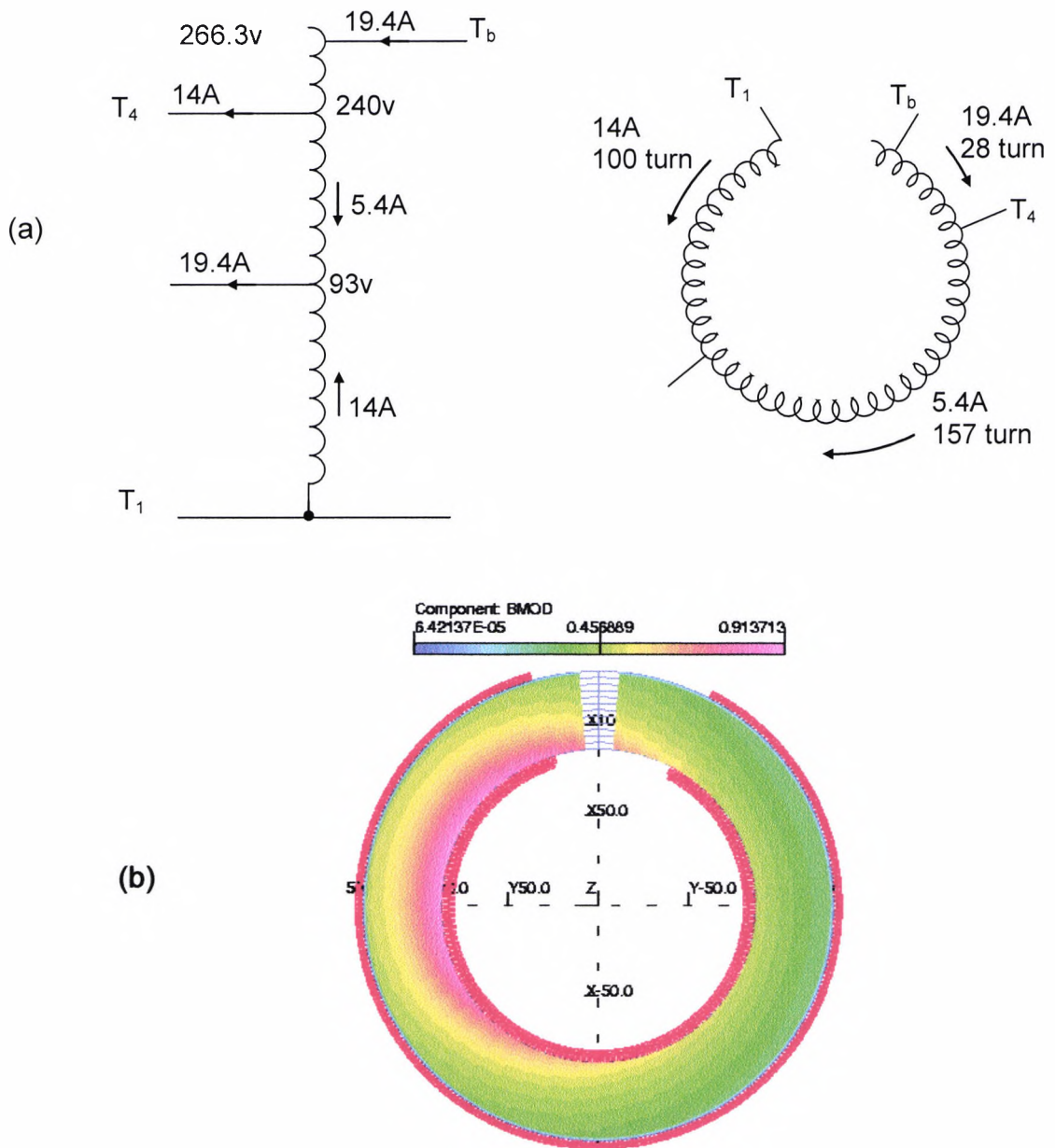


Fig. 5.19 Effects of operational regime 5 determined by brush (T_b) and tap positions (T_1 , T_4) shown in (a) on saturation level and distribution of core flux density (B) in one of the designs of commercial voltage stabilisers investigated. Total number of turns $N = 285$, maximum flux density $0.9T$.

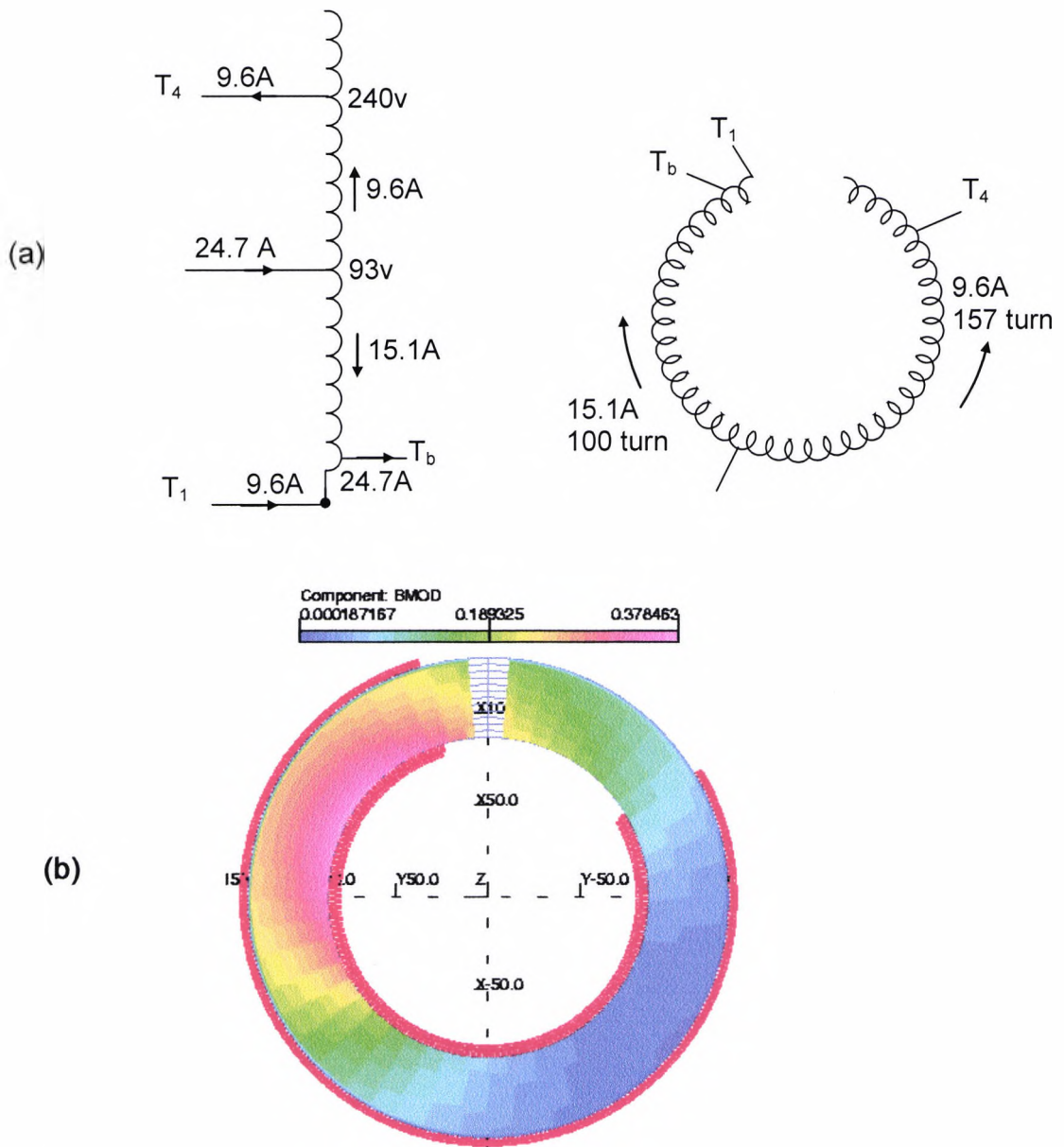
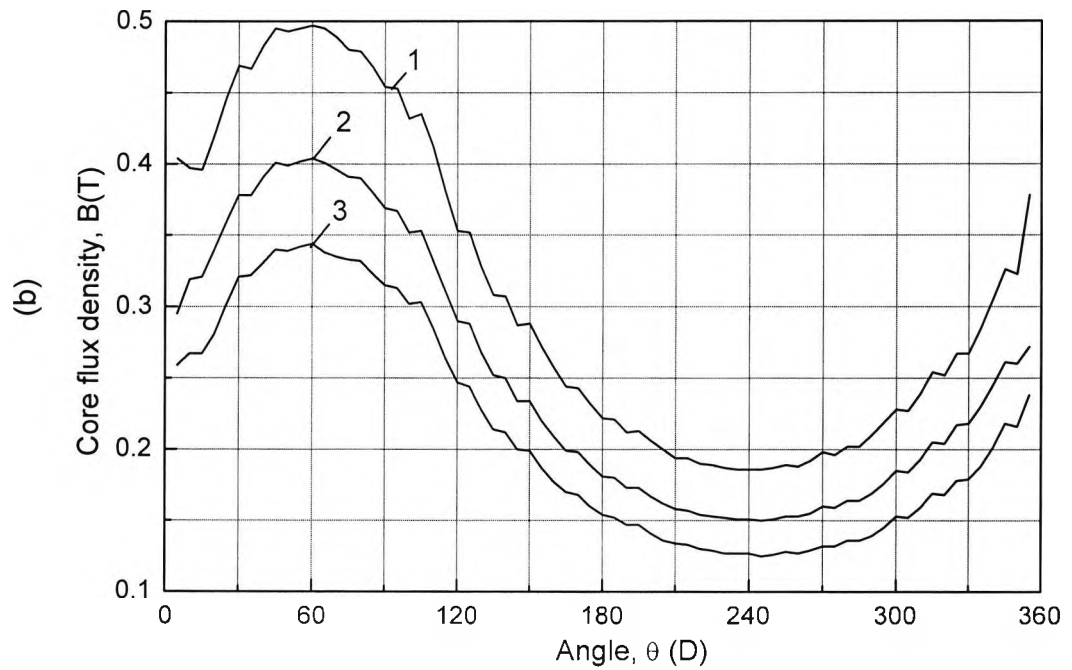
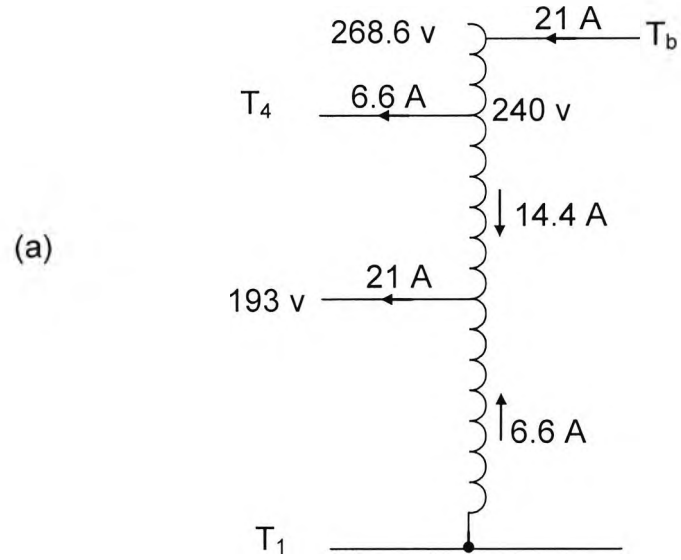


Fig. 5.20 Effects of operational regime 6 determined by brush (T_b) and tap positions (T_1, T_4) shown in (a) on saturation level and distribution of core flux density (B) in one of the designs of commercial voltage stabilisers investigated. Total number of turns $N = 257$, maximum flux density $0.4T$.

Comparison of graphs (b) and (d) of Fig. 5.21 show that the particular brush and tap positions shown in Fig. 5.21(c) result in higher level of saturation and more uniform flux distribution in the core (Fig. 5.21(d)) than that obtained from Fig. 5.21(a) which gives higher non-uniformity and lower level of saturation (Fig.

5.21(b)). These, together with eddy current effects in the top plate contribute to the distribution and magnitude of magnetic field in air around the core.



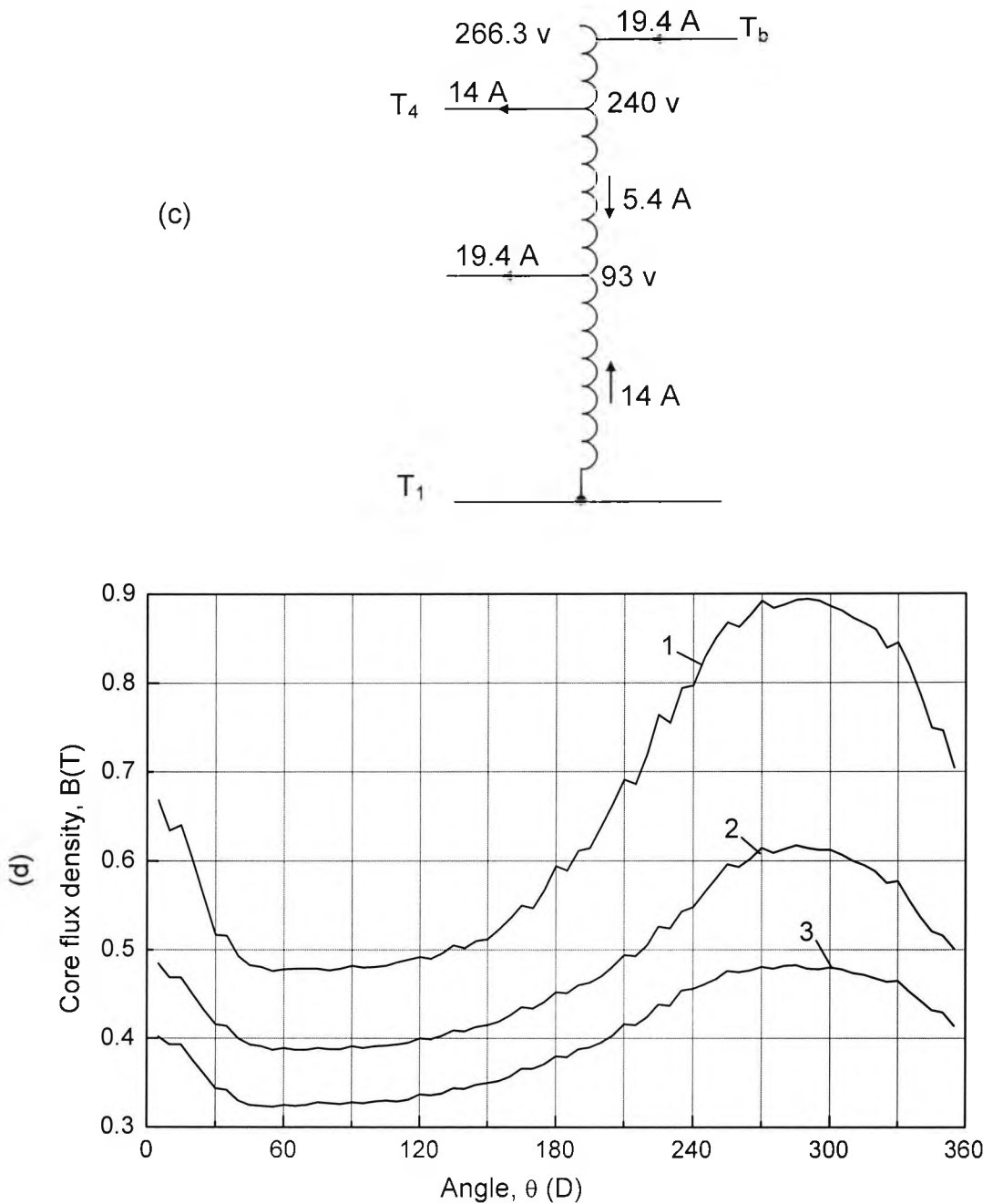


Fig. 5.21 Effects of operational regimes determined by brush (T_b) and tap positions (T_1 , T_4 at turn 257, etc.) shown in (a) and (c) on the saturation level and distribution of core flux density in the TS 1225 variable transformer. The graphs in (b) and (d) show flux densities along three circular contours inside the core (near the inner (1) and outer (3) radii and in the middle (2) of the core) on xy-plane (z at the mid height of the core).

5.2.5. Effects of core saturation on the top plate

Modelling results show that the magnitude and distribution of magnetic flux around the transformer core is affected by saturation conditions in the core. This leakage field outside the core can induce eddy current in top and bottom plates of transformer and other nearby constructive elements. Large circulating currents induced by the leakage flux were found to circulate in the bottom plate. Any eddy currents induced in the top plate may result in its temperature rise and, hence contribute to a rise in the temperature of the brush gear. This may deteriorate the normally intensive thermal regime of the brush contact.

Fig. 5.22 and Fig. 5.23 show some of these effects. Also can be seen from Fig. 5.22, the aluminium top plate acts as a shield as a result of eddy currents set up in it by leakage and stray fields. The magnitude and distribution of field in air are also affected by brush position (Fig. 5.23).

Fig. 5.24 shows the distribution of flux density along these circular contours in air on xy-plane. It also shows that the peak flux density rotates with brush position T_b .

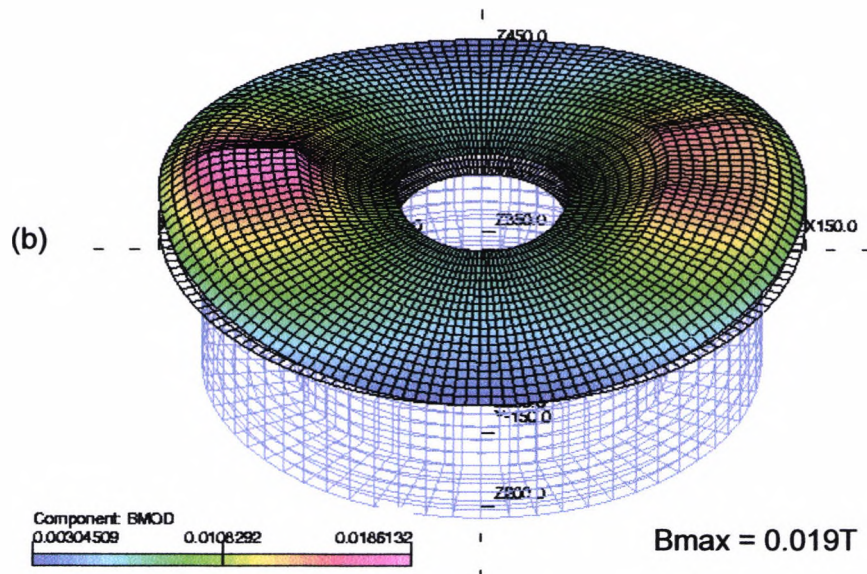
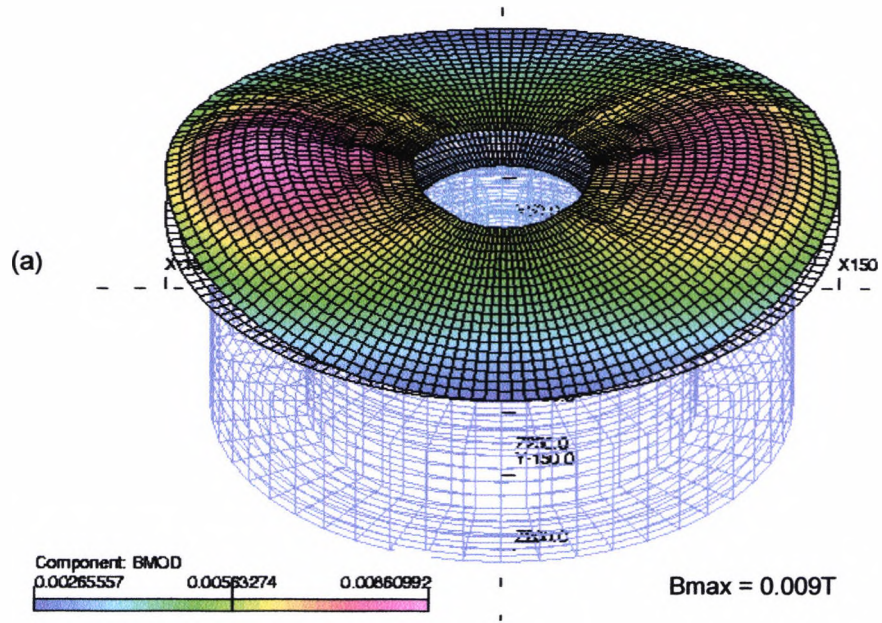


Fig. 5.22 Effects of core saturation and eddy currents in the top plate on the magnitude and distribution of magnetic field in air above the core (30 mm above the core) in the presence (a) and absence (b) of the top plate. Total number of turns $N = 296$ and brush position at turn 148 ($\theta = 180^\circ$)

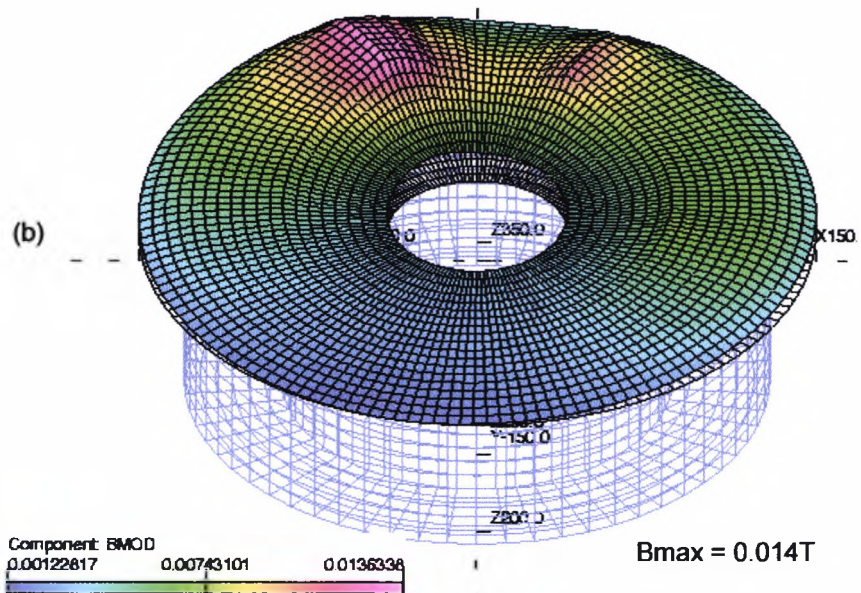
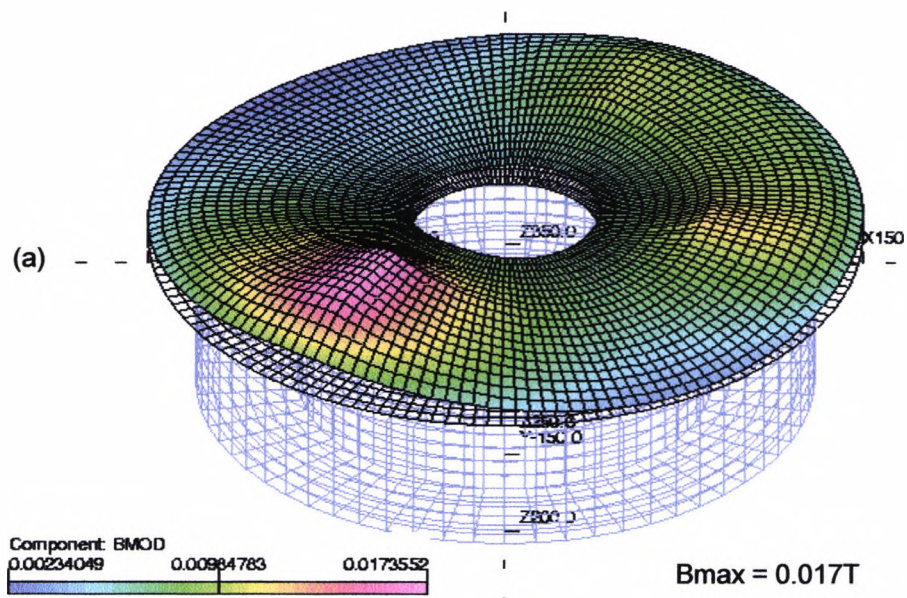


Fig. 5.23 Effects of core saturation and brush position on the magnitude and distribution of magnetic field in air above the core (5 mm above the core) in the absence of the top plate: (a) Brush position at turn 100 (T_{b1} , $\theta = 135^\circ$). (b) Brush position at turn 207 (T_{b3} , $\theta = 240^\circ$). Total number of turns $N = 296$.

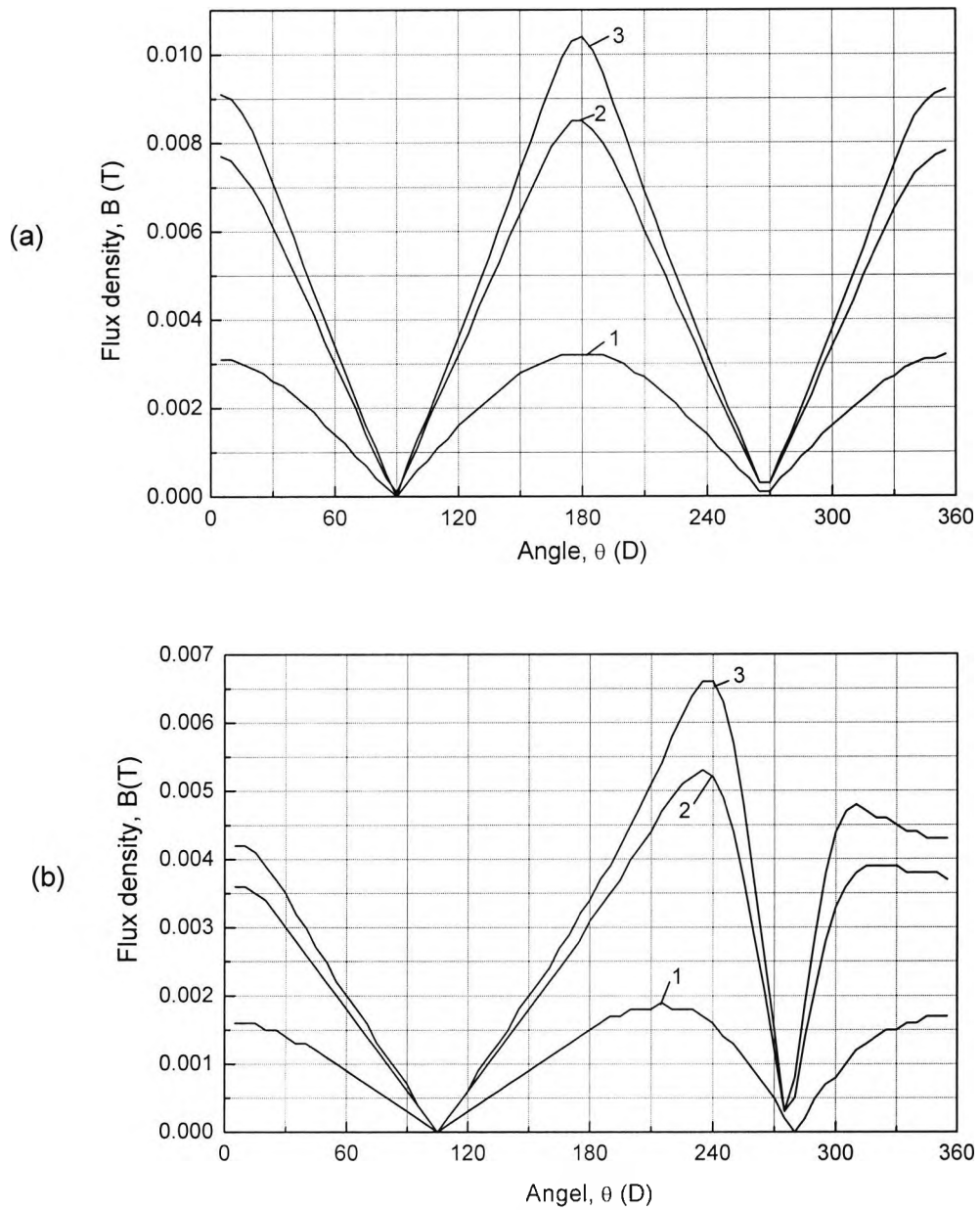


Fig. 5.24 Effects of core saturation and eddy currents in the top plate on magnetic field distribution in air above the core: (a) with top plate, $N=296$, brush position at $\theta=180^\circ$, (b) without top plate, $N=258$, brush position at $\theta=240^\circ$. The graphs show flux densities along three circular contours (with radius $r = 40$ (1), 80 (2), and 110 (3) mm) on xy -plane above the core ($z = 65.5$ mm).

5.3. Study of the Effects of Higher Harmonics

The higher harmonics of current in an autotransformer give rise to magnetic fields of high frequencies. These could contribute to core loss due to eddy currents that may result from these high-frequency fields. In addition, high-frequency leakage flux could contribute to the production of eddy currents in the constructive elements in the vicinity of the core and transformer winding. One of these constructive elements investigated was the transformer top plate, which holds the brush gear. Any significant rise in temperature in the top plate due to eddy current produced by higher harmonics could significantly deteriorate the thermal regime of an autotransformer. Modelling investigations were carried out to valuate the eddy-current effects of higher harmonics by simulations with variable excitation frequency. Fig. 5.25 shows the horizontal planes through the thickness of the top plate on which eddy current contours were calculated. Figs. (Fig. 5.26–Fig. 5.33) show some of the results. These results show that although the overall eddy-current effect in the top plate due to magnetic fields from higher harmonics is low, these could be eddy-current 'hot spot' (Fig. 5.30–Fig. 5.33) in the top plate which could contribute to its temperature rise.

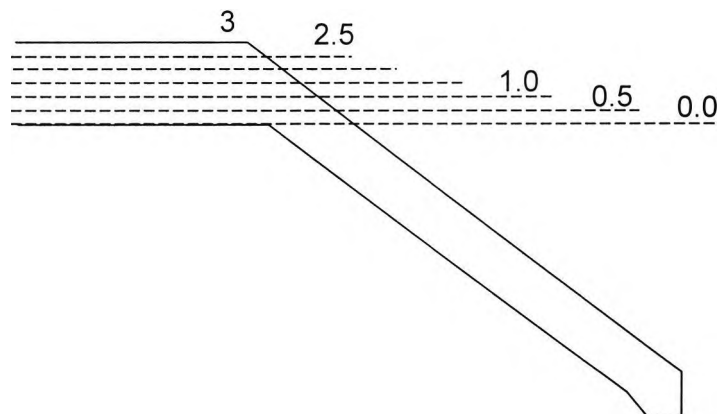


Fig. 5.25 Schematic diagram of part of the top plate showing various sections through the plate thickness used for calculating eddy currents (J).

The following figures show the vector Contours of eddy currents (J) induced in the aluminium top plate top view (at various sections through the top plate thickness):

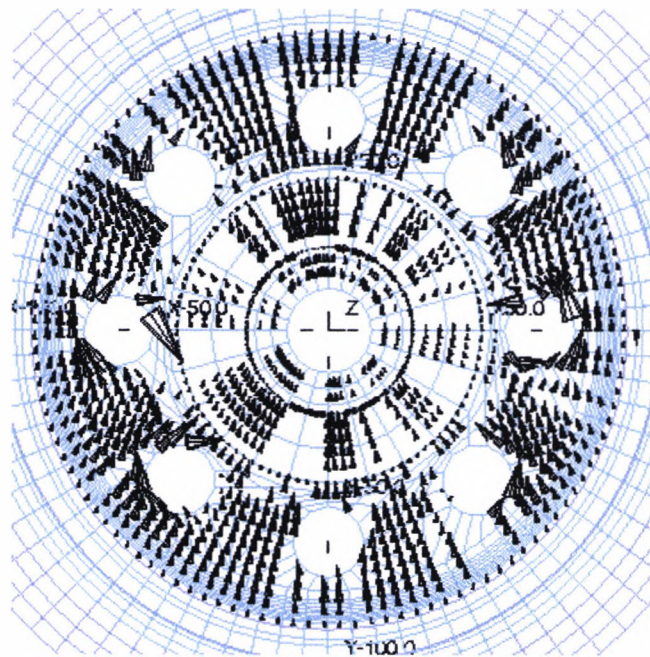


Fig. 5.26 Distribution of eddy current on the bottom surface of the top plate ($J_{\max} = 29 \text{ A/mm}^2$, $f = 50 \text{ Hz}$).

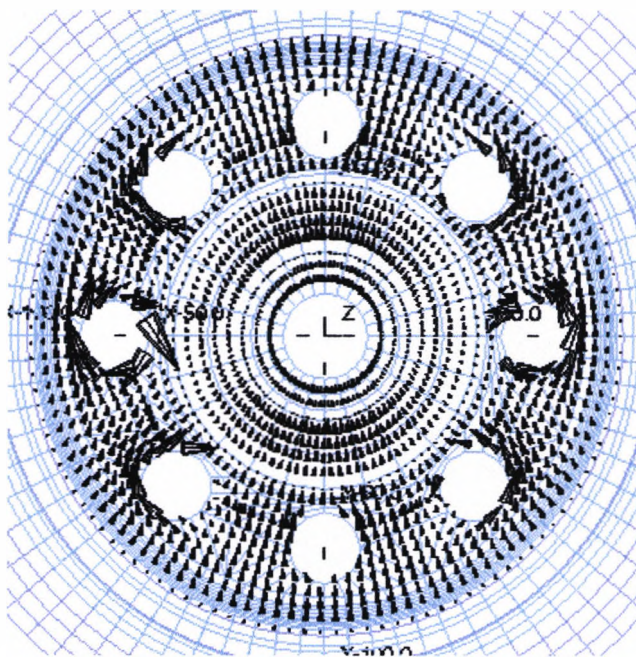


Fig. 5.27 Distribution of eddy current on the section through 0.5 mm from bottom surface of the plate ($J_{\max} = 18 \text{ A/mm}^2$, $f = 50 \text{ Hz}$).

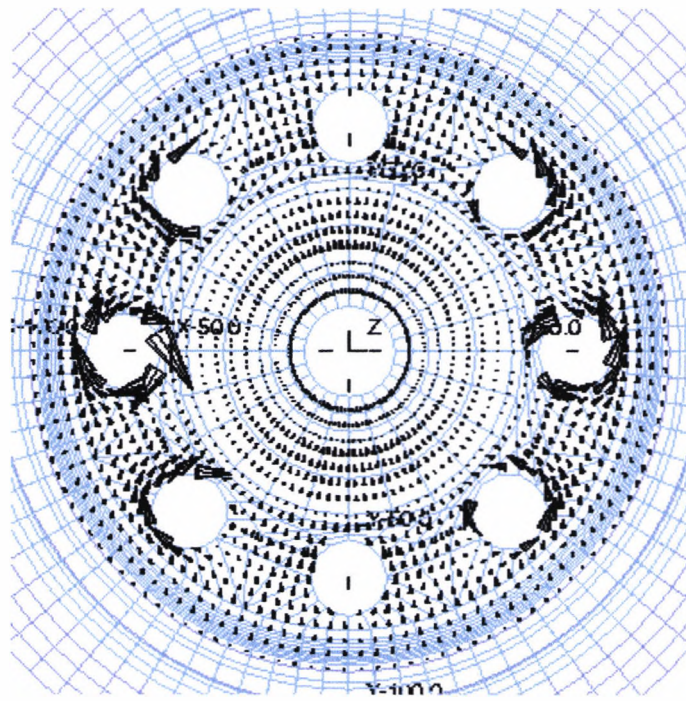


Fig. 5.28 Distribution of eddy current on the section through 1.0 mm from bottom surface of the plate ($J_{\max} = 8.4 \text{ A/mm}^2$, $f = 50 \text{ Hz}$).

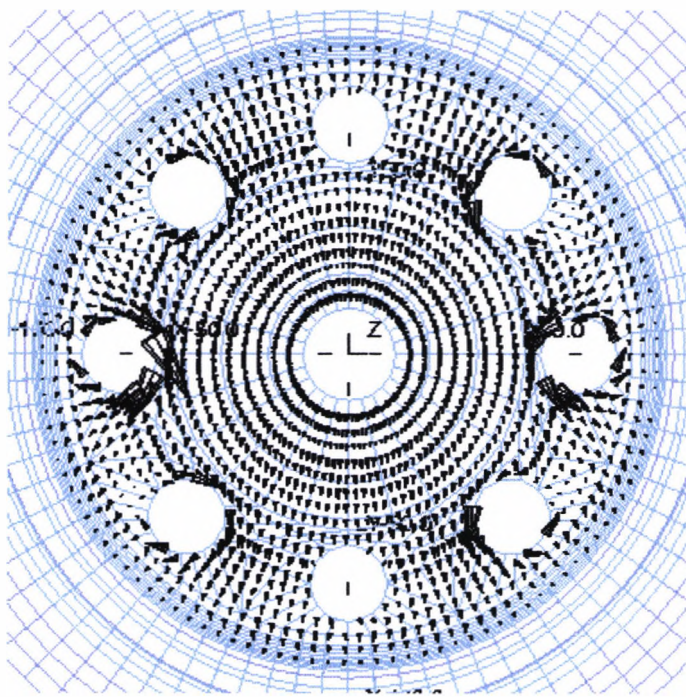


Fig. 5.29 Distribution of eddy current on the section through 2.5 mm from bottom surface of the plate ($J_{\max} = 15.7 \text{ A/mm}^2$, $f = 50 \text{ Hz}$).

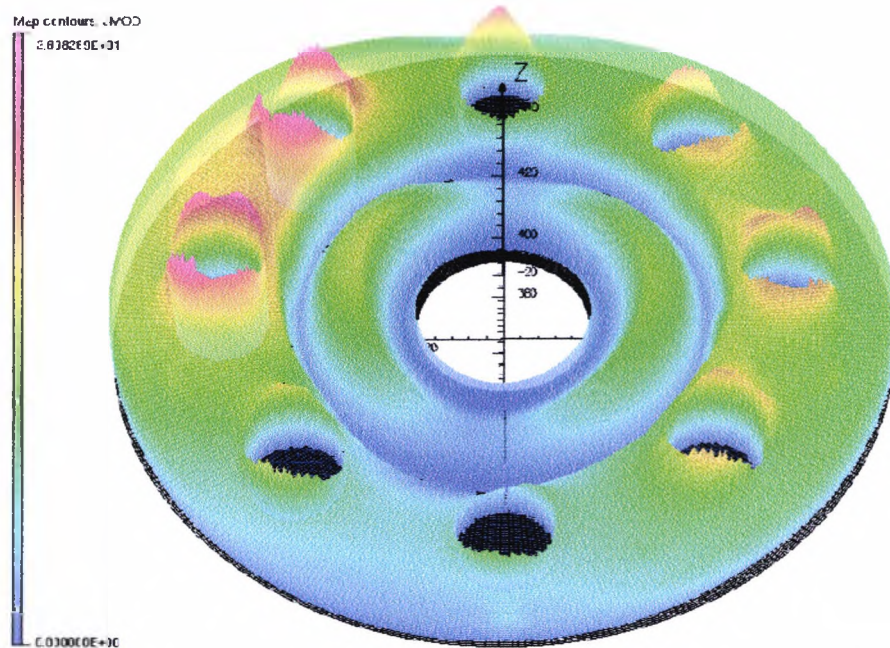


Fig. 5.30 Colour contour of current density at bottom surface of the top plate ($J_{\max} = 29 \text{ A/mm}^2$ at $f = 50 \text{ Hz}$).

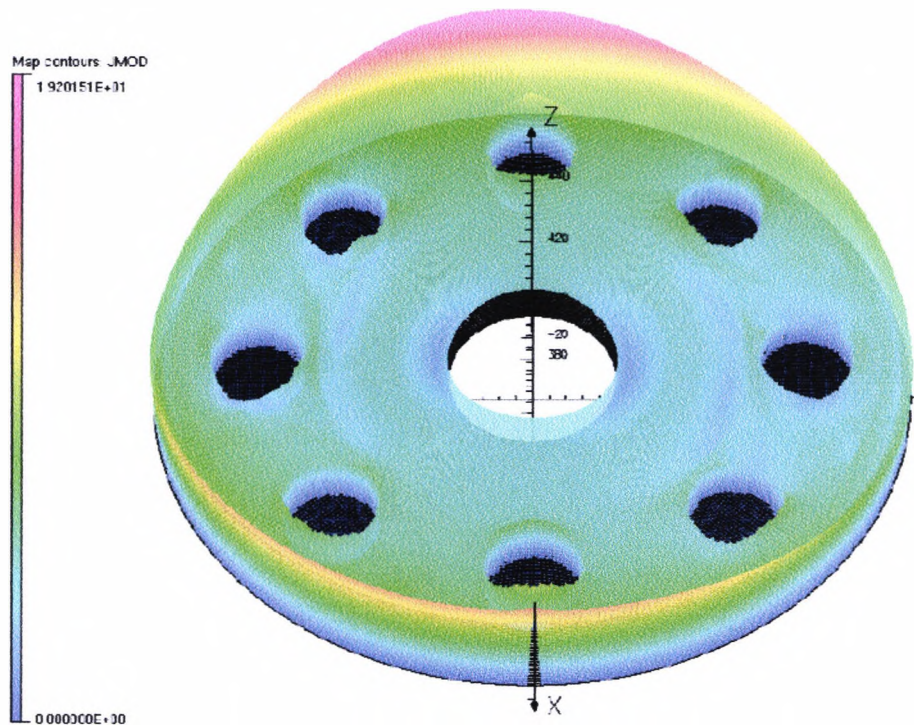


Fig. 5.31 Colour contour of current density at top surface of the top plate $J_{\max} = 19 \text{ A/mm}^2$ at $f = 50 \text{ Hz}$

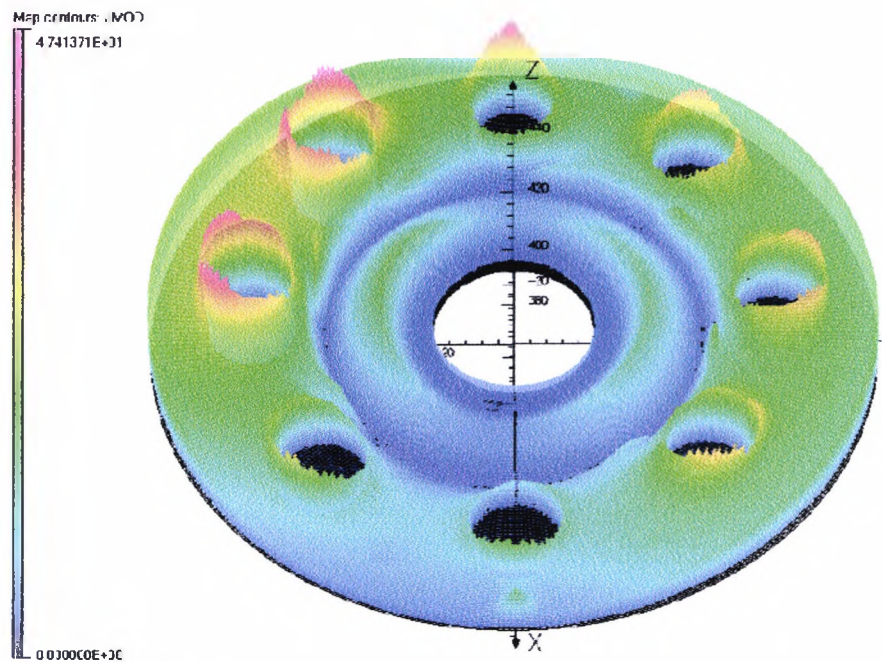


Fig. 5.32 Colour contour of current density at bottom surface of the top plate $J_{\max} = 47 \text{ A/mm}^2$ at $f = 350 \text{ Hz}$.

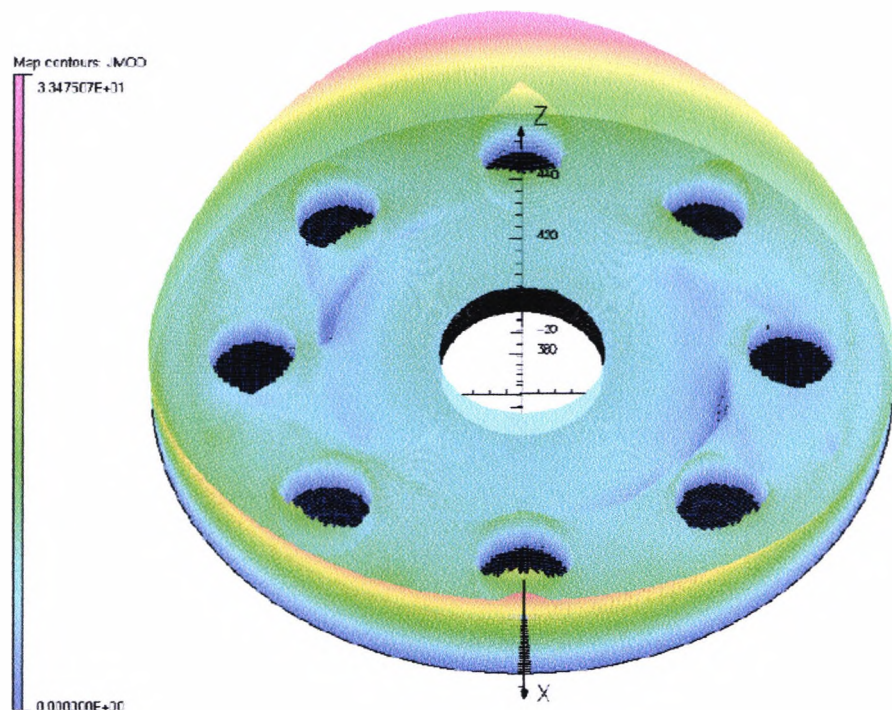


Fig. 5.33 Colour contour of current density at top surface of the top plate $J_{\max} = 33 \text{ A/mm}^2$ at $f = 350 \text{ Hz}$

Table 5.4 Maximum Eddy-current, J_{\max} (A/mm²) at various sections through the top plate thickness and due different frequencies.

f (Hz)	J_{\max} (A/mm ²) at various sections through top plate thickness (3 mm)				
	0.0 (bottom surface)	0.5	1.0	2.5	3.0 (top surface)
50	29.0	18.0	8.4	15.7	19.7
150	39.4	17.7	8.4	19.0	29.0
250	44.5	16.8	8.4	18	32.9
350	48.0	16.0	8.4	17.9	34.8

Chapter 6.

Conclusions

6.1. Work done

The work presented in this thesis constitutes an important contribution towards the development of an integral modelling and design environment for variable transformers and other similar electromagnetic devices. The following original contributions have been made which directly correspond to the aims and objectives set out in section 1.4:

(a) For the first time detailed methodologies have been developed for the mathematical modelling of variable transformers and their realisation using the numerical finite element (FE) method. This renders unnecessary the use of approximate analytical methods and extremely expensive and time consuming experimental techniques for the design and analysis of variable transformers. The realisation of the 3D FE models which were used for modelling investigations posed a difficult problem because of the complex topology of large variable transformers, especially the tightly wound helical winding around its toroidal core. The software macros developed in terms of command input files automatically realise the unique placement of the winding turns. The efficient use of the generic electromagnetic package Opera-3d together with these software macros made the pre-processing stage of accurate model setup quickly and effectively.

(b) The experimental investigation of commercial variable transformers conducted in industry constituted a vital part of the work undertaken in this research. This established the hitherto poorly studied magnetic field distribution in the 3D space around the transformer core. It is this field which has been shown to be responsible for eddy current and/or circulating current losses in the top plate and other constructive elements of commercial variable transformers. It has been shown that the distribution and magnitude of this field are very much dependent upon the operational regimes of the transformer which are characterised by the brush and tap positions.

(c) The validation of some of the initial FE modelling results by comparing them with those obtained from the above experimental work formed an integral part of the subsequent more extensive simulation work carried out in this research. The good agreement obtained in most of the cases between these two sets of results established confidence in the modelling methodologies developed and in the 3D FE models that were developed to realise these methodologies for further simulation studies.

(d) The 3D FE models developed were used to carry out extensive simulation studies to investigate commercial variable transformers. This comprised, for example, the investigation of the transformer core for various design parameters. It has been shown that the distribution of magnetic flux density inside the core is predominantly non-uniform and the degree of this non-uniformity increase with the reduction in the core size. However, the overall saturation level is reduced because of the redistribution of the core flux. This should result in the reduction in the core losses. The modelling studies carried out also gave a vital insight into the effects of operational regimes on the core saturation. It has been shown that the distribution of currents in the winding determined by the brush and tap positions for various operational regimes effect the flux distribution and, hence the saturation level in the core. The study of the effects of saturation conditions in the transformer core on the magnitude and distribution of magnetic field in air above the transformer core constituted a particular interest. It is this leakage field which is responsible for eddy current effects in the transformer top plate made of aluminium. This leakage field was

investigated for 50Hz power frequency and for higher frequencies of harmonics. The eddy currents induced in the top plate at various frequencies were quantified which gave an indication of possible losses contributing to its temperature rise.

6.2. Future work

The modelling methodologies and the FE models developed in the work could constitute the basis for further investigation of commercial variable transformers. It would be possible in future to carry out their detail thermal analysis, analysis of various transient effects, and the effects of shorted turns in the winding.

For thermal analysis the coupled or decoupled solution of electromagnetic and thermal problems could be obtained using the FE models developed. These could also form the basis of the solution of coupled electric circuit and magnetic field problem which would be necessary for transient analysis of variable transformers.

The accuracy of some of the FE modelling results presented in this work could be improved by refining the local and global discretisation of FE models developed. These further improvements of the FE models could not been done at the time this work was carried out because of the lack computing power and some inflexibilities of the software used.

Overall, the work presented in this thesis constituted an important contribution in the design and analysis of variable transformers and other similar electromagnetic devices.

References

- [1] A. G. Armstrong, C. J. Collie, J. S. Simkin, C.W. Trowbridge, "The solution of three-dimensional magnetic problems using scalar potentials" Proc COMPUMAG Conf, Grenoble, p.1-2, 1978.
- [2] A. Ahmed and P. Auriol, "Conformal mapping method for calculation of rectangular winding parameters", IEEE Trans. on MAG, VOL.28, No.5, pp.2823-2825, September 1992.
- [3] B. Baodong, D. Xie, J. Cui et al "Optimal transposition design of transformer windings by genetic algorithms", 1995 IEEE Trans. Magn. 6 3572-3574.
- [4] C. M Arturi "3D FE analysis of the axial forces on the step-up transformer-windings with helicoidal LV", 1995 IEEE Trans. v 31 Magn. 3 2032-2035.
- [5] C. W. Trowbridge "An Introduction to Computer Aided Electromagnetic Analysis" Pbk.ISBN 0 95 16262 0 5 Published by Vector Fields Ltd., 1990
- [6] C. M. Arturi, "Model of a highly saturated 3-phase autotransformer with tertiary winding and 5-limb core and analysis of a time-varying short-circuit transient". European Trans. Elec. Power Engineering, vol.4, no.6, 1994, pp.513-524.
- [7] C. S. Biddlecombe, E.A. Heighway, J. Simkin, C.W. Trowbridge, "Methods for eddy current computation in three dimensions", Proc COMPUMAG Conf., Chicago, 1981.
- [8] D. Pavlik, D. Johnson and R. S. Girgis "Calculation and Reduction of Stray and Losses in Core-Form transformers using a Highly Accurate Finite Element Modelling Technique" IEEE Transactions on Power Delivery, Vol. 8, No 1, January 1993.
- [9] D. Rodger, P.J.Leonard, H.C.Lai, "Surface elements for modelling 3D fields around thin iron sheets", IEEE Trans Magn., Vol. 29, No 2, pp. 1483-1486, March 1993.
- [10] E. Kriezis, T. D. Tsiboukis, S. M. Panas and A. T. Tegopoulos, "Eddy currents: theory and applications". Proc. IEEE, vol. 80, no. 10, 1992, pp. 1559-1589.
- [11] E. Karplus and W. N. Tuttle, "Alternating-Current Apparatus" General Radio Company, Cambridge, Mass, a corporation of Massachusetts. US Patent No. 2,009,013. 6. June 1, 1934, s. no 728,470, 6 Claims (Cl. 171-119).
- [12] E. B. Makram, Rebekah L. Thompson and Adly A. Girgis "A new Laboratory Experiment for Transformer Modeling in the Presence of Harmonic Distortion Using a Computer Controlled harmonic Generator" IEEE Transactions on Power Systems, Vol. 3, No 4, November 1988.

- [13] G. Pualo, S. Tenbohlen, M. Linders and G.krost "Integration of Power Transformer Monitoring and Overload Calculation into the Power System Control Surface" IEEE/PES Transmission and Distribution Conference 2002, Yokohama Japan.
- [14] G. Smiley "Adjustable Transformer with Stabilized Contact Track" General Radio Company, Cambridge, Mass., a corporation of Massachusetts. U.S. Patent No. 2,949,592. Apr. 19, 1951, s. no. 221,878. 1 Claim. (Cl. 336-148).
- [15] Handbook of Voltage Control with the Variac Autotransformer, © 1963 by General Radio Company, Form 3080-A January 1963, West Concord, Massachusetts, USA.
- [16] I. V. Yakimets and V. G. Narovlyanskii, "Autotransformer with a voltage-stabilised tertiary winding". Electrical Technology, no.1, 1995, pp.21-30.
- [17] J. C. Olivares, S. V. Kulkarni, J. Canedo, R. Escarela, J. Driesen and P. Moreno " Impact of the Joint Design Parameters on Transformer Losses" International Journal of Power and Energy Systems, Vol. 23, No. 3, 2003.
- [18] J. C. Olivares, S. V. Kulkarni, J. Canedo, R. Escarela, J. Driesen and P. Moreno " Impact of the Joint Design Parameters on Transformer Losses" International Journal of Power and Energy Systems, Vol. 23, No. 3, 2003
- [19] J. D. Kraus 1992 Electromagnetics (London: McGraw-Hill Inc.).
- [20] J. K. Sykulski, E. Sykulska, S.T. Hughes "Application of Finite Element Modelling in LVDT Design" COMPEL-The International Journal for computation and mathematics in Electrical & Electronic Engineering, vol.11, No.1, p.73-76, 1992.
- [21] J. M. Dedulle, G. Meunier, "3D Anisotropic Magnetic Fields in Transformer Core Laminated with Grain-Oriented Steel-Sheet", INTERMAG, 1990.
- [22] J. P. Martin, J Wendling and Y. Tournier, "Specifics of the short-circuit behaviour of concentrically-wound transformers and autotransformers". IEEE trans. Power App. and Sys., vol. 99. no.6.1980. pp. 2069-2077
- [23] J. P. Abreu, C. A. M. Guimapaes and G. Paulillo, "A proposal for a power converter autotransformer". Proc. IEEE Int. Electrical Machines and Drives Conference, Milwaukee, USA, 1997, pp. 61-64.
- [24] J. Simkin and C.W. Trowbridge, "On the use of the total scalar potential in the numerical solution of field problems in electromagnetic" International Journal of numerical Methods in Engineering, Vol.14, pp 423-440, 1979.
- [25] J. Simkin, C.W. Trowbridge, "Which Potential?" RL-78-001/B, January 1978.
- [26] J. D. Kraus "Electromagnetics" © 1991 Fourth Edition McGraw-Hill USA.

- [27] K. B. Niclas, R. R. Pereira and A. P. Chang, "Transmission lines accurately model autotransformers". *Microwave & RF*, vol. 31, no. 11, 1992, pp.72-76.
- [28] K. J. Binns, P. J. Lawrenson and C. W. Trowbridge, *The Analytical and Numerical Solution of Electric and Magnetic Fields*. 3rd ed. Chichester, John Wiley & Sons. 1992.
- [29] L. F. Blume, C.; Boyajian, A. Camilli et al, *Transformer Engineering: A Treatise on the theory, Operation and Application of transformers*, Chapman & Hall Ltd., 1951.
- [30] M. Rahman "Mathematical Modelling and Computer Aided Design of Field Coupled Electro-mechanical Transducers". PhD thesis, Department of Systems Science
- [31] M. Chiampi, A. L. Negro and Michele Tartaglia "A Finite Element Method to Compute Three-Dimensional Magnetic Field Distribution in Transformer Cores" *IEEE Transactions on Magnetics*, Vol. MAG-16, No. 6 November 1980.
- [32] M. Steurer and Klaus Frohlich "The Impact of Inrush Currents on the Mechanical Stress of High Voltage Power Transformer Coils" *IEEE Transactions on Power Delivery*, Vol. 17, No. 1, January 2002.
- [33] Morganite "Carbon Brushes and Electrical Machines" Published by Morganite Electrical Carbon Limited, 1978. Printed by J S G Services Limited, Swansea UK.
- [34] O. C. Zienkiewicz and R. I. Taylor, "The Finite Element Method" Maidenhead, McGraw-Hill Inc., 1991.
- [35] OPFRA-3d Version 9 2003, TOSCA Version 9 2003. and ELEKTRA Version 9 2003, Vector Fields Limited, Oxford, UK.
- [36] P. P. Silvester and R L Ferrari 1990 "Finite Elements for Electrical Engineers" (Cambridge: Cambridge University Press)
- [37] P. P. Silvester, R. P. Gupta, "Effective computational models for anisotropic soft B-H curves", *IEEE Trans Magn.* Vol.27, No.5, pp. 3804-3807, 1991.
- [38] P. Silvester and Konpad, "Analysis of transformer leakage phenomena by higher order finite elements". *IEEE Trans. PAS*, vol.6, 1973, pp. 1843-1855.
- [39] R. S. Masti, W. Desmet and W. Heylen "On the Influence of Core Laminations upon Power Transformer noise" *Proceedings of ISMA 2004* pp. 3851-3861.
- [40] S. H. Khan, J. M. El-Shawish, K T V Grattan, L. Finkelstein "Finite Element Modelling of Variable Transformers used for Voltage Regulation and

- Control" Paper presented at Sensors and their Applications VIII, 7-10 September 1997. Section B: Sensor Modelling, p 41-46, 1997.
- [41] S. H. Khan, J. M. El-Shawish, L. Finkelstein K T V Grattan "Design Investigation of Commercial Voltage Stabilisers by 3D Finite Element Modelling" Paper presented at Sensors and their Applications XI, 7-10 September 2001. Section 8: Industrial Applications of Sensor, p 455-461.
- [42] S. H. Khan, J. M. El-Shawish, L. Finkelstein K T V Grattan "Finite Element Modelling of Saturation and Eddy Current Effects in Commercial Variable Transformers" IEEE Transactions on Magnetics, p 2783-2786 VOL. 37, No. 4, July 2001.
- [43] S. H. Khan, J. M. El-Shawish, L. Finkelstein K T V Grattan "Investigation of Variable Transformers by 3D Field Modelling – Comparison of Modelling and Experimental Results" Paper presented at ICEM 28-30 August 2000 Espoo Finland, p 262-266.
- [44] S. Ramo, J. R. Whinnery and T. V. Duzer, "Fields and Waves in Communication Electronics" 3rd edition, Chichester, John Wiley & Sons, 1993.
- [45] T. Aragona, A. Babare, G. Doolio et al, "The importance of short-circuit tests for the large rating autotransformers". Energia Electrica, vol. 74, no. 5, 1997, pp. 290-310.
- [46] T. K. Saha "Review of modern diagnostic techniques for assessing insulation condition in aged transformers" IEEE Transactions on Dielectrics and Electrical Insulation Vol. 10, No. 5; October 2003, pp. 903-917.
- [47] T. Nakata, N. Takahashi, F. Fujiwara and Y. Shiraki, "3D magnetic field analysis using special elements", IEEE Trans. Magn. Vol. 26, No 2, pp. 2465-2470, 1990.
- [48] X. S. Chen and Paul Neudorfer "Digital Modeling of Modern Single-Phase Distribution Transformers" IEE International Conference on Advances in Power System Control, Operation and Management, November 1991, Hong Kong.
- [49] B. Baodong, D. Xie, J. Cui et al "Optimal transposition design of transformer windings by genetic algorithms", 1995 IEEE Trans. Magn. 6 3572-3574.
- [50] C M Arturi "3D FE analysis of the axial forces on the step-up transformer-windings with helicoidal LV", 1995 IEEE Trans. v 31 Magn. 3 2032-2035.
- [51] C. M. Arturi, "Model of a highly saturated 3-phase autotransformer with tertiary winding and 5-limb core and analysis of a time-varying short-circuit transient". European Trans. Elec. Power Engineering, vol.4, no.6, 1994, pp.513-524.

- [52] E. E. Kriezis, T. D. Tsiboukis, S. M. Panas and A. T. Tegopoulos, "Eddy currents: theory and applications". Proc. IEEE, vol. 80, no. 10, 1992, pp. 1559-1589.
- [53] Eduard Karplus and William Norris Tuttle, "Alternating-Current Apparatus" General Radio Company, Cambridge, Mass, a corporation of Massachusetts. US Patent No. 2,009,013. 6. June 1, 1934, s. no 728,470, 6 Claims (Cl. 171-119).
- [54] Gilbert Smiley "Adjustable Transformer with Stabilized Contact Track" General Radio Company, Cambridge, Mass., a corporation of Massachusetts. U.S. Patent No. 2,949,592. Apr. 19, 1951, s. no. 221,878. 1 Claim. (Cl. 336-148).
- [55] I. V. Yakimets and V. G. Narovlyanskii, "Autotransformer with a voltage-stabilised tertiary winding". Electrical Technology, no.1, 1995, pp.21-30.
- [56] J. D. Kraus 1992 Electromagnetics (London: McGraw-Hill Inc.).
- [57] J. P. Martin, J Wendling and Y. Tournier, "Specifics of the short-circuit behaviour of concentrically-wound transformers and autotransformers". IEEE trans. Power App. and Sys., vol. 99. no.6.1980. pp. 2069-2077.
- [58] J. P.O. Abreu, C. A. M. Guimapaes and G. Paulillo, "A proposal for a power converter autotransformer". Proc. IEEE Int. Electrical Machines and Drives Conference, Milwaukee, USA, 1997, pp. 61-64.
- [59] K. B. Niclas, R. R. Pereira and A. P. Chang, "Transmission lines accurately model autotransformers". Microwave & RF, vol. 31, no. 11, 1992, pp.72-76.
- [60] K. J. Binns, P. J. Lawrenson and C. W. Trowbridge, The Analytical and Numerical Solution of Electric and Magnetic Fields. 3rd ed. Chichester, John Wiley & Sons. 1992.
- [61] L. F. Blume, C;. Boyajian, A. Camilli et al, Transformer Engineering: A Treatise on the theory, Operation and Application of transformers, Chapman & Hall Ltd., 1951.
- [62] O. C. Zienkiewicz and R. I. Taylor, "The Finite Element Method" Maidenhead, McGraw-Hill Inc., 1991.
- [63] OPFRA-3d Version 9 2003, TOSCA Version 9 2003. and ELEKTRA Version 9 2003, Vector Fields Limited, Oxford, UK.
- [64] P. P. Silvester and R L Ferrari 1990 "Finite Elements for Electrical Engineers" (Cambridge: Cambridge University Press)
- [65] P. Silvester and Konpad, "Analysis of transformer leakage phenomena by higher order finite elements". IEEE Trans. PAS, vol.6, 1973, pp. 1843-1855.

- [66] S. Ramo, J. R. Whinnery and T. V. Duzer, "Fields and Waves in Communication Electronics" 3rd edition, Chichester, John Wiley & Sons, 1993.
- [67] T. Aragona, A. Babare, G. Doolio et al, "The importance of short-circuit tests for the large rating autotransformers". *Energia Electrica*, vol. 74, no. 5, 1997, pp. 290-310.
- [68] C W Trowbridge "An Introduction to Computer Aided Electromagnetic Analysis" Pbk. ISBN 0 95 16262 0 5 Published by Vector Fields Ltd., 1990
- [69] Handbook of Voltage Control with the Variac Autotransformer, © 1963 by General Radio Company, Form 3080-A January 1963, West Concord, Massachusetts, USA.
- [70] Morganite "Carbon Brushes and Electrical Machines" Published by Morganite Electrical Carbon Limited, 1978. Printed by J S G Services Limited, Swansea UK.
- [71] M Rahman "Mathematical Modelling and Computer Aided Design of Field Coupled Electro-mechanical Transducers". PhD thesis, Department of Systems Science
- [72] John D. Kraus "Electromagnetics" © 1991 Fourth Edition McGraw-Hill USA.
- [73] Ahmed and Ph. Auriol, "Conformal mapping method for calculation of rectangular winding parameters", *IEEE Trans. on MAG*, VOL.28, No.5, pp.2823-2825, September 1992.
- [74] T. Nakata, N.Takahashi, F. Fujiwara and Y.Shiraki, "3D magnetic field analysis using special elements", *IEEE Trans. Magn.* Vol. 26, No 2, pp. 2465-2470, 1990.
- [75] D.Rodger, P.J.Leonard, H.C.Lai, "Surface elements for modelling 3D fields around thin iron sheets", *IEEE Trans Magn.*, Vol. 29, No 2, pp. 1483-1486, March 1993.
- [76] J. Simkin and C.W. Trowbridge, "On the use of the total scalar potential in the numerical solution of field problems in electromagnetic" *International Journal of numerical Methods in Engineering*, Vol.14, pp 423-440, 1979.
- [77] J. M. Dedulle, G. Meunier, "3D Anisotropic Magnetic Fields in Transformer Core Laminated with Grain-Oriented Steel-Sheet", *INTERMAG*, 1990.
- [78] P. P. Silvester, R. P. Gupta, "Effective computational models for anisotropic soft B-H curves", *IEEE Trans Magn.* Vol.27, No.5, pp. 3804-3807, 1991.
- [79] C. S. Biddlecombe, E.A. Heighway, J. Simkin, C.W. Trowbridge, "Methods for eddy current computation in three dimensions", *Proc COMPUMAG Conf.*, Chicago, 1981.

- [80] J. Simkin, C.W. Trowbridge, "Which Potential?" RL-78-001/B, January 1978.
- [81] A. G. Armstrong, C. J. Collie, J. S. Simkin, C.W. Trowbridge, "The solution of three-dimensional magnetic problems using scalar potentials" Proc COMPUMAG Conf, Grenoble, p.1-2, 1978.
- [82] J. K. Sykulski, E. Sykulska, S.T. Hughes "Application of Finite Element Modelling in LVDT Design" COMPEL-The International Journal for computation and mathematics in Electrical & Electronic Engineering, vol.11, No.1, p.73-76, 1992.
- [83] S. H. Khan, J. M. El-Shawish, K T V Grattan, L. Finkelstein "Finite Element Modelling of Variable Transformers used for Voltage Regulation and Control" Paper presented at Sensors and their Applications VIII, 7-10 September 1997. Section B: Sensor Modelling, p 41-46, 1997.
- [84] S. H. Khan, J. M. El-Shawish, L. Finkelstein K T V Grattan "Investigation of Variable Transformers by 3D Field Modelling – Comparison of Modelling and Experimental Results" Paper presented at ICEM 28-30 August 2000 Espoo Finland, p 262-266.
- [85] S. H. Khan, J. M. El-Shawish, L. Finkelstein K T V Grattan "Design Investigation of Commercial Voltage Stabilisers by 3D Finite Element Modelling" Paper presented at Sensors and their Applications XI, 7-10 September 2001. Section 8: Industrial Applications of Sensor, p 455-461.
- [86] S. H. Khan, J. M. El-Shawish, L. Finkelstein K T V Grattan "Finite Element Modelling of Saturation and Eddy Current Effects in Commercial Variable Transformers" IEEE Transactions on Magnetics, p 2783-2786 VOL. 37, No. 4, July 2001.

Appendix 1: Technical Features and Specifications of the Instruments used in Experimental Measurements

The main specifications of the instruments used for the experimental measurements are the following:

Gauss meter (GM05):

Range 1	0 to 3 Tesla, resolution 1 milliTesla
Range 2	0 – to 299.9 milliTesla, resolution 100 micro Tesla
Range 3	0 – to 2.999 milliTesla, resolution 2 milliTesla
Range 4	0 – to 299.9 milliTesla, resolution 100 micro Tesla
Accuracy (at 20°C)	Better than $\pm 1\%$ (DC) traceable to NPL Standards
Reproducibility	Better than 0.5%
Frequency Range	DC and 15Hz to 10kHz
Temperature Coefficient	$\pm 0.1\%$ of reading/ $^{\circ}\text{C}$ including probe
Averaging time constant	100 milliseconds
Operating Temp Range	0°C to + 50°C
Functions	DC, DC Peak, AC RMS, AC RMS MAX, AC Peak
Facilities	Store and Recall on 0–99 samples

Hall Probe:

Transverse Probe	Thickness 1mm
	Width 4mm
	Length 90mm (not including handle)
	Length 230mm (including handle)
	Hall sensor active area 0.2mm \times 0.2mm
	approximately
	Cable length 1.5m

Power Analyser (PM1200):

Features:

IEEE485 or RS232 (150-9600 baud) remote control

Parallel (Centronics) and RS232 printer output

Chart Recorder Output

Non-volatile calibration and set-up data

16 Key keyboard

4.5digit led display

16 led indicators

Scaling Functions:

W	True Power
VA	Apparent Power
PP	Power Factor
VRMS	RMS Voltage
ARMS	RMS Current
VCF	Voltage Crest Factor
ACF	Current Crest Factor
AJNST	Peak Inrush Current
FREQ	Frequency
HARM	Harmonic Analysis
THO	Total Harmonic Distortion
VAR	Reactive Power

Display:

The display has a total of sixteen function lamps (two red, four yellow and ten green) "o" located above most of the sixteen keys and a four and a half digit led display. When lit, the 11k" and "M" lamps (yellow) indicate that the value displayed is 1000 or 1,000,000 times larger than the value of the function being measured.

RMS Voltage (V rms):

Range	2V to 1000V pk (autoranging in 7 ranges: 15V, 31V, 62V, 125V, 250V, 500V and 1000V pk)
Display	4 1/2 digits
Frequency Range	DC and 5Hz to 50kHz
Crest Factor	Up to 19.9 (limit 1000V pk)
Accuracy 23±5°C Sine wave	±0.1% of reading ±0.1% of range ±0.05%/kHz ± 1 digit

Input Impedance	2M Ω and 10pF on all ranges
Peak Input Voltage	Continuous 1000V across input terminals < 1 second 2500V across input terminals
RMS Current (Arms):	
Range	20mA to 20A rms (175A pk) (auto ranging) in 7 ranges: 0.24A, 0.72A, 2.5A, 6.5A, 19.5A 58A and 175A peak
Display	4½ digits
Frequency Range	DC and 5Hz to 50kHz
Crest Factor	Up to 19.9 (limit 175A pk)
Input Resistance	0.025 Ω max inc. fuse circuit
Accuracy 23 \pm 5°C Sine wave	\pm 0.1% of reading \pm 0.10% of range \pm 0.05%/kHz \pm 1 digit

Power (W):

Range	40mW to 13kW (auto ranging) in 49 ranges corresponding to V and A ranges
Display	4½ digits with polarity according to direction of power flow
Frequency range	DC and 5Hz to 50kHz
Accuracy 23 \pm 5°C Sine wave	\pm [(Vrdg \times Aerror) + (Ardg \times Verror)] \pm (0.25 \div PF)%/kHz \pm 1 digit
Polarity	+ indicates positive power flow – indicates negative power flow

	0°	90°	180°	270°	360°
W	+	–	–	+	
PF	–	–	+	+	
VARs	+	+	–	–	

The displacement angle is the angle of the current fundamental with reference to the voltage fundamental.

Apparent Power (VA):

Range	40mVA to 13kVA (auto ranging) in 49 ranges corresponding to V and A ranges
Display	4½ digits
Frequency Range	DC and 5Hz to 50kHz
Accuracy 23 ±5°C Sine wave	$\pm [(Vrdg \times Aerror) + (Ardg \times Verror)] \pm 1$ digit

Reactive Power (VA):

Range	40mW to 13kW (auto ranging) in V and A ranges.
Display	4½ digits and polarity
Frequency Range	DC and 5Hz to 50kHz
Accuracy 23 ±5°C Sine wave	$\pm [(Vrdg \times Aerror) + (Ardg \times Verror)] \pm (0.25 \div PF)\% / kHz \pm 1$ digit
Polarity	+indicates inductive load –indicates capacitive load

Power Factor (PF):

Range	+1.000 to –1.000
Display Resolution	4½ digits
Accuracy 23 ±5°C Sine wave	$\pm 0.001 \pm (0.002 \div PF) / kHz$
Polarity	+ indicates leading PF – indicates lagging PF

Voltage Crest Factor (Vcf):

Range	1.00 to 19.99
Display	3 digits
Accuracy 23 ±5°C Sine wave	$\pm 0.1\% \pm 1$ digit

Current Crest Factor (Acf):

Range	1.00 to 19.99
Display	3 digits
Accuracy 23 ±5°C Sine wave	$\pm 0.1\% \pm 1$ digit

Instantaneous Peak Current (Ainst):

Range 0.05A to 175A pk on specified starting range or auto ranging in 7 ranges comprising 0.24A, 0.72A, 2.15A, 6.5A, 19.5A, 58A and 175A.

Display resolution 4 1/2 digits with polarity

Accuracy 23 ±5°C Sine wave ± 2.0% of range ± 1 digit

Sampling Interval 25µs

AC Signal Frequency (FREQ):

Range 5Hz to 20KHz on selected channel

Display 4 1/2 digits

Accuracy 23 ±5°C Sine wave +0.2% of reading

Harmonic Analysis (HARM):

RMS Current 20mA to 20A rms (175A pk) in seven ranges: 0.24A, 0.72A, 2.15A, 6.5A, 19.5A, 58A and 175A pk

RMS Voltage 2 to 660V rms (1000Vpk) in seven ranges: 15V, 31V, 62V, 125V, 250V, 500V and 1000V pk

Frequency Range DC 5Hz to 50kHz

Display 4 1/2 digits

Accuracy 23 ±5°C Sine wave Fundamental: ± 0.1% of reading ± 0.1% of range +0.05%/kHz + 1 digit

Harmonics: + (0.1 + 0.05/kHz)% of fundamental + 1 digit

Total Harmonic Distortion (THD):

Range using prog 5 = 1 0.1 to 199.9%

Range using prog 5 = 0 3.0 to 199.9%

Display 4 1/2 digits

Frequency Range DC and 5Hz to 50 kHz

Accuracy ± 2.0% ± 0.01%/kHz ± 1 digit

Integrator:

Range 1mW/hr to 19999MW / hr

Interval	0.001hr
Elapsed time	0.001hr to 19999 hr or continuous
Environmental conditions	
Temp	0°C to +50°C
Storage	-40°C to +70°C
Humidity	10% to 90% RH non-condensation

Overcurrent protection:

Fuse HRC 11/4" (32mm) 2OAT

Dielectric Strength:

Inputs - Case	5kV AC 50/60 Hz 1 minute
Inputs - Power Supply	5kV AC 50/60 Hz 1 minute
Power Supply - Case	2kV AC 50/60 Hz 1 minute

Power Supply:

AC Input Voltage	110V ac to 220V ac + 20%
Frequency	47 to 440 Hz
Protection	Fuse 20mm 1AT
Consumption	16W, 28 VA max

Physical Data:

Weight	5Kg
Height	102mm
Width	215mm
Depth	360mm

Clip-on Power meter (HEME 1000 P)

Current measurement:

Measurement principle	Through the use of Hall-effect sensors in the magnetic circuit, both DC and AC true RMS current (DC coupled) can be measured
Ranges (Auto ranging):	200A AC-DC; 1000A AC-DC
Resolution	100 mA for 200A range 1A for 1000A range
Accuracy	1 % of range \pm 1A within specified conditions
Temperature coefficient:	0.1 % / K

Frequency range	Direct current and 15 Hz to 1000Hz
Influence of position of cable within jaw area	<2% typical
Crest factor	maximum 7 (peak current, 1200A)
Maximum overload	10,000A
Signal integration time	200 ms
Measurement rate	approx. 2 per second

Voltage measurement:

Measurement principle	DC coupled direct voltage, true RMS
Ranges (Auto ranging)	200 V AC – DC, 750 V AC-DC
Resolution	100 mV for 200 V range 1V for 750 V range
Accuracy	0.5 % of range \pm 1 count within specified conditions
Temperature coefficient	0.1 %/ K
Frequency range	DC and 1 5 Hz
Input impedance	1 M Ω
Maximum overload	to 1000 V RMS
Measurement rate	approx. 2 per second

Display:

13 mm (half inch) high liquid crystal display. 3 1/2-digit (2000 counts). Last measured value displayed for 30 seconds before automatic power-off. DC + or –, AC indications are displayed (with a display test)

Environmental Conditions:

Reference conditions	23°C \pm 1°C (f = 50 Hz, sinusoidal) (with current carrying cable at the centre of the jaws opening)
Working temperature	0°C to + 40°C
Functional temperature	-10°C to +50°C
Relative humidity	80% at 40°C

DC Power supply:

A conventional DC power supply made by Claud Lyons Ltd.

Input	220V AC
Output	with voltage adjustment switch between 13.8 V DC or 6-15 V DC

Appendix 2: Command Input Files used in FE Modelling

1. Command input file defining conductor turns used in models for case-1

```
COND
DEFI GRAC
108.5*cos(15*(2*pi/325)) 108.5*sin(15*(2*pi/325)) 15*(2*pi/325)*180/pi
0.0    0.0    0.0
0.0    0.0    0.0
1.896525  1.896525
24    0.0
36    1.0
(0/3.6)    1  0.0
  0  0  0
0.001
QUIT
//*****//
$DO #W 17*(2*pi/325) 163*(2*pi/325) 2*(2*pi/325)
$para #x 108.5*cos(#W)
$para #y 108.5*sin(#W)
COND
DEFI GRAC
#x    #y    28.5+280  #W*180/pi
0.0    0.0    0.0
0.0    0.0    0.0
1.896525  1.896525
24    0.0
36    1.0
-(11.98/3.6)    1  0.0
  0  0  0
0.001
QUIT
$END DO
//*****/brush position/*****//
```

\$DO #W 165*(2*pi/325) 311*(2*pi/325) 2*(2*pi/325)

\$para #x 108.5*cos(#W)

\$para #y 108.5*sin(#W)

COND

DEFI GRAC

#x #y 28.5+280 #W*180/pi

0.0 0.0 0.0

0.0 0.0 0.0

1.896525 1.896525

24 0.0

36 1.0

(12.03/3.6) 1 0.0

0 0 0

0.001

QUIT

\$END DO

////////////////////////////////////

\$DO #W 16*(2*pi/325) 164*(2*pi/325) 2*(2*pi/325)

\$para #x 107.25*cos(#W)

\$para #y 107.25*sin(#W)

COND

DEFI GRAC

#x #y 28.5+280 #W*180/pi

0.0 0.0 0.0

0.0 0.0 0.0

1.896525 1.896525

25.25 0.0

38.5 1.0

-(11.98/3.6) 1 0.0

0 0 0

0.001

QUIT

```

$END DO
//*****//brush position/*****//
$DO #W 166*(2*pi/325) 310*(2*pi/325) 2*(2*pi/325)
$para #x 107.25*cos(#W)
$para #y 107.25*sin(#W)
COND
DEFI GRAC
#x      #y  28.5+280  #W*180/pi
0.0     0.0    0.0
0.0     0.0    0.0
1.896525 1.896525
25.25   0.0
38.5    1.0
(12.03/3.6) 1 0.0
0 0 0
0.001
QUIT
$END DO

```

- the following executable command 'macros' (command input file) define, calculate and realise the correct winding turns around the large core:

```

$DO      #W      15*(2*pi/325)  221*(2*pi/325)+0.01  (2*pi/325)
$para    #x      152*cos(#W)
$para    #y      152*sin(#W)
COND
DEFI GRAC
#x      #y      28.5+380      #W*180/pi
0.0     0.0     0.0
0.0     0.0     0.0
1.896525 1.896525
24      0.0
36      1.0
(6.6/3.6) 1      0.0

```

```

0          0          0
0.001
QUIT
$END DO
$DO      #W      222*(2*pi/325)  271*(2*pi/325)+0.01  (2*pi/325)
$para   #x      152*cos(#W)
$para   #y      152*sin(#W)
COND
DEFI GRAC
#x      #y      28.5+380      #W*180/pi
0.0     0.0     0.0
0.0     0.0     0.0
1.896525  1.896525
24      0.0
36      1.0
(-14.4/3.6)  1      0.0
0       0       0
0.001
QUIT
$END DO
$DO      #W      272*(2*pi/325)  302*(2*pi/325)+0.01  (2*pi/325)
$para   #x      152*cos(#W)
$para   #y      152*sin(#W)
COND
DEFI GRAC
#x      #y      28.5+380      #W*180/pi
0.0     0.0     0.0
0.0     0.0     0.0
1.896525  1.896525
24      0.0
36      1.0
(-21/3.6)  1  0.0
0       0       0

```

```
0.001
QUIT
$END DO
```

3. Command input files calculating the flux density B_z over the core case-1 with and without top plate at two levels of heights z_4 and z_6 .

```
//3Bz4-3Bz6.comi//
$ open 1 Bz-r2z4.dat write
$ form 1 expo 8
$ form 2 string 100 string=' Bz, over the core without top plate'
$ assi 2 1
$ write 1
$ assi 1 1
$ do #TH 0 2*pi 2*pi/72
$ para #x 87*cos(#TH)
$ para #y 87*sin(#T
$ const #z 358
poin x=#x, y=#y, z=#z
$ para #bz bz*1000
$ write 1 #bz
$ end do
$ close 1
////////////////////////////////
$ open 1 Bz-r3z4.dat write
$ form 1 expo 8
$ form 2 string 100 string=' Bz, over the core without top plate'
$ assi 2 1
$ write 1
$ assi 1 1
$ do #TH 0 2*pi 2*pi/72
$ para #x 110*cos(#TH)
```

```

$ para #y 110*sin(#TH)
$ const #z 358
poin x=#x, y=#y, z=#z
$ para #bz bz*1000
$ write 1 #bz
$ end do
$ close 1
//////////
$ open 1 Bz-r5z4.dat write
$ form 1 expo 8
$ form 2 string 100 string=' Bz, over the core without top plate'
$ assi 2 1
$ write 1
$ assi 1 1
$ do #TH 0 2*pi 2*pi/72
$ para #x 130*cos(#TH)
$ para #y 130*sin(#TH)
$ const #z 358
poin x=#x, y=#y, z=#z
$ para #bz bz*1000
$ write 1 #bz
$ end do
$ close 1
//////////
$ open 1 Bz-r2z6.dat write
$ form 1 expo 8
$ form 2 string 100 string=' Bz, over the core with top plate'
$ assi 2 1
$ write 1
$ assi 1 1
$ do #TH 0 2*pi 2*pi/72
$ para #x 87*cos(#TH)

```

```

$ para #y 87*sin(#TH)
$ const #z 380
poin x=#x, y=#y, z=#z
$ para #bz bz*1000
$ write 1 #bz
$ end do
$ close 1
//////////
$ open 1 Bz-r3z6.dat write
$ form 1 expo 8
$ form 2 string 100 string=' Bz, over the core without top plate'
$ assi 2 1
$ write 1
$ assi 1 1
$ do #TH 0 2*pi 2*pi/72
$ para #x 110*cos(#TH)
$ para #y 110*sin(#TH)
$ const #z 380
poin x=#x, y=#y, z=#z
$ para #bz bz*1000
$ write 1 #bz
$ end do
$ close 1
//////////
$ open 1 Bz-r5z6.dat write
$ form 1 expo 8
$ form 2 string 100 string=' Bz, over the core without top plate'
$ assi 2 1
$ write 1
$ assi 1 1
$ do #TH 0 2*pi 2*pi/72
$ para #x 130*cos(#TH)

```

```

$ para #y 130*sin(#TH)
$ const #z 380
poin x=#x, y=#y, z=#z
$ para #bz bz*1000
$ write 1 #bz
$ end do
$ close 1

```

4. Command input file for, calculating the flux density around the core case-1 at radius r_6 and three levels of heights z_1 ; z_2 and z_3 .

```

//3Bxy.comi//
$ open 1 r6z3.dat write
$ form 1 expo 8
$ form 2 string 100 string=' Bx,y beside the core without top plate'
$ assi 2 1
$ write 1
$ assi 1 1
$ do #TH 0 2*pi 2*pi/72
$ para #x 136*cos(#TH)
$ para #y 136*sin(#TH)
$ const #z 337
poin x=#x,y=#y,z=#z
$ para #bx (bx*1000)**2
$ para #by (by*1000)**2
$ para #bxy sqrt(#bx+#by)
$ write 1 #bxy
$ end do
$ close 1
//////////
$ open 1 r6z2.dat write
$ form 1 expo 8
$ form 2 string 100 string=' Bx,y beside the core without top plate'
$ assi 2 1

```

```

$ write 1
$ assi 1 1
$ do #TH 0 2*pi 2*pi/72
$ para #x 136*cos(#TH)
$ para #y 136*sin(#TH)
$ const #z 308
poin x=#x,y=#y,z=#z
$ para #bx (bx*1000)**2
$ para #by (by*1000)**2
$ para #bxy sqrt(#bx+#by)
$ write 1 #bxy
$ end do
$ close 1
//////////
$ open 1 r6z1.dat write
$ form 1 expo 8
$ form 2 string 100 string=' Bx,y beside the core without top plate'
$ assi 2 1
$ write 1
$ assi 1 1
$ do #TH 0 2*pi 2*pi/72
$ para #x 136*cos(#TH)
$ para #y 136*sin(#TH)
$ const #z 280
poin x=#x,y=#y,z=#z
$ para #bx (bx*1000)**2
$ para #by (by*1000)**2
$ para #bxy sqrt(#bx+#by)
$ write 1 #bxy
$ end do
$ close 1
//*****//

```

5. Command input file defining conductor turns used in models for case-2

```
$DO #W 55*(2*pi/325) 103*(2*pi/325) 2*(2*pi/325)
```

```
$para #x 108.5*cos(#W)
```

```
$para #y 108.5*sin(#W)
```

```
COND
```

```
DEFI GRAC
```

```
#x      #y      28.5+280  #W*180/pi
```

```
0.0     0.0     0.0
```

```
0.0     0.0     0.0
```

```
1.896525 1.896525
```

```
24      0.0
```

```
36      1.0
```

```
(20.24/3.6) 1 0.0
```

```
0 0 0
```

```
0.001
```

```
QUIT
```

```
$END DO
```

```
//*****//
```

```
$DO #W 105*(2*pi/325) 311*(2*pi/325) 2*(2*pi/325)
```

```
$para #x 108.5*cos(#W)
```

```
$para #y 108.5*sin(#W)
```

```
COND
```

```
DEFI GRAC
```

```
#x      #y      28.5+280  #W*180/pi
```

```
0.0     0.0     0.0
```

```
0.0     0.0     0.0
```

```
1.896525 1.896525
```

```
24      0.0
```

```
36      1.0
```

```
-(4.64/3.6) 1 0.0
```

```
0 0 0
```

```
0.001
```

```

QUIT
$END DO
//*****//
$DO #W 54*(2*pi/325) 104*(2*pi/325) 2*(2*pi/325)
$para #x 107.25*cos(#W)
$para #y 107.25*sin(#W)
COND
DEFI GRAC
#x      #y 28.5+280 #W*180/pi
0.0     0.0     0.0
0.0     0.0     0.0
1.896525 1.896525
25.25   0.0
38.5    1.0
(20.24/3.6) 1 0.0
0 0 0
0.001
QUIT
$END DO
//*****//
$DO #W 106*(2*pi/325) 310*(2*pi/325) 2*(2*pi/325)
$para #x 107.25*cos(#W)
$para #y 107.25*sin(#W)
COND
DEFI GRAC
#x      #y 28.5+280 #W*180/pi
0.0     0.0     0.0
0.0     0.0     0.0
1.896525 1.896525
25.25   0.0
38.5    1.0
-(4.64/3.6) 1 0.0

```

```

0 0 0
0.001
QUIT
$END DO
// In case of brush position-1 (Tb2) at turn number 159//:
$DO #W 15*(2*pi/325) 39*(2*pi/325) 2*(2*pi/325)
$para #x 108.5*cos(#W)
$para #y 108.5*sin(#W)
COND
DEFI GRAC
#x      #y      28.5+280 #W*180/pi
0.0     0.0     0.0
0.0     0.0     0.0
1.896525 1.896525
24      0.0
36      1.0
(0/3.6) 1 0.0
  0 0 0
0.001
QUIT
$END DO
//*****//
$DO #W 16*(2*pi/325) 38*(2*pi/325) 2*(2*pi/325)
$para #x 108.5*cos(#W)
$para #y 108.5*sin(#W)
COND
DEFI GRAC
#x      #y      28.5+280 #W*180/pi
0.0     0.0     0.0
0.0     0.0     0.0
1.896525 1.896525
24      0.0

```

```

36      1.0
(0/3.6)      1 0.0
  0  0  0
0.001
QUIT
$END DO
/*****/
$DO #W 55*(2*pi/325)  157*(2*pi/325)  2*(2*pi/325)
$para #x 108.5*cos(#W)
$para #y 108.5*sin(#W)
COND
DEFI GRAC
#x      #y      28.5+280  #W*180/pi
0.0      0.0      0.0
0.0      0.0      0.0
1.896525  1.896525
24      0.0
36      1.0
(15.23/3.6)      1 0.0
  0  0  0
0.001
QUIT
$END DO
/*****/
$DO #W 159*(2*pi/325)  311*(2*pi/325)  2*(2*pi/325)
$para #x 108.5*cos(#W)
$para #y 108.5*sin(#W)
COND
DEFI GRAC
#x      #y      28.5+280  #W*180/pi
0.0      0.0      0.0
0.0      0.0      0.0

```

```

1.896525  1.896525
24      0.0
36      1.0
-(9.38/3.6)  1 0.0
  0  0  0
0.001
QUIT
$END DO
/*****/
$DO #W 54*(2*pi/325) 158*(2*pi/325) 2*(2*pi/325)
$para #x 107.25*cos(#W)
$para #y 107.25*sin(#W)
COND
DEFI GRAC
#x      #y  28.5+280  #W*180/pi
0.0     0.0     0.0
0.0     0.0     0.0
1.896525  1.896525
25.25    0.0
38.5     1.0
(15.23/3.6)  1 0.0
  0  0  0
0.001
QUIT
$END DO
/*****/
$DO #W 160*(2*pi/325) 310*(2*pi/325) 2*(2*pi/325)
$para #x 107.25*cos(#W)
$para #y 107.25*sin(#W)
COND
DEFI GRAC
#x      #y  28.5+280  #W*180/pi

```

```

0.0    0.0    0.0
0.0    0.0    0.0
1.896525  1.896525
25.25    0.0
38.5    1.0
-(9.38/3.6)    1  0.0
0  0  0
0.001
QUIT
$END DO
//*****//
// In case of brush position (Tb3) at turn number 213 //
$DO #W 55*(2*pi/325)  211*(2*pi/325)  2*(2*pi/325)
$para #x 108.5*cos(#W)
$para #y 108.5*sin(#W)
COND
DEFI GRAC
#x    #y    28.5+280  #W*180/pi
0.0    0.0    0.0
0.0    0.0    0.0
1.896525  1.896525
24    0.0
36    1.0
-(9.1/3.6)    1  0.0
  0  0  0
0.001
QUIT
$END DO
/*****/
$DO #W 213*(2*pi/325)  311*(2*pi/325)  2*(2*pi/325)
$para #x 108.5*cos(#W)
$para #y 108.5*sin(#W)

```

```

COND
DEFI GRAC
#x      #y      28.5+280  #W*180/pi
0.0     0.0     0.0
0.0     0.0     0.0
1.896525 1.896525
24      0.0
36      1.0
(15.73/3.6) 1 0.0
0 0 0
0.001
QUIT
$END DO
/*****/
$DO #W 54*(2*pi/325) 212*(2*pi/325) 2*(2*pi/325)
$para #x 107.25*cos(#W)
$para #y 107.25*sin(#W)
COND
DEFI GRAC
#x      #y      28.5+280  #W*180/pi
0.0     0.0     0.0
0.0     0.0     0.0
1.896525 1.896525
25.25   0.0
38.5    1.0
-(9.1/3.6) 1 0.0
0 0 0
0.001
QUIT
$END DO
/*****/
$DO #W 214*(2*pi/325) 310*(2*pi/325) 2*(2*pi/325)

```

```
$para #x 107.25*cos(#W)
$para #y 107.25*sin(#W)
COND
DEFI GRAC
#x      #y  28.5+280  #W*180/pi
0.0     0.0     0.0
0.0     0.0     0.0
1.896525  1.896525
25.25   0.0
38.5    1.0
(15.73/3.6)  1  0.0
0  0  0
0.001
QUIT
$END DO
```

Appendix 3: Calculations of winding resistance (R) for various conductor sizes

The resistance R of the original winding consisting of N turns is calculated using conductor parameters:

$$L_{T1} \text{ (length of single turn T1)} = (50 + 74) * 2 = 248 \text{ mm}$$

$$L_{T2} \text{ (length of single turn T2)} = (52.5 + 79) * 2 = 263 \text{ mm}$$

$$N \text{ (total number of turns)} = 295 \text{ turn}$$

$$\text{The length of the winding } L_w = N/2 (L_{T1} + L_{T2}) = (295)/2 * (248 + 263) = 75.373 \text{ m}$$

$$A_T \text{ (single turn cross-section area)} = 3.6 \times 10^{-6} \text{ m}^2$$

$$\text{Copper conductivity } (\sigma) = 5.8 \times 10^7 \text{ siemens}$$

$$\text{The winding resistance } R = N/2 (L_{T1} + L_{T2}) / \sigma A_T = 75.373 \text{ m} / (5.8 \times 10^7 \text{ mho/m} \cdot 3.6 \times 10^{-6} \text{ m}^2) = 75.373 / 208.8 = 0.361 \Omega$$

Winding resistance (R) In case of 25% reduction in h:

$$L_{T1} \text{ (length of single turn T1)} = (50 + 56) * 2 = 212 \text{ mm}$$

$$L_{T2} \text{ (length of single turn T2)} = (52.5 + 61) * 2 = 227 \text{ mm}$$

$$N \text{ (total number of turns)} = 295 \text{ turn}$$

$$\text{The length of the winding } L_w = N/2 (L_{T1} + L_{T2}) = (295)/2 * (212 + 227) = 64.753 \text{ m}$$

$$A_T \text{ (single turn cross-section area)} = 3.6 \times 10^{-6} \text{ m}^2$$

$$\text{Copper conductivity } (\sigma) = 5.8 \times 10^7 \text{ siemens}$$

$$\begin{aligned} \text{The winding resistance } R &= N/2 (L_{T1} + L_{T2}) / \sigma A_T \\ &= 64.753 \text{ m} / (5.8 \times 10^7 \text{ mho/m} \cdot 3.6 \times 10^{-6} \text{ m}^2) \\ &= 64.753 / 208.8 = 0.31 \Omega \end{aligned}$$

Winding resistance (R) In case of 25% reduction in w:

$$L_{T1} \text{ (length of single turn T1)} = (38 + 74) * 2 = 224 \text{ mm}$$

$$L_{T2} \text{ (length of single turn T2)} = (40.5 + 79) * 2 = 239 \text{ mm}$$

$$N \text{ (total number of turns)} = 295 \text{ turn}$$

$$\text{The length of the winding } L_w = N/2 (L_{T1} + L_{T2}) = (295)/2 (224 + 239) = 68.293 \text{ m}$$

$$A_T \text{ (single turn cross-section area)} = 3.6 \times 10^{-6} \text{ m}^2$$

$$\text{Copper conductivity } (\sigma) = 5.8 \times 10^7 \text{ siemens}$$

$$\begin{aligned} \text{The winding resistance } R &= N/2 (L_{T1} + L_{T2}) / \sigma A_T \\ &= 68.293 \text{ m} / (5.8 \times 10^7 \text{ mho/m} \cdot 3.6 \times 10^{-6} \text{ m}^2) \\ &= 68.293 / 208.8 = 0.327 \Omega \end{aligned}$$

Winding resistance (R) In case of 25% reduction in h and w :

$$L_{T1} \text{ (length of single turn } T1) = (38 + 56) * 2 = 188 \text{ mm}$$

$$L_{T2} \text{ (length of single turn } T2) = (40.5 + 61) * 2 = 203 \text{ mm}$$

$$N \text{ (total number of turns)} = 295 \text{ turn}$$

$$\text{The length of the winding } L_w = N/2 (L_{T1} + L_{T2}) = (295/2) (188 + 203) = 57.673 \text{ m}$$

$$A_T \text{ (single turn cross-section area)} = 3.6 \times 10^{-6} \text{ m}^2$$

$$\text{Copper conductivity } (\sigma) = 5.8 \times 10^7 \text{ siemens}$$

$$\begin{aligned} \text{The winding resistance } R &= N/2 (L_{T1} + L_{T2}) / \sigma A_T \\ &= 57.673 \text{ m} / (5.8 \times 10^7 \text{ mho/m} \cdot 3.6 \times 10^{-6} \text{ m}^2) \\ &= 57.673 / 208.8 = 0.276 \Omega \end{aligned}$$

Winding resistance (R) in case of large size toroidal core:

$$L_s \text{ (Single turn length)} = (50 + 74) * 2 = 248 \text{ mm}$$

$$N \text{ (total number of turns)} = 288 \text{ turn}$$

$$\text{The winding length} = N (L_s) = 288 (248) = 71.424 \text{ m}$$

$$A_T \text{ (single turn cross-section area)} = 3.6 \times 10^{-6} \text{ m}^2$$

$$\text{Copper conductivity } (\sigma) = 5.8 \times 10^7 \text{ siemens}$$

$$\begin{aligned} \text{The winding resistance } R &= N (L_s) / \sigma A_T \\ &= 71.424 \text{ m} / (5.8 \times 10^7 \text{ mho/m} \cdot 3.6 \times 10^{-6} \text{ m}^2) \\ &= 71.424 / 208.8 = 0.342 \text{ ohm} \end{aligned}$$

Appendix 4: Main geometric and parameters of one of the designs of type TS1225 variable transformer.

Core: Toroidal	Outer diameter = 256.5 mm
	Inner diameter = 174 mm
	Thickness = 57 mm
Material Grade	Unisil 46 (30M5), B-H curve shown in Error! Reference
Electric Conductivity (σ)	2.08x106 s/m
Brush:	3 off
	Grade of Carbon: EG8101
	Brush size: 16.24x2.9 mm
	Spring pressure: 250-300 gms each brush voltage drop (Contact plate to track): \cong 0.7V at 25A
Winding:	Brush contact pick up: Wound braid
Wire	2.24 mm
Turns	295 (293 used)
	End Stop Hard
Plates:	Top and Base: Aluminium

Appendix 5: Experimental Measurements of Flux Density

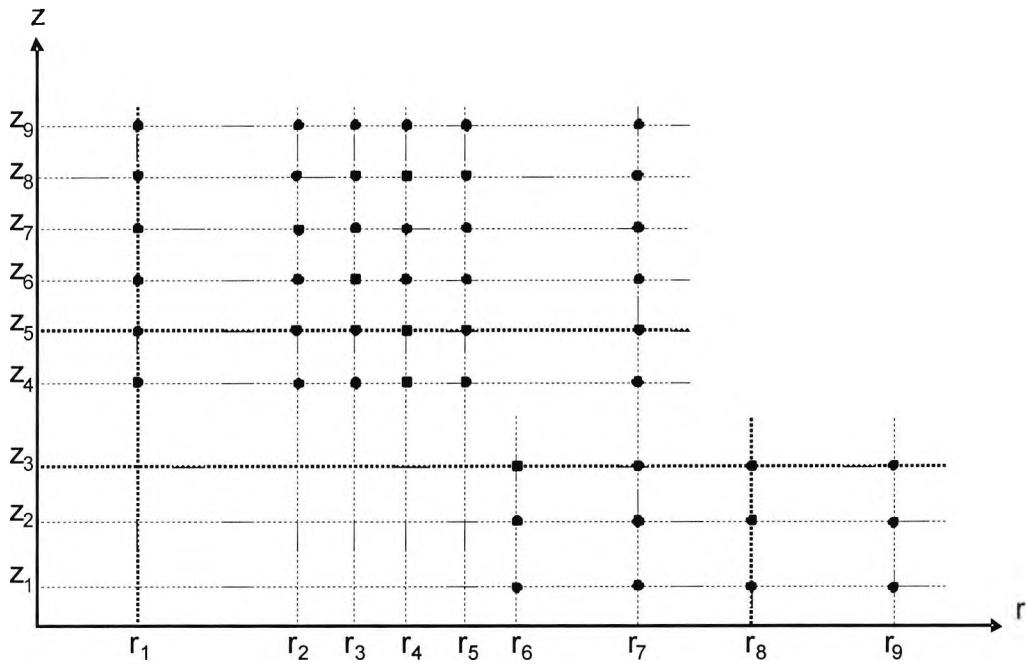


Fig. 1: r-z sensor positions, over and beside the core

Table 1: r-z distances in mm of sensor positions

Z ₉	230 35	230 87	230 110	230 120	230 130		230 140		
Z ₈	200 35	200 87	200 110	200 120	200 130		200 140		
Z ₇	170 35	170 87	170 110	170 120	170 130		170 140		
Z ₆	117 35	117 87	117 110	117 120	117 130		117 140		
Z ₅	103 35	103 87	103 110	103 120	103 130		103 140		
Z ₄	91 35	91 87	91 110	91 120	91 130		91 140		
Z ₃						70 134	70 140	70 150	70 170
Z ₂						41 134	41 140	41 150	41 170
Z ₁						13 134	13 140	13 150	13 170
	r ₁	r ₂	r ₃	r ₄	r ₅	r ₆	r ₇	r ₈	r ₉

Table 2: The values of voltage supply; currents and frequency during the experimental measurements

r	r ₁						r ₂					
Z	Z ₄	Z ₅	Z ₆	Z ₇	Z ₈	Z ₉	Z ₄	Z ₅	Z ₆	Z ₇	Z ₈	Z ₉
I ₁ (Am)	11.9	11.9	11.97	11.95	11.98	12	11.91	11.88	11.87	11.92	11.86	11.88
I ₃ (Am)	25.2	25.2	23.67	23.8	24	24.2	23.71	23.66	23.68	23.78	23.68	23.65
V _i (v)	239.8	239.8	239.8	240.9	241.5	240.6	240.8	240.8	240.9	240.9	240.1	240.5
f (Hz)	50	50	50	50	50	50.09	49.99	49.93	50.05	50.01	50.01	50.05

r	r ₃						r ₄					
Z	Z ₄	Z ₅	Z ₆	Z ₇	Z ₈	Z ₉	Z ₄	Z ₅	Z ₆	Z ₇	Z ₈	Z ₉
I ₁ (Am)	11.86	11.93	11.94	11.97	11.89	11.9	11.97	11.91	11.86	11.9	11.93	11.9
I ₃ (Am)	23.63	23.93	23.91	23.94	23.75	23.81	24.23	24.03	23.95	24.03	24.14	23.8
V _i (v)	240	240.1	240.5	240.8	240.3	240.8	241	240.5	239.2	239.8	240.2	240.7
f (Hz)	50	49.97	50.01	49.98	50	50.08	50.05	50	50.05	49.98	50.04	50.04

r	r ₅						r ₇					
Z	Z ₄	Z ₅	Z ₆	Z ₇	Z ₈	Z ₉	Z ₄	Z ₅	Z ₆	Z ₇	Z ₈	Z ₉
I ₁ (Am)	11.86	11.94	11.99	11.98	11.89	11.98	11.95	11.96	12.08	11.86	11.9	11.97
I ₃ (Am)	23.78	23.93	24.19	24.91	24.12	23.98	23.98	24.08	24.22	23.72	23.79	23.97
V _i (v)	239.8	239.9	240.8	240.8	240	240.1	240.2	240.4	240.3	240.8	240.9	240.5
f (Hz)	50.01	50.16	50.01	50.01	50.14	49.98	49.84	50.04	50.01	50.1	50.1	49.98

Table 3: The values of voltage supply; currents and frequency during the experimental measurements

r	r ₁				r ₂			
Z	Z ₆	Z ₇	Z ₈	Z ₉	Z ₆	Z ₇	Z ₈	Z ₉
I ₁ (Am)	11.96	12.05	11.99	11.98	11.92	12.07	11.94	12.05
I ₃ (Am)	24.19	24.27	24	24.17	24.14	24.31	24.1	24.22
V _i (v)	240.4	241.2	241.2	240.2	240	240.9	240	240.6
f (Hz)	50	50.08	50	49.97	50	50.03	50	50.01

r	r ₃				r ₄			
Z	Z ₆	Z ₇	Z ₈	Z ₉	Z ₆	Z ₇	Z ₈	Z ₉
I ₁ (Am)	11.96	12.1	11.93	12.13	11.88	12.08	12.14	11.89
I ₃ (Am)	24.22	24.4	24.17	24.53	24.03	24.38	24.45	23.94
V _i (v)	240.3	240.7	240.2	240	240.6	239.7	240.6	240.5
f (Hz)	50	50.02	50	50	50	49.97	50.04	49.95

r	r ₅				r ₇			
	Z ₆	Z ₇	Z ₈	Z ₉	Z ₆	Z ₇	Z ₈	Z ₉
I ₁ (Am)	11.93	12.12	12.06	11.95	11.96	12.12	12.06	11.92
I ₃ (Am)	24.14	24.38	24.27	24.09	24.3	24.42	24.33	23.93
V _i (v)	241.7	240.6	240	242.1	241.4	240.6	240	241.4
f (Hz)	50.08	50.03	50	50.02	50.02	49.95	49.98	50.05

Table 4: The values of voltage supply; currents and frequency during the experimental measurements

Measurement of perpendicular field (without top plate)												
r	r ₆			r ₇			r ₈			r ₉		
	Z ₁	Z ₂	Z ₃	Z ₁	Z ₂	Z ₃	Z ₁	Z ₂	Z ₃	Z ₁	Z ₂	Z ₃
I ₁ (Am)	11.92	11.94	11.9	11.93	11.93	11.9	11.96	11.9	11.9	11.94	11.9	11.9
I ₃ (Am)	23.93	23.79	23.85	23.77	23.95	24	23.94	23.82	23.86	24.9	24.2	23.95
V _i (v)	240	240	240.8	239.9	240.6	240	240.2	240	240.2	240	240.8	240.4
f (Hz)	50.12	50.13	50.11	50.01	50	50	49.97	50.02	50.13	50	50.13	50.08

Measurement of perpendicular field (with top plate)												
r	r ₆			r ₇			r ₈			r ₉		
	Z ₁	Z ₂	Z ₃	Z ₁	Z ₂	Z ₃	Z ₁	Z ₂	Z ₃	Z ₁	Z ₂	Z ₃
I ₁ (Am)	11.88	12.13	12.07	11.83	12.16	12.07	11.85	12.21	12.08	12.23	12.19	12.09
I ₃ (Am)	23.97	24.21	24.17	23.9	24.29	24.07	23.93	24.3	24.09	24.65	24.48	24.34
V _i (v)	241	240.5	240	240.6	241.3	240.8	240.9	240.8	240.1	240.7	241	240.7
f (Hz)	49.95	50.01	50	50.03	50.07	50	50.04	50.02	49.91	50	50.12	49.96

Measurement of parallel field (without top plate)												
r	r ₆			r ₇			r ₈			r ₉		
	Z ₁	Z ₂	Z ₃	Z ₁	Z ₂	Z ₃	Z ₁	Z ₂	Z ₃	Z ₁	Z ₂	Z ₃
I ₁ (Am)	12.2	12.01	12.02	12.16	12.03	12.03	12.2	12.05	12.07	12.09	12.07	12.06
I ₃ (Am)	24.6	24.3	24.32	24.56	24.26	24.35	24.6	24.36	24.4	24.57	24.5	24.35
V _i (v)	240.8	240	240	240	240.5	240	240.9	240.2	240.2	240.4	240.3	240.8
f (Hz)	50	50.05	50.12	50	50.08	50	50	50	50.09	50.02	50.04	50.11

Measurement of parallel field (with top plate)												
r	r ₆			r ₇			r ₈			r ₉		
	Z ₁	Z ₂	Z ₃	Z ₁	Z ₂	Z ₃	Z ₁	Z ₂	Z ₃	Z ₁	Z ₂	Z ₃
I ₁ (Am)	11.87	12	12	11.93	11.94	12.05	11.94	11.94	12.12	11.96	11.97	12.28
I ₃ (Am)	23.95	24.25	24.3	24.08	24.6	24.37	24.16	24.09	24.56	24.19	24.16	24.9
V _i (v)	240.3	240.1	240	240.4	240.2	240.5	240.6	240.3	240.8	240.8	240.8	240.1
f (Hz)	50.08	50	50	50.01	49.97	49.94	50.05	49.98	50.08	50.02	50.04	49.97

Table 5: The values of voltage supply; currents and frequency during the experimental measurements

r	r ₁				r ₂			
Z	Z ₆	Z ₇	Z ₈	Z ₉	Z ₆	Z ₇	Z ₈	Z ₉
I ₁ (Am)	11.96	12.05	11.99	11.98	11.92	12.07	11.94	12.05
I ₃ (Am)	24.19	24.27	24	24.17	24.14	24.31	24.1	24.22
V _i (v)	240.4	241.2	241.2	240.2	240	240.9	240	240.6
f (Hz)	50	50.08	50	49.97	50	50.03	50	50.01

r	r ₃				r ₄			
Z	Z ₆	Z ₇	Z ₈	Z ₉	Z ₆	Z ₇	Z ₈	Z ₉
I ₁ (Am)	11.96	12.1	11.93	12.13	11.88	12.08	12.14	11.89
I ₃ (Am)	24.22	24.4	24.17	24.53	24.03	24.38	24.45	23.94
V _i (v)	240.3	240.7	240.2	240	240.6	239.7	240.6	240.5
f (Hz)	50	50.02	50	50	50	49.97	50.04	49.95

r	r ₅				r ₇			
Z	Z ₆	Z ₇	Z ₈	Z ₉	Z ₆	Z ₇	Z ₈	Z ₉
I ₁ (Am)	11.93	12.12	12.06	11.95	11.96	12.12	12.06	11.92
I ₃ (Am)	24.14	24.38	24.27	24.09	24.3	24.42	24.33	23.93
V _i (v)	241.7	240.6	240	242.1	241.4	240.6	240	241.4
f (Hz)	50.08	50.03	50	50.02	50.02	49.95	49.98	50.05

Table 6: The values of voltage supply; currents and frequency during the experimental measurements of flux density beside the core (coil-2)

Brush position	Sensor position	V (v)	I ₁ (Am)	I ₂ (Am)	I ₃ (Am)
T _{b1} (100)	r ₆ Z ₂	240.1	15.73	9.1	24.97
T _{b2} (154)	r ₆ Z ₂	240.5	9.42	15.32	24.88
T _{b3} (207)	r ₆ Z ₂	241.4	4.63	20.34	24.95

Table 7: Flux density B (mT) measurements at position $r_6 z_2$, beside the core (coil-2), without top plate and the brush position at Tb1, (P – Parallel, PP – Perpendicular)

θ°	P. field	PP. field
0	0.14	9.79
5	0.12	10.15
10	0.15	10.73
15	0.53	11.72
20	3.02	13.32
25	5.08	10.30
30	5.48	8.56
35	5.65	6.74
40	5.73	5.20
45	5.70	4.06
50	5.71	2.83
55	5.76	1.81
60	5.81	0.59
65	5.88	0.36
70	6.02	1.50
75	6.08	2.80
80	6.03	3.98
85	6.13	5.05
90	5.79	6.44
95	5.81	7.32
100	5.93	8.48
105	6.00	9.76
110	6.05	11.19
115	6.04	12.94
120	5.76	15.09
125	4.60	18.10
130	0.35	20.05
135	2.43	16.80
140	2.96	14.75
145	3.18	13.46
150	3.34	12.51
155	3.41	11.39
160	3.49	10.51
165	3.54	9.65
170	3.55	8.78
175	3.58	8.03
180	3.56	7.27

θ°	P. field	PP. field
185	3.63	6.62
190	3.69	5.95
195	3.71	5.16
200	3.65	4.48
205	3.68	3.80
210	3.71	3.11
215	3.76	2.46
220	3.78	1.76
225	3.79	1.16
230	3.79	0.43
235	3.85	0.12
240	3.82	0.78
245	3.83	1.39
250	3.84	2.16
255	3.86	2.81
260	3.84	3.44
265	3.86	4.06
270	3.86	4.87
275	3.86	5.71
280	3.86	6.46
285	3.76	7.31
290	3.73	8.31
295	3.50	9.45
300	2.47	11.37
305	0.97	10.55
310	0.46	9.85
315	0.28	9.51
320	0.19	9.33
325	0.15	9.21
330	0.14	9.14
335	0.13	9.12
340	0.15	9.12
345	0.15	9.19
350	0.14	9.33
355	0.14	9.48
360	0.13	9.75

Table 8: Flux density B (mT) measurements at position $r_6 z_2$, beside the core (coil-2), without top plate and the brush position at Tb2, (P – Parallel, PP – Perpendicular)

θ°	P. field	PP. field
0	0.99	9.70
5	0.95	9.94
10	0.84	10.18
15	0.50	11.21
20	1.17	11.10
25	2.24	9.63
30	2.61	8.47
35	2.85	7.42
40	2.97	6.51
45	3.06	5.73
50	3.21	4.92
55	3.33	4.22
60	3.41	3.46
65	3.56	2.77
70	3.68	2.12
75	3.79	1.35
80	3.81	0.61
85	3.95	0.01
90	4.10	0.71
95	4.09	1.33
100	4.17	2.02
105	4.26	2.63
110	4.34	3.34
115	4.45	4.04
120	4.53	4.82
125	4.62	5.61
130	4.64	6.25
135	4.75	6.99
140	4.86	7.88
145	4.93	8.65
150	5.01	9.46
155	5.04	10.40
160	5.16	11.33
165	5.26	12.42
170	5.30	13.69
175	5.26	15.09
180	5.01	17.19

θ°	P. field	PP. field
185	3.88	20.81
190	1.26	18.63
195	3.23	15.60
200	3.86	13.71
205	4.24	11.93
210	4.49	10.42
215	4.67	9.10
220	4.83	7.76
225	4.91	6.62
230	5.03	5.36
235	5.17	4.19
240	5.24	3.18
245	5.37	2.12
250	5.47	1.00
255	5.62	0.13
260	5.69	0.92
265	5.83	1.93
270	6.01	3.02
275	6.16	4.22
280	6.30	5.64
285	6.41	6.80
290	6.54	8.58
295	6.39	10.83
300	4.47	12.94
305	2.07	11.22
310	1.56	10.44
315	1.35	10.03
320	1.22	9.75
325	1.14	9.55
330	1.08	9.42
335	1.05	9.33
340	1.05	9.29
345	1.06	9.32
350	1.05	9.38
355	1.02	9.50
360	0.97	9.64

Table 9: Flux density B_{mod} (mT) measurements at position $r_6 z_2$, beside the core (coil-2), without top plate and the brush position at T_{b3} , (P – Parallel, PP – Perpendicular)

θ°	P. field	PP. field	θ°	P. field	PP. field
0	0.03	6.32	185	2.00	5.17
5	0.02	6.35	190	2.02	5.60
10	0.01	6.47	195	2.01	6.08
15	0.11	6.75	200	1.95	6.50
20	0.95	7.40	205	1.95	6.88
25	1.51	6.46	210	1.96	7.43
30	1.64	5.87	215	1.94	7.94
35	1.72	5.33	220	1.91	8.55
40	1.76	4.86	225	1.87	9.12
45	1.77	4.47	230	1.86	10.00
50	1.80	4.05	235	1.60	11.10
55	1.81	3.67	240	0.77	12.75
60	1.82	3.30	245	3.19	16.17
65	1.86	2.96	250	6.58	13.35
70	1.88	2.60	255	7.37	9.88
75	1.89	2.20	260	7.54	7.32
80	1.88	1.88	265	7.68	5.44
85	1.92	1.58	270	7.75	3.58
90	1.99	1.21	275	7.79	1.64
95	1.92	0.81	280	7.76	0.04
100	1.92	0.52	285	7.67	2.02
105	1.92	0.23	290	7.67	4.01
110	1.93	0.02	295	7.37	6.23
115	1.95	0.28	300	6.30	10.05
120	1.96	0.65	302	5.68	10.87
125	1.97	0.95	305	1.86	9.93
130	1.95	1.30	310	0.56	8.42
135	1.97	1.60	315	0.33	7.60
140	1.97	1.97	320	0.22	7.12
145	2.09	2.29	325	0.15	6.82
150	1.98	2.59	330	0.12	6.58
155	1.97	2.96	335	0.09	6.41
160	1.99	3.28	340	0.08	6.30
165	2.02	3.65	345	0.08	6.23
170	2.01	4.07	350	0.07	6.23
175	2.01	4.38	355	0.05	6.23
180	1.99	4.82	360	0.03	6.26

Table 10: Flux density B_{mod} (mT) measurements at position $r_2 z_4$, over the core (coil-2), without top plate. For the three brush positions T_{b1} , T_{b2} and T_{b3}

θ°	T_{b1}	T_{b2}	T_{b3}
0	7.89	7.49	4.90
5	8.07	7.55	4.89
10	8.30	7.62	4.90
15	8.59	7.81	4.94
20	8.73	7.89	4.95
25	8.26	7.62	4.81
30	7.26	6.99	4.45
35	6.11	6.27	4.08
40	5.08	5.57	3.77
45	4.16	4.96	3.43
50	3.14	4.30	3.11
55	2.24	3.73	2.82
60	1.23	3.09	2.54
65	0.41	2.59	2.22
70	0.29	2.03	2.03
75	1.25	1.45	1.74
80	2.22	0.92	1.46
85	3.05	0.40	1.22
90	4.01	0.18	0.96
95	5.02	0.60	0.70
100	6.06	1.11	0.47
105	7.09	1.67	0.26
110	8.22	2.20	0.15
115	9.36	2.73	0.25
120	10.57	3.27	0.45
125	11.91	3.81	0.68
130	12.89	4.39	0.93
133	13.22	4.72	1.02
135	12.92	5.01	1.18
140	12.16	5.67	1.41
145	11.21	6.28	1.66
150	10.39	6.91	1.92
155	9.58	7.73	2.21
160	8.93	8.42	2.47
165	8.17	9.16	2.77
170	7.43	9.97	3.01
175	6.81	10.87	3.31

θ°	T_{b1}	T_{b2}	T_{b3}
180	6.19	11.77	3.59
185	5.57	12.75	3.90
190	4.98	13.25	4.23
195	4.37	12.66	4.56
200	3.83	11.60	4.91
205	3.27	10.38	5.29
210	2.72	9.35	5.72
215	2.19	8.08	6.12
220	1.72	7.06	6.57
225	1.22	6.09	7.10
230	0.63	5.07	7.67
235	0.15	4.08	8.21
240	0.28	3.19	8.89
245	0.80	2.33	9.41
250	1.30	1.50	8.95
255	1.83	0.69	7.72
260	2.39	0.08	6.31
265	2.98	0.90	4.65
270	3.51	1.77	3.24
275	4.03	2.76	1.73
280	4.66	3.59	0.22
285	5.31	4.66	1.14
290	5.98	5.67	2.77
295	6.68	6.82	4.21
300	7.36	7.84	5.67
305	7.74	8.32	6.28
310	7.71	8.24	6.23
315	7.63	8.05	5.98
320	7.56	7.86	5.73
325	7.51	7.69	5.51
330	7.44	7.55	5.34
335	7.43	7.46	5.21
340	7.47	7.39	5.11
345	7.52	7.34	5.01
350	7.60	7.34	4.94
355	7.72	7.37	4.89
360	7.87	7.41	4.86

Table 11: Flux density B_{mod} (mT) measurements at position $r_6 z_2$, beside the core (coil-2), without top plate. For the three brush positions T_{b1} , T_{b2} and T_{b3}

θ°	T_{b1}	T_{b2}	T_{b3}
0	9.79	9.70	6.32
5	10.15	9.94	6.35
10	10.73	10.18	6.47
15	11.72	11.21	6.75
18	12.68	11.74	7.12
20	13.32	11.10	7.40
25	10.30	9.63	6.46
30	8.56	8.47	5.87
35	6.74	7.42	5.33
40	5.20	6.51	4.86
45	4.06	5.73	4.47
50	2.83	4.92	4.05
55	1.81	4.22	3.67
60	0.59	3.46	3.30
65	0.36	2.77	2.96
70	1.50	2.12	2.60
75	2.80	1.35	2.20
80	3.98	0.61	1.88
85	5.05	0.01	1.58
90	6.44	0.71	1.21
95	7.32	1.33	0.81
100	8.48	2.02	0.52
105	9.76	2.63	0.23
110	11.19	3.34	0.02
115	12.94	4.04	0.28
120	15.09	4.82	0.65
125	18.10	5.61	0.95
130	20.05	6.25	1.30
135	16.80	6.99	1.60
140	14.75	7.88	1.97
145	13.46	8.65	2.29
150	12.51	9.46	2.59
155	11.39	10.40	2.96
160	10.51	11.33	3.28
165	9.65	12.42	3.65
170	8.78	13.69	4.07
175	8.03	15.09	4.38
180	7.27	17.19	4.82

θ°	T_{b1}	T_{b2}	T_{b3}
185	6.62	20.81	5.17
190	5.95	18.63	5.60
195	5.16	15.60	6.08
200	4.48	13.71	6.50
205	3.80	11.93	6.88
210	3.11	10.42	7.43
215	2.46	9.10	7.94
220	1.76	7.76	8.55
225	1.16	6.62	9.12
230	0.43	5.36	10.00
235	0.12	4.19	11.10
240	0.78	3.18	12.75
245	1.39	2.12	16.17
250	2.16	1.00	13.35
255	2.81	0.13	9.88
260	3.44	0.92	7.32
265	4.06	1.93	5.44
270	4.87	3.02	3.58
275	5.71	4.22	1.64
280	6.46	5.64	0.04
285	7.31	6.80	2.02
290	8.31	8.58	4.01
295	9.45	10.83	6.23
300	11.37	12.94	10.05
302	10.94	12.36	10.87
305	10.55	11.22	9.93
310	9.85	10.44	8.42
315	9.51	10.03	7.60
320	9.33	9.75	7.12
325	9.21	9.55	6.82
330	9.14	9.42	6.58
335	9.12	9.33	6.41
340	9.12	9.29	6.30
345	9.19	9.32	6.23
350	9.33	9.38	6.23
355	9.48	9.50	6.23
360	9.75	9.64	6.26

Table 12: Flux density B_{mod} (mT) measurements at r_1 z positions over the core (coil-1) without top plate

θ°	r_1z_4	r_1z_5	r_1z_6	r_1z_7	r_1z_8	r_1z_9
0	3.06	2.87	2.44	1.09	0.61	0.33
5	3.04	2.85	2.48	1.09	0.63	0.34
10	2.96	2.81	2.47	1.07	0.64	0.34
15	2.88	2.73	2.46	1.05	0.64	0.34
20	2.78	2.65	2.42	1.02	0.63	0.34
25	2.65	2.52	2.36	0.98	0.62	0.34
30	2.51	2.38	2.28	0.93	0.60	0.33
35	2.35	2.23	2.18	0.87	0.58	0.32
40	2.16	2.06	2.06	0.80	0.55	0.30
45	1.97	1.88	1.94	0.73	0.52	0.29
50	1.77	1.68	1.79	0.65	0.48	0.26
55	1.54	1.49	1.64	0.57	0.44	0.24
60	1.19	1.28	1.47	0.48	0.39	0.21
65	0.94	1.05	1.30	0.39	0.34	0.18
70	0.65	0.84	1.13	0.30	0.29	0.15
75	0.27	0.61	0.94	0.21	0.23	0.12
80	0.03	0.45	0.75	0.11	0.18	0.09
85	0.26	0.17	0.56	0.03	0.13	0.06
90	0.47	0.03	0.37	0.01	0.07	0.04
95	0.72	0.17	0.22	0.07	0.05	0.03
100	0.95	0.39	0.16	0.16	0.04	0.02
105	1.25	0.60	0.23	0.25	0.06	0.04
110	1.47	0.82	0.37	0.34	0.11	0.06
115	1.69	1.03	0.55	0.44	0.15	0.09
120	1.92	1.26	0.76	0.52	0.21	0.12
125	2.12	1.47	0.95	0.61	0.26	0.16
130	2.30	1.66	1.13	0.69	0.33	0.20
135	2.49	1.87	1.32	0.77	0.38	0.23
140	2.65	2.06	1.53	0.85	0.43	0.26
145	2.78	2.23	1.69	0.91	0.48	0.29
150	2.91	2.39	1.88	0.97	0.52	0.33
155	3.05	2.54	2.03	1.03	0.57	0.35
160	3.11	2.66	2.16	1.07	0.61	0.38
165	3.17	2.77	2.29	1.11	0.65	0.40
170	3.15	2.84	2.39	1.13	0.68	0.42
175	3.09	2.88	2.46	1.15	0.70	0.43
180	2.96	2.90	2.52	1.16	0.72	0.44
185	2.86	2.89	2.55	1.16	0.73	0.45
190	2.75	2.87	2.56	1.15	0.74	0.46
195	2.64	2.81	2.55	1.13	0.74	0.46
200	2.44	2.73	2.53	1.09	0.74	0.46
205	2.25	2.61	2.45	1.05	0.72	0.45
210	2.07	2.48	2.37	1.00	0.70	0.45
215	1.83	2.31	2.27	0.94	0.68	0.43
220	1.57	2.13	2.15	0.88	0.65	0.41
225	1.35	1.95	2.03	0.81	0.62	0.39
230	1.10	1.74	1.88	0.72	0.58	0.37
235	0.88	1.53	1.72	0.64	0.54	0.34
240	0.68	1.33	1.55	0.55	0.49	0.31
245	0.53	1.10	1.38	0.45	0.44	0.28
250	0.46	0.90	1.18	0.36	0.38	0.25
255	0.49	0.67	0.99	0.26	0.33	0.22
260	0.63	0.44	0.79	0.17	0.27	0.18
265	0.78	0.22	0.58	0.08	0.21	0.14
270	0.98	0.03	0.39	0.01	0.15	0.11
275	1.13	0.12	0.20	0.02	0.10	0.07
280	1.35	0.33	0.07	0.10	0.04	0.04
285	1.52	0.54	0.11	0.20	1E-3	0.01
290	1.72	0.78	0.28	0.29	1E-3	0
295	1.88	1.00	0.49	0.38	0.04	0
300	2.06	1.22	0.69	0.48	0.09	0.01
305	2.22	1.43	0.88	0.56	0.15	0.04
310	2.37	1.64	1.09	0.66	0.21	0.07
315	2.50	1.84	1.27	0.73	0.26	0.11
320	2.63	2.00	1.46	0.80	0.32	0.14
325	2.72	2.17	1.66	0.86	0.37	0.17
330	2.82	2.33	1.81	0.93	0.42	0.20
335	2.89	2.46	1.97	0.98	0.46	0.23
340	2.97	2.61	2.11	1.03	0.50	0.25
345	2.98	2.71	2.23	1.06	0.54	0.28
350	3.02	2.79	2.33	1.09	0.57	0.30
355	3.04	2.85	2.41	1.10	0.59	0.32
360	3.06	2.89	2.46	1.11	0.61	0.33

Table 13: Flux density B_{mod} (mT) measurements at r_2 z positions over the core (coil-1) without top plate

θ°	r_2z_4	r_2z_5	r_2z_6	r_2z_7	r_2z_8	r_2z_9	θ°	r_2z_4	r_2z_5	r_2z_6	r_2z_7	r_2z_8	r_2z_9
0	10.72	8.23	6.12	2.17	1.27	0.76	185	12.58	9.28	6.70	2.36	1.43	0.90
5	10.74	8.24	6.13	2.17	1.28	0.76	190	12.06	9.06	6.57	2.33	1.42	0.90
10	10.81	8.22	6.08	2.15	1.28	0.77	195	11.23	8.62	6.33	2.29	1.40	0.88
15	10.87	8.15	5.99	2.10	1.26	0.76	200	10.33	8.12	6.00	2.21	1.36	0.87
20	10.74	7.93	5.80	2.05	1.23	0.74	205	9.37	7.54	5.65	2.12	1.31	0.85
25	10.16	7.61	5.54	1.97	1.19	0.72	210	8.59	6.92	5.25	2.01	1.26	0.82
30	9.30	7.10	5.18	1.87	1.14	0.70	215	7.79	6.33	4.83	1.89	1.20	0.79
35	8.45	6.48	4.83	1.75	1.06	0.66	220	6.98	5.75	4.44	1.76	1.12	0.75
40	7.58	5.87	4.39	1.61	0.99	0.62	225	6.48	5.20	4.03	1.62	1.04	0.70
45	6.80	5.37	3.96	1.49	0.91	0.57	230	5.65	4.53	3.53	1.45	0.95	0.65
50	5.98	4.67	3.53	1.33	0.82	0.53	235	4.99	4.00	3.15	1.30	0.83	0.59
55	5.25	4.09	3.12	1.18	0.74	0.47	240	4.26	3.37	2.69	1.13	0.74	0.53
60	4.45	3.48	2.65	1.00	0.63	0.46	245	3.55	2.91	2.27	0.94	0.63	0.46
65	3.80	2.93	2.23	0.84	0.52	0.34	250	2.93	2.35	1.87	0.78	0.53	0.39
70	3.07	2.38	1.84	0.66	0.42	0.27	255	2.24	1.80	1.46	0.59	0.41	0.32
75	2.32	1.86	1.40	0.49	0.31	0.20	260	1.56	1.23	1.01	0.41	0.30	0.24
80	1.74	1.29	0.95	0.31	0.20	0.13	265	0.92	0.78	0.57	0.24	0.18	0.17
85	1.04	0.74	0.52	0.14	0.10	0.07	270	0.29	0.25	0.14	0.05	0.07	0.09
90	0.43	0.22	0.13	0.03	0.02	0.02	275	0.17	0.09	0.05	0.03	0.02	0.02
95	0.18	0.16	0.15	0.09	0.01	1E-3	280	0.84	0.58	0.50	0.11	0.01	0.03
100	0.75	0.66	0.52	0.24	0.09	0.02	285	1.50	1.16	0.91	0.27	0.07	0.03
105	1.47	1.19	0.97	0.41	0.19	0.07	290	2.22	1.69	1.37	0.46	0.19	0.02
110	2.18	1.73	1.40	0.59	0.30	0.14	295	2.87	2.27	1.81	0.65	0.30	0.09
115	2.86	2.23	1.81	0.77	0.42	0.20	300	3.59	2.83	2.24	0.83	0.42	0.16
120	3.50	2.81	2.26	0.95	0.52	0.28	305	4.29	3.33	2.66	1.00	0.53	0.23
125	4.20	3.31	2.68	1.12	0.64	0.35	310	5.07	3.93	3.09	1.18	0.64	0.30
130	4.82	3.86	3.05	1.29	0.74	0.42	315	5.84	4.54	3.56	1.33	0.74	0.38
135	5.65	4.47	3.50	1.47	0.84	0.49	320	6.60	5.13	3.95	1.49	0.88	0.44
140	6.49	5.06	3.97	1.62	0.94	0.56	325	7.33	5.71	4.39	1.62	0.93	0.50
145	7.16	5.66	4.40	1.76	1.03	0.62	330	8.26	6.34	4.85	1.76	1.01	0.55
150	7.93	6.24	4.85	1.90	1.11	0.66	335	9.06	6.89	5.19	1.86	1.08	0.60
155	8.74	6.84	5.24	2.03	1.20	0.72	340	9.84	7.36	5.54	1.97	1.15	0.65
160	9.67	7.36	5.61	2.13	1.26	0.77	345	10.50	7.76	5.79	2.04	1.19	0.69
165	10.51	8.08	6.07	2.23	1.33	0.81	350	10.66	8.03	5.98	2.10	1.24	0.72
170	11.58	8.65	6.38	2.29	1.37	0.84	355	10.72	8.16	6.09	2.14	1.27	0.73
175	12.34	9.11	6.60	2.35	1.40	0.86	360	10.74	8.22	6.15	2.16	1.29	0.76
180	12.79	9.34	6.72	2.36	1.42	0.88							

Table 14: Flux density B_{mod} (mT) measurements at r_3 z positions over the core (coil-1) without top plate

θ°	r_3z_4	r_3z_5	r_3z_6	r_3z_7	r_3z_8	r_3z_9	θ°	r_3z_4	r_3z_5	r_3z_6	r_3z_7	r_3z_8	r_3z_9
0	11.89	10.03	7.37	2.64	1.58	0.97	185	15.38	11.97	8.37	2.84	1.76	1.12
5	11.93	10.03	7.38	2.63	1.58	0.97	190	14.05	11.52	8.22	2.80	1.75	1.11
10	12.05	10.03	7.36	2.59	1.57	0.97	195	12.72	10.74	7.90	2.73	1.72	1.10
15	12.26	10.03	7.28	2.53	1.55	0.95	200	11.54	9.92	7.46	2.63	1.67	1.06
20	12.16	9.86	7.11	2.45	1.51	0.93	205	10.53	9.17	6.99	2.51	1.61	1.03
25	11.10	9.36	6.79	2.34	1.46	0.89	210	9.50	8.31	6.47	2.36	1.55	0.99
30	9.98	8.65	6.39	2.21	1.39	0.84	215	8.58	7.60	5.92	2.19	1.46	0.94
35	8.82	7.89	5.89	2.05	1.31	0.79	220	7.66	6.82	5.37	2.02	1.36	0.88
40	7.89	6.99	5.34	1.89	1.21	0.74	225	6.92	6.22	4.87	1.84	1.25	0.81
45	7.13	6.27	4.81	1.72	1.12	0.67	230	5.94	5.39	4.34	1.63	1.13	0.73
50	6.14	5.56	4.28	1.52	1.00	0.60	235	5.23	4.71	3.79	1.45	1.02	0.66
55	5.31	4.95	3.78	1.35	0.89	0.53	240	4.41	4.04	3.26	1.25	0.88	0.57
60	4.43	4.12	3.25	1.14	0.77	0.45	245	3.62	3.43	2.76	1.04	0.77	0.49
65	3.66	3.49	2.74	0.94	0.65	0.36	250	2.92	2.82	2.27	0.83	0.64	0.41
70	2.91	2.87	2.25	0.75	0.52	0.29	255	2.20	2.18	1.82	0.62	0.51	0.32
75	2.13	2.18	1.79	0.54	0.40	0.20	260	1.49	1.59	1.36	0.41	0.36	0.23
80	1.42	1.56	1.27	0.34	0.27	0.13	265	0.68	0.94	0.81	0.23	0.22	0.14
85	0.70	0.92	0.78	0.14	0.15	0.05	270	0.06	0.35	0.32	0.03	0.10	0.06
90	0.08	0.33	0.31	0.03	0.04	0.02	275	0.45	0.13	0.01	0.07	0.01	0.00
95	0.54	0.21	0.11	0.17	0.05	0.05	280	1.19	0.82	0.49	0.27	0.06	0.02
100	1.20	0.81	0.51	0.36	0.15	0.12	285	1.96	1.43	0.96	0.47	0.17	0.08
105	1.94	1.45	1.01	0.57	0.28	0.20	290	2.77	2.09	1.48	0.69	0.32	0.16
110	2.69	2.06	1.50	0.77	0.41	0.29	295	3.58	2.75	2.01	0.89	0.44	0.25
115	3.42	2.67	1.97	0.97	0.54	0.38	300	4.22	3.34	2.48	1.10	0.57	0.34
120	4.25	3.30	2.48	1.18	0.68	0.46	305	5.01	4.02	2.95	1.31	0.69	0.42
125	5.04	3.96	2.95	1.38	0.80	0.55	310	5.86	4.67	3.45	1.51	0.83	0.50
130	5.74	4.60	3.47	1.59	0.92	0.62	315	6.79	5.39	4.02	1.69	0.95	0.57
135	6.60	5.29	3.97	1.77	1.04	0.70	320	7.56	6.06	4.57	1.85	1.05	0.65
140	7.50	6.00	4.49	1.98	1.17	0.77	325	8.53	6.77	5.06	2.01	1.16	0.71
145	8.33	6.75	5.00	2.15	1.28	0.84	330	9.59	7.60	5.61	2.16	1.27	0.77
150	9.21	7.43	5.56	2.30	1.38	0.90	335	10.60	8.35	6.08	2.30	1.34	0.82
155	10.25	8.20	6.10	2.46	1.48	0.96	340	11.80	9.13	6.57	2.42	1.42	0.87
160	11.22	9.00	6.61	2.58	1.56	1.01	345	12.47	9.68	6.92	2.50	1.47	0.90
165	12.32	9.78	7.12	2.70	1.63	1.05	350	12.28	9.94	7.18	2.57	1.52	0.94
170	13.61	10.74	7.63	2.78	1.69	1.08	355	12.05	9.96	7.34	2.61	1.56	0.95
175	14.74	11.40	8.05	2.84	1.73	1.10	360	11.97	9.91	7.39	2.63	1.58	0.97
180	15.74	11.83	8.30	2.86	1.76	1.12							

Table 15: Flux density B_{mod} (mT) at r_4 z positions over the core (coil-1) without top plate

θ°	r_{4Z4}	r_{4Z5}	r_{4Z6}	r_{4Z7}	r_{4Z8}	r_{4Z9}	θ°	r_{4Z4}	r_{4Z5}	r_{4Z6}	r_{4Z7}	r_{4Z8}	r_{4Z9}
0	10.23	7.83	5.91	2.30	1.44	0.89	185	12.57	9.16	6.65	2.51	1.64	1.04
5	10.22	7.82	5.92	2.30	1.45	0.90	190	11.64	8.82	6.53	2.48	1.60	1.04
10	10.27	7.78	5.86	2.27	1.43	0.90	195	10.71	8.33	6.27	2.42	1.57	1.03
15	10.28	7.66	5.77	2.22	1.40	0.88	200	9.76	7.70	5.93	2.34	1.53	1.01
20	9.94	7.44	5.61	2.16	1.37	0.86	205	8.90	7.14	5.53	2.24	1.46	0.97
25	9.14	7.06	5.36	2.08	1.31	0.83	210	8.07	6.57	5.13	2.12	1.39	0.94
30	8.36	6.57	5.03	1.98	1.25	0.80	215	7.31	5.93	4.70	1.99	1.31	0.89
35	7.37	5.95	4.60	1.83	1.17	0.76	220	6.55	5.38	4.28	1.85	1.22	0.84
40	6.53	5.33	4.21	1.71	1.09	0.70	225	5.90	4.86	3.82	1.69	1.13	0.78
45	5.88	4.79	3.79	1.56	0.99	0.65	230	5.11	4.24	3.44	1.52	1.01	0.71
50	5.12	4.25	3.36	1.40	0.90	0.58	235	4.46	3.77	2.99	1.35	0.90	0.64
55	4.43	3.73	2.99	1.25	0.79	0.52	240	3.80	3.20	2.59	1.17	0.80	0.57
60	3.76	3.15	2.56	1.07	0.68	0.45	245	3.14	2.65	2.18	1.00	0.68	0.50
65	3.08	2.62	2.14	0.90	0.56	0.38	250	2.46	2.14	1.79	0.82	0.56	0.41
70	2.41	2.07	1.78	0.72	0.45	0.30	255	1.86	1.67	1.40	0.63	0.44	0.34
75	1.79	1.61	1.34	0.54	0.33	0.22	260	1.18	1.15	0.97	0.45	0.31	0.25
80	1.20	1.08	0.94	0.37	0.21	0.15	265	0.58	0.60	0.58	0.27	0.19	0.18
85	0.54	0.58	0.53	0.19	0.12	0.07	270	0.04	0.18	0.19	0.10	0.08	0.10
90	0.15	0.18	0.19	0.06	0.05	0.03	275	0.58	0.26	0.07	0.03	0.02	0.03
95	0.69	0.35	0.17	0.10	0.10	0.03	280	1.23	0.77	0.46	0.16	0.09	0
100	1.29	0.82	0.52	0.26	0.20	0.08	285	1.84	1.28	0.87	0.34	0.20	0.04
105	1.98	1.34	0.92	0.43	0.32	0.15	290	2.53	1.79	1.30	0.52	0.31	0.11
110	2.54	1.87	1.31	0.62	0.42	0.23	295	3.21	2.33	1.69	0.72	0.43	0.19
115	3.17	2.36	1.72	0.79	0.55	0.31	300	3.92	2.89	2.14	0.90	0.55	0.35
120	3.84	2.88	2.13	0.97	0.67	0.39	305	4.57	3.43	2.53	1.06	0.67	0.35
125	4.51	3.36	2.57	1.16	0.78	0.46	310	5.26	3.94	2.92	1.24	0.78	0.42
130	5.19	3.88	2.95	1.34	0.89	0.54	315	6.01	4.52	3.35	1.41	0.89	0.50
135	5.95	4.44	3.32	1.51	1.00	0.61	320	6.73	5.11	3.74	1.57	0.99	0.56
140	6.73	5.01	3.80	1.69	1.12	0.69	325	7.54	5.65	4.17	1.71	1.08	0.62
145	7.43	5.61	4.18	1.84	1.22	0.75	330	8.47	6.23	4.59	1.86	1.17	0.68
150	8.17	6.18	4.65	1.99	1.30	0.81	335	9.20	6.75	4.94	1.97	1.25	0.73
155	9.04	6.80	5.11	2.13	1.39	0.86	340	10.03	7.26	5.30	2.09	1.32	0.78
160	9.94	7.39	5.50	2.24	1.46	0.91	345	10.39	7.62	5.55	2.17	1.37	0.82
165	10.87	7.97	5.90	2.35	1.52	0.95	350	10.39	7.80	5.73	2.24	1.42	0.84
170	11.89	8.53	6.21	2.42	1.56	0.98	355	10.28	7.85	5.85	2.28	1.44	0.87
175	12.64	8.92	6.48	2.48	1.60	1.01	360	10.24	7.86	5.90	2.30	1.46	0.89
180	12.91	9.18	6.64	2.51	1.61	1.03							

Table 16: Flux density B_{mod} (mT) measurements at r_5 z positions over the core (coil-1) without top plate

θ°	r_5Z_4	r_5Z_5	r_5Z_6	r_5Z_7	r_5Z_8	r_5Z_9
0	9.04	7.13	5.54	2.28	1.44	0.90
5	9.04	7.13	5.54	2.28	1.44	0.91
10	9.06	7.10	5.50	2.25	1.43	0.90
15	9.02	7.03	5.42	2.21	1.40	0.89
20	8.70	6.84	5.26	2.13	1.37	0.87
25	8.05	6.51	5.03	2.05	1.32	0.84
30	7.29	6.03	4.73	1.94	1.25	0.82
35	6.49	5.52	4.39	1.80	1.18	0.77
40	5.83	5.00	4.00	1.66	1.10	0.72
45	5.22	4.49	3.63	1.51	1.00	0.66
50	4.60	3.97	3.26	1.35	0.90	0.60
55	4.01	3.53	2.88	1.19	0.81	0.53
60	3.35	2.97	2.46	1.01	0.69	0.46
65	2.79	2.54	2.09	0.85	0.58	0.39
70	2.18	2.03	1.74	0.68	0.47	0.31
75	1.64	1.61	1.36	0.51	0.34	0.23
80	1.03	1.14	0.96	0.34	0.23	0.15
85	0.53	0.66	0.56	0.18	0.13	0.08
90	0.25	0.25	0.24	0.07	0.06	0.03
95	0.64	0.23	0.16	0.14	0.09	0.03
100	1.15	0.63	0.47	0.29	0.17	0.08
105	1.76	1.10	0.81	0.46	0.29	0.15
110	2.31	1.58	1.19	0.64	0.40	0.23
115	2.87	2.04	1.57	0.82	0.52	0.31
120	3.48	2.53	1.97	1.01	0.64	0.38
125	4.07	2.99	2.34	1.19	0.75	0.47
130	4.68	3.44	2.74	1.35	0.86	0.54
135	5.36	3.94	3.06	1.52	0.97	0.61
140	6.01	4.49	3.52	1.69	1.09	0.68
145	6.69	5.00	3.91	1.85	1.18	0.75
150	7.40	5.55	4.32	2.00	1.28	0.81
155	8.11	6.09	4.71	2.14	1.36	0.87
160	8.92	6.66	5.10	2.25	1.44	0.92
165	9.71	7.24	5.51	2.36	1.50	0.97
170	10.43	7.72	5.84	2.44	1.55	1.00
175	10.93	8.16	6.11	2.49	1.59	1.02
180	11.44	8.40	6.26	2.51	1.61	1.04
185	11.08	8.41	6.29	2.51	1.61	1.05
190	10.30	8.14	6.17	2.47	1.60	1.04
195	9.56	7.68	5.95	2.41	1.57	1.03
200	8.77	7.20	5.61	2.33	1.52	1.01
205	7.98	6.65	5.25	2.21	1.47	0.98
210	7.25	6.13	4.89	2.08	1.40	0.94
215	6.57	5.56	4.52	1.96	1.31	0.90
220	5.95	5.03	4.10	1.81	1.23	0.84
225	5.34	4.54	3.70	1.67	1.14	0.78
230	4.67	3.99	3.29	1.49	1.02	0.71
235	4.04	3.49	2.89	1.32	0.93	0.64
240	3.39	2.97	2.47	1.14	0.81	0.57
245	2.82	2.49	2.10	0.97	0.69	0.50
250	2.31	2.02	1.77	0.79	0.58	0.42
255	1.72	1.60	1.37	0.61	0.45	0.34
260	1.10	1.13	1.00	0.43	0.33	0.25
265	0.54	0.72	0.60	0.25	0.21	0.18
270	0.07	0.28	0.27	0.08	0.11	0.10
275	0.44	0.11	0.06	0.04	0.03	0.03
280	1.02	0.56	0.37	0.20	0.06	0
285	1.59	1.01	0.77	0.36	0.17	0.04
290	2.28	1.50	1.15	0.54	0.29	0.11
295	2.81	1.99	1.52	0.72	0.41	0.19
300	3.44	2.48	1.94	0.91	0.53	0.27
305	4.02	2.96	2.31	1.08	0.64	0.34
310	4.64	3.47	2.78	1.25	0.75	0.42
315	5.37	3.99	3.06	1.42	0.86	0.50
320	6.04	4.49	3.49	1.56	0.96	0.57
325	6.74	5.03	3.87	1.72	1.05	0.62
330	7.47	5.55	4.28	1.86	1.14	0.68
335	8.16	6.06	4.65	1.97	1.22	0.73
340	8.84	6.56	4.94	2.08	1.29	0.78
345	9.19	6.85	5.16	2.16	1.34	0.82
350	9.17	7.03	5.35	2.22	1.39	0.84
355	9.12	7.12	5.46	2.26	1.42	0.87
360	9.06	7.14	5.51	2.28	1.43	0.89

Table 17: Flux density B_{mod} (mT) measurements at r_7 z positions over the core (coil-1) without top plate

θ°	r_7z_4	r_7z_5	r_7z_6	r_7z_7	r_7z_8	r_7z_9
0	6.78	5.79	4.76	2.07	1.35	0.90
5	6.75	5.76	4.77	2.07	1.35	0.91
10	6.71	5.72	4.73	2.04	1.34	0.90
15	6.60	5.61	4.65	1.99	1.31	0.89
20	6.32	5.43	4.52	1.92	1.27	0.86
25	5.88	5.15	4.32	1.84	1.22	0.83
30	5.38	4.82	4.06	1.73	1.16	0.80
35	4.87	4.36	3.76	1.60	1.09	0.74
40	4.39	3.96	3.43	1.46	1.00	0.69
45	3.90	3.51	3.12	1.33	0.91	0.63
50	3.45	3.09	2.77	1.17	0.81	0.56
55	2.99	2.70	2.46	1.03	0.72	0.50
60	2.48	2.29	2.10	0.87	0.61	0.43
65	2.03	1.94	1.81	0.72	0.51	0.35
70	1.61	1.55	1.47	0.55	0.39	0.27
75	1.16	1.17	1.15	0.39	0.28	0.20
80	0.73	0.77	0.80	0.24	0.16	0.13
85	0.33	0.41	0.48	0.09	0.06	0.06
90	0.18	0.13	0.20	0.03	0.02	0.02
95	0.56	0.27	0.14	0.12	0.07	0.04
100	0.98	0.63	0.38	0.29	0.17	0.11
105	1.42	1.00	0.69	0.47	0.28	0.18
110	1.85	1.38	1.03	0.63	0.39	0.26
115	2.28	1.81	1.37	0.80	0.51	0.33
120	2.75	2.21	1.70	0.95	0.61	0.41
125	3.18	2.61	2.02	1.12	0.73	0.48
130	3.65	2.99	2.33	1.27	0.83	0.55
135	4.11	3.37	2.68	1.43	0.94	0.63
140	4.66	3.81	3.01	1.60	1.04	0.70
145	5.14	4.19	3.35	1.74	1.14	0.77
150	5.63	4.62	3.70	1.87	1.23	0.83
155	6.18	5.09	4.05	1.99	1.30	0.88
160	6.72	5.53	4.41	2.10	1.38	0.93
165	7.24	5.98	4.70	2.19	1.43	0.97
170	7.76	6.37	4.99	2.25	1.48	1.00
175	8.08	6.65	5.21	2.29	1.51	1.03
180	8.24	6.81	5.34	2.31	1.53	1.04

θ°	r_7z_4	r_7z_5	r_7z_6	r_7z_7	r_7z_8	r_7z_9
185	8.03	6.78	5.38	2.30	1.52	1.04
190	7.62	6.56	5.28	2.25	1.51	1.04
195	7.08	6.23	5.11	2.19	1.48	1.02
200	6.54	5.84	4.87	2.11	1.44	0.99
205	5.96	5.36	4.55	2.00	1.38	0.95
210	5.46	4.98	4.20	1.87	1.30	0.91
215	4.99	4.55	3.87	1.74	1.23	0.86
220	4.46	4.08	3.51	1.60	1.13	0.81
225	3.97	3.65	3.17	1.45	1.05	0.75
230	3.46	3.22	2.81	1.29	0.93	0.68
235	3.02	2.81	2.48	1.13	0.83	0.60
240	2.53	2.39	2.16	0.97	0.72	0.53
245	2.12	2.01	1.85	0.81	0.60	0.45
250	1.66	1.66	1.56	0.64	0.49	0.38
255	1.20	1.28	1.18	0.49	0.38	0.30
260	0.74	0.86	0.86	0.32	0.26	0.22
265	0.34	0.48	0.52	0.15	0.15	0.14
270	0.05	0.13	0.21	0.01	0.05	0.07
275	0.36	0.12	0.02	0.03	0.01	0.01
280	0.82	0.53	0.31	0.20	0.06	0.01
285	1.26	0.88	0.62	0.35	0.16	0.06
290	1.73	1.28	0.99	0.51	0.28	0.14
295	2.17	1.67	1.31	0.68	0.39	0.21
300	2.65	2.10	1.65	0.84	0.51	0.29
305	3.05	2.46	1.99	1.00	0.62	0.37
310	3.59	2.87	2.31	1.17	0.72	0.44
315	4.05	3.25	2.66	1.32	0.83	0.51
320	4.54	3.67	2.96	1.46	0.92	0.58
325	5.07	4.09	3.29	1.60	1.01	0.64
330	5.60	4.55	3.61	1.72	1.09	0.69
335	6.08	4.94	3.91	1.84	1.16	0.75
340	6.51	5.30	4.20	1.93	1.23	0.80
345	6.71	5.53	4.40	1.99	1.27	0.83
350	6.75	5.63	4.56	2.04	1.31	0.86
355	6.77	5.70	4.65	2.07	1.34	0.88
360	6.78	5.79	4.76	2.08	1.36	0.90

Table 18: flux density B_{mod} (mT) measurements at $r z_4$ positions over the core (coil-1) without top plate

θ°	r_1z_4	r_2z_4	r_3z_4	r_4z_4	r_5z_4	r_7z_4
0	3.06	10.72	11.89	10.23	9.04	6.78
5	3.04	10.74	11.93	10.22	9.04	6.75
10	2.96	10.81	12.05	10.27	9.06	6.71
15	2.88	10.87	12.26	10.28	9.02	6.60
20	2.78	10.74	12.16	9.94	8.70	6.32
25	2.65	10.16	11.10	9.14	8.05	5.88
30	2.51	9.30	9.98	8.36	7.29	5.38
35	2.35	8.45	8.82	7.37	6.49	4.87
40	2.16	7.58	7.89	6.53	5.83	4.39
45	1.97	6.80	7.13	5.88	5.22	3.90
50	1.77	5.98	6.14	5.12	4.60	3.45
55	1.54	5.25	5.31	4.43	4.01	2.99
60	1.19	4.45	4.43	3.76	3.35	2.48
65	0.94	3.80	3.66	3.08	2.79	2.03
70	0.65	3.07	2.91	2.41	2.18	1.61
75	0.27	2.32	2.13	1.79	1.64	1.16
80	0.03	1.74	1.42	1.20	1.03	0.73
85	0.26	1.04	0.70	0.54	0.53	0.33
90	0.47	0.43	0.08	0.15	0.25	0.18
95	0.72	0.18	0.54	0.69	0.64	0.56
100	0.95	0.75	1.20	1.29	1.15	0.98
105	1.25	1.47	1.94	1.98	1.76	1.42
110	1.47	2.18	2.69	2.54	2.31	1.85
115	1.69	2.86	3.42	3.17	2.87	2.28
120	1.92	3.50	4.25	3.84	3.48	2.75
125	2.12	4.20	5.04	4.51	4.07	3.18
130	2.30	4.82	5.74	5.19	4.68	3.65
135	2.49	5.65	6.60	5.95	5.36	4.11
140	2.65	6.49	7.50	6.73	6.01	4.66
145	2.78	7.16	8.33	7.43	6.69	5.14
150	2.91	7.93	9.21	8.17	7.40	5.63
155	3.05	8.74	10.25	9.04	8.11	6.18
160	3.11	9.67	11.22	9.94	8.92	6.72
165	3.17	10.51	12.32	10.87	9.71	7.32
170	3.15	11.58	13.61	11.39	10.06	7.83
175	3.09	12.55	14.74	12.34	10.93	8.02
180	2.96	12.69	15.74	12.91	11.44	8.24

θ°	r_1z_4	r_2z_4	r_3z_4	r_4z_4	r_5z_4	r_7z_4
185	2.86	12.79	15.38	12.57	11.08	8.03
190	2.75	12.06	14.05	11.64	10.30	7.62
195	2.64	11.23	12.72	10.71	9.56	7.08
200	2.44	10.33	11.54	9.76	8.77	6.54
205	2.25	9.37	10.53	8.90	7.98	5.96
210	2.07	8.59	9.50	8.07	7.25	5.46
215	1.83	7.79	8.58	7.31	6.57	4.99
220	1.57	6.98	7.66	6.55	5.95	4.46
225	1.35	6.48	6.92	5.90	5.34	3.97
230	1.10	5.65	5.94	5.11	4.67	3.46
235	0.88	4.99	5.23	4.46	4.04	3.02
240	0.68	4.26	4.41	3.80	3.39	2.53
245	0.53	3.55	3.62	3.14	2.82	2.12
250	0.46	2.93	2.92	2.46	2.31	1.66
255	0.49	2.24	2.20	1.86	1.72	1.20
260	0.63	1.56	1.49	1.18	1.10	0.74
265	0.78	0.92	0.68	0.58	0.54	0.34
270	0.98	0.29	0.06	0.04	0.07	0.05
275	1.13	0.17	0.45	0.58	0.44	0.36
280	1.35	0.84	1.19	1.23	1.02	0.82
285	1.52	1.50	1.96	1.84	1.59	1.26
290	1.72	2.22	2.77	2.53	2.28	1.73
295	1.88	2.87	3.58	3.21	2.81	2.17
300	2.06	3.59	4.22	3.92	3.44	2.65
305	2.22	4.29	5.01	4.57	4.02	3.05
310	2.37	5.07	5.86	5.26	4.64	3.59
315	2.50	5.84	6.79	6.01	5.37	4.05
320	2.63	6.60	7.56	6.73	6.04	4.54
325	2.72	7.33	8.53	7.54	6.74	5.07
330	2.82	8.26	9.59	8.47	7.47	5.60
335	2.89	9.06	10.60	9.20	8.16	6.08
340	2.97	9.84	11.80	10.03	8.84	6.51
345	2.98	10.50	12.47	10.39	9.19	6.71
350	3.02	10.66	12.28	10.39	9.17	6.76
355	3.04	10.72	12.05	10.28	9.12	6.75
360	3.06	10.74	11.97	10.24	9.06	6.71

Table 19: Flux density B_{mod} (mT) measurements at r_1 z positions over the core (coil-1) with top plate

θ°	r_1z_6	r_1z_7	r_1z_8	r_1z_9
0	2.69	1.24	0.75	0.45
5	2.68	1.25	0.75	0.45
10	2.64	1.24	0.74	0.45
15	2.56	1.23	0.74	0.45
20	2.48	1.21	0.72	0.44
25	2.37	1.18	0.70	0.42
30	2.23	1.13	0.67	0.41
35	2.07	1.08	0.64	0.39
40	1.92	1.01	0.60	0.36
45	1.76	0.94	0.56	0.34
50	1.56	0.88	0.51	0.30
55	1.37	0.80	0.45	0.28
60	1.17	0.71	0.40	0.24
65	0.99	0.62	0.35	0.20
70	0.78	0.51	0.29	0.16
75	0.58	0.42	0.23	0.12
80	0.37	0.32	0.16	0.09
85	0.17	0.21	0.09	0.06
90	0.02	0.11	0.03	0.03
95	0.15	0.03	0.00	0.02
100	0.35	1E-3	0.02	0.02
105	0.57	0.09	0.06	0.02
110	0.75	0.20	0.12	0.06
115	0.95	0.29	0.18	0.10
120	1.15	0.40	0.25	0.14
125	1.36	0.50	0.31	0.17
130	1.53	0.59	0.36	0.21
135	1.73	0.67	0.43	0.24
140	1.90	0.77	0.48	0.28
145	2.04	0.85	0.53	0.31
150	2.18	0.92	0.58	0.33
155	2.31	0.99	0.63	0.36
160	2.41	1.05	0.66	0.39
165	2.50	1.10	0.69	0.41
170	2.56	1.14	0.71	0.42
175	2.60	1.17	0.73	0.43
180	2.60	1.19	0.74	0.45

θ°	r_1z_6	r_1z_7	r_1z_8	r_1z_9
185	2.59	1.20	0.75	0.45
190	2.56	1.21	0.74	0.45
195	2.49	1.20	0.74	0.45
200	2.41	1.17	0.72	0.44
205	2.31	1.14	0.70	0.43
210	2.18	1.09	0.67	0.41
215	2.05	1.04	0.64	0.39
220	1.88	0.98	0.60	0.36
225	1.71	0.91	0.56	0.33
230	1.50	0.84	0.51	0.30
235	1.32	0.76	0.46	0.27
240	1.14	0.66	0.40	0.24
245	0.94	0.58	0.34	0.20
250	0.72	0.49	0.28	0.17
255	0.53	0.38	0.22	0.13
260	0.33	0.27	0.15	0.08
265	0.13	0.19	0.09	0.05
270	0.06	0.09	0.03	0.02
275	0.21	0.01	0	0
280	0.41	0.03	0.01	0.00
285	0.63	0.11	0.07	0.02
290	0.83	0.21	0.12	0.06
295	1.04	0.31	0.19	0.09
300	1.24	0.42	0.25	0.13
305	1.42	0.53	0.32	0.17
310	1.62	0.62	0.38	0.21
315	1.80	0.71	0.44	0.25
320	1.95	0.79	0.49	0.28
325	2.10	0.88	0.54	0.32
330	2.25	0.95	0.58	0.34
335	2.38	1.02	0.62	0.37
340	2.48	1.09	0.66	0.39
345	2.56	1.14	0.69	0.41
350	2.62	1.17	0.71	0.43
355	2.68	1.20	0.73	0.44
360	2.69	1.23	0.74	0.45

Table 20: Flux density B_{mod} (mT) measurements at r_2 z positions over the core (coil-1) with top plate

θ°	r_2z_6	r_2z_7	r_2z_8	r_2z_9
0	6.45	2.51	1.46	0.94
5	6.41	2.52	1.46	0.93
10	6.33	2.50	1.46	0.93
15	6.19	2.46	1.42	0.91
20	6.02	2.40	1.39	0.88
25	5.72	2.32	1.34	0.85
30	5.39	2.24	1.28	0.81
35	5.03	2.10	1.20	0.77
40	4.54	1.96	1.11	0.71
45	4.07	1.83	1.03	0.66
50	3.65	1.65	0.93	0.59
55	3.23	1.49	0.83	0.53
60	2.77	1.32	0.73	0.46
65	2.31	1.14	0.61	0.38
70	1.93	0.91	0.50	0.32
75	1.47	0.73	0.36	0.23
80	1.06	0.52	0.25	0.14
85	0.64	0.33	0.14	0.07
90	0.14	0.14	0.02	0.01
95	0.19	0.00	0.01	0.01
100	0.65	0.11	0.11	0.06
105	1.07	0.30	0.21	0.13
110	1.49	0.54	0.33	0.20
115	1.94	0.70	0.47	0.28
120	2.38	0.91	0.59	0.36
125	2.80	1.10	0.70	0.44
130	3.21	1.29	0.81	0.51
135	3.69	1.47	0.92	0.57
140	4.15	1.66	1.03	0.65
145	4.55	1.83	1.11	0.71
150	5.01	1.99	1.21	0.77
155	5.45	2.14	1.29	0.82
160	5.88	2.27	1.36	0.86
165	6.26	2.38	1.40	0.90
170	6.60	2.48	1.45	0.92
175	6.85	2.54	1.48	0.94
180	6.99	2.58	1.50	0.95

θ°	r_2z_6	r_2z_7	r_2z_8	r_2z_9
185	6.96	2.59	1.50	0.94
190	6.81	2.58	1.49	0.93
195	6.54	2.53	1.46	0.91
200	6.28	2.47	1.42	0.89
205	5.81	2.38	1.37	0.86
210	5.38	2.26	1.30	0.81
215	4.93	2.13	1.21	0.77
220	4.48	1.96	1.13	0.70
225	4.02	1.83	1.05	0.66
230	3.55	1.65	0.94	0.59
235	3.06	1.47	0.83	0.52
240	2.65	1.29	0.73	0.45
245	2.17	1.08	0.61	0.38
250	1.76	0.90	0.49	0.30
255	1.34	0.70	0.38	0.22
260	0.86	0.48	0.25	0.14
265	0.38	0.28	0.12	0.06
270	0.00	0.08	0.02	0.01
275	0.33	0.01	0.02	0.01
280	0.77	0.17	0.11	0.07
285	1.18	0.34	0.22	0.14
290	1.64	0.56	0.35	0.22
295	2.07	0.75	0.47	0.30
300	2.51	0.94	0.57	0.38
305	2.96	1.14	0.70	0.45
310	3.41	1.34	0.82	0.53
315	3.88	1.52	0.92	0.60
320	4.30	1.67	1.02	0.65
325	4.73	1.84	1.11	0.71
330	5.11	1.98	1.18	0.77
335	5.46	2.11	1.27	0.81
340	5.81	2.24	1.32	0.85
345	6.08	2.34	1.37	0.88
350	6.28	2.41	1.41	0.90
355	6.36	2.47	1.45	0.92
360	6.44	2.49	1.46	0.92

Table 21: Flux density B_{mod} (mT) measurements at r_3 z positions over the core (coil-1) with top plate

θ°	r_3z_6	r_3z_7	r_3z_8	r_3z_9
0	6.82	2.62	1.59	1.05
5	6.81	2.63	1.59	1.06
10	6.79	2.62	1.58	1.06
15	6.74	2.58	1.54	1.04
20	6.46	2.52	1.51	1.02
25	6.16	2.45	1.45	0.99
30	5.81	2.34	1.39	0.96
35	5.36	2.22	1.31	0.91
40	4.88	2.07	1.20	0.85
45	4.37	1.91	1.11	0.79
50	3.89	1.75	1.00	0.72
55	3.47	1.58	0.90	0.65
60	2.96	1.38	0.79	0.58
65	2.54	1.20	0.67	0.50
70	2.05	0.95	0.55	0.41
75	1.63	0.77	0.42	0.32
80	1.13	0.58	0.26	0.23
85	0.66	0.37	0.14	0.15
90	0.23	0.21	0.03	0.06
95	0.14	0.03	0.01	0.01
100	0.53	0.11	0.10	0.02
105	0.94	0.29	0.21	0.08
110	1.36	0.47	0.34	0.17
115	1.85	0.70	0.47	0.25
120	2.33	0.91	0.60	0.35
125	2.92	1.12	0.73	0.43
130	3.30	1.30	0.84	0.51
135	3.79	1.49	0.96	0.59
140	4.28	1.71	1.10	0.67
145	4.77	1.86	1.20	0.74
150	5.21	2.05	1.30	0.80
155	5.70	2.22	1.38	0.87
160	6.19	2.38	1.46	0.93
165	6.66	2.50	1.53	0.97
170	7.08	2.60	1.60	1.01
175	7.43	2.68	1.63	1.04
180	7.66	2.73	1.65	1.05

θ°	r_3z_6	r_3z_7	r_3z_8	r_3z_9
185	7.67	2.75	1.66	1.06
190	7.47	2.74	1.64	1.06
195	7.19	2.69	1.61	1.04
200	6.79	2.62	1.56	1.02
205	6.30	2.52	1.50	0.98
210	5.79	2.39	1.44	0.95
215	5.31	2.27	1.35	0.90
220	4.79	2.10	1.24	0.84
225	4.30	1.93	1.15	0.78
230	3.79	1.73	1.03	0.71
235	3.30	1.55	0.91	0.64
240	2.81	1.37	0.79	0.56
245	2.40	1.17	0.67	0.49
250	1.94	0.97	0.54	0.41
255	1.51	0.73	0.41	0.32
260	1.01	0.54	0.27	0.23
265	0.55	0.33	0.15	0.14
270	0.12	0.14	0.04	0.06
275	0.16	0.00	0.03	1E-3
280	0.66	0.12	0.13	0.02
285	1.14	0.32	0.25	0.10
290	1.57	0.52	0.37	0.28
295	2.04	0.74	0.50	0.27
300	2.56	0.97	0.63	0.35
305	2.95	1.14	0.75	0.45
310	3.42	1.35	0.88	0.53
315	3.97	1.56	1.01	0.61
320	4.45	1.70	1.10	0.68
325	4.91	1.88	1.20	0.75
330	5.39	2.05	1.30	0.82
335	5.80	2.19	1.38	0.88
340	6.23	2.31	1.46	0.92
345	6.48	2.43	1.50	0.96
350	6.68	2.51	1.55	1.00
355	6.78	2.58	1.58	1.03
360	6.84	2.62	1.59	1.04

Table 22: Flux density B_{mod} (mT) measurements at r_4 z positions over the core (coil-1) with top plate

θ°	r_4z_6	r_4z_7	r_4z_8	r_4z_9
0	6.58	2.42	1.58	1.01
5	6.57	2.42	1.58	1.01
10	6.52	2.39	1.57	1.00
15	6.38	2.35	1.54	0.98
20	6.19	2.29	1.50	0.95
25	5.89	2.20	1.46	0.92
30	5.53	2.09	1.40	0.88
35	5.11	1.97	1.32	0.82
40	4.64	1.81	1.23	0.77
45	4.18	1.67	1.14	0.70
50	3.69	1.50	1.04	0.64
55	3.23	1.36	0.93	0.57
60	2.77	1.15	0.82	0.50
65	2.33	0.99	0.70	0.42
70	1.93	0.79	0.60	0.33
75	1.46	0.57	0.46	0.25
80	1.05	0.41	0.32	0.16
85	0.55	0.23	0.20	0.08
90	0.08	0.05	0.08	0.03
95	0.24	0.03	0.02	0.02
100	0.66	0.17	0.07	0.07
105	1.07	0.39	0.18	0.15
110	1.52	0.58	0.29	0.23
115	1.91	0.75	0.43	0.32
120	2.42	0.93	0.54	0.40
125	2.85	1.14	0.70	0.48
130	3.33	1.31	0.81	0.56
135	3.80	1.49	0.94	0.63
140	4.27	1.66	1.05	0.72
145	4.71	1.81	1.15	0.78
150	5.14	1.98	1.25	0.84
155	5.67	2.13	1.35	0.90
160	6.13	2.26	1.43	0.94
165	6.53	2.36	1.50	0.98
170	6.99	2.46	1.56	1.01
175	7.30	2.51	1.61	1.04
180	7.49	2.55	1.63	1.05

θ°	r_4z_6	r_4z_7	r_4z_8	r_4z_9
185	7.49	2.55	1.64	1.05
190	7.29	2.52	1.63	1.04
195	6.98	2.46	1.60	1.01
200	6.62	2.38	1.56	0.99
205	6.10	2.27	1.51	0.95
210	5.60	2.15	1.44	0.90
215	5.11	2.00	1.35	0.85
220	4.61	1.86	1.27	0.78
225	4.11	1.69	1.16	0.72
230	3.58	1.52	1.04	0.65
235	3.12	1.32	0.93	0.57
240	2.65	1.14	0.82	0.50
245	2.24	0.97	0.69	0.42
250	1.80	0.75	0.58	0.34
255	1.35	0.56	0.45	0.25
260	0.89	0.36	0.33	0.16
265	0.47	0.19	0.19	0.07
270	0.03	0.03	0.07	0.01
275	0.29	0.06	0	0.01
280	0.73	0.21	0.07	0.07
285	1.17	0.41	0.19	0.14
290	1.64	0.60	0.32	0.23
295	2.08	0.80	0.44	0.32
300	2.57	0.99	0.56	0.41
305	2.95	1.18	0.69	0.48
310	3.46	1.37	0.83	0.57
315	3.95	1.53	0.94	0.64
320	4.41	1.69	1.04	0.72
325	4.86	1.84	1.15	0.77
330	5.32	1.97	1.23	0.83
335	5.68	2.10	1.32	0.88
340	6.06	2.21	1.40	0.93
345	6.32	2.29	1.45	0.96
350	6.49	2.36	1.51	0.99
355	6.55	2.41	1.55	1.01
360	6.58	2.43	1.57	1.01

Table 23: Flux density B_{mod} (mT) measurements at r_5 z positions over the core (coil-1) with top plate

θ°	r_5z_6	r_5z_7	r_5z_8	r_5z_9
0	5.52	2.45	1.53	1.02
5	5.43	2.46	1.53	1.02
10	5.35	2.44	1.52	1.01
15	5.19	2.40	1.50	1.00
20	5.02	2.34	1.46	0.97
25	4.75	2.25	1.40	0.94
30	4.43	2.15	1.34	0.89
35	4.09	2.03	1.26	0.85
40	3.66	1.88	1.18	0.79
45	3.26	1.74	1.09	0.72
50	2.90	1.58	1.00	0.65
55	2.52	1.42	0.89	0.58
60	2.10	1.23	0.78	0.51
65	1.81	1.02	0.66	0.43
70	1.39	0.83	0.54	0.34
75	1.02	0.65	0.43	0.27
80	0.68	0.46	0.29	0.18
85	0.24	0.29	0.16	0.10
90	0.02	0.10	0.05	0.02
95	0.35	1E-3	0.00	0.01
100	0.71	0.12	0.07	0.05
105	1.11	0.33	0.18	0.12
110	1.40	0.52	0.32	0.20
115	1.79	0.71	0.44	0.28
120	2.24	0.89	0.56	0.38
125	2.59	1.08	0.69	0.47
130	2.99	1.25	0.78	0.55
135	3.36	1.42	0.90	0.67
140	3.73	1.63	1.06	0.70
145	4.09	1.79	1.13	0.77
150	4.46	1.95	1.24	0.84
155	4.85	2.11	1.32	0.90
160	5.23	2.26	1.40	0.95
165	5.54	2.37	1.48	0.98
170	5.88	2.48	1.53	1.01
175	6.08	2.55	1.57	1.03
180	6.19	2.59	1.60	1.05

θ°	r_5z_6	r_5z_7	r_5z_8	r_5z_9
185	6.16	2.61	1.60	1.05
190	5.99	2.59	1.59	1.04
195	5.70	2.54	1.56	1.02
200	5.36	2.46	1.51	0.99
205	4.99	2.35	1.46	0.95
210	4.59	2.23	1.38	0.91
215	4.12	2.09	1.30	0.86
220	3.73	1.91	1.21	0.79
225	3.28	1.76	1.11	0.73
230	2.85	1.58	1.01	0.66
235	2.46	1.38	0.89	0.58
240	2.06	1.20	0.78	0.51
245	1.73	1.04	0.66	0.43
250	1.35	0.83	0.53	0.35
255	0.95	0.62	0.41	0.27
260	0.57	0.44	0.28	0.18
265	0.19	0.25	0.16	0.09
270	0.07	0.08	0.05	0.02
275	0.45	0.02	0.00	0.00
280	0.77	0.17	0.09	0.06
285	1.21	0.36	0.20	0.13
290	1.56	0.57	0.32	0.23
295	1.95	0.74	0.44	0.30
300	2.33	0.94	0.57	0.39
305	2.69	1.12	0.71	0.47
310	3.09	1.31	0.82	0.56
315	3.46	1.49	0.94	0.63
320	3.88	1.64	1.04	0.71
325	4.26	1.81	1.14	0.78
330	4.61	1.95	1.22	0.83
335	4.89	2.09	1.30	0.88
340	5.18	2.21	1.38	0.93
345	5.36	2.30	1.43	0.97
350	5.44	2.38	1.47	0.99
355	5.50	2.43	1.52	1.03
360	5.52	2.45	1.53	1.04

Table 24: Flux density B_{mod} (mT) measurements at r_7 z positions over the core (coil-1) with top plate

θ°	r_7z_6	r_7z_7	r_7z_8	r_7z_9
0	4.79	2.31	1.52	0.90
5	4.72	2.30	1.52	0.90
10	4.68	2.29	1.52	0.90
15	4.56	2.24	1.50	0.89
20	4.41	2.18	1.47	0.86
25	4.19	2.11	1.43	0.83
30	3.93	2.01	1.36	0.80
35	3.60	1.88	1.28	0.74
40	3.31	1.75	1.20	0.69
45	2.99	1.62	1.11	0.63
50	2.66	1.47	1.02	0.56
55	2.37	1.31	0.93	0.50
60	2.04	1.15	0.81	0.43
65	1.71	0.97	0.71	0.35
70	1.39	0.81	0.58	0.27
75	1.04	0.67	0.44	0.20
80	0.68	0.43	0.32	0.13
85	0.39	0.26	0.20	0.06
90	0.09	0.09	0.09	0.02
95	0.15	1E-3	0.02	0.04
100	0.42	0.11	0.03	0.11
105	0.73	0.28	0.13	0.18
110	1.08	0.45	0.26	0.26
115	1.40	0.63	0.40	0.33
120	1.76	0.81	0.53	0.41
125	2.15	1.01	0.64	0.48
130	2.44	1.16	0.75	0.55
135	2.74	1.29	0.87	0.63
140	3.12	1.47	0.99	0.70
145	3.42	1.63	1.07	0.77
150	3.77	1.78	1.19	0.83
155	4.16	1.93	1.28	0.88
160	4.46	2.07	1.38	0.93
165	4.74	2.17	1.48	0.97
170	4.96	2.27	1.55	1.00
175	5.16	2.34	1.59	1.03
180	5.29	2.38	1.63	1.04

θ°	r_7z_6	r_7z_7	r_7z_8	r_7z_9
185	5.32	2.39	1.65	1.04
190	5.20	2.38	1.64	1.04
195	5.02	2.33	1.62	1.02
200	4.73	2.27	1.58	0.99
205	4.41	2.16	1.53	0.95
210	4.11	2.04	1.45	0.91
215	3.74	1.91	1.37	0.86
220	3.39	1.76	1.28	0.81
225	3.00	1.61	1.17	0.75
230	2.64	1.47	1.08	0.68
235	2.30	1.31	0.96	0.60
240	2.01	1.13	0.84	0.53
245	1.67	0.95	0.71	0.45
250	1.32	0.76	0.60	0.38
255	1.01	0.59	0.46	0.30
260	0.64	0.40	0.32	0.22
265	0.32	0.24	0.20	0.14
270	0.02	0.07	0.09	0.07
275	0.19	0.01	0	0.01
280	0.53	0.13	0.05	0.01
285	0.82	0.31	0.17	0.06
290	1.18	0.48	0.28	0.14
295	1.48	0.66	0.41	0.21
300	1.85	0.84	0.54	0.29
305	2.22	1.02	0.66	0.37
310	2.57	1.20	0.79	0.44
315	2.93	1.36	0.91	0.51
320	3.25	1.50	1.01	0.58
325	3.54	1.64	1.11	0.64
330	3.82	1.78	1.21	0.69
335	4.12	1.92	1.30	0.75
340	4.40	2.00	1.37	0.80
345	4.58	2.11	1.45	0.83
350	4.71	2.18	1.49	0.86
355	4.77	2.24	1.53	0.88
360	4.79	2.31	1.56	0.90

Table 25: Flux density B_{mod} (mT) measurements of perpendicular field beside the core (coil-1), without top plate

θ°	r_6z_1	r_7z_1	r_8z_1	r_9z_1
0	17.02	11.93	8.98	5.84
5	17.05	11.92	9.03	5.79
10	17.36	12.01	9.03	5.70
15	17.78	12.16	9.01	5.63
20	18.40	12.17	8.90	5.46
25	16.10	11.26	8.42	5.21
30	14.12	10.14	7.76	4.88
35	12.55	9.20	7.11	4.56
40	11.56	8.32	6.46	4.17
45	10.43	7.50	5.86	3.76
50	9.44	6.75	5.16	3.37
55	8.27	5.92	4.61	2.97
60	7.04	5.07	3.90	2.54
65	5.82	4.32	3.34	2.16
70	4.61	3.56	2.70	1.76
75	3.51	2.77	2.13	1.35
80	2.52	1.99	1.52	0.94
85	1.38	1.21	0.95	0.57
90	0.30	0.41	0.35	0.20
95	0.37	0.14	0.03	0.00
100	1.56	0.87	0.58	0.34
105	2.62	1.64	1.17	0.73
110	3.69	2.40	1.73	1.11
115	4.65	3.13	2.33	1.51
120	5.81	3.95	2.94	1.90
125	6.85	4.70	3.51	2.30
130	8.09	5.52	4.10	2.69
135	9.27	6.30	4.72	3.11
140	10.52	7.16	5.40	3.58
145	11.55	8.00	6.04	3.96
150	12.71	8.88	6.67	4.42
155	13.91	9.85	7.33	4.81
160	14.91	10.69	8.00	5.28
165	16.26	11.78	8.82	5.77
170	17.71	12.94	9.62	6.13
175	19.86	14.38	10.44	6.53
180	22.33	15.83	11.22	6.77

θ°	r_6z_1	r_7z_1	r_8z_1	r_9z_1
183	23.34	16.36	11.29	6.83
185	22.51	16.25	11.47	6.87
190	19.37	14.98	11.04	6.73
195	17.51	13.71	10.32	6.46
200	16.06	12.71	9.60	6.10
205	14.71	11.58	8.82	5.71
210	13.14	10.54	8.13	5.31
215	11.86	9.56	7.47	4.86
220	10.64	8.57	6.75	4.47
225	9.50	7.76	6.14	4.12
230	8.23	6.84	5.46	3.75
235	7.23	5.96	4.80	3.44
240	6.09	5.07	4.12	2.59
245	5.05	4.21	3.34	2.22
250	4.13	3.49	2.70	1.82
255	3.17	2.72	2.18	1.41
260	2.29	1.95	1.57	0.96
265	1.27	1.19	0.99	0.53
270	0.40	0.47	0.37	0.11
275	0.39	0.14	0.03	0.09
280	1.39	0.90	0.59	0.47
285	2.37	1.69	1.18	0.87
290	3.34	2.42	1.78	1.24
295	4.15	3.24	2.36	1.68
300	5.15	4.05	2.95	2.08
305	6.65	4.87	3.51	2.45
310	7.79	5.69	4.18	2.86
315	8.93	6.60	4.86	3.27
320	10.18	7.44	5.53	3.66
325	11.32	8.36	6.20	4.07
330	12.64	9.36	6.92	4.50
335	14.26	10.41	7.67	4.89
340	16.35	11.61	8.49	5.24
345	18.53	12.55	8.94	5.59
350	17.86	12.47	9.07	5.81
355	17.23	12.17	9.04	5.92
360	16.91	11.97	8.97	5.89

Table 26: Flux density B_{mod} (mT) measurements of perpendicular field beside the core (coil-1), without top plate

θ°	r_6Z_2	r_7Z_2	r_8Z_2	r_9Z_2
0	13.80	12.27	10.07	6.97
5	13.86	12.36	10.07	6.94
10	14.26	12.54	10.06	6.91
15	14.98	12.52	9.88	6.82
20	14.15	11.63	9.26	6.62
25	12.31	10.41	8.49	6.30
30	10.95	9.33	7.69	5.84
35	9.73	8.37	6.92	5.40
40	8.74	7.42	6.23	4.89
45	7.84	6.59	5.50	4.51
50	6.85	5.75	4.81	3.92
55	5.88	4.99	4.15	3.49
60	5.01	4.08	3.36	2.99
65	4.03	3.34	2.79	2.49
70	3.15	2.52	2.16	2.03
75	2.40	1.75	1.49	1.60
80	1.44	0.89	0.79	1.08
85	0.61	0.17	0.09	0.60
90	0.12	0.45	0.38	0.17
95	0.88	1.20	0.95	0.07
100	1.78	1.94	1.51	0.52
105	2.65	2.77	2.25	0.97
110	3.44	3.50	2.85	1.43
115	4.27	4.31	3.53	1.85
120	5.15	5.10	4.17	2.34
125	5.98	5.90	4.87	2.80
130	6.87	6.73	5.46	3.25
135	7.75	7.53	6.23	3.73
140	8.73	8.43	6.98	4.29
145	9.69	9.28	7.54	4.77
150	10.80	10.19	8.37	5.27
155	11.69	11.15	9.28	5.75
160	12.86	12.27	10.03	6.25
165	14.23	13.46	10.97	6.76
170	15.82	14.73	11.87	7.35
175	17.97	16.31	12.64	7.80
180	21.32	16.67	12.84	8.14

θ°	r_6Z_2	r_7Z_2	r_8Z_2	r_9Z_2
185	18.29	15.06	12.17	8.27
190	15.80	13.66	11.25	8.06
195	14.36	12.40	10.30	7.68
200	13.14	11.30	9.41	7.20
205	11.84	10.25	8.60	6.69
210	10.65	9.21	7.82	6.18
215	9.42	8.31	6.96	5.69
220	8.46	7.26	6.25	5.19
225	7.53	6.48	5.42	4.57
230	6.52	5.54	4.69	4.03
235	5.66	4.70	4.03	3.56
240	4.79	3.88	3.33	3.07
245	3.89	3.18	2.75	2.59
250	3.06	2.42	2.01	2.11
255	2.20	1.57	1.48	1.65
260	1.40	0.82	0.75	1.17
265	0.47	0.14	0.18	0.72
270	0.13	0.38	0.28	0.27
275	0.97	1.18	0.86	0
280	1.74	1.95	1.58	0.45
285	2.62	2.73	2.29	0.90
290	3.51	3.64	3.02	1.39
295	4.38	4.44	3.69	1.88
300	5.31	5.22	4.41	2.37
305	6.23	6.02	5.03	2.82
310	7.21	6.99	5.86	3.33
315	8.16	7.84	6.56	3.81
320	9.22	8.81	7.30	4.26
325	10.23	9.81	8.09	4.90
330	11.60	10.95	8.93	5.34
335	12.80	11.89	9.65	5.85
340	14.95	12.99	10.26	6.28
345	15.04	12.84	10.37	6.62
350	14.28	12.47	10.25	6.82
355	13.85	12.29	10.16	6.90
360	13.78	12.24	10.11	6.92

Table 27: Flux density B_{mod} (mT) measurements of perpendicular field beside the core (coil-1), without top plate

θ°	r_6Z_3	r_7Z_3	r_8Z_3	r_9Z_3
0	15.61	10.69	8.30	5.62
5	15.53	10.71	8.30	5.61
10	15.64	10.83	8.38	5.61
15	15.97	11.00	8.36	5.56
20	16.86	10.75	8.17	5.41
25	14.52	9.88	7.70	5.17
30	12.84	9.13	7.09	4.86
35	11.66	8.21	6.56	4.50
40	10.42	7.46	5.94	4.10
45	9.35	6.77	5.35	3.74
50	8.31	6.02	4.84	3.34
55	7.23	5.33	4.22	2.95
60	6.21	4.58	3.62	2.57
65	5.13	3.92	3.19	2.20
70	4.19	3.21	2.63	1.82
75	3.30	2.52	2.05	1.45
80	2.22	1.89	1.53	1.05
85	1.25	1.17	0.99	0.68
90	0.33	0.52	0.44	0.30
95	0.46	0.01	0	0.00
100	1.35	0.63	0.42	0.22
105	2.37	1.29	0.93	0.60
110	3.34	2.00	1.53	0.98
115	4.37	2.67	2.05	1.34
120	5.29	3.36	2.58	1.74
125	6.23	4.02	3.12	2.11
130	7.29	4.74	3.68	2.52
135	8.29	5.46	4.26	2.92
140	9.28	6.30	4.89	3.34
145	10.34	6.96	5.46	3.75
150	11.42	7.78	6.07	4.17
155	12.59	8.53	6.72	4.62
160	13.93	9.49	7.50	5.09
165	15.29	10.48	8.23	5.53
170	17.01	11.50	8.94	6.01
175	18.73	12.87	9.74	6.23
180	21.43	14.15	10.37	6.54

θ°	r_6Z_3	r_7Z_3	r_8Z_3	r_9Z_3
183	23.43	14.84	10.46	6.68
185	22.46	14.16	10.44	6.63
190	19.69	13.02	9.97	6.51
195	18.11	12.10	9.40	6.25
200	16.35	11.12	8.74	5.92
205	14.89	10.34	8.06	5.57
210	13.74	9.43	7.41	5.22
215	12.10	8.59	6.85	4.81
220	10.76	7.81	6.21	4.37
225	9.64	6.84	5.57	3.88
230	8.53	6.14	4.85	3.49
235	7.40	5.39	4.25	3.06
240	6.37	4.61	3.66	2.62
245	5.21	3.94	3.14	2.27
250	4.28	3.22	2.57	1.91
255	3.12	2.53	2.01	1.54
260	2.18	1.86	1.46	1.14
265	1.21	1.23	0.93	0.77
270	0.29	0.54	0.41	0.41
275	0.53	0.00	0.03	0.01
280	1.49	0.68	0.46	0.15
285	2.41	1.35	1.03	0.54
290	3.44	2.13	1.51	0.90
295	4.53	2.85	2.15	1.33
300	5.70	3.53	2.73	1.75
305	6.92	4.28	3.32	2.14
310	7.89	4.99	3.91	2.54
315	8.97	5.80	4.55	2.99
320	10.18	6.67	5.16	3.43
325	11.56	7.49	5.83	3.83
330	12.70	8.44	6.54	4.30
335	14.30	9.41	7.19	4.66
340	15.89	10.40	7.89	5.01
345	17.88	10.99	8.28	5.31
350	16.73	10.96	8.38	5.47
355	15.97	10.72	8.38	5.56
360	15.64	10.70	8.33	5.61

Table 28: Flux density B_{mod} (mT) measurements of perpendicular field beside the core (coil-1), with top plate

θ°	r_6Z_1	r_7Z_1	r_8Z_1	r_9Z_1
0	15.22	11.57	8.67	6.08
5	15.20	11.58	8.68	6.13
10	15.31	11.67	8.68	6.04
15	15.60	11.83	8.66	5.96
20	16.33	11.80	8.54	5.79
25	14.65	10.90	7.98	5.53
30	13.02	9.91	7.37	5.15
35	11.64	8.81	6.71	4.82
40	10.52	8.15	5.97	4.37
45	9.68	7.51	5.39	3.97
50	8.58	6.57	4.86	3.58
55	7.62	5.70	4.32	3.15
60	6.58	4.88	3.70	2.74
65	5.60	4.07	3.12	2.31
70	4.43	3.37	2.55	1.94
75	3.49	2.57	1.94	1.55
80	2.64	1.75	1.29	1.14
85	1.50	1.00	0.69	0.69
90	0.53	0.23	0.17	0.29
95	0.15	0.31	0.22	0.01
100	1.24	1.03	0.68	0.37
105	2.18	1.75	1.23	0.72
110	3.10	2.46	1.80	1.13
115	3.93	3.11	2.35	1.54
120	4.97	3.93	2.90	1.97
125	5.93	4.79	3.46	2.39
130	6.80	5.46	4.07	2.81
135	7.86	6.16	4.46	3.19
140	8.95	7.03	5.35	3.60
145	9.79	7.71	5.82	4.03
150	10.77	8.58	6.38	4.44
155	12.00	9.42	7.21	4.86
160	13.23	10.37	7.86	5.32
165	14.66	11.40	8.57	5.89
170	16.04	12.56	9.33	6.35
175	17.90	13.84	10.06	6.79
180	20.51	15.01	10.46	7.07

θ°	r_6Z_1	r_7Z_1	r_8Z_1	r_9Z_1
182	21.76	15.61	10.87	7.42
185	20.46	14.74	10.39	7.15
190	17.94	13.58	9.87	7.03
195	16.19	12.40	9.17	6.71
200	14.91	11.43	8.55	6.32
205	13.56	10.41	7.74	5.89
210	12.21	9.45	7.07	5.44
215	11.02	8.65	6.44	4.96
220	9.94	7.59	5.78	4.53
225	8.93	7.00	5.14	4.14
230	7.78	5.97	4.52	3.60
235	6.79	5.22	4.06	3.20
240	5.83	4.47	3.44	2.74
245	4.92	3.76	2.86	2.32
250	3.92	3.04	2.28	1.99
255	3.12	2.36	1.86	1.52
260	2.10	1.66	1.25	1.08
265	1.25	0.82	0.63	0.67
270	0.53	0.17	0.14	0.29
275	0.25	0.37	0.24	0
280	1.14	0.99	0.74	0.36
285	2.03	1.65	1.27	0.79
290	2.68	2.47	1.89	1.25
295	3.94	2.97	2.42	1.63
300	4.98	3.82	2.93	2.10
305	6.11	4.76	3.59	2.51
310	7.01	5.48	4.12	2.89
315	8.18	6.34	4.77	3.35
320	9.19	7.13	5.43	3.80
325	10.38	8.02	6.04	4.22
330	11.62	8.96	6.77	4.71
335	12.93	9.95	7.39	5.14
340	14.69	11.04	8.09	5.54
345	16.25	11.87	8.49	5.79
350	15.98	11.93	8.65	6.01
355	15.33	11.69	8.66	6.12
360	15.10	11.58	8.64	6.14

Table 29: Flux density B_{mod} (mT) measurements of perpendicular field beside the core (coil-1), with top plate

θ°	r_6Z_2	r_7Z_2	r_8Z_2	r_9Z_2
0	14.23	12.54	10.26	6.93
5	14.22	12.55	10.25	6.89
10	14.45	12.70	10.28	6.86
15	14.92	12.90	10.23	6.73
20	15.80	12.51	9.92	6.50
25	14.00	11.48	9.21	6.09
30	12.20	10.34	8.32	5.66
35	10.99	9.27	7.60	5.21
40	9.80	8.26	6.85	4.73
45	8.87	7.44	6.14	4.26
50	7.89	6.70	5.51	3.81
55	7.04	5.88	4.85	3.33
60	6.06	5.04	4.19	2.80
65	5.11	4.20	3.49	2.39
70	4.16	3.26	2.87	1.93
75	3.29	2.46	2.15	1.49
80	2.26	1.72	1.44	0.98
85	1.50	0.94	0.78	0.55
90	0.58	0.13	0.15	0.11
95	0.09	0.35	0.34	0.18
100	0.82	1.10	0.95	0.66
105	1.84	1.93	1.60	1.09
110	2.62	2.69	2.27	1.55
115	3.58	3.38	2.98	2.02
120	4.41	4.25	3.59	2.50
125	5.30	5.09	4.25	2.94
130	6.17	5.85	4.86	3.39
135	7.18	6.80	5.63	3.88
140	8.22	7.67	6.31	4.38
145	9.17	8.52	7.15	4.92
150	10.07	9.49	7.88	5.37
155	11.22	10.52	8.76	5.91
160	12.58	11.62	9.54	6.45
165	13.65	12.69	10.38	6.94
170	15.20	14.05	11.46	7.44
175	17.14	15.61	12.36	7.93
180	19.86	16.98	13.01	8.14

θ°	r_6Z_2	r_7Z_2	r_8Z_2	r_9Z_2
183	21.79	17.41	13.36	8.23
185	21.07	16.59	12.84	8.05
190	18.06	15.08	12.12	7.77
195	16.25	13.74	11.22	7.34
200	14.77	12.62	10.30	6.80
205	13.39	11.40	9.41	6.31
210	12.20	10.33	8.50	5.82
215	10.92	9.30	7.69	5.25
220	9.77	8.30	6.89	4.78
225	8.86	7.40	6.22	4.28
230	7.83	6.53	5.51	3.76
235	6.88	5.68	4.79	3.29
240	5.89	4.92	4.13	2.80
245	4.99	4.03	3.40	2.32
250	4.08	3.31	2.73	1.88
255	3.14	2.42	2.05	1.45
260	2.38	1.72	1.36	0.96
265	1.40	0.86	0.70	0.47
270	0.50	0.09	0.11	0.10
275	0.18	0.51	0.36	0.27
280	1.15	1.29	1.04	0.71
285	1.91	2.12	1.77	1.17
290	2.93	2.93	2.41	1.66
295	3.67	3.67	3.04	2.12
300	4.74	4.64	3.85	2.67
305	5.50	5.43	4.51	3.08
310	6.57	6.35	5.32	3.59
315	7.54	7.20	6.05	4.12
320	8.62	8.16	6.85	4.57
325	9.79	9.22	7.58	5.09
330	11.01	10.27	8.40	5.60
335	12.29	11.37	9.24	6.06
340	14.02	12.56	9.97	6.43
345	16.29	13.22	10.42	6.69
350	15.19	12.92	10.48	6.80
355	14.53	12.65	10.39	6.84
360	14.28	12.53	10.35	6.86

Table 30: Flux density B_{mod} (mT) measurements of perpendicular field beside the core (coil-1), with top plate

θ°	r_6Z_3	r_7Z_3	r_8Z_3	r_9Z_3
0	15.81	11.60	8.84	5.89
5	15.84	11.58	8.83	5.88
10	16.04	11.67	8.80	5.85
15	16.47	11.82	8.77	5.78
20	17.21	11.79	8.51	5.60
25	15.14	10.94	7.97	5.32
30	13.68	9.90	7.40	4.96
35	12.11	8.99	6.67	4.59
40	10.86	8.16	5.98	4.17
45	9.88	7.34	5.38	3.80
50	8.95	6.59	4.83	3.41
55	7.96	5.81	4.25	3.00
60	6.87	5.06	3.68	2.56
65	5.82	4.29	3.10	2.23
70	4.79	3.51	2.54	1.86
75	3.63	2.78	1.95	1.46
80	2.64	1.96	1.31	0.97
85	1.70	1.21	0.69	0.59
90	0.64	0.53	0.12	0.18
95	0.06	0.07	0.18	0.07
100	0.90	0.78	0.82	0.43
105	2.06	1.60	1.39	0.84
110	3.00	2.32	1.94	1.19
115	4.02	3.07	2.43	1.66
120	5.09	3.84	3.11	2.01
125	6.08	4.55	3.70	2.48
130	7.03	5.42	4.27	2.85
135	8.28	6.19	4.92	3.24
140	9.45	7.01	5.56	3.65
145	10.58	7.90	6.23	4.06
150	11.74	8.75	6.84	4.53
155	13.06	9.78	7.53	4.99
160	14.20	10.81	8.26	5.48
165	15.85	11.79	9.06	5.89
170	17.35	12.89	9.88	6.37
175	19.32	14.19	10.65	6.69
180	21.93	15.77	11.25	6.92

θ°	r_6Z_3	r_7Z_3	r_8Z_3	r_9Z_3
183	23.86	16.18	11.56	6.99
185	23.04	15.63	11.08	6.97
190	20.12	14.36	10.35	6.74
195	18.67	13.27	9.76	6.43
200	16.57	12.17	9.07	5.99
205	15.25	11.13	8.29	5.61
210	13.83	10.10	7.45	5.17
215	12.64	9.19	6.82	4.74
220	11.41	8.19	6.09	4.25
225	10.09	7.34	5.46	3.80
230	9.00	6.54	4.83	3.37
235	8.03	5.68	4.23	2.94
240	6.83	4.86	3.59	2.50
245	5.80	4.12	2.97	2.11
250	4.64	3.33	2.30	1.75
255	3.62	2.59	1.83	1.36
260	2.46	1.77	1.14	0.90
265	1.52	1.01	0.63	0.47
270	0.57	0.34	0.07	0.13
275	0.26	0.21	0.36	0.11
280	1.30	0.99	0.93	0.51
285	2.23	1.73	0.93	0.92
290	3.32	2.44	2.07	1.34
295	4.36	3.21	2.64	1.73
300	5.63	4.04	3.24	2.15
305	6.65	4.83	3.88	2.61
310	7.56	5.66	4.56	3.01
315	8.71	6.48	5.17	3.42
320	9.88	7.33	5.84	3.80
325	11.19	8.24	6.54	4.26
330	12.64	9.06	7.18	4.68
335	13.86	10.09	7.85	5.07
340	15.75	11.29	8.52	5.41
345	17.71	12.08	8.95	5.69
350	16.55	12.02	9.00	5.85
355	16.04	11.75	8.93	5.90
360	15.75	11.59	8.91	5.92

Table 31: Flux density B_{mod} (mT) measurements of parallel field beside the core (coil-1), with top plate

θ°	r_1z_6	r_1z_7	r_1z_8	r_1z_9
0	0.49	0.36	0.23	0.13
5	0.31	0.14	0	1E-3
10	0.10	0.06	0.29	0.27
15	0.11	0.50	0.71	0.52
20	1.29	1.66	1.31	0.83
25	3.17	2.59	1.90	1.14
30	3.49	2.94	2.31	1.42
35	3.58	3.12	2.50	1.59
40	3.69	3.29	2.62	1.72
45	3.80	3.40	2.75	1.85
50	3.97	3.56	2.90	1.94
55	4.13	3.68	2.96	2.02
60	4.26	3.80	3.05	2.11
65	4.31	3.88	3.12	2.17
70	4.31	3.95	3.19	2.23
75	4.40	4.04	3.24	2.28
80	4.49	4.10	3.29	2.31
85	4.55	4.13	3.32	2.34
90	4.60	4.19	3.35	2.36
95	4.64	4.20	3.38	2.38
100	4.66	4.24	3.40	2.40
105	4.70	4.26	3.40	2.40
110	4.77	4.28	3.41	2.40
115	4.81	4.29	3.41	2.40
120	4.81	4.29	3.41	2.38
125	4.84	4.31	3.40	2.36
130	4.86	4.31	3.38	2.33
135	4.90	4.29	3.35	2.30
140	4.92	4.26	3.30	2.24
145	4.92	4.19	3.19	2.14
150	4.84	4.10	3.05	1.97
155	4.82	4.05	2.93	1.78
160	4.77	4.03	2.86	1.71
165	4.73	3.92	2.67	1.57
170	4.68	3.63	2.31	1.29
175	4.38	2.96	1.72	0.90
180	3.34	1.30	0.78	0.38

θ°	r_6z_1	r_7z_1	r_8z_1	r_9z_1
185	0.71	0.86	0.44	0.07
190	2.28	1.95	1.23	0.57
195	2.78	2.50	1.80	0.96
200	3.21	2.93	2.19	1.23
205	3.53	3.16	2.44	1.44
210	3.80	3.38	2.63	1.62
215	3.96	3.48	2.77	1.75
220	3.96	3.54	2.85	1.85
225	4.01	3.63	2.92	1.94
230	4.12	3.73	2.99	2.00
235	4.20	3.78	3.00	2.05
240	4.21	3.80	3.03	2.10
245	4.27	3.84	3.07	2.13
250	4.30	3.86	3.09	2.16
255	4.34	3.89	3.12	2.19
260	4.42	3.94	3.15	2.22
265	4.51	3.97	3.18	2.24
270	4.53	4.01	3.20	2.25
275	4.54	4.03	3.22	2.27
280	4.56	4.06	3.24	2.28
285	4.61	4.09	3.26	2.29
290	4.64	4.11	3.27	2.29
295	4.68	4.14	3.28	2.29
300	4.75	4.17	3.28	2.28
305	4.77	4.19	3.28	2.26
310	4.79	4.22	3.26	2.23
315	4.86	4.21	3.23	2.18
320	4.87	4.18	3.18	2.11
325	4.88	4.13	3.09	2.03
330	4.80	4.03	2.93	1.87
335	4.67	3.80	2.67	1.69
340	4.32	3.32	2.19	1.44
345	2.46	2.02	1.58	1.04
350	1.03	1.03	0.89	0.63
355	0.68	0.59	0.47	0.35
360	0.49	0.35	0.18	0.17

Table 32: Flux density B_{mod} (mT) measurements of parallel field beside the core (coil-1), with top plate

θ°	r_6Z_2	r_7Z_2	r_8Z_2	r_9Z_2
0	0.66	0.17	0.49	0.18
5	0.51	0.02	0.19	0
10	0.36	0.13	0	0.25
15	0.07	0.71	0.44	0.54
20	1.20	2.20	1.07	0.91
25	3.31	3.17	1.90	1.26
30	3.76	3.58	2.36	1.52
35	3.70	3.76	2.64	1.75
40	4.05	3.88	2.85	1.89
45	4.20	3.98	2.98	2.01
50	4.31	4.12	3.07	2.12
55	4.44	4.19	3.17	2.20
60	4.56	4.26	3.26	2.28
65	4.62	4.32	3.35	2.33
70	4.62	4.36	3.41	2.39
75	4.67	4.42	3.48	2.44
80	4.84	4.49	3.54	2.48
85	4.86	4.51	3.59	2.51
90	4.95	4.52	3.64	2.52
95	4.97	4.53	3.67	2.54
100	5.00	4.55	3.68	2.56
105	5.09	4.55	3.71	2.57
110	5.14	4.55	3.71	2.56
115	5.23	4.57	3.73	2.55
120	5.24	4.58	3.74	2.54
125	5.28	4.58	3.74	2.53
130	5.35	4.56	3.75	2.50
135	5.38	4.54	3.73	2.48
140	5.45	4.50	3.71	2.40
145	5.46	4.46	3.67	2.35
150	5.49	4.43	3.62	2.26
155	5.51	4.39	3.64	2.14
160	5.59	4.32	3.45	1.98
165	5.52	4.14	3.27	1.78
170	5.49	3.95	2.96	1.46
175	5.32	3.10	2.40	1.04
180	4.41	1.05	1.24	0.42

θ°	r_6Z_2	r_7Z_2	r_8Z_2	r_9Z_2
185	1.16	1.51	0.07	0.05
190	2.79	2.74	1.18	0.64
195	3.40	3.27	1.87	1.07
200	3.65	3.58	2.30	1.39
205	3.97	3.83	2.60	1.62
210	4.15	3.97	2.79	1.80
215	4.24	4.05	2.93	1.93
220	4.28	4.09	3.01	2.03
225	4.34	4.14	3.08	2.11
230	4.44	4.17	3.14	2.17
235	4.50	4.20	3.19	2.21
240	4.52	4.20	3.23	2.25
245	4.57	4.21	3.27	2.30
250	4.61	4.23	3.30	2.33
255	4.67	4.25	3.34	2.35
260	4.73	4.27	3.38	2.38
265	4.82	4.30	3.41	2.40
270	4.81	4.32	3.45	2.42
275	4.88	4.34	3.49	2.43
280	4.92	4.35	3.51	2.44
285	4.93	4.47	3.54	2.45
290	5.01	4.40	3.57	2.46
295	5.11	4.43	3.60	2.46
300	5.12	4.43	3.62	2.45
305	5.19	4.45	3.63	2.44
310	5.23	4.47	3.64	2.44
315	5.31	4.46	3.63	2.38
320	5.33	4.43	3.61	2.32
325	5.36	4.37	3.54	2.24
330	5.35	4.26	3.41	2.07
335	5.28	4.03	3.21	1.86
340	5.08	3.34	2.82	1.51
345	4.19	1.97	2.04	1.15
350	1.55	0.86	1.29	0.74
355	0.90	0.43	0.77	0.44
360	0.67	0.21	0.45	0.17

Table 33: Flux density B_{mod} (mT) measurements of parallel field beside the core (coil-1), with top plate

θ°	r_6Z_3	r_7Z_3	r_8Z_3	r_9Z_3
0	0.54	0.72	0	0.47
5	0.36	0.49	0.22	0.26
10	0.12	0.19	0.50	0.02
15	0.16	0.14	0.93	0.13
20	1.67	1.08	1.47	0.41
25	2.84	2.05	2.03	0.73
30	3.27	2.51	2.44	1.00
35	3.48	2.86	2.63	1.29
40	3.64	3.02	2.84	1.52
45	3.78	3.18	2.97	1.65
50	3.85	3.32	3.01	1.78
55	3.99	3.44	3.08	1.89
60	4.09	3.56	3.16	1.98
65	4.21	3.67	3.20	2.05
70	4.28	3.75	3.23	2.12
75	4.34	3.84	3.26	2.19
80	4.46	3.94	3.28	2.26
85	4.53	4.00	3.30	2.29
90	4.60	4.06	3.30	2.34
95	4.62	4.12	3.29	2.36
100	4.67	4.17	3.29	2.38
105	4.71	4.23	3.28	2.40
110	4.77	4.26	3.26	2.42
115	4.85	4.32	3.23	2.44
120	4.87	4.34	3.22	2.44
125	4.86	4.37	3.18	2.44
130	4.84	4.39	3.13	2.43
135	4.86	4.39	3.08	2.42
140	4.88	4.40	3.00	2.38
145	4.87	4.40	2.92	2.35
150	4.86	4.40	2.83	2.29
155	4.84	4.36	2.70	2.19
160	4.81	4.31	2.53	2.08
165	4.70	4.17	2.25	1.91
170	4.57	3.89	1.91	1.72
175	4.26	3.39	1.36	1.36
180	3.40	2.13	0.48	0.95

θ°	r_6Z_3	r_7Z_3	r_8Z_3	r_9Z_3
185	0.56	0.07	0.52	0.41
190	2.21	1.43	1.46	0.01
195	2.80	2.08	2.07	0.43
200	3.26	2.55	2.43	0.80
205	3.49	2.87	2.67	1.09
210	3.73	3.06	2.83	1.31
215	3.84	3.20	2.95	1.51
220	3.93	3.31	3.00	1.66
225	4.00	3.41	3.05	1.76
230	4.04	3.48	3.10	1.85
235	4.11	3.56	3.12	1.92
240	4.17	3.64	3.17	1.98
245	4.24	3.69	3.19	2.04
250	4.22	3.75	3.19	2.09
255	4.31	3.79	3.19	2.13
260	4.33	3.84	3.19	2.16
265	4.38	3.91	3.19	2.20
270	4.43	3.95	3.19	2.23
275	4.47	4.00	3.17	2.26
280	4.47	4.04	3.15	2.28
285	4.51	4.10	3.15	2.29
290	4.59	4.14	3.12	2.31
295	4.63	4.21	3.11	2.31
300	4.70	4.24	3.08	2.32
305	4.68	4.25	3.04	2.31
310	4.72	4.28	3.00	2.29
315	4.74	4.28	2.93	2.28
320	4.72	4.28	2.84	2.23
325	4.73	4.23	2.71	2.15
330	4.66	4.13	2.57	2.07
335	4.57	3.98	2.28	1.91
340	4.21	3.54	1.98	1.70
345	3.36	2.31	1.31	1.43
350	1.41	1.50	0.68	1.12
355	0.86	1.05	0.23	0.80
360	0.61	0.72	0	0.50

Table 34: flux density B_{mod} (mT) measurements, beside the core (coil-2), without top plate, the brush position at T_{b1} , $r = 234$ mm, $z = 41$ mm, (P – Parallel, PP – Perpendicular)

θ°	P. field	PP. field
0	0	1.64
5	0.02	1.61
10	0.06	1.57
15	0.11	1.52
20	0.17	1.46
25	0.23	1.38
30	0.29	1.29
35	0.36	1.18
40	0.41	1.07
45	0.46	0.95
50	0.50	0.82
55	0.54	0.70
60	0.58	0.55
65	0.61	0.42
70	0.64	0.28
75	0.66	0.16
80	0.68	0.04
85	0.70	0.01
90	0.72	0.10
95	0.72	0.22
100	0.74	0.36
105	0.75	0.49
110	0.75	0.61
115	0.75	0.75
120	0.75	0.88
125	0.75	1.02
130	0.74	1.14
135	0.72	1.27
140	0.69	1.41
145	0.66	1.53
150	0.62	1.64
155	0.56	1.77
160	0.50	1.88
165	0.41	1.99
170	0.33	2.08
175	0.23	2.15
180	0.12	2.19

θ°	P. field	PP. field
185	0.03	2.20
190	0.03	2.17
195	0.13	2.09
200	0.23	1.99
205	0.35	1.86
210	0.45	1.70
215	0.53	1.53
220	0.60	1.36
225	0.67	1.16
230	0.72	0.97
235	0.77	0.78
240	0.80	0.58
245	0.83	0.37
250	0.86	0.19
255	0.87	0.04
260	0.88	0.05
265	0.88	0.24
270	0.88	0.42
275	0.86	0.60
280	0.84	0.79
285	0.80	0.97
290	0.75	1.12
295	0.69	1.26
300	0.63	1.37
305	0.55	1.45
310	0.47	1.52
315	0.40	1.58
320	0.34	1.61
325	0.28	1.63
330	0.22	1.65
335	0.17	1.66
340	0.12	1.66
345	0.08	1.66
350	0.05	1.66
355	0.01	1.64
360	1E-3	1.64

Appendix 6: Experimental and Simulation flux density Measurements used for FE Modelling Validation

Table 1: Flux density measurement Bz (mT) over core case-1 without top plate at $r_2 z_4$.

Angle (deg.)	Bz Exp. r2z4 (mT)	Bz Sim. r2z4 (mT)	% Difference	Angle (deg.)	Bz Exp. r2z4 (mT)	Bz Sim. r2z4 (mT)	% Difference
0	10.72	10.94	-2.03	185	12.58	12.53	0.41
5	10.74	10.97	-2.15	190	12.06	11.57	4.08
10	10.81	11.01	-1.83	195	11.23	10.63	5.34
15	10.87	10.86	0.11	200	10.33	9.73	5.79
20	10.74	10.30	4.14	205	9.37	8.87	5.32
25	10.16	9.46	6.90	210	8.59	8.05	6.32
30	9.3	8.59	7.65	215	7.79	7.25	6.89
35	8.45	7.75	8.26	220	6.98	6.49	7.09
40	7.58	6.95	8.36	225	6.48	5.74	11.45
45	6.8	6.16	9.34	230	5.65	5.02	11.20
50	5.98	5.41	9.46	235	4.99	4.31	13.66
55	5.25	4.68	10.86	240	4.26	3.61	15.24
60	4.45	3.96	11.02	245	3.55	2.92	17.68
65	3.8	3.25	14.45	250	2.93	2.24	23.51
70	3.07	2.55	16.88	255	2.24	1.57	30.12
75	2.32	1.86	19.81	260	1.56	0.89	42.74
80	1.74	1.17	32.49	265	0.92	0.22	75.72
85	1.04	0.49	52.61	270	0.29	0.45	-53.79
90	0.43	0.19	56.47	275	0.17	1.12	-556.74
95	0.18	0.87	-381.29	280	0.84	1.79	-113.21
100	0.75	1.55	-106.43	285	1.5	2.47	-64.72
105	1.47	2.23	-51.97	290	2.22	3.16	-42.24
110	2.18	2.93	-34.18	295	2.87	3.85	-34.28
115	2.86	3.62	-26.70	300	3.59	4.56	-27.05
120	3.5	4.33	-23.76	305	4.29	5.28	-23.13
125	4.2	5.05	-20.27	310	5.07	6.02	-18.72
130	4.82	5.78	-20.01	315	5.84	6.77	-16.00
135	5.65	6.53	-15.65	320	6.6	7.56	-14.58
140	6.49	7.31	-12.69	325	7.33	8.37	-14.25
145	7.16	8.12	-13.39	330	8.26	9.21	-11.53
150	7.93	8.96	-12.93	335	9.06	10.05	-10.93
155	8.74	9.83	-12.44	340	9.84	10.73	-9.09
160	9.67	10.74	-11.06	345	10.5	11.05	-5.27
165	10.51	11.70	-11.28	350	10.66	11.03	-3.45
170	11.58	12.67	-9.42	355	10.72	10.96	-2.25
175	12.34	13.46	-9.11	360	10.74	10.94	-1.84
180	12.79	13.45	-5.13				

Table 2: Flux density measurement Bz (mT) over core case-1 without top plate at $r_3 z_4$.

Angle (deg.)	Bz Exp. r3z4 (mT)	Bz Sim. r3z4 (mT)	% Difference	Angle (deg.)	Bz Exp. r3z4 (mT)	Bz Sim. r3z4 (mT)	% Difference
0	11.89	11.95	-0.51	185	15.38	13.93	9.44
5	11.93	12.02	-0.75	190	14.05	12.73	9.36
10	12.05	12.14	-0.78	195	12.72	11.63	8.59
15	12.26	12.05	1.73	200	11.54	10.60	8.13
20	12.16	11.39	6.30	205	10.53	9.64	8.43
25	11.1	10.39	6.35	210	9.5	8.74	8.04
30	9.98	9.39	5.90	215	8.58	7.87	8.26
35	8.82	8.45	4.19	220	7.66	7.04	8.10
40	7.89	7.56	4.19	225	6.92	6.23	9.91
45	7.13	6.71	5.94	230	5.94	5.45	8.22
50	6.14	5.89	4.14	235	5.23	4.68	10.42
55	5.31	5.09	4.19	240	4.41	3.93	10.85
60	4.43	4.31	2.77	245	3.62	3.19	11.92
65	3.66	3.54	3.25	250	2.92	2.45	16.00
70	2.91	2.79	4.26	255	2.2	1.72	21.67
75	2.13	2.04	4.27	260	1.49	1.00	33.05
80	1.42	1.30	8.57	265	0.68	0.27	59.71
85	0.7	0.56	19.74	270	0.06	0.45	-649.70
90	0.08	0.17	-116.48	275	0.45	1.17	-160.97
95	0.54	0.91	-67.97	280	1.19	1.90	-59.90
100	1.2	1.64	-36.94	285	1.96	2.64	-34.55
105	1.94	2.38	-22.85	290	2.77	3.38	-21.99
110	2.69	3.13	-16.33	295	3.58	4.13	-15.41
115	3.42	3.88	-13.55	300	4.22	4.90	-16.05
120	4.25	4.65	-9.35	305	5.01	5.68	-13.36
125	5.04	5.42	-7.64	310	5.86	6.48	-10.62
130	5.74	6.22	-8.34	315	6.79	7.31	-7.68
135	6.6	7.03	-6.58	320	7.56	8.18	-8.18
140	7.5	7.88	-5.02	325	8.53	9.09	-6.55
145	8.33	8.75	-5.08	330	9.59	10.05	-4.81
150	9.21	9.67	-5.02	335	10.6	11.05	-4.25
155	10.25	10.65	-3.87	340	11.8	11.87	-0.62
160	11.22	11.69	-4.17	345	12.47	12.21	2.11
165	12.32	12.82	-4.04	350	12.28	12.09	1.55
170	13.61	14.04	-3.14	355	12.05	11.97	0.62
175	14.74	15.11	-2.54	360	11.97	11.95	0.17
180	15.74	15.16	3.69				

Table 3: Flux density measurement Bz (mT) over core case-1 without top plate at $r_5 z_4$.

Angle (deg.)	Bz Exp. $r_5 z_4$ (mT)	Bz Sim. $r_5 z_4$ (mT)	% Difference	Angle (deg.)	Bz Exp. $r_5 z_4$ (mT)	Bz Sim. $r_5 z_4$ (mT)	% Difference
0	9.04	10.23	-13.11	185	11.08	11.77	-6.26
5	9.04	10.25	-13.37	190	10.3	10.84	-5.21
10	9.06	10.30	-13.74	195	9.56	9.94	-3.99
15	9.02	10.20	-13.06	200	8.77	9.10	-3.73
20	8.7	9.67	-11.11	205	7.98	8.30	-3.95
25	8.05	8.87	-10.13	210	7.25	7.53	-3.87
30	7.29	8.05	-10.42	215	6.57	6.80	-3.47
35	6.49	7.27	-11.98	220	5.95	6.09	-2.40
40	5.83	6.52	-11.85	225	5.34	5.41	-1.33
45	5.22	5.80	-11.18	230	4.67	4.73	-1.32
50	4.6	5.09	-10.74	235	4.04	4.07	-0.72
55	4.01	4.41	-9.89	240	3.39	3.42	-0.87
60	3.35	3.74	-11.51	245	2.82	2.78	1.49
65	2.79	3.08	-10.24	250	2.31	2.14	7.26
70	2.18	2.42	-11.19	255	1.72	1.51	12.17
75	1.64	1.78	-8.43	260	1.1	0.88	19.81
80	1.03	1.14	-10.42	265	0.54	0.26	52.70
85	0.53	0.50	5.67	270	0.07	0.37	-432.34
90	0.25	0.14	45.02	275	0.44	1.00	-127.34
95	0.64	0.77	-20.83	280	1.02	1.63	-59.83
100	1.15	1.41	-22.64	285	1.59	2.27	-42.47
105	1.76	2.05	-16.52	290	2.28	2.91	-27.47
110	2.31	2.70	-16.70	295	2.81	3.55	-26.51
115	2.87	3.35	-16.60	300	3.44	4.21	-22.47
120	3.48	4.00	-15.07	305	4.02	4.88	-21.51
125	4.07	4.67	-14.83	310	4.64	5.57	-20.15
130	4.68	5.36	-14.49	315	5.37	6.29	-17.13
135	5.36	6.06	-13.14	320	6.04	7.01	-16.14
140	6.01	6.77	-12.71	325	6.74	7.77	-15.32
145	6.69	7.51	-12.30	330	7.47	8.56	-14.64
150	7.4	8.29	-11.99	335	8.16	9.37	-14.84
155	8.11	9.10	-12.21	340	8.84	10.04	-13.56
160	8.92	9.96	-11.64	345	9.19	10.33	-12.45
165	9.71	10.87	-11.90	350	9.17	10.28	-12.12
170	10.43	11.81	-13.26	355	9.12	10.22	-12.11
175	10.93	12.64	-15.63	360	9.06	10.23	-12.86
180	11.44	12.72	-11.18				

Table 4: Flux density measurement Bz (mT) over core case-1 without top plate at $r_2 z_6$.

Angle (deg.)	Bz Exp. r2z6 (mT)	Bz Sim. r2z6 (mT)	% Difference	Angle (deg.)	Bz Exp. r2z6 (mT)	Bz Sim. r2z6 (mT)	% Difference
0	6.12	6.35	-3.71	185	6.7	6.93	-3.39
5	6.13	6.34	-3.43	190	6.57	6.79	-3.27
10	6.08	6.28	-3.32	195	6.33	6.53	-3.19
15	5.99	6.16	-2.85	200	6	6.20	-3.34
20	5.8	5.97	-2.85	205	5.65	5.82	-3.00
25	5.54	5.70	-2.83	210	5.25	5.41	-3.03
30	5.18	5.37	-3.59	215	4.83	4.98	-3.12
35	4.83	4.99	-3.34	220	4.44	4.54	-2.32
40	4.39	4.59	-4.55	225	4.03	4.10	-1.75
45	3.96	4.17	-5.33	230	3.53	3.66	-3.59
50	3.53	3.74	-6.08	235	3.15	3.21	-1.98
55	3.12	3.31	-6.18	240	2.69	2.77	-2.90
60	2.65	2.88	-8.64	245	2.27	2.32	-2.40
65	2.23	2.44	-9.59	250	1.87	1.88	-0.64
70	1.84	2.01	-9.16	255	1.46	1.44	1.35
75	1.4	1.57	-12.40	260	1.01	1.00	1.04
80	0.95	1.14	-19.90	265	0.57	0.56	1.85
85	0.52	0.71	-35.61	270	0.14	0.12	14.16
90	0.13	0.27	-109.18	275	0.05	0.32	-538.86
95	0.15	0.16	-7.75	280	0.5	0.76	-51.81
100	0.52	0.60	-14.48	285	0.91	1.20	-31.77
105	0.97	1.03	-6.14	290	1.37	1.64	-19.69
110	1.4	1.46	-4.61	295	1.81	2.08	-14.96
115	1.81	1.90	-4.99	300	2.24	2.52	-12.58
120	2.26	2.34	-3.42	305	2.66	2.96	-11.38
125	2.68	2.77	-3.54	310	3.09	3.40	-10.10
130	3.05	3.21	-5.36	315	3.56	3.84	-7.81
135	3.5	3.65	-4.34	320	3.95	4.27	-8.10
140	3.97	4.09	-3.07	325	4.39	4.69	-6.84
145	4.4	4.53	-2.95	330	4.85	5.09	-4.96
150	4.85	4.96	-2.33	335	5.19	5.46	-5.17
155	5.24	5.39	-2.81	340	5.54	5.78	-4.24
160	5.61	5.79	-3.30	345	5.79	6.02	-4.04
165	6.07	6.17	-1.72	350	5.98	6.20	-3.63
170	6.38	6.51	-2.01	355	6.09	6.30	-3.46
175	6.6	6.77	-2.58	360	6.15	6.35	-3.21
180	6.72	6.93	-3.12				

Table 5: Flux density measurement Bz (mT) over core case-1 without top plate at $r_3 z_6$.

Angle (deg.)	Bz Exp. r3z6 (mT)	Bz Sim. r3z6 (mT)	% Difference	Angle (deg.)	Bz Exp. r3z6 (mT)	Bz Sim. r3z6 (mT)	% Difference
0	7.37	6.77	8.20	185	8.37	7.54	9.89
5	7.38	6.76	8.44	190	8.22	7.34	10.67
10	7.36	6.71	8.90	195	7.9	7.01	11.24
15	7.28	6.59	9.54	200	7.46	6.60	11.50
20	7.11	6.37	10.35	205	6.99	6.15	11.98
25	6.79	6.07	10.64	210	6.47	5.68	12.14
30	6.39	5.69	11.01	215	5.92	5.21	12.01
35	5.89	5.26	10.67	220	5.37	4.73	11.87
40	5.34	4.81	9.84	225	4.87	4.26	12.55
45	4.81	4.36	9.39	230	4.34	3.79	12.77
50	4.28	3.90	8.95	235	3.79	3.32	12.48
55	3.78	3.44	9.08	240	3.26	2.85	12.51
60	3.25	2.98	8.35	245	2.76	2.39	13.39
65	2.74	2.52	7.93	250	2.27	1.93	14.91
70	2.25	2.07	8.03	255	1.82	1.47	18.97
75	1.79	1.62	9.60	260	1.36	1.02	25.02
80	1.27	1.17	7.97	265	0.81	0.57	30.11
85	0.78	0.72	7.57	270	0.32	0.11	64.63
90	0.31	0.27	11.56	275	0.01	0.34	-3302.10
95	0.11	0.17	-57.13	280	0.49	0.79	-61.98
100	0.51	0.62	-21.50	285	0.96	1.25	-30.03
105	1.01	1.07	-5.66	290	1.48	1.70	-15.16
110	1.5	1.52	-1.07	295	2.01	2.16	-7.58
115	1.97	1.97	0.17	300	2.48	2.62	-5.75
120	2.48	2.42	2.44	305	2.95	3.09	-4.58
125	2.95	2.88	2.53	310	3.45	3.55	-2.91
130	3.47	3.33	3.91	315	4.02	4.02	0.06
135	3.97	3.80	4.35	320	4.57	4.48	1.91
140	4.49	4.26	5.06	325	5.06	4.94	2.31
145	5	4.73	5.36	330	5.61	5.39	3.90
150	5.56	5.20	6.42	335	6.08	5.81	4.45
155	6.1	5.67	7.00	340	6.57	6.17	6.06
160	6.61	6.14	7.16	345	6.92	6.45	6.81
165	7.12	6.58	7.55	350	7.18	6.63	7.69
170	7.63	6.99	8.36	355	7.34	6.72	8.38
175	8.05	7.33	8.93	360	7.39	6.77	8.44
180	8.3	7.55	9.00				

Table 6: Flux density measurement Bz (mT) over core case-1 without top plate at r_5 Z_6 .

Angle (deg.)	Bz Exp. r5z6 (mT)	Bz Sim. r5z6 (mT)	% Difference	Angle (deg.)	Bz Exp. r5z6 (mT)	Bz Sim. r5z6 (mT)	% Difference
0	5.54	6.02	-8.61	185	6.29	6.71	-6.67
5	5.54	6.00	-8.39	190	6.17	6.53	-5.77
10	5.5	5.96	-8.30	195	5.95	6.23	-4.66
15	5.42	5.85	-7.93	200	5.61	5.86	-4.46
20	5.26	5.66	-7.62	205	5.25	5.46	-3.97
25	5.03	5.39	-7.08	210	4.89	5.04	-3.09
30	4.73	5.05	-6.68	215	4.52	4.62	-2.17
35	4.39	4.67	-6.32	220	4.1	4.20	-2.32
40	4	4.27	-6.76	225	3.7	3.78	-2.05
45	3.63	3.87	-6.51	230	3.29	3.35	-1.92
50	3.26	3.45	-5.93	235	2.89	2.94	-1.60
55	2.88	3.04	-5.68	240	2.47	2.52	-2.17
60	2.46	2.64	-7.17	245	2.1	2.11	-0.67
65	2.09	2.23	-6.78	250	1.77	1.71	3.56
70	1.74	1.83	-5.14	255	1.37	1.30	4.95
75	1.36	1.43	-5.10	260	1	0.90	10.11
80	0.96	1.03	-7.40	265	0.6	0.50	17.18
85	0.56	0.63	-13.24	270	0.27	0.10	64.70
90	0.24	0.24	0.83	275	0.06	0.31	-411.48
95	0.16	0.16	0.88	280	0.37	0.71	-91.57
100	0.47	0.55	-18.00	285	0.77	1.11	-44.38
105	0.81	0.95	-17.43	290	1.15	1.52	-31.83
110	1.19	1.35	-13.37	295	1.52	1.92	-26.47
115	1.57	1.75	-11.37	300	1.94	2.33	-20.14
120	1.97	2.15	-9.15	305	2.31	2.74	-18.68
125	2.34	2.55	-9.17	310	2.78	3.16	-13.50
130	2.74	2.96	-8.12	315	3.06	3.57	-16.76
135	3.06	3.38	-10.32	320	3.49	3.98	-14.17
140	3.52	3.79	-7.60	325	3.87	4.39	-13.51
145	3.91	4.20	-7.50	330	4.28	4.79	-11.93
150	4.32	4.62	-6.98	335	4.65	5.16	-11.03
155	4.71	5.04	-7.01	340	4.94	5.49	-11.05
160	5.1	5.45	-6.93	345	5.16	5.73	-11.09
165	5.51	5.85	-6.20	350	5.35	5.89	-10.11
170	5.84	6.22	-6.47	355	5.46	5.98	-9.48
175	6.11	6.52	-6.76	360	5.51	6.02	-9.21
180	6.26	6.73	-7.46				

Table 7: Flux density measurement Bxy (mT) around core case-1 without top plate at r₆ z₁.

Angle (deg.)	Bxy Exp. r6z1 (mT)	Bxy Sim. r6z1 (mT)	% Difference	Angle (deg.)	Bxy Exp. r6z1 (mT)	Bxy Sim. r6z1 (mT)	% Difference
0	17.02	17.17	-0.88	185	22.51	22.15	1.60
5	17.05	17.31	-1.52	190	19.37	20.14	-3.98
10	17.36	17.76	-2.30	195	17.51	18.33	-4.68
15	17.78	18.66	-4.95	200	16.06	16.81	-4.67
20	18.4	17.92	2.61	205	14.71	15.46	-5.10
25	16.1	16.15	-0.31	210	13.14	14.22	-8.22
30	14.12	14.73	-4.32	215	11.86	13.08	-10.29
35	12.55	13.48	-7.41	220	10.64	12.06	-13.35
40	11.56	12.32	-6.57	225	9.5	10.71	-12.74
45	10.43	11.24	-7.77	230	8.23	9.74	-18.35
50	9.44	9.82	-4.03	235	7.23	8.81	-21.85
55	8.27	8.95	-8.22	240	6.09	7.94	-30.38
60	7.04	8.09	-14.91	245	5.05	7.17	-41.98
65	5.82	7.27	-24.91	250	4.13	6.48	-56.90
70	4.61	6.5	-41.00	255	3.17	5.87	-85.17
75	3.51	5.84	-66.38	260	2.29	5.38	-134.93
80	2.52	5.3	-110.32	265	1.27	5.01	-294.49
85	1.38	4.95	-258.70	270	0.4	4.81	-1102.50
90	0.3	4.81	-1503.33	275	0.39	4.92	-1161.54
95	0.37	4.87	-1216.22	280	1.39	5.29	-280.58
100	1.56	5.12	-228.21	285	2.37	5.79	-144.30
105	2.62	5.56	-112.21	290	3.34	6.41	-91.92
110	3.69	6.14	-66.40	295	4.15	7.12	-71.57
115	4.65	6.81	-46.45	300	5.15	7.91	-53.59
120	5.81	7.57	-30.29	305	6.65	8.78	-32.03
125	6.85	8.39	-22.48	310	7.79	9.72	-24.78
130	8.09	9.24	-14.22	315	8.93	11.26	-26.09
135	9.27	10.5	-13.27	320	10.18	12.3	-20.83
140	10.52	11.4	-8.37	325	11.32	13.41	-18.46
145	11.55	12.45	-7.79	330	12.64	14.66	-15.98
150	12.71	13.56	-6.69	335	14.26	16.09	-12.83
155	13.91	14.72	-5.82	340	16.35	17.35	-6.12
160	14.91	15.95	-6.98	345	18.53	17.92	3.29
165	16.26	17.32	-6.52	350	17.86	17.61	1.40
170	17.71	18.93	-6.89	355	17.23	17.24	-0.06
175	19.86	20.99	-5.69	360	16.91	17.17	-1.54
180	22.33	24.42	-9.36				

Table 8: Flux density measurement Bxy (mT) around core case-1 without top plate at r₆ Z₂.

Angle (deg.)	Bxy Exp. r6z2 (mT)	Bxy Sim. r6z2 (mT)	% Difference	Angle (deg.)	Bxy Exp. r6z2 (mT)	Bxy Sim. r6z2 (mT)	% Difference
0	13.8	14.58	-5.65	185	18.29	19.28	-5.41
5	13.86	14.7	-6.06	190	15.8	17.44	-10.38
10	14.26	15.2	-6.59	195	14.36	15.86	-10.45
15	14.98	16.22	-8.28	200	13.14	14.57	-10.88
20	14.15	15.69	-10.88	205	11.84	13.45	-13.60
25	12.31	14.12	-14.70	210	10.65	12.43	-16.71
30	10.95	12.91	-17.90	215	9.42	11.5	-22.08
35	9.73	11.86	-21.89	220	8.46	10.69	-26.36
40	8.74	10.91	-24.83	225	7.53	9.55	-26.83
45	7.84	10.05	-28.19	230	6.52	8.79	-34.82
50	6.85	8.8	-28.47	235	5.66	8.06	-42.40
55	5.88	8.13	-38.27	240	4.79	7.4	-54.49
60	5.01	7.48	-49.30	245	3.89	6.82	-75.32
65	4.03	6.85	-69.98	250	3.06	6.32	-106.54
70	3.15	6.28	-99.37	255	2.2	5.89	-167.73
75	2.4	5.78	-140.83	260	1.4	5.54	-295.71
80	1.44	5.4	-275.00	265	0.47	5.27	-1021.28
85	0.61	5.17	-747.54	270	0.13	5.11	-3830.77
90	0.12	5.1	-4150.00	275	0.97	5.18	-434.02
95	0.88	5.14	-484.09	280	1.74	5.44	-212.64
100	1.78	5.31	-198.31	285	2.62	5.8	-121.37
105	2.65	5.61	-111.70	290	3.51	6.24	-77.78
110	3.44	6.03	-75.29	295	4.38	6.76	-54.34
115	4.27	6.53	-52.93	300	5.31	7.35	-38.42
120	5.15	7.1	-37.86	305	6.23	8.01	-28.57
125	5.98	7.72	-29.10	310	7.21	8.75	-21.36
130	6.87	8.37	-21.83	315	8.16	10.1	-23.77
135	7.75	9.44	-21.81	320	9.22	10.91	-18.33
140	8.73	10.13	-16.04	325	10.23	11.81	-15.44
145	9.69	10.98	-13.31	330	11.6	12.84	-10.69
150	10.8	11.89	-10.09	335	12.8	14.07	-9.92
155	11.69	12.84	-9.84	340	14.95	15.11	-1.07
160	12.86	13.85	-7.70	345	15.04	15.48	-2.93
165	14.23	14.98	-5.27	350	14.28	15.06	-5.46
170	15.82	16.36	-3.41	355	13.85	14.63	-5.63
175	17.97	18.2	-1.28	360	13.78	14.58	-5.81
180	21.32	21.67	-1.64				

Table 9: Flux density measurement Bxy (mT) around core case-1 without top plate at r₆ z₃.

Angle (deg.)	Bxy Exp. r6z3 (mT)	Bxy Sim. r6z3 (mT)	% Difference	Angle (deg.)	Bxy Exp. r6z3 (mT)	Bxy Sim. r6z3 (mT)	% Difference
0	15.61	16.63	-6.53	185	22.46	21.46	4.45
5	15.53	16.78	-8.05	190	19.69	19.52	0.86
10	15.64	17.21	-10.04	195	18.11	17.78	1.82
15	15.97	18.1	-13.34	200	16.35	16.31	0.24
20	16.86	17.39	-3.14	205	14.89	15.01	-0.81
25	14.52	15.68	-7.99	210	13.74	13.82	-0.58
30	12.84	14.32	-11.53	215	12.1	12.72	-5.12
35	11.66	13.11	-12.44	220	10.76	11.74	-9.11
40	10.42	11.99	-15.07	225	9.64	10.43	-8.20
45	9.35	10.94	-17.01	230	8.53	9.5	-11.37
50	8.31	9.57	-15.16	235	7.4	8.61	-16.35
55	7.23	8.73	-20.75	240	6.37	7.78	-22.14
60	6.21	7.91	-27.38	245	5.21	7.03	-34.93
65	5.13	7.12	-38.79	250	4.28	6.37	-48.83
70	4.19	6.39	-52.51	255	3.12	5.8	-85.90
75	3.3	5.75	-74.24	260	2.18	5.33	-144.50
80	2.22	5.25	-136.49	265	1.21	4.98	-311.57
85	1.25	4.92	-293.60	270	0.29	4.79	-1551.72
90	0.33	4.79	-1351.52	275	0.53	4.89	-822.64
95	0.46	4.84	-952.17	280	1.49	5.24	-251.68
100	1.35	5.08	-276.30	285	2.41	5.72	-137.34
105	2.37	5.5	-132.07	290	3.44	6.3	-83.14
110	3.34	6.05	-81.14	295	4.53	6.98	-54.08
115	4.37	6.69	-53.09	300	5.7	7.73	-35.61
120	5.29	7.41	-40.08	305	6.92	8.57	-23.84
125	6.23	8.2	-31.62	310	7.89	9.48	-20.15
130	7.29	9.02	-23.73	315	8.97	10.97	-22.30
135	8.29	10.23	-23.40	320	10.18	11.98	-17.68
140	9.28	11.1	-19.61	325	11.56	13.04	-12.80
145	10.34	12.11	-17.12	330	12.7	14.24	-12.13
150	11.42	13.18	-15.41	335	14.3	15.62	-9.23
155	12.59	14.3	-13.58	340	15.89	16.82	-5.85
160	13.93	15.49	-11.20	345	17.88	17.37	2.85
165	15.29	16.8	-9.88	350	16.73	17.07	-2.03
170	17.01	18.36	-7.94	355	15.97	16.7	-4.57
175	18.73	20.34	-8.60	360	15.64	16.63	-6.33
180	21.43	23.69	-10.55				

Table 10: Flux density measurement Bz (mT) over core 1 with top plate at r2z6.

Angle (deg.)	Bz Exp. r2z6 (mT)	Bz Sim. r2z6 (mT)	% Difference	Angle (deg.)	Bz Exp. r2z6 (mT)	Bz Sim. r2z6 (mT)	% Difference
0	6.45	6.82	-5.7	185	6.96	7.29	-4.7
5	6.41	6.71	-4.7	190	6.81	7.08	-3.9
10	6.33	6.56	-3.7	195	6.54	6.77	-3.6
15	6.19	6.38	-3.0	200	6.28	6.43	-2.3
20	6.02	6.16	-2.3	205	5.81	6.02	-3.6
25	5.72	5.86	-2.5	210	5.38	5.56	-3.3
30	5.39	5.49	-1.9	215	4.93	5.14	-4.3
35	5.03	5.13	-1.9	220	4.48	4.72	-5.4
40	4.54	4.75	-4.6	225	4.02	4.30	-7.1
45	4.07	4.36	-7.2	230	3.55	3.78	-6.5
50	3.65	3.86	-5.7	235	3.06	3.27	-7.0
55	3.23	3.37	-4.3	240	2.65	2.79	-5.1
60	2.77	2.89	-4.5	245	2.17	2.33	-7.5
65	2.31	2.45	-6.2	250	1.76	1.87	-6.4
70	1.93	2.00	-3.9	255	1.34	1.41	-5.2
75	1.47	1.55	-5.6	260	0.86	0.97	-13.4
80	1.06	1.13	-6.3	265	0.38	0.53	-40.6
85	0.64	0.70	-8.9	270	0.02	0.09	-9104.0
90	0.14	0.27	-89.8	275	0.33	0.35	-7.5
95	0.19	0.17	9.7	280	0.77	0.80	-3.6
100	0.65	0.60	7.0	285	1.18	1.23	-4.6
105	1.07	1.03	3.6	290	1.64	1.69	-3.2
110	1.49	1.48	0.9	295	2.07	2.15	-3.9
115	1.94	1.93	0.8	300	2.51	2.61	-4.0
120	2.38	2.38	0.2	305	2.96	3.09	-4.3
125	2.8	2.84	-1.6	310	3.41	3.58	-5.0
130	3.21	3.33	-3.8	315	3.88	4.09	-5.3
135	3.69	3.83	-3.9	320	4.3	4.49	-4.4
140	4.15	4.25	-2.3	325	4.73	4.88	-3.3
145	4.55	4.66	-2.5	330	5.11	5.27	-3.1
150	5.01	5.08	-1.4	335	5.46	5.67	-3.8
155	5.45	5.55	-1.9	340	5.81	6.01	-3.4
160	5.88	6.00	-2.0	345	6.08	6.28	-3.2
165	6.26	6.41	-2.4	350	6.28	6.50	-3.5
170	6.6	6.80	-3.1	355	6.36	6.68	-5.0
175	6.85	7.14	-4.2	360	6.44	6.82	-5.8
180	6.99	7.40	-5.9				

Table 11: Flux density measurement Bz (mT) over core 1 with top plate at r3z6.

Angle (deg.)	Bz Exp. r3z6 (mT)	Bz Sim. r3z6 (mT)	% Difference	Angle (deg.)	Bz Exp. r3z6 (mT)	Bz Sim. r3z6 (mT)	% Difference
0	6.82	7.45	-9.2	185	7.67	8.24	-7.5
5	6.81	7.42	-8.9	190	7.47	8.05	-7.7
10	6.79	7.33	-8.0	195	7.19	7.71	-7.2
15	6.74	7.20	-6.9	200	6.79	7.22	-6.3
20	6.46	6.91	-7.0	205	6.3	6.70	-6.4
25	6.16	6.55	-6.4	210	5.79	6.17	-6.6
30	5.81	6.13	-5.6	215	5.31	5.63	-6.0
35	5.36	5.64	-5.2	220	4.79	5.09	-6.3
40	4.88	5.14	-5.4	225	4.3	4.56	-6.1
45	4.37	4.64	-6.1	230	3.79	4.04	-6.6
50	3.89	4.13	-6.1	235	3.3	3.52	-6.8
55	3.47	3.62	-4.5	240	2.81	3.02	-7.4
60	2.96	3.13	-5.7	245	2.4	2.52	-4.9
65	2.54	2.64	-3.8	250	1.94	2.02	-4.3
70	2.05	2.15	-5.1	255	1.51	1.54	-1.7
75	1.63	1.68	-2.8	260	1.01	1.05	-4.2
80	1.13	1.20	-6.4	265	0.55	0.57	-3.8
85	0.66	0.73	-10.9	270	0.12	0.09	23.5
90	0.23	0.26	-14.8	275	0.16	0.39	-142.6
95	0.14	0.20	-45.8	280	0.66	0.87	-31.7
100	0.53	0.67	-27.0	285	1.14	1.35	-18.6
105	0.94	1.14	-21.6	290	1.57	1.84	-17.1
110	1.36	1.62	-18.8	295	2.04	2.33	-14.3
115	1.85	2.09	-13.2	300	2.56	2.83	-10.5
120	2.33	2.58	-10.6	305	2.95	3.33	-12.9
125	2.92	3.07	-5.0	310	3.42	3.84	-12.3
130	3.3	3.56	-8.0	315	3.97	4.36	-9.8
135	3.79	4.07	-7.4	320	4.45	4.87	-9.5
140	4.28	4.58	-7.0	325	4.91	5.38	-9.6
145	4.77	5.10	-6.9	330	5.39	5.89	-9.3
150	5.21	5.63	-8.1	335	5.8	6.34	-9.4
155	5.7	6.16	-8.1	340	6.23	6.74	-8.2
160	6.19	6.69	-8.1	345	6.48	7.09	-9.3
165	6.66	7.22	-8.4	350	6.68	7.26	-8.7
170	7.08	7.67	-8.3	355	6.78	7.38	-8.9
175	7.43	8.03	-8.0	360	6.84	7.45	-8.9
180	7.66	8.30	-8.4				

Table 12: Flux density measurement Bz (mT) over core 1 with top plate at r5z6.

Angle (deg.)	Bz Exp. r5z6 (mT)	Bz Sim. r5z6 (mT)	% Difference	Angle (deg.)	Bz Exp. r5z6 (mT)	Bz Sim. r5z6 (mT)	% Difference
0	5.52	6.57	-19.1	185	6.16	7.29	-18.3
5	5.43	6.53	-20.2	190	5.99	7.11	-18.6
10	5.35	6.46	-20.8	195	5.7	6.81	-19.6
15	5.19	6.37	-22.7	200	5.36	6.35	-18.5
20	5.02	6.09	-21.3	205	4.99	5.89	-18.1
25	4.75	5.77	-21.5	210	4.59	5.43	-18.3
30	4.43	5.41	-22.0	215	4.12	4.93	-19.7
35	4.09	4.95	-21.1	220	3.73	4.46	-19.5
40	3.66	4.51	-23.2	225	3.28	4.00	-22.0
45	3.26	4.07	-24.9	230	2.85	3.53	-23.9
50	2.9	3.61	-24.5	235	2.46	3.08	-25.2
55	2.52	3.17	-25.8	240	2.06	2.64	-28.3
60	2.1	2.74	-30.6	245	1.73	2.20	-27.1
65	1.81	2.31	-27.4	250	1.35	1.77	-30.9
70	1.39	1.88	-35.4	255	0.95	1.34	-41.4
75	1.02	1.47	-43.9	260	0.57	0.92	-60.8
80	0.68	1.05	-54.3	265	0.19	0.49	-160.0
85	0.24	0.64	-165.1	270	0.07	0.07	-5.9
90	0.02	0.23	-1031.9	275	0.45	0.35	22.9
95	0.35	0.18	47.3	280	0.77	0.77	0.2
100	0.71	0.60	16.1	285	1.21	1.19	1.3
105	1.11	1.01	9.1	290	1.56	1.62	-3.7
110	1.4	1.42	-1.5	295	1.95	2.05	-5.1
115	1.79	1.84	-2.8	300	2.33	2.49	-6.9
120	2.24	2.27	-1.2	305	2.69	2.92	-8.7
125	2.59	2.69	-3.9	310	3.09	3.37	-9.1
130	2.99	3.12	-4.5	315	3.46	3.84	-10.8
135	3.36	3.58	-6.4	320	3.88	4.28	-10.3
140	3.73	4.02	-7.7	325	4.26	4.74	-11.2
145	4.09	4.48	-9.5	330	4.61	5.20	-12.8
150	4.46	4.96	-11.2	335	4.89	5.59	-14.4
155	4.85	5.42	-11.7	340	5.18	5.95	-14.8
160	5.23	5.89	-12.6	345	5.36	6.27	-16.9
165	5.54	6.38	-15.1	350	5.44	6.40	-17.7
170	5.88	6.77	-15.1	355	5.5	6.50	-18.2
175	6.08	7.09	-16.6	360	5.52	6.57	-19.1
180	6.19	7.36	-18.9				

Table 13: Flux density measurement Bxy (mT) beside core case-1 with top plate at r6z1.

Angle (deg.)	Bxy Exp. r6z1 (mT)	Bxy Sim. r6z1 (mT)	% Difference	Angle (deg.)	Bxy Exp. r6z1 (mT)	Bxy Sim. r6z1 (mT)	% Difference
0	15.22	17.02	-11.9	185	20.46	22.40	-9.5
5	15.2	17.20	-13.2	190	17.94	20.69	-15.4
10	15.31	17.61	-15.0	195	16.19	18.40	-13.6
15	15.6	18.41	-18.0	200	14.91	16.56	-11.1
20	16.33	17.18	-5.2	205	13.56	15.02	-10.8
25	14.65	15.77	-7.6	210	12.21	13.45	-10.1
30	13.02	13.94	-7.0	215	11.02	12.20	-10.7
35	11.64	12.58	-8.1	220	9.94	11.01	-10.7
40	10.52	11.31	-7.6	225	8.93	9.69	-8.5
45	9.68	9.96	-2.9	230	7.78	8.62	-10.8
50	8.58	8.88	-3.5	235	6.79	7.58	-11.6
55	7.62	7.83	-2.7	240	5.83	6.55	-12.4
60	6.58	6.80	-3.4	245	4.92	5.42	-10.2
65	5.6	5.68	-1.4	250	3.92	4.48	-14.2
70	4.43	4.74	-6.9	255	3.12	3.37	-8.2
75	3.49	3.64	-4.3	260	2.1	2.55	-21.5
80	2.64	2.80	-6.0	265	1.25	1.83	-46.1
85	1.5	2.02	-34.5	270	0.53	1.33	-150.1
90	0.53	1.31	-147.9	275	0.25	1.65	-558.2
95	0.15	1.38	-822.9	280	1.14	2.30	-102.1
100	1.24	1.92	-54.6	285	2.03	3.10	-52.7
105	2.18	2.65	-21.7	290	2.68	4.19	-56.4
110	3.1	3.69	-19.1	295	3.94	5.13	-30.2
115	3.93	4.59	-16.9	300	4.98	6.26	-25.8
120	4.97	5.67	-14.1	305	6.11	7.29	-19.3
125	5.93	6.65	-12.2	310	7.01	8.34	-19.0
130	6.8	7.65	-12.4	315	8.18	9.59	-17.2
135	7.86	8.82	-12.2	320	9.19	10.76	-17.1
140	8.95	9.90	-10.6	325	10.38	12.00	-15.6
145	9.79	11.02	-12.5	330	11.62	13.31	-14.6
150	10.77	12.17	-13.0	335	12.93	15.06	-16.5
155	12	13.61	-13.4	340	14.69	16.67	-13.5
160	13.23	14.97	-13.2	345	16.25	18.44	-13.5
165	14.66	16.58	-13.1	350	15.98	17.75	-11.1
170	16.04	18.37	-14.5	355	15.33	17.31	-12.9
175	17.9	20.60	-15.1	360	15.1	17.08	-13.1
180	20.51	23.33	-13.8				

Table 14: Flux density measurement Bxy (mT) beside core case-1 with top plate at r6z2.

Angle (deg.)	Bxy Exp. r6z2 (mT)	Bxy Sim. r6z2 (mT)	% Difference	Angle (deg.)	Bxy Exp. r6z2 (mT)	Bxy Sim. r6z2 (mT)	% Difference
0	14.23	12.86	9.6	185	21.07	17.35	17.7
5	14.22	13.02	8.4	190	18.06	15.91	11.9
10	14.45	13.42	7.1	195	16.25	14.02	13.7
15	14.92	14.23	4.6	200	14.77	12.55	15.0
20	15.8	13.18	16.6	205	13.39	11.39	14.9
25	14	12.06	13.8	210	12.2	10.14	16.9
30	12.2	10.54	13.6	215	10.92	9.24	15.4
35	10.99	9.53	13.3	220	9.77	8.37	14.3
40	9.8	8.60	12.2	225	8.86	7.33	17.2
45	8.87	7.53	15.1	230	7.83	6.57	16.1
50	7.89	6.75	14.4	235	6.88	5.82	15.4
55	7.04	6.00	14.8	240	5.89	5.08	13.8
60	6.06	5.25	13.4	245	4.99	4.22	15.5
65	5.11	4.39	14.1	250	4.08	3.56	12.8
70	4.16	3.72	10.5	255	3.14	2.72	13.2
75	3.29	2.89	12.2	260	2.38	2.21	7.3
80	2.26	2.34	-3.5	265	1.4	1.77	-26.3
85	1.5	1.85	-23.2	270	0.5	1.45	-190.2
90	0.58	1.39	-140.3	275	0.18	1.66	-822.6
95	0.09	1.47	-1537.3	280	1.15	2.04	-77.7
100	0.82	1.77	-115.9	285	1.91	2.53	-32.5
105	1.84	2.20	-19.8	290	2.93	3.35	-14.3
110	2.62	2.97	-13.5	295	3.67	4.00	-9.0
115	3.58	3.60	-0.5	300	4.74	4.86	-2.5
120	4.41	4.41	0.0	305	5.5	5.60	-1.9
125	5.3	5.12	3.4	310	6.57	6.36	3.2
130	6.17	5.83	5.5	315	7.54	7.32	2.9
135	7.18	6.74	6.1	320	8.62	8.19	5.0
140	8.22	7.53	8.4	325	9.79	9.09	7.1
145	9.17	8.34	9.0	330	11.01	10.06	8.6
150	10.07	9.18	8.8	335	12.29	11.49	6.5
155	11.22	10.31	8.1	340	14.02	12.78	8.9
160	12.58	11.32	10.0	345	16.29	14.31	12.1
165	13.65	12.59	7.8	350	15.19	13.57	10.6
170	15.2	13.98	8.0	355	14.53	13.12	9.7
175	17.14	15.81	7.8	360	14.28	12.91	9.6
180	19.86	18.23	8.2				

Table 15: Flux density measurement Bxy (mT) beside core case-1 with top plate at r6z3.

Angle (deg.)	Bxy Exp. r6z3 (mT)	Bxy Sim. r6z3 (mT)	% Difference	Angle (deg.)	Bxy Exp. r6z3 (mT)	Bxy Sim. r6z3 (mT)	% Difference
0	15.81	16.93	-7.1	185	23.04	22.28	3.3
5	15.84	17.10	-8.0	190	20.12	20.58	-2.3
10	16.04	17.51	-9.1	195	18.67	18.30	2.0
15	16.47	18.31	-11.2	200	16.57	16.47	0.6
20	17.21	17.08	0.7	205	15.25	14.93	2.1
25	15.14	15.68	-3.6	210	13.83	13.37	3.3
30	13.68	13.85	-1.3	215	12.64	12.13	4.0
35	12.11	12.51	-3.3	220	11.41	10.94	4.1
40	10.86	11.25	-3.6	225	10.09	9.63	4.6
45	9.88	9.90	-0.2	230	9	8.57	4.8
50	8.95	8.83	1.4	235	8.03	7.54	6.2
55	7.96	7.78	2.2	240	6.83	6.52	4.6
60	6.87	6.76	1.6	245	5.8	5.39	7.1
65	5.82	5.64	3.0	250	4.64	4.45	4.0
70	4.79	4.71	1.7	255	3.62	3.36	7.2
75	3.63	3.62	0.3	260	2.46	2.54	-3.3
80	2.64	2.78	-5.5	265	1.52	1.82	-20.1
85	1.7	2.01	-18.4	270	0.57	1.33	-133.2
90	0.64	1.32	-105.6	275	0.26	1.65	-533.0
95	0.06	1.39	-2211.2	280	1.3	2.30	-76.7
100	0.9	1.91	-112.5	285	2.23	3.08	-38.3
105	2.06	2.64	-28.2	290	3.32	4.17	-25.6
110	3	3.67	-22.4	295	4.36	5.10	-17.0
115	4.02	4.57	-13.6	300	5.63	6.23	-10.6
120	5.09	5.64	-10.8	305	6.65	7.25	-9.0
125	6.08	6.61	-8.8	310	7.56	8.29	-9.7
130	7.03	7.60	-8.1	315	8.71	9.53	-9.4
135	8.28	8.77	-5.9	320	9.88	10.70	-8.3
140	9.45	9.84	-4.2	325	11.19	11.93	-6.6
145	10.58	10.95	-3.5	330	12.64	13.23	-4.7
150	11.74	12.10	-3.1	335	13.86	14.97	-8.0
155	13.06	13.53	-3.6	340	15.75	16.58	-5.2
160	14.2	14.89	-4.8	345	17.71	18.34	-3.6
165	15.85	16.48	-4.0	350	16.55	17.66	-6.7
170	17.35	18.27	-5.3	355	16.04	17.21	-7.3
175	19.32	20.49	-6.0	360	15.75	16.98	-7.8
180	21.93	23.21	-5.9				

Table 16: Flux density measurement Bz (mT) over core case-2 for (Tb1) at r2z4.

Angle (deg.)	Bz Exp. Tb1 (mT)	Bz Sim. Tb1 (mT)	% Difference	Angle (deg.)	Bz Exp. Tb1 (mT)	Bz Sim. Tb1 (mT)	% Difference
0	7.89	5.09	-3.88	185	5.57	4.32	-10.77
5	8.07	5.1	-4.29	190	4.98	4.65	-9.93
10	8.3	5.13	-4.69	195	4.37	4.99	-9.43
15	8.59	5.06	-2.43	200	3.83	5.35	-8.96
20	8.73	4.82	2.63	205	3.27	5.73	-8.32
25	8.26	4.49	6.65	210	2.72	6.13	-7.17
30	7.26	4.16	6.52	215	2.19	6.56	-7.19
35	6.11	3.83	6.13	220	1.72	7.02	-6.85
40	5.08	3.52	6.63	225	1.22	7.51	-5.77
45	4.16	3.21	6.41	230	0.63	8.06	-5.08
50	3.14	2.92	6.11	235	0.15	8.65	-5.36
55	2.24	2.64	6.38	240	0.28	9.13	-2.70
60	1.23	2.36	7.09	245	0.8	8.84	6.06
65	0.41	2.09	5.86	250	1.3	7.72	13.74
70	0.29	1.82	10.34	255	1.83	6.24	19.17
75	1.25	1.55	10.92	260	2.39	4.76	24.56
80	2.22	1.29	11.64	265	2.98	3.3	29.03
85	3.05	1.03	15.57	270	3.51	1.86	42.59
90	4.01	0.78	18.75	275	4.03	0.44	74.57
95	5.02	0.52	25.71	280	4.66	0.99	-350.00
100	6.06	0.27	42.55	285	5.31	2.42	-112.28
105	7.09	0.01	96.15	290	5.98	3.86	-39.35
110	8.22	0.24	-60.00	295	6.68	5.26	-24.94
115	9.36	0.49	-96.00	300	7.36	6.26	-10.41
120	10.57	0.75	-66.67	305	7.74	6.53	-3.98
125	11.91	1	-47.06	310	7.71	6.29	-0.96
130	12.89	1.26	-35.48	315	7.63	6.03	-0.84
135	12.92	1.51	-27.97	320	7.56	5.82	-1.57
140	12.16	1.77	-25.53	325	7.51	5.64	-2.36
145	11.21	2.04	-22.89	330	7.44	5.49	-2.81
150	10.39	2.3	-19.79	335	7.43	5.36	-2.88
155	9.58	2.57	-16.29	340	7.47	5.26	-2.94
160	8.93	2.85	-15.38	345	7.52	5.19	-3.59
165	8.17	3.13	-13.00	350	7.6	5.14	-4.05
170	7.43	3.41	-13.29	355	7.72	5.11	-4.50
175	6.81	3.71	-12.08	360	7.87	5.09	-4.73
180	6.19	4.01	-11.70				

Table 17: Flux density measurement Bz (mT) over core case-2 for (Tb2) at r2z4.

Angle (deg.)	Bz Exp. Tb2 (mT)	Bz Sim. Tb2 (mT)	% Difference	Angle (deg.)	Bz Exp. Tb2 (mT)	Bz Sim. Tb2 (mT)	% Difference
0	7.49	7.56	-0.87	185	12.75	12.61	1.07
5	7.55	7.64	-1.20	190	13.25	11.76	11.24
10	7.62	7.72	-1.29	195	12.66	10.66	15.82
15	7.81	7.56	3.19	200	11.6	9.55	17.67
20	7.89	7.08	10.32	205	10.38	8.49	18.22
25	7.62	6.43	15.64	210	9.35	7.47	20.09
30	6.99	5.78	17.28	215	8.08	6.50	19.60
35	6.27	5.16	17.76	220	7.06	5.56	21.30
40	5.57	4.55	18.30	225	6.09	4.65	23.73
45	4.96	3.96	20.15	230	5.07	3.77	25.71
50	4.3	3.39	21.15	235	4.08	2.90	28.84
55	3.73	2.83	24.11	240	3.19	2.05	35.66
60	3.09	2.28	26.22	245	2.33	1.21	48.10
65	2.59	1.74	32.97	250	1.5	0.37	75.34
70	2.03	1.20	40.97	255	0.69	0.47	31.86
75	1.45	0.66	54.14	260	0.08	1.31	-1543.70
80	0.92	0.13	85.37	265	0.9	2.17	-140.98
85	0.4	0.39	1.54	270	1.77	3.04	-71.52
90	0.18	0.92	-412.12	275	2.76	3.93	-42.29
95	0.6	1.45	-141.82	280	3.59	4.84	-34.92
100	1.11	1.98	-78.64	285	4.66	5.79	-24.20
105	1.67	2.52	-50.82	290	5.67	6.76	-19.24
110	2.2	3.06	-39.08	295	6.82	7.72	-13.20
115	2.73	3.61	-32.14	300	7.84	8.40	-7.11
120	3.27	4.16	-27.31	305	8.32	8.54	-2.63
125	3.81	4.73	-24.11	310	8.24	8.31	-0.83
130	4.39	5.31	-20.86	315	8.05	8.08	-0.38
135	5.01	5.90	-17.70	320	7.86	7.90	-0.53
140	5.67	6.51	-14.86	325	7.69	7.75	-0.84
145	6.28	7.15	-13.86	330	7.55	7.64	-1.20
150	6.91	7.81	-13.09	335	7.46	7.56	-1.30
155	7.73	8.51	-10.10	340	7.39	7.50	-1.52
160	8.42	9.24	-9.77	345	7.34	7.48	-1.86
165	9.16	10.01	-9.33	350	7.34	7.48	-1.87
170	9.97	10.83	-8.63	355	7.37	7.50	-1.82
175	10.87	11.68	-7.50	360	7.41	7.56	-1.96
180	11.77	12.54	-6.57				

Table 18: Flux density measurement Bz (mT) over core case-2 for (Tb3) at r2z4.

Angle (deg.)	Bz Exp. Tb3 (mT)	Bz Sim. Tb3 (mT)	% Difference	Angle (deg.)	Bz Exp. Tb3 (mT)	Bz Sim. Tb3 (mT)	% Difference
0	4.9	8.12	-2.90	185	3.9	4.70	15.61
5	4.89	8.34	-3.31	190	4.23	4.16	16.55
10	4.9	8.54	-2.84	195	4.56	3.62	17.16
15	4.94	8.33	3.01	200	4.91	3.09	19.26
20	4.95	7.57	13.24	205	5.29	2.57	21.39
25	4.81	6.54	20.83	210	5.72	2.05	24.49
30	4.45	5.50	24.20	215	6.12	1.54	29.64
35	4.08	4.50	26.34	220	6.57	1.03	40.08
40	3.77	3.53	30.54	225	7.1	0.52	57.23
45	3.43	2.58	37.94	230	7.67	0.01	97.74
50	3.11	1.66	47.10	235	8.21	0.50	-230.01
55	2.82	0.75	66.42	240	8.89	1.01	-259.54
60	2.54	0.15	87.84	245	9.41	1.52	-90.24
65	2.22	1.05	-155.95	250	8.95	2.04	-57.07
70	2.03	1.95	-573.30	255	7.72	2.57	-40.33
75	1.74	2.86	-129.15	260	6.31	3.10	-29.78
80	1.46	3.79	-70.72	265	4.65	3.64	-22.30
85	1.22	4.73	-55.22	270	3.24	4.20	-19.60
90	0.96	5.70	-42.19	275	1.73	4.77	-18.36
95	0.7	6.71	-33.64	280	0.22	5.36	-14.99
100	0.47	7.75	-27.92	285	1.14	5.96	-12.32
105	0.26	8.84	-24.64	290	2.77	6.59	-10.16
110	0.15	9.97	-21.27	295	4.21	7.20	-7.83
115	0.25	11.14	-19.05	300	5.67	7.65	-3.94
120	0.45	12.22	-15.57	305	6.28	7.78	-0.49
125	0.68	12.72	-6.76	310	6.23	7.69	0.32
130	0.93	12.21	5.24	315	5.98	7.60	0.44
135	1.18	11.36	12.06	320	5.73	7.54	0.21
140	1.41	10.55	13.26	325	5.51	7.52	-0.09
145	1.66	9.77	12.83	330	5.34	7.52	-1.02
150	1.92	9.04	13.04	335	5.21	7.54	-1.52
155	2.21	8.34	12.98	340	5.11	7.60	-1.71
160	2.47	7.67	14.09	345	5.01	7.68	-2.16
165	2.77	7.03	13.89	350	4.94	7.80	-2.60
170	3.01	6.42	13.56	355	4.89	7.94	-2.90
175	3.31	5.83	14.38	360	4.86	8.12	-3.16
180	3.59	5.25	15.11				

Table 19: Flux density measurement Bxy (mT) beside core case-2 for (Tb1) at r6z2

Angle (deg.)	Bxy Exp. Tb1 (mT)	Bxy Sim. Tb1 (mT)	% Difference	Angle (deg.)	Bxy Exp. Tb1 (mT)	Bxy Sim. Tb1 (mT)	% Difference
0	9.79	6.88	-8.82	185	6.62	6.25	-20.79
5	10.15	6.95	-9.41	190	5.95	6.62	-18.22
10	10.73	7.17	-10.89	195	5.16	7.01	-15.37
15	11.72	7.44	-10.19	200	4.48	7.42	-14.20
20	13.32	7.19	2.84	205	3.8	7.85	-14.11
25	10.3	6.59	-2.03	210	3.11	8.31	-11.81
30	8.56	6.11	-4.07	215	2.46	8.81	-11.01
35	6.74	5.70	-6.85	220	1.76	9.39	-9.84
40	5.2	5.33	-9.62	225	1.16	10.04	-10.09
45	4.06	4.99	-11.67	230	0.43	11.09	-10.86
50	2.83	4.42	-9.10	235	0.12	12.34	-11.21
55	1.81	4.10	-11.61	240	0.78	14.44	-13.24
60	0.59	3.80	-15.05	245	1.39	14.82	8.35
65	0.36	3.52	-18.78	250	2.16	14.11	-5.70
70	1.5	3.25	-24.98	255	2.81	12.25	-24.01
75	2.8	3.00	-36.21	260	3.44	10.83	-47.96
80	3.98	2.76	-46.60	265	4.06	9.77	-79.56
85	5.05	2.54	-60.71	270	4.87	8.99	-151.23
90	6.44	2.40	-98.42	275	5.71	8.28	-404.93
95	7.32	2.21	-172.33	280	6.46	8.35	-20786.72
100	8.48	2.14	-310.91	285	7.31	8.83	-337.23
105	9.76	2.11	-816.80	290	8.31	9.75	-143.03
110	11.19	2.13	-10553.62	295	9.45	11.06	-77.53
115	12.94	2.20	-686.24	300	11.37	11.18	-11.25
120	15.09	2.32	-256.69	305	10.55	10.15	-2.20
125	18.1	2.48	-161.30	310	9.85	8.83	-4.85
130	20.05	2.68	-106.27	315	9.51	8.16	-7.32
135	16.8	2.90	-81.17	320	9.33	7.71	-8.26
140	14.75	3.24	-64.53	325	9.21	7.41	-8.63
145	13.46	3.49	-52.56	330	9.14	7.21	-9.51
150	12.51	3.78	-45.78	335	9.12	7.06	-10.15
155	11.39	4.07	-37.59	340	9.12	6.95	-10.36
160	10.51	4.38	-33.48	345	9.19	6.87	-10.33
165	9.65	4.69	-28.42	350	9.33	6.83	-9.56
170	8.78	5.00	-22.85	355	9.48	6.82	-9.50
175	8.03	5.32	-21.45	360	9.75	6.88	-9.87
180	7.27	5.68	-17.83				

Table 20: Flux density measurement Bxy (mT) beside core case-2 for (Tb2) at r6z2

Angle (deg.)	Bxy Exp. Tb2 (mT)	Bxy Sim. Tb2 (mT)	% Difference	Angle (deg.)	Bxy Exp. Tb2 (mT)	Bxy Sim. Tb2 (mT)	% Difference
0	9.7	10.30	-6.17	185	20.81	19.75	5.08
5	9.94	10.54	-6.04	190	18.63	17.72	4.89
10	10.18	11.13	-9.34	195	15.6	15.71	-0.68
15	11.21	11.38	-1.51	200	13.71	14.17	-3.35
20	11.1	10.88	2.01	205	11.93	12.89	-8.03
25	9.63	9.84	-2.16	210	10.42	11.74	-12.64
30	8.47	8.98	-5.98	215	9.1	10.67	-17.23
35	7.42	8.24	-11.05	220	7.76	9.69	-24.83
40	6.51	7.59	-16.61	225	6.62	8.90	-34.37
45	5.73	7.01	-22.33	230	5.36	7.82	-45.98
50	4.92	6.02	-22.42	235	4.19	7.24	-72.72
55	4.22	5.51	-30.51	240	3.18	6.73	-111.69
60	3.46	5.07	-46.39	245	2.12	6.35	-199.64
65	2.77	4.71	-69.88	250	1	6.12	-512.01
70	2.12	4.43	-108.98	255	0.13	6.06	-4565.16
75	1.35	4.24	-214.28	260	0.92	6.22	-575.84
80	0.61	4.14	-578.73	265	1.93	6.57	-240.58
85	0.01	4.12	-41100	270	3.02	7.09	-134.85
90	0.71	4.23	-496.14	275	4.22	8.06	-90.90
95	1.33	4.66	-250.45	280	5.64	8.82	-56.34
100	2.02	5.03	-149.02	285	6.8	9.78	-43.88
105	2.63	5.44	-107.01	290	8.58	10.99	-28.04
110	3.34	5.90	-76.53	295	10.83	12.47	-15.16
115	4.04	6.39	-58.05	300	12.94	13.05	-0.87
120	4.82	6.91	-43.43	305	11.22	12.49	-11.36
125	5.61	7.49	-33.59	310	10.44	11.47	-9.91
130	6.25	8.12	-29.96	315	10.03	10.94	-9.06
135	6.99	8.77	-25.51	320	9.75	10.58	-8.46
140	7.88	9.72	-23.36	325	9.55	10.34	-8.29
145	8.65	10.40	-20.18	330	9.42	10.20	-8.26
150	9.46	11.16	-17.97	335	9.33	10.11	-8.34
155	10.4	11.99	-15.26	340	9.29	10.05	-8.19
160	11.33	12.88	-13.67	345	9.32	10.02	-7.56
165	12.42	13.86	-11.57	350	9.38	10.04	-7.01
170	13.69	14.99	-9.53	355	9.5	10.12	-6.50
175	15.09	16.43	-8.90	360	9.64	10.30	-6.83
180	17.19	18.57	-8.04				

Table 21: Flux density measurement Bxy (mT) beside core case-2 for (Tb3) at r6z2,

Angle (deg.)	Bxy Exp. Tb3 (mT)	Bxy Sim. Tb3 (mT)	% Difference	Angle (deg.)	Bxy Exp. Tb3 (mT)	Bxy Sim. Tb3 (mT)	% Difference
0	6.32	11.00	-12.40	185	5.17	7.44	-12.31
5	6.35	11.54	-13.74	190	5.6	6.85	-15.06
10	6.47	12.60	-17.45	195	6.08	6.31	-22.24
15	6.75	13.16	-12.32	200	6.5	5.82	-29.98
20	7.4	12.61	5.34	205	6.88	5.38	-41.61
25	6.46	11.12	-7.94	210	7.43	4.98	-60.12
30	5.87	9.90	-15.68	215	7.94	4.62	-87.73
35	5.33	8.92	-32.37	220	8.55	4.31	-144.65
40	4.86	8.14	-56.55	225	9.12	4.09	-252.81
45	4.47	7.53	-85.57	230	10	4.01	-832.53
50	4.05	6.66	-135.24	235	11.1	4.10	-3313.01
55	3.67	6.38	-252.33	240	12.75	4.26	-445.57
60	3.3	6.34	-973.74	245	16.17	4.49	-223.13
65	2.96	6.52	-1711.65	250	13.35	4.80	-122.28
70	2.6	6.90	-359.78	255	9.88	5.18	-84.48
75	2.2	7.42	-164.91	260	7.32	5.64	-64.09
80	1.88	8.05	-102.23	265	5.44	6.17	-52.04
85	1.58	8.74	-73.17	270	3.58	6.76	-38.81
90	1.21	9.49	-47.35	275	1.64	7.67	-34.33
95	0.81	11.07	-51.18	280	0.04	8.29	-28.37
100	0.52	12.22	-44.05	285	2.02	9.02	-23.37
105	0.23	13.48	-38.07	290	4.01	9.87	-18.79
110	0.02	14.88	-33.00	295	6.23	10.90	-15.39
115	0.28	16.59	-28.23	300	10.05	11.41	-0.36
120	0.65	18.96	-25.67	305	9.93	11.15	-5.73
125	0.95	20.40	-12.69	310	8.42	10.59	-7.50
130	1.3	18.17	9.37	315	7.6	10.35	-8.81
135	1.6	16.32	2.87	320	7.12	10.17	-8.96
140	1.97	14.57	1.24	325	6.82	10.08	-9.47
145	2.29	13.55	-0.70	330	6.58	10.07	-10.13
150	2.59	12.66	-1.18	335	6.41	10.09	-10.66
155	2.96	11.83	-3.85	340	6.3	10.15	-11.30
160	3.28	11.04	-5.08	345	6.23	10.24	-11.48
165	3.65	10.30	-6.76	350	6.23	10.39	-11.40
170	4.07	9.61	-9.51	355	6.23	10.63	-12.15
175	4.38	9.00	-12.09	360	6.26	11.00	-12.86
180	4.82	8.46	-16.33				

Publications:

Section B: Sensor Modelling

Paper presented at Sensors and their Applications VIII, 7-10 September 1997

41

Finite Element Modelling of Variable Transformers Used for Voltage Regulation and Control

S H Khan J M El-Shawish K T V Grattan L Finkelstein

Measurement and Instrumentation Centre, Department of Electrical, Electronic and Information Engineering, City University, Northampton Square, London EC1V, 0HB, UK

Abstract—This paper concerns the finite element investigation of variable autotransformers used for voltage control and regulation. Various 3D models of a commercial variable transformer is developed for modelling and computation of magnetic field distribution in the complex geometry of the transformers. Some of the preliminary results are given in terms of magnetic flux density across the cross-section of the transformer core. The results validate the models for the simplistic cases investigated and establish confidence in the adopted modelling approach.

1. Introduction

Variable transformers are adjustable autotransformers which differ from the conventional transformers in that there is an electrical contact between the primary and secondary windings. Unlike conventional transformers which have two or more windings, an autotransformer has a single winding, all or part of which is common to both the primary and secondary circuits. Compared to conventional transformers, autotransformers may have lower leakage reactance and losses, smaller magnetizing current, and usually lower cost. Variable transformers are widely used in many applications related to measurement, control and testing: voltage and current control in development and experimental work, testing of electrical and electronic equipment, testing and calibration of electrical measuring instruments (e.g. voltmeters, ammeters, etc.), speed control of electrical motors, etc. Fig. 1 shows the simplified longitudinal section of a 25 A commercial variable transformer (type TS 1225) used as a voltage regulator. It consists of a laminated toroidal core made of ferromagnetic steel and fixed to the metallic (or nonmetallic) base plate. A single-layer toroidal winding is tightly and closely wound on the toroidal core, the turns of which, although lying side by side on the outer surface, overlap on the inner surface. This is due to the significant difference in circumferential lengths of the inner and outer surfaces of the toroidal core, especially for large transformers. The output voltage is varied by rotating the top plate, made of aluminium which holds one or multiple segmented brushes (through a brush holder attached to it (not shown in Fig. 1)) that slide over the winding turns on the outer surface of the toroidal core. The brush track which acts as the commutator is made by stripping off insulation from the outer surface of each turn of the winding. For large

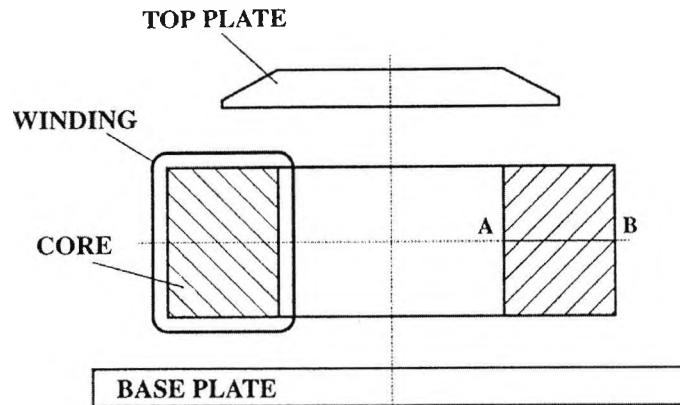


Fig. 1. Simplified longitudinal section of a variable transformer (type TS 1225) showing its main constructive elements (not drawn to scale).

variable transformers the commutator surface is usually gold-plated to increase the effectiveness and reliability of commutation. The brush, made of electrographite is always in contact with one or more turns and continuously taps off the desired fraction of the winding input voltage.

Although conventional transformers are well covered in the literature [1-4], very few studies have been done so far which cover autotransformers and, to our knowledge none concerning the type of variable transformers investigated in this paper. Despite the fact that variable transformers are, in general fairly robust and reliable electrical devices comprehensive studies are needed to understand and quantify, in details various electromagnetic, thermal and electromechanical processes associated with these, apparently simple but practically complicated devices. A detailed study and investigation into these processes are necessary for the CAD, optimization, and performance evaluation and prediction of the transformers. This is especially justified with the recent reports of sudden and unexplained failures of some of the variable transformers working as stabilizers as a result of thermal run away. Some of these failures seem to be related to the so called shorted turn losses, mechanical damage to insulation and brush contacts, but the exact causes and mechanism of these failures are still unknown. Furthermore, there are also reports of large unwanted circulating and eddy currents in various constructive parts of the transformer resulting in the temperature rise and local 'hot spots'. The mechanical damage to the insulation may be attributed to the long-term accumulated effects of such electromagnetic and mechanical factors as the voltage transients in the winding at switch on, high current overloads and switch-on current surges producing high transient magnetic fields and, hence large mechanical forces on the winding, increased copper loss and vibration of the winding at frequencies higher than the nominal 50 Hz (in the presence of higher harmonics). Magnetic flux density in the core needs to be limited in order to avoid saturation and excessive core losses due to hysteresis and, possibly eddy currents, especially in the case of any insulation loss between the laminations. Saturation of the core may give rise to leakage flux inducing eddy currents and large circulating currents in the nearby constructive parts of the transformer. In general, iron saturation introduces nonlinear effects in the performance of the transformer. In this way various effects which are detrimental to the normal performance of variable transformers are essentially related to the electromagnetic processes in the transformer which

need to be understood, investigated and quantified. Thus the importance of modelling and computation of magnetic field distribution in variable transformers cannot be underestimated for effective design, and measurement and control.

2. Finite Element Modelling of Magnetic Fields in Variable Transformers

In general, the 3D magnetic field distribution in the variable transformer shown in Fig. 1 is given by the following nonlinear Poisson's equation [5, 6]:

$$\text{curl} \left(\frac{1}{\mu} \text{curl} \mathbf{A} \right) = \mathbf{J} - \sigma \left(\frac{\partial \mathbf{A}}{\partial t} \right) \quad (1)$$

where the vectors \mathbf{A} and \mathbf{J} are magnetic vector potential and source current density respectively, and μ and σ are, respectively permeability and conductivity. For given geometric and material parameters of the transformer, the above equation is solved in the 3D region Ω of the transformer using the numerical finite element method (FEM) [7, 8]. For this the following simplifying assumptions are made: (i) The continuous N-turn toroidal winding of the variable transformer is replaced by N single-turn coils tightly and compactly wound around the toroidal core. This is justified given the closely wound toroidal winding and it simplifies the definition of the 3D finite element (FE) models. (ii) There is no displacement current. (iii) The magnetic circuit in the transformer is piece-wise homogeneous and isotropic, and there is no hysteresis effect. (iv) The source current density \mathbf{J} is constant and uniformly distributed over the conductor cross-section. Because of the asymmetry, both in the geometry and field distribution in the variable transformer shown in Fig. 1, the above equation must be solved in 3D taking into account saturation nonlinearities and eddy-current effects. For this various 3D FE models of the transformer have been developed using the commercial software package OPERA-3d [9]. Despite the flexibility and user-friendliness of the software package, the complex geometry and the need for incorporating detail geometric features make the 3D model definition of the transformer quite complicated and time consuming. For effective and efficient model definition a systematic modelling approach has been adopted to set up the basic 3D model. During the course of model development substantial effort has been put into the FE realization of the N single-turn coils because of the way the original toroidal winding, which they replace is wound. As explained in Section 1, the single-turn coils, although lie side by side on the outer surface of the core, overlap on its other surfaces because of the difference in circumferential lengths between the inner and outer surfaces. The complex geometric features of the base and top plates also pose many challenges for model building.

Figs. 2-6 show various stages of development of the 3D FE model for the TS 1225 variable transformer under investigation. The basic model-building strategy for 3D models in OPERA-3d involves the definition of a 2D base plane which contains the 'foot prints' of all the geometric features of the device being modelled. The base plane is then extruded or swept through in space in the third dimension to create the volume discretization. The typical model shown in Figs. 2-6 contains over 50k 8-noded hexahedral elements including the air regions surrounding the transformer. It has been used to calculate the magnetic field distribution in the transformer for various linear and nonlinear magnetostatic cases without eddy current effects using TOSCA – the analysis module for magnetostatic cases in OPERA-3d.

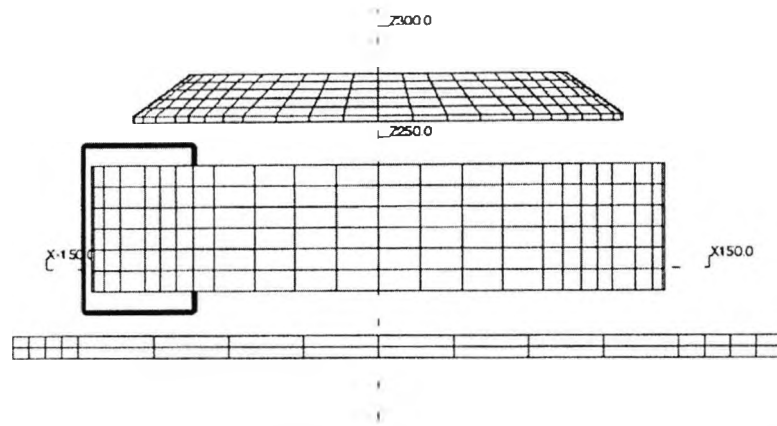


Fig. 2. 2D wire-frame representation of the 3D finite element model of the variable transformer TS 1225 showing the main constructive features.

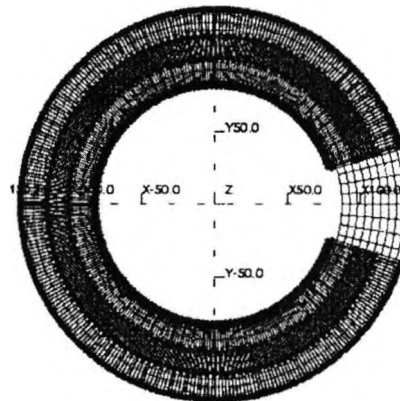


Fig. 3. Top view of the wound core of the variable transformer TS 1225 showing details of the winding arrangement. (continuous N-turn toroidal winding is replaced by N single-turn coils).

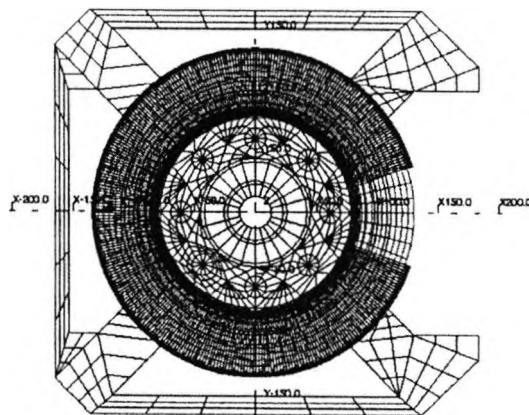


Fig. 4. Top view of the full 3D finite element model of the variable transformer TS 1225 showing details of the top and base plates, and the winding.

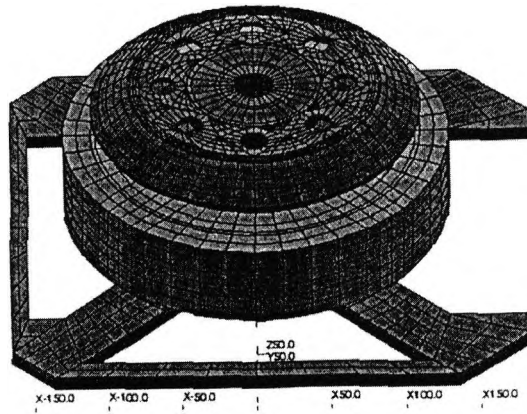


Fig. 5 3D finite element model of the variable transformer TS 1225 showing clearly various volume layers and subdivisions in base and top plates, and in the core (winding not shown).

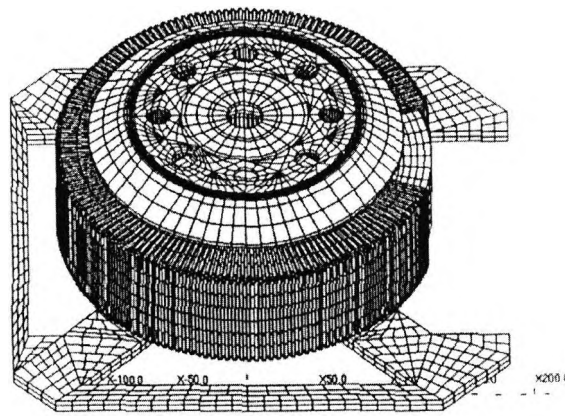


Fig. 6 Full 3D finite element model of the variable transformer TS 1225 showing the compact arrangement of overlapping single-turn coils around the toroidal core.

3. Results and Discussion

Fig. 7 shows some of the initial modelling results obtained for simplistic magnetostatic cases, for which analytical solutions are known. This comprises the first step to establish confidence in the adopted modelling approach and to validate the results obtained so far. As can be seen from Fig. 7, the modelling results (curve 1) are in good agreement with analytical ones (curve 2). The slight disagreement between the two curves is mainly attributed to the discretization errors in FE modelling which can be minimized by further mesh refinement. Although comparison of simulation results with experimental data is the ultimate way to evaluate modelling accuracy, analytical results, if exist also provide the first step towards model validation. One other technique that has been successfully used to assess the modelling accuracy is to calculate the magnetomotive force (m.m.f.) for a given coil from FE field computation

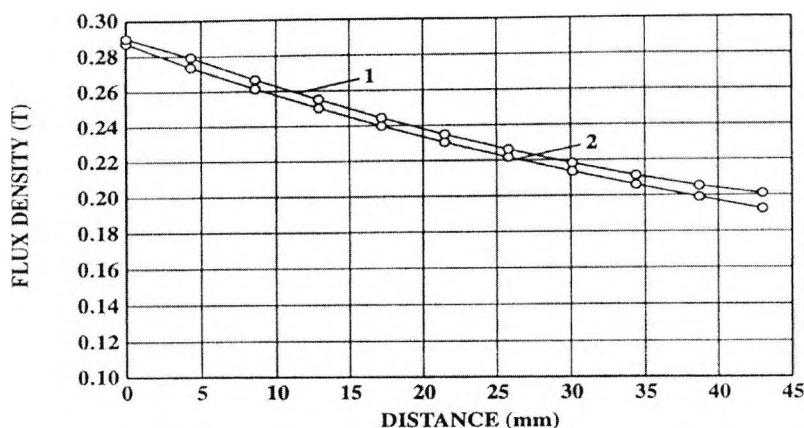


Fig. 7. Variation of magnetic flux density B in the transformer core along line AB shown in Fig. 1: 1 – modelling, 2 – analytical.

results using Ampère's Law [6]: $\oint \mathbf{H} \cdot d\mathbf{l} = Ni$, where \mathbf{H} is the calculated magnetic field intensity vector and $d\mathbf{l}$ is the infinitesimal element of any path l enclosing the total current Ni (m.m.f.).

4. Conclusions

Methodologies have been developed for the 3D FE modelling of a commercial variable transformer. Some of the preliminary results of 3D FE modelling of magnetic field distribution in the transformer have been shown to give good agreement with corresponding analytical results. This establishes confidence in the adopted modelling strategy and the developed FE models of the transformer.

5. Acknowledgements

The authors would like to thank Messrs. W. Lyons, D. Maule, N. Lee and others at Claude Lyons Limited, UK for active collaborations and many useful discussions.

References

- [1] L F Blume, G Boyajian, A Camilli *et al* 1951 *Transformer Engineering: A Treatise on the Theory, Operation and Application of Transformers* (Chapman & Hall Ltd.)
- [2] P Silvester and A Konrad 1973 *IEEE Trans. PAS* **6** 1843-1855
- [3] C M Arturi 1995 *IEEE Trans. Magn.* **3** 2036-2039
- [4] B Baodong, D Xie, J Cui *et al* 1995 *IEEE Trans. Magn.* **6** 3572-3574
- [5] K J Binns, P J Lawrenson, and C W Trowbridge 1992 *The Analytical and Numerical Solution of Electric and Magnetic Fields* (Chichester: John Wiley & Sons)
- [6] J D Kraus 1992 *Electromagnetics* (London: McGraw-Hill Inc.)
- [7] O C Zienkiewicz and R I Taylor 1991 *The Finite Element Method* (Maidenhead: McGraw-Hill Inc.)
- [8] P P Silvester and R L Ferrari 1990 *Finite Elements for Electrical Engineers* (Cambridge: Cambridge University Press)
- [9] OPERA-3d, Version 2.609 1997, Vector Fields Limited, Oxford, UK.

Design Investigation of Commercial Voltage Stabilisers by 3D Finite Element Modelling

S H Khan, J M El-Shawish, K T V Grattan, and L Finkelstein

Measurement and Instrumentation Centre, Department of Electrical, Electronic and Information Engineering, City University, Northampton Square, London EC1V 0HB, UK

Abstract: This paper presents some of the results of investigation of various designs of commercial variable transformers used as voltage stabilisers. The investigation is carried out by 3D finite element (FE) modelling and computation of nonlinear magnetic field distribution in various designs of such transformers. The effects of electromagnetic and geometric parameters, and various operational regimes (brush and tap positions) on the distribution of magnetic field and saturation level in the core are calculated and discussed. Their effects on magnetic field distribution in the air above the core are also discussed. These factors ultimately define the overall size and performance of the voltage stabilisers investigated in this paper. Results are presented in terms of flux plots and design curves.

1. Introduction

Variable transformers are widely used for voltage regulation and control in many applications. Unlike conventional transformers, variable transformers do not have any electrical contact between the primary and secondary windings. It is basically an adjustable autotransformer with a sliding tapping which supplies completely variable voltage over a required range. Compared to conventional transformers, variable transformers may have lower leakage reactance and losses, smaller magnetising current, and in some cases lower cost. Voltage stabilisers serve as essential subsystems in many systems where the safety and reliability of the system as a whole is critically dependent upon their long-term safe, robust

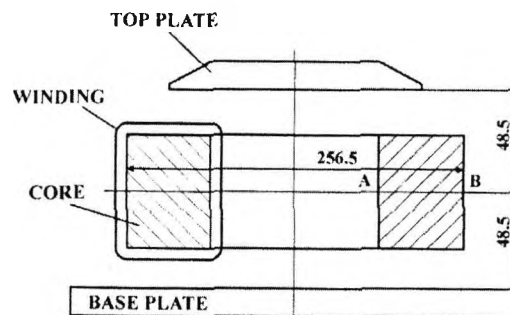


Fig. 1. Simplified longitudinal section of one of the designs of commercial voltage stabilisers investigated (dimensions in mm, not drawn to scale).

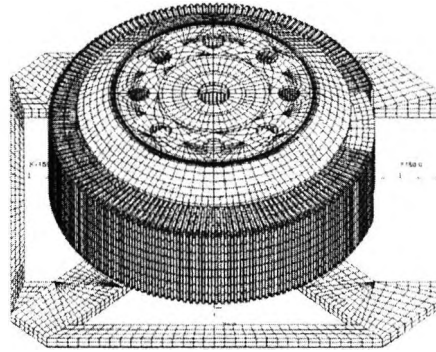


Fig. 2. Typical 3D FE model of the commercial voltage stabiliser shown in Fig.1.

and reliable operation. Fig. 1 shows the simplified longitudinal section of one of the designs (e.g. type TS 1225) of the commercial variable transformer investigated. This type of variable transformers is normally used as either three-phase or single phase voltage stabilisers (with nominal parameters: 240 V/0-240 V, 0-275 V, 30 A, 7.2 kVA). It consists of a single-layer helical winding tightly and closely wound on the toroidal core. The core is made of spirally wound grain-oriented silicon steel. The winding turns lie side by side on the outer surface but overlap on the inner surface because of the significant difference in circumferential lengths of the inner and outer surfaces of the core, especially for large transformers. The output voltage is varied by rotating the aluminium top plate which holds one or multiple segmented brushes (attached to the brush gear not shown in Fig. 1) that traverse the winding turns (brush track made by stripping off insulation from the outer surface of each of the winding turns) on the outer surface of the core. Despite the fact that these voltage stabilisers are seemingly simple and robust electrical devices, they rely on complex electromagnetic, thermal and electromechanical processes that underlie their efficient, reliable and safe operation. For the effective design of these transformers it is necessary to calculate and investigate the distribution magnetic fields in the complex topology and evaluate the effects of various design parameters on the field distribution. This paper investigates the effects of geometric and electromagnetic parameters on the saturation level in the toroidal core that ultimately determines the overall size of such transformers.

2. Investigation of Various Designs of Variable Transformers

As mentioned above this paper investigates commercial variable transformers used as voltage stabilisers in order to quantify, mainly the effects of design parameters on the saturation level in the core. The main modelling activities involve the computation of

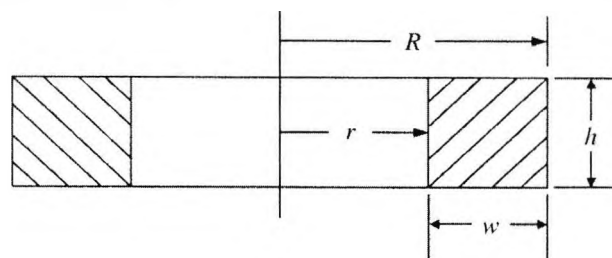


Fig. 3. Longitudinal section of the toroidal core showing the main geometric parameters investigated.

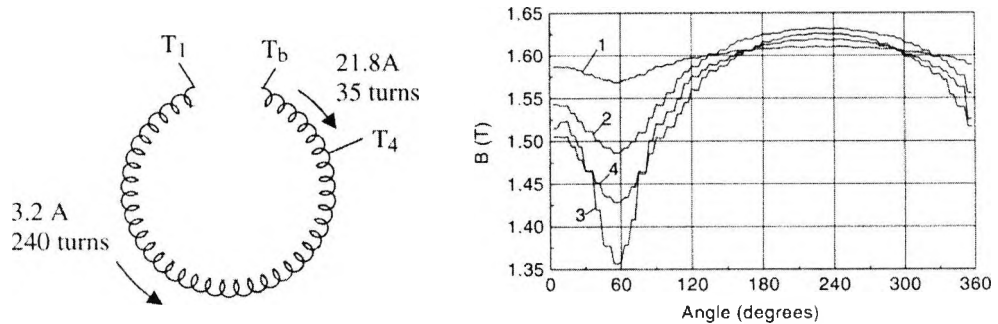


Fig. 4. Variation of magnitude and distribution of flux density in the toroidal core (right) for various changes in geometric parameters h and w shown in Fig. 3 (outer radius $R = \text{const.}$). The graphs show the flux density distribution along a circular contour near the inner radius in the cross section on the xy -plane at the mid-height of the core for brush (T_b) and tap positions (T_1 , T_4) shown on the left. 1 – initial core size, 2 – h reduced by 25%, 3 – w reduced by 25%, 4 – $h \times w$ reduced by 44%.

magnetic field distributions in such stabilisers. The aim is to investigate the magnitude and distribution of magnetic field in the toroidal core and minimise its size for the same level of saturation. This paper presents some of the results of such an investigation based on 3D modelling of variable transformers using finite the finite element method (FEM) [1], which numerically solves the appropriate non-linear Poisson's equation in 3D [2]. For this commercial finite element (FE) software packages Opera-3D, Tosca, and Elektra [3] were used on Sun workstations running under Unix. The FE modelling methodologies have been validated by comparing some of the modelling results with corresponding experimental data which showed good agreement and thus established confidence in subsequent modelling studies [4]. Fig. 2 shows an example of typical FE models used. In order to minimise the size of the toroidal core the geometric parameters shown in Fig. 3 have been investigated. The optimisation problem here is to find the minimum core size that would ensure an acceptable level of core saturation for various operational regimes of voltage stabilisers given by, for example, brush and tap positions. For this, several other factors are also needed to be taken into account in relation to the geometric parameters shown in Fig. 3. The inner and outer radii r and R determine the core width w and the overall 'foot print' of the transformer. The outer radius R also determines the total length of the brush track and hence the total number of winding turns N that can be placed side by side on the track for a given conductor size used for the transformer winding. This means that the value of R cannot be taken less than a given lower threshold since the number of winding turns N , constituting the brush track, directly determines the range and the resolution of the variability of voltage that can be achieved by a given transformer design. The lower threshold for the height of the core h is determined by the minimum surface area of the brush track that is needed to accommodate an adequate number and size of segmented brushes that traverse the track.

3. Some Results and Discussions

Figs. 4-9 show some of the results of design investigation of commercial voltage stabilisers discussed earlier. Figures 4 and 5 show the combined effects of the variation of geometric parameters of the core and the operational regimes determined by various brush (T_b) and tap positions (T_1 and T_4). As can be seen, these factors have significant effects on the magnetic field distribution and local and overall saturation level in the core. Although these graphs

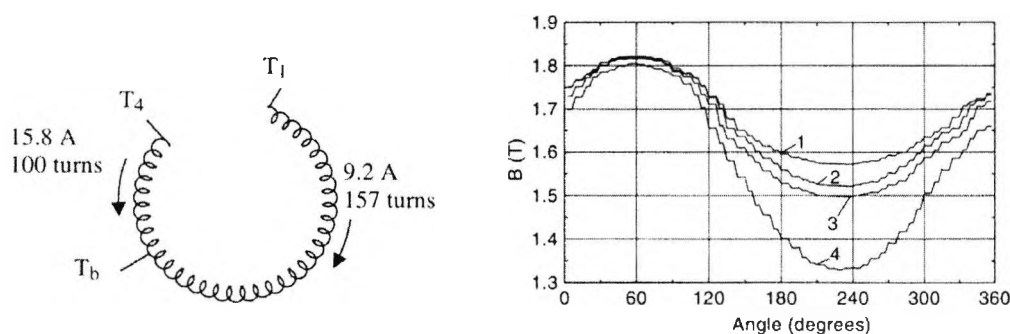


Fig. 5. Variation of magnitude and distribution of flux density in the toroidal core (right) for various changes in geometric parameters h and w shown in Fig. 3 (outer radius $R = \text{const.}$). The graphs show the flux density distribution along a circular contour near the inner radius in the cross section on the xy -plane at the mid-height of the core for brush (T_b) and tap positions (T_1, T_4) shown on the left. 1 – initial core size, 2 – h reduced by 25%, 3 – w reduced by 25%, 4 – $h \times w$ reduced by 44%.

represent the magnetic field distribution in the core along a closed contour near the inner radius of the core, further investigations suggest that the pattern of distribution remains the same over the entire section of the core. The 'dip' in the graphs shown in Figs. 4 and 5 correspond to brush or tap positions. It is clear from these graphs that the distribution of flux density inside the core is predominantly non-uniform and, for given brush and tap positions, the degree of this non-uniformity increases with the reduction in core size. By comparing the graphs 1 and 4 in these figures it can be seen that with the reduction in core size the overall saturation level in the core is reduced. However this does not seem to affect the maximum value of the flux density which is more localised in the second case (Fig. 5) than that in the first (Fig. 4). This means, although the maximum saturation level at localised areas inside the core is not largely affected by core size, the overall saturation level is reduced because of the redistribution of flux over the effective section of the core. This should lead to the reduction in core losses for various operational regimes of these voltage stabilisers.

Figs. 6 and 7 represent some of the simulation results that show the effects of brush (T_b) and

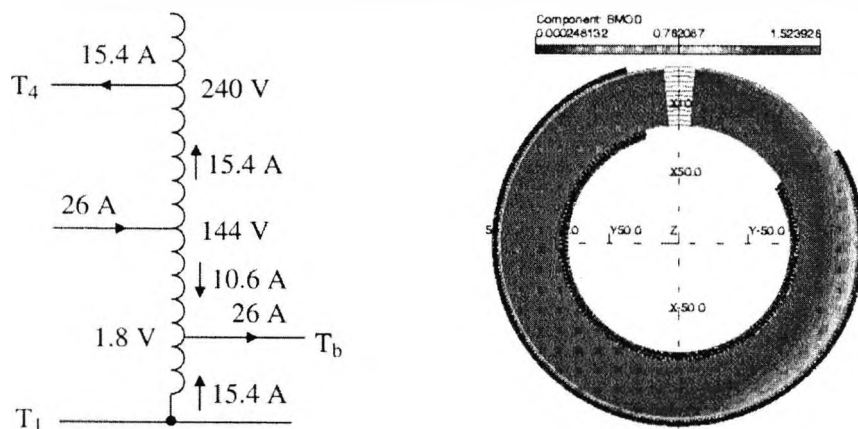


Fig. 6. Effects of operational regimes determined by brush (T_b) and tap positions (T_1, T_4) (shown on the left) on saturation level and distribution of core flux density (right) in one of the designs of commercial voltage stabilisers investigated. Total number of turns $N = 257$ and maximum flux density 1.52 T.

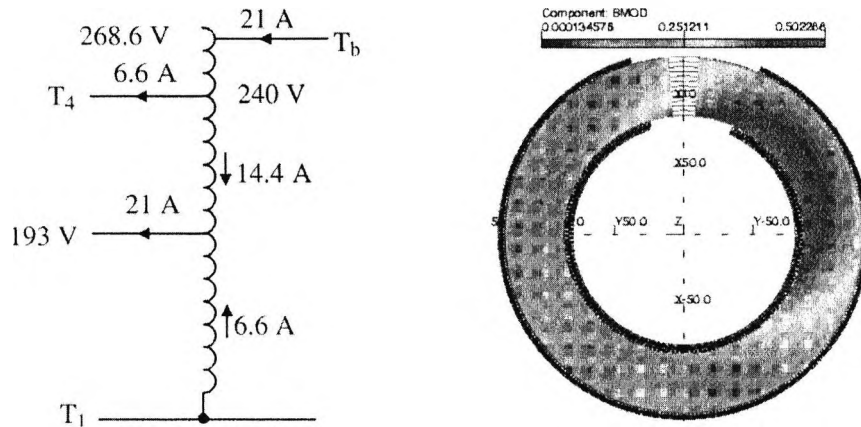


Fig. 7. Effects of operational regimes determined by brush (T_b) and tap positions (T_1 , T_4 at turn 257, etc.) shown on the left on saturation level and distribution of core flux density (right) in one of the designs of commercial voltage stabilisers investigated. Total number of turns $N=288$ and maximum flux density 0.5 T.

tap positions (T_1 and T_4) alone on the level of saturation and magnetic field distribution in the core. In both cases the geometric parameters of the core are kept constant. The schematics on the left in Figs. 6 and 7 represent two of the six operational regimes that were investigated for commercial variable transformers working as voltage stabilisers. The distribution of current in various sections of the winding, which is determined by brush (T_b) and tap positions (T_1 , T_4), also determines the distribution of magnetic flux in the core. Consequently, this determines the saturation level and distribution of flux density in the core. For example, comparison of flux density distributions shown on the right in Figs. 6 and 7 show that the particular brush and tap positions shown in Fig. 6 results in higher level of saturation (maximum flux density 1.52 T) and more uniform flux distribution in the core than that obtained from Fig. 7 which gives higher non-uniformity and lower level of saturation (maximum flux density 0.5 T).

The effects of core saturation and any eddy currents in the top plate on the distribution and magnitude of magnetic field in air above the core are shown in Figs. 8 and 9. Since this field is dependent upon the level of saturation in the core, it is ultimately dependent upon the size of the core and various operational regimes of the stabilisers investigated. This 'stray' fields need to be minimised in order to reduce losses due to possible circulating currents that may be induced in various constructive parts around the core.

4. Conclusions

It has been shown that the 3D FE modelling is an effective approach for design investigation of commercial voltage stabilisers. Some of the results of such an investigation presented in this paper show that the magnitude and distribution of magnetic field in the core are very much dependent upon the geometric parameters and operational regimes (given by brush and tap positions) of such stabilisers. It has been shown that this distribution is predominantly non-uniform in nature. In addition, it is clear from the results presented that for the specific designs of the voltage stabiliser investigated in this paper the core size may be reduced without increasing the saturation level, which is attributed to the redistribution of magnetic

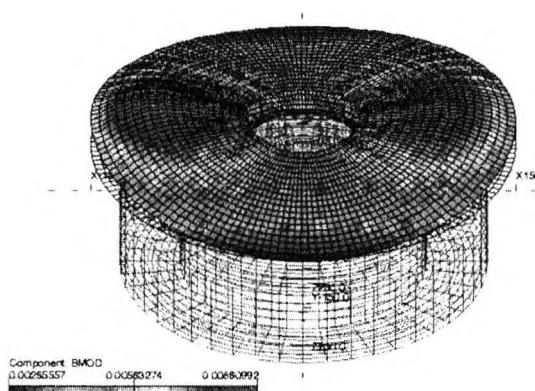


Fig. 8. Effects of core saturation and eddy currents in the top plate on magnetic field distribution in air above the core with the top plate. Total number of turns $N=296$, brush position at $\theta=180^\circ$, and maximum flux density 0.009 T.

flux in the core. The level of saturation in the core and various operational regimes also affect the magnitude and distribution of magnetic field in the air above the core.

5. Acknowledgements

The authors would like to thank Messrs. William Lyons and Derek Maule at Claude Lyons Limited, UK for active collaboration over the years and for providing us with experimental facilities. The authors would also like to thank Messrs. Nigel Lee (formerly at Claude

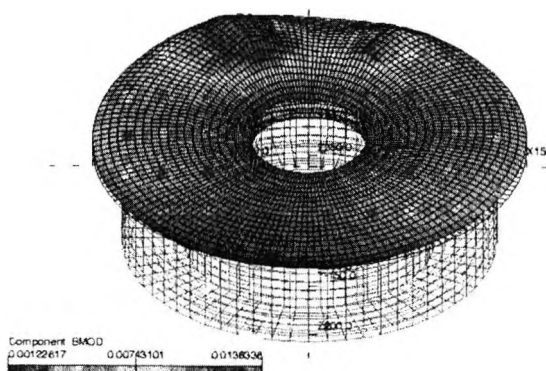


Fig. 9. Effects of core saturation and eddy currents in the top plate on magnetic field distribution in air above the core without the top plate. Total number of turns $N=258$, brush position at $\theta=240^\circ$, maximum flux density 0.014 T.

Lyons) and Niall Gray at Claude Lyons for many useful discussions and assistance with the experimental work.

References

- [1] Binns K J, Lawrenson P J, and Trowbridge CW 1992 *The Analytical and Numerical Solution of Electric and Magnetic Fields*, 3rd ed. (Chichester: John Wiley & Sons).
- [2] Ramo S, Whinnery J R and Duzer T V 1993 *Fields and Waves in Communication Electronics*, 3rd edition (Chichester, John Wiley & Sons).
- [3] Opera-3d Version 2.609 1997, Tosca Version 6.6 1996, and Elektra Version 2.6 1996, Vector Fields Limited, Oxford, UK.
- [4] Khan S H, El-Shawish J M, Finkelstein L, and Grattan K T V 2000 *Proceedings of ICEM 2000 Conference*, Helsinki, Finland 262-266.



Helsinki University of
Technology
Espoo Finland

Investigation of Variable Transformers by 3D Field Modelling – Comparison of Modelling and Experimental Results

S. H. Khan, J. M. El-Shawish, L. Finkelstein, and
K. T. V. Grattan

Measurement and Instrumentation Centre
Department of Electrical, Electronic and Information Engineering
City University, Northampton Square, London EC1V 0HB, UK
Telephone +44 (02)0 7477 8183
Fax +44 (02)0 7477 8568
Email: S.H.Khan@city.ac.uk

ABSTRACT

This paper investigates commercial variable transformers by 3D finite element (FE) field modelling. FE modelling methodologies have been developed for design, investigation, and performance evaluation of variable transformers used as voltage stabilisers. Experimental studies have been carried out to validate the developed modelling methodologies. It presents some of the modelling results and compares them with corresponding experimental data showing good agreement. This validates the modelling methodologies and establishes confidence on the developed FE models.

Keywords: Variable transformers, modelling and simulation, field modelling, finite element modelling.

1 INTRODUCTION

Despite the recent introduction of solid-state devices variable transformers are still widely used as voltage regulators in many applications. A variable transformer is basically an adjustable autotransformer with a sliding tapping which supplies completely variable voltage over a required range. They differ from conventional transformers in that there is an electrical contact between the primary and secondary windings. Compared to conventional transformers, autotransformers may have lower leakage reactance and losses, smaller magnetising current, and in some cases lower cost. They serve as essential subsystems in many systems

where the safety and reliability of the system as a whole is critically dependent upon their long-term safe, robust and reliable operation.

Although conventional transformers are well covered in literature [1, 2], very few studies have been carried out so far that concern autotransformers and, to our knowledge none concerning modelling, design and validation of variable transformers. Most of the published literature in this area concerns analytical and experimental studies of large and specialised tapped autotransformers [3-8]. In [3] the transmission-line model is used to study specialised autotransformers widely used for impedance matching of two single-ended circuits, and in [4] the nonlinear electrical circuit model is used to analyse short-circuit transients in large power autotransformers. Attempts have been made in [5] to take into account the effects of tertiary winding parameters and in [6] the effects of higher harmonics on autotransformer performance using analytical techniques are considered. Extensive experimental studies are carried out in [7, 8] to investigate and understand the mechanisms of mechanical and thermal effects of short-circuit faults in large power autotransformers. A major deficiency is that none of the work concerns variable transformers and hardly addresses the critical design issues mentioned below in relation to them. The analytical techniques used are unsuitable for tackling the complicated nonlinear problems involved. Although experimental techniques are important, their use is extremely expensive, very time consuming and

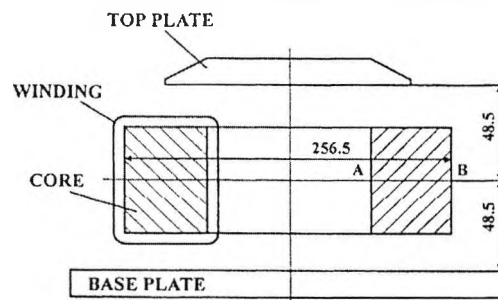


Fig. 1. Simplified longitudinal section of a variable transformer (e.g. type TS 1225) showing its main constructive elements (dimensions in mm, not drawn to scale).

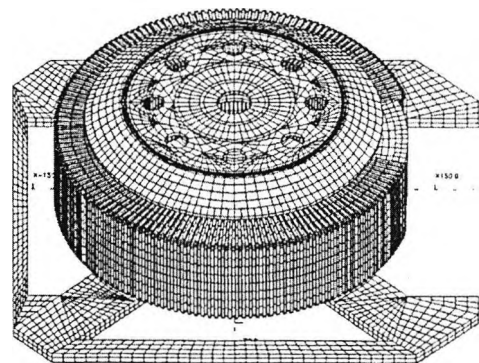


Fig. 2. Typical 3D finite element model of the TS 1225 commercial variable transformer under investigation.

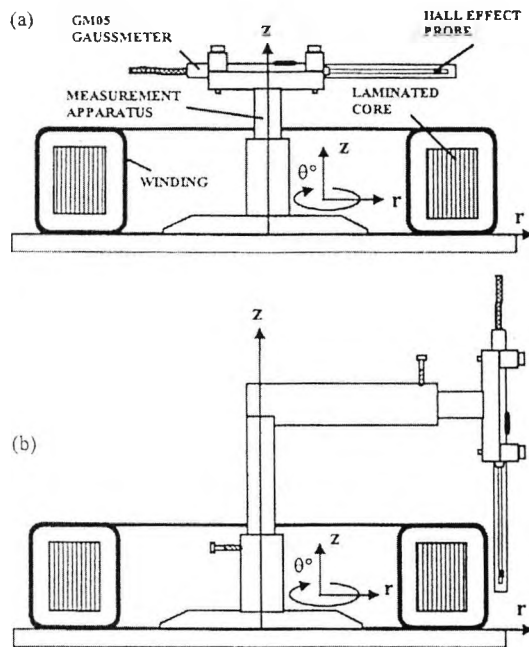


Fig. 3. Schematic diagrams showing the arrangement of experimental apparatus for the measurement of magnetic field (a) over and (b) around the toroidal core of the transformer shown in Fig. 1.

thus best used for the validation of initial simulation results. This paper investigates commercial variable transformers experimentally and by 3D FE modelling. This is necessitated by the fact that although variable transformers are generally simple and robust electrical devices, they rely on complex electromagnetic, thermal and electromechanical processes that underlie their efficient, reliable and safe operation. These interrelated processes need to be understood and quantified in order to be able to design variable transformers that would ensure their long-term safe and reliable operation. This can only be done effectively and efficiently by mathematical modelling which will help understand and quantify the complex processes in variable transformers and eliminate various undesirable effects associated with them.

2 THE MAIN CONSTRUCTIVE FEATURES OF THE VARIABLE TRANSFORMER

Fig. 1 shows the simplified longitudinal section of one of the designs (e.g. type TS 1225) of the commercial variable transformers under investigation. They are normally used as commercial voltage stabilisers. It consists of a single-layer toroidal winding tightly and closely wound on the toroidal core. The core is made of spirally wound grain-oriented silicon steel. The winding turns lie side by side on the outer surface but overlap on the inner surface because of the significant difference in circumferential lengths of the inner and outer surface of the core, especially for large transformers. The output voltage is varied by rotating the aluminium top plate which holds one or multiple segmented brushes (attached to the brush gear not shown in Fig. 1) that traverse the winding turns on the outer surface of the core. The brush track, which acts as the commutator, is made by stripping off insulation from the outer surface of each of the

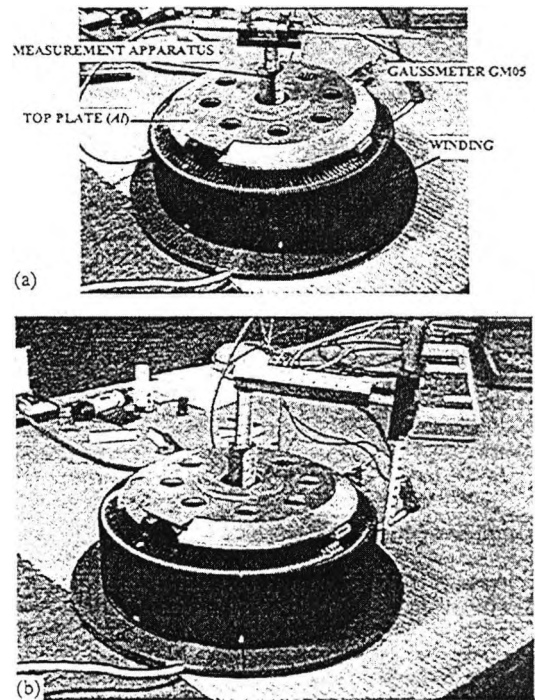


Fig. 4. Photographs showing the arrangement of experimental apparatus corresponding to the diagrams shown in Figs. 3(a), (b) respectively (brush gear is not shown).

winding turns. In large variable transformers the commutator surface is coated with gold to increase the reliability and effectiveness of commutation. The segmented brushes made of electrographite are always in contact with the commutator and overlap one or more turns and continuously tap off the desired fraction of the winding output voltage.

3 FINITE ELEMENT MODELLING OF VARIABLE TRANSFORMERS

The 3D finite element (FE) modelling of variable transformers is mainly based on the mathematical modelling and computation of magnetic field distributions in the 3D problem domain $\Omega(r, \theta, z)$ by solving appropriate field equations. This leads, in general, to the solution of the following nonlinear Poisson's equation in terms of magnetic vector potential A and current density J [9-11]:

$$\nabla \times \frac{1}{\mu} \nabla \times A = J \text{ in } \Omega(r, \theta, z) \quad (1)$$

In the conducting sub-domains of Ω where eddy currents can flow (e.g. A top and base plates, iron core, etc.) the current density

$$J = J_e + J_s = -\sigma \left(\frac{\partial A}{\partial t} + \nabla V \right) \quad (2)$$

consists of the source current density J_s and eddy current density J_e . In Eq. (2) V is the electric scalar potential. Considering this and the necessary current continuity

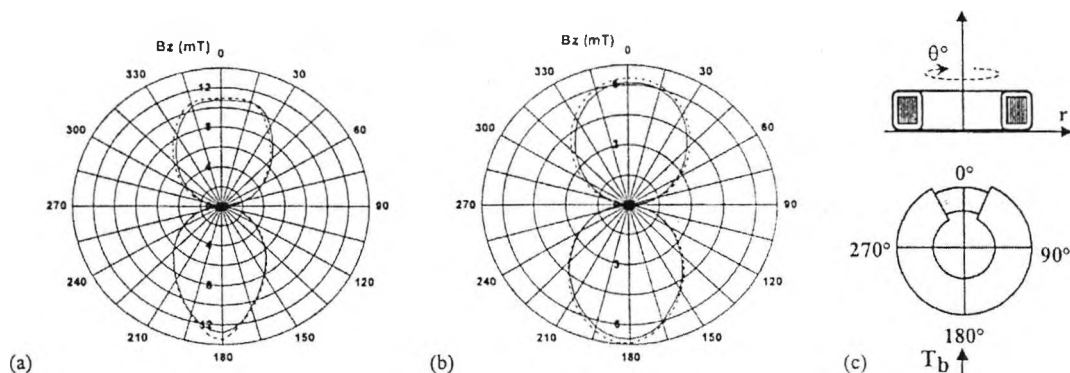


Fig. 5. Validation of FE modelling: comparison of flux density values obtained from modelling (broken lines) with corresponding experimental data (solid lines) measured in air over the toroidal core (without top and bottom plates) shown schematically on the right (c); (a) $z = 91$ mm, (b) $z = 117$ mm. Other parameters: $r = 87$ mm, $I_1 = 12.04$ A, $I_2 = 12.11$ A, total number of turns $N = 296$, taps T_1 at turn no. 1, T_2 at turn no. 296, T_3 the brush position (T_b) at turn no. 149 ($\theta = 180^\circ$).

condition $\nabla \cdot J = 0$, the vector potential formulation ($A-V$) of fields in the conducting sub-domains are given by the following two equations [11]:

$$\nabla \times \frac{1}{\mu} \nabla \times A + \sigma \left(\frac{\partial A}{\partial t} + \nabla V \right) = 0 \quad (3)$$

$$\nabla \cdot \sigma \left(\frac{\partial A}{\partial t} + \nabla V \right) = 0 \quad (4)$$

Since Eq. (4) is essentially the result of taking the divergence of Eq. (3), they are not independent. However, the uniqueness of their solutions is ensured by explicitly applying Coulomb gauge condition $\nabla \cdot A = 0$ to these coupled equations (together with the condition $A \cdot n = 0$ imposed on the external boundaries to conductors). This results in the following governing equations

$$\nabla \times \frac{1}{\mu} \nabla \times A - \nabla \frac{1}{\mu} \nabla \cdot A + \sigma \left(\frac{\partial A}{\partial t} + \nabla V \right) = 0 \quad (5)$$

$$\nabla \cdot \sigma \left(\frac{\partial A}{\partial t} + \nabla V \right) = 0 \quad (6)$$

which describe the magnetic fields in the conducting sub-domains of the 3D problem domain Ω . This vector potential formulation of fields is directly combined with the reduced (ϕ) and total (ψ , $\nabla \cdot \mu \nabla \psi = 0$) magnetic scalar potential formulations of fields in the non-conducting sub-domains [9]. To exactly couple these field descriptions the equality of the normal flux and tangential field intensity interface conditions ($B_{n1} = B_{n2}$, $H_{t1} = H_{t2}$) are also imposed.

Under appropriate boundary conditions on external boundaries of the problem domain, the solution of the field equation was obtained by numerical FE technique [12]. For this various 3D FE models of the commercial variable transformer shown in Figs. 1 and 4 were developed using the commercial FE package OPERA-3d [13]. A detail description of the systematic model-building strategy used for this purpose can be found in [14]. Fig. 2 shows such a FE model. These models

were used to obtain the steady-state and transient solutions of field equations by which the magnetic field distributions in the 3D problem domain of the transformer were obtained. Such simulations allow the investigation of magnetic field distribution in and around the transformer core taking into account saturation and eddy-current effects for various design parameters (e.g. geometric, material and electrical) and brush and tap positions under no-load and full-load operational conditions. The modelling results may be used to calculate the copper and iron losses in the transformer which include hysteresis, eddy-current and circulating-current losses primarily in the transformer core and in any short-circuited winding turns (caused, for example by insulation damage and brush position), and in other constructive elements (top and base plates, brush gear, etc.). In addition, such modelling results are essential in the investigation of the nature and magnitude of any magnetic forces acting on the winding for various tap and brush positions. This forces may cause the tightly wound turns to vibrate (at power and at higher frequencies in the presence of harmonics) which may result in insulation damage and ultimately lead to shorted turns. The FE models may also be used to study and quantify the effects of harmonics of primary and secondary (load) currents on magnetic field distribution and losses in the transformer. The validation of modelling results against experimental data is of fundamental importance in the applicability and possible refinement of FE modelling methodologies described above.

4 EXPERIMENTAL INVESTIGATION OF VARIABLE TRANSFORMERS

Experimental investigations of one of the designs of commercial variable transformers TS 1225 were carried out to validate and refine the FE models developed above. The main aim was to measure the magnetic field distribution in air around the toroidal core for various operational regimes

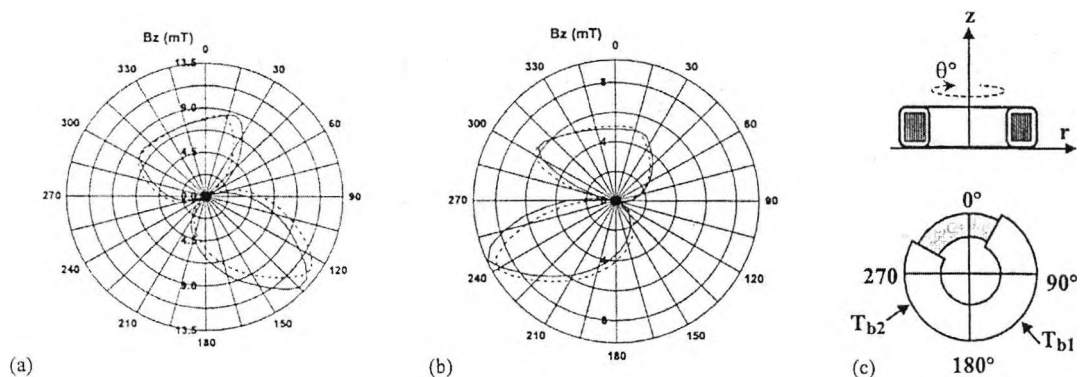


Fig. 6. Validation of FE modelling: comparison of flux density values obtained from modelling (broken lines) with corresponding experimental data (solid lines) measured in air over the toroidal core (without top and bottom plates) shown schematically on the right (c); (a) $I_1 = 15.73$ A, $I_2 = 9.1$ A, tap T_3 the brush position (T_{b1}) at turn no. 100 ($\theta = 126^\circ$), (b) $I_1 = 4.66$ A, $I_2 = 20.34$ A, tap T_3 the brush position (T_{b2}) at turn no. 207 ($\theta = 245^\circ$). Other parameters: $r = 87$ mm, $z = 117$ mm, total number of turns $N = 257$.

and configurations of the transformer. For this, a number of different experimental models of the TS 1225 variable transformer were used. The experimental apparatus shown in Figs. 3 and 4 were specially designed to hold the Gaussmeter (GM05) and fix the position of the Hall probe in the cylindrical system of coordinates r, θ, z . It allowed the Hall probe to be placed at various positions of interest in the 3D space around the core easily and accurately. Some of the technical characteristics of the Gaussmeter used are as follows: accuracy (at 20°C) better than $\pm 1\%$ (d.c.), reproducibility better than 0.5%, temperature coefficient $\pm 0.1\%$ of reading/ $^\circ\text{C}$ including probe.

5 SOME OF THE RESULTS OF FE MODELLING AND DISCUSSIONS

5.1 Comparison of modelling and experimental results

Figs. 5-7 show the comparison of some of the modelling results with those obtained by experiments described above. Overall, the modelling results are in good agreement with experimental data which validates the adopted modelling strategies. The differences between these results shown,

especially in Fig. 6 are mainly attributable to both modelling and experimental errors which can only be minimised but never completely eliminated. These include discretisation errors due to finite number and size of volume elements used in FE modelling, various measurement errors associated with the Gaussmeter used, its precise positioning, some variations of input currents over the period of experiments, etc. In addition to validating the FE models, the experimental results were also used to refine these models for more complicated simulation studies. It is clear from Figs. 5-7 that the magnitude and distribution of magnetic fields over the transformer core vary considerably depending upon the tap and brush positions. This affects the eddy currents and, possibly any circulating currents induced in the top and base plates of the transformer.

5.2 Eddy-current effects

Fig. 8 shows the contours of eddy currents induced in the top plate by time varying magnetic fields produced by currents in the toroidal winding. It qualitatively demonstrates the eddy current effects of the leakage flux from the core. However, comparison of Figs. 5(b) and 7 shows that these eddy currents do not appear to have much effect on the

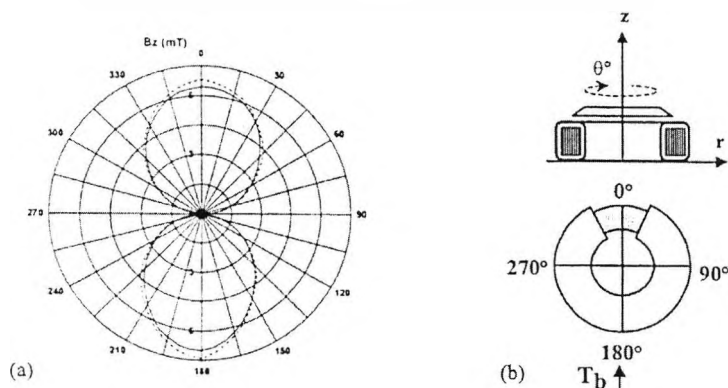


Fig. 7. Validation of FE modelling: comparison of flux density values obtained from modelling (broken lines) with corresponding experimental data (solid lines) measured in air over the toroidal core (with the aluminium top plate) shown schematically on the right (b); (a) $z = 117$ mm, $r = 87$ mm, $I_1 = 12.04$ A, $I_2 = 12.11$ A, total number of turns $N = 296$, taps T_1 at turn no. 1, T_5 at turn no. 296, T_3 the brush position (T_b) at turn no. 149 ($\theta = 180^\circ$).

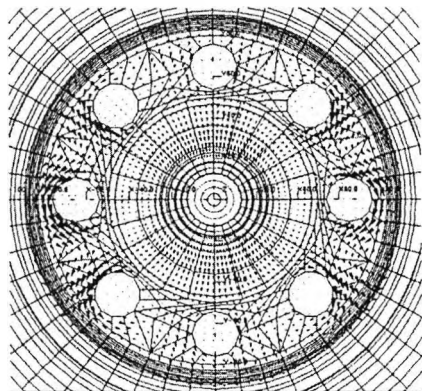


Fig. 8. Contours showing the eddy currents induced in the aluminium top plate viewed from the top (section through the middle of the plate thickness); the position of the top plate and other parameters correspond to those shown in Fig. 7.

distribution and magnitude of magnetic fields over the transformer core. This is most likely owing to the relatively small thickness of the top plate (about 3-4 mm) compared to the skin depth of aluminium at the nominal operating frequency of the transformer (50 Hz). This situation is, however likely to change at higher frequencies in the presence of harmonics and with the increased saturation of the transformer core. Further modelling investigations are needed to quantify in detail the electromagnetic and thermal effects of eddy currents both in the nonmagnetic conducting parts of the transformer and in its conducting magnetic core.

6 CONCLUSIONS

Modelling methodologies have been developed for 3D FE modelling of commercial variable transformers. Experimental investigations were carried out to measure the magnetic field in air around the core for various operational regimes and configurations of the TS 1225 transformers. Some of the modelling results have been validated against experimental data showing good agreement. Simulation studies are being carried out at present to understand and quantify the complex processes in variable transformers and to eliminate various electromagnetic and thermal effects that are detrimental to their performance. This will undoubtedly lead to better design in terms of geometric, material and other physical parameters that would deliver better performance, increased reliability and longer life.

7 ACKNOWLEDGEMENTS

The authors would like to thank Messrs. William Lyons and Derek Maule at Claude Lyons Limited, UK for active collaboration over the years and for providing us with experimental facilities. The authors would also like to thank Mr. Nigel Lee, also at Claude Lyons for many useful discussions and assistance with the experimental work.

REFERENCES

[1] L. F. BLUME, G. BOYAJIAN, A. CAMILLI et al, *Transformer Engineering: A Treatise on the Theory,*

Operation and Application of Transformers, Chapman & Hall Ltd., 1951.

- [2] P. SILVESTER and KONRAD, "Analysis of transformer leakage phenomena by higher order finite elements". *IEEE Trans. PAS*, vol. 6, 1973, pp. 1843-1855.
- [3] K. B. NICLAS, R. R. PEREIRA and A. P. CHANG, "Transmission lines accurately model autotransformers". *Microwave & RF*, vol. 31, no. 11, 1992, pp. 72-76.
- [4] C. M. ARTURI, "Model of a highly saturated 3-phase autotransformer with tertiary winding and 5-limb core and analysis of a time-varying short-circuit transient". *European Trans. Elec. Power Engineering*, vol. 4, no. 6, 1994, pp. 513-524.
- [5] I. V. YAKIMETS and V. G. NAROVLYANSKII, "Autotransformer with a voltage-stabilised tertiary winding". *Electrical Technology*, no. 1, 1995, pp. 21-30.
- [6] J. P. G. ABREU, C. A. M. GUIMARAES and G. PAULILLO, "A proposal for a power converter autotransformer". *Proc. IEEE Int. Electrical Machines and Drives Conference*, Milwaukee, USA, 1997, pp. 6.1-6.4.
- [7] T. ARAGONA, A. BABARE, G. DOGLIO et al, "The importance of short-circuit tests for the large rating autotransformers". *Energia Elettrica*, vol. 74, no. 5, 1997, pp. 290-310.
- [8] J-P MARTIN, J WENDLING and Y. TOURNIER, "Specifics of the short-circuit behaviour of concentrically-wound transformers and autotransformers". *IEEE trans. Power App. and Sys.*, vol. 99, no. 6, 1980, pp. 2069-2077.
- [9] K. J. BINNS, P. J. LAWRENSON and C. W. TROWBRIDGE, *The Analytical and Numerical Solution of Electric and Magnetic Fields*. Chichester, John Wiley & Sons, 1992.
- [10] S. RAMO, J. R. WHINNERY and T. V. DUZER, *Fields and Waves in Communication Electronics*. 3rd edition, Chichester, John Wiley & Sons, 1993.
- [11] E. E. KRIEZIS, T. D. TSIBOUKIS, S. M. PANAS and A. T. TEGOPOULOS, "Eddy currents: theory and applications". *Proc. IEEE*, vol. 80, no. 10, 1992, pp. 1559-1589.
- [12] O. C. ZIENKIEWICZ and R. I. TAYLOR, *The Finite Element Method*. Maidenhead, McGraw-Hill Inc., 1991.
- [13] OPERA-3d Version 2.609 1997, TOSCA Version 6.6 1996, and ELEKTRA Version 2.6 1996, Vector Fields Limited, Oxford, UK.
- [14] S. H. KHAN, J. M. EL-SHAWISH, K. T. V. GRATTAN and L. FINKELSTEIN, "Finite element modelling of variable transformers used for voltage regulation and control". *Sensors and Their Applications VIII*, ed. A. T. Augousti and N. M. White, Bristol, Institute of Physics Publishing, 1997, pp. 41-46.

Finite Element Modeling of Saturation and Eddy Current Effects in Commercial Variable Transformers

S. H. Khan, *Member, IEEE*, J. M. El-Shawish, L. Finkelstein, and K. T. V. Grattan

Abstract—This paper presents the methodologies and some of the results of performance modeling of variable transformers. This is done by finite element (FE) modeling and computation of 3D magnetic field distribution in commercial variable transformers used as voltage stabilizers. The results are presented in terms of the effects of core saturation and eddy currents in the top plate on magnetic field distribution in and around the transformer core. It is shown that the magnitude and distribution of this field is affected by operational regimes characterized by brush and tap positions which determine the current distribution in the winding.

Index Terms—Computational magnetics, finite element modeling, numerical methods, variable transformers.

I. INTRODUCTION

VARIABLE transformers are basically adjustable autotransformers with sliding tapping which supply completely variable voltage over a required range. Unlike conventional transformers, variable transformers do not have any electrical contact between the primary and secondary windings. Despite the recent introduction of solid-state devices, variable transformers are still widely used in many applications for voltage regulation and control. However, although conventional transformers are well covered in literature, there are only few studies reported so far that cover autotransformers [1], [2] and, to our knowledge, none concerning the voltage stabilizers investigated in this paper.

Fig. 1 shows the simplified longitudinal section of the commercial variable transformer under investigation (type TS 1225). This type of variable transformers is normally used as either three-phase or single phase voltage stabilizers (with nominal parameters: 240 V/0-240 V, 0-275 V, 30 A, 7.2 kVA). The basic constructive elements include a single-layer helical winding tightly and closely wound on the toroidal core made of spirally wound grain-oriented silicon steel (such as Unisil 30M5 with electric conductivity $\sigma = 2.08 \times 10^6$ S/m and typical B-H curve shown in Fig. 2). The winding turns lie side by side on the outer surface but overlap on the inner surface because of the difference in circumferential lengths of the inner and outer surfaces of the core. The output voltage is varied by rotating the aluminum top plate which holds one or multiple segmented brushes (not shown in Fig. 1) that traverse the winding turns on the outer surface of the core. The brush track, which acts as the commutator, is made by stripping

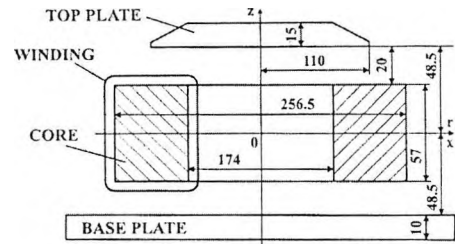


Fig. 1. Schematic diagram showing the simplified longitudinal section of the TS 1225 variable transformer investigated (dimensions in mm, not drawn to scale).

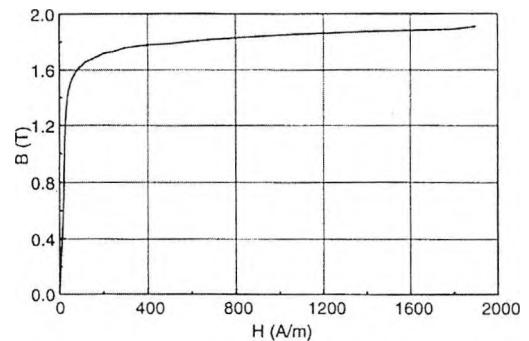


Fig. 2. Magnetization curve of Unisil 30M5 grain-oriented silicon steel used in TS 1225 transformer core.

off insulation from the outer surface of each of the winding turns. In large variable transformers, the commutator surface is coated with gold to increase the reliability and effectiveness of commutation. The brush is always in contact with the commutator and overlaps one or more turns and continuously taps off the desired fraction of the winding output voltage.

Despite the fact that variable transformers are generally simple and robust electrical devices, they rely on complex electromagnetic, thermal and electromechanical processes that underlie their efficient, reliable and safe operation. The simplistic analytical and time consuming experimental techniques used in [1] and [2] are deficient in tackling critical design issues associated with these interrelated processes. These processes need to be understood and quantified in order to be able to design variable transformers that would ensure their long-term safe and reliable operation. This can only be done effectively and efficiently by mathematical modeling and simulation.

Manuscript received October 31, 2000.

This work was conducted in collaboration with Claude Lyons Limited, UK.

The authors are with the Department of Electrical, Electronic and Information Engineering, City University, Northampton Square, London EC1V 0HB, UK (email: s.h.khan@city.ac.uk).

Publisher Item Identifier S 0018-9464(01)07184-9.

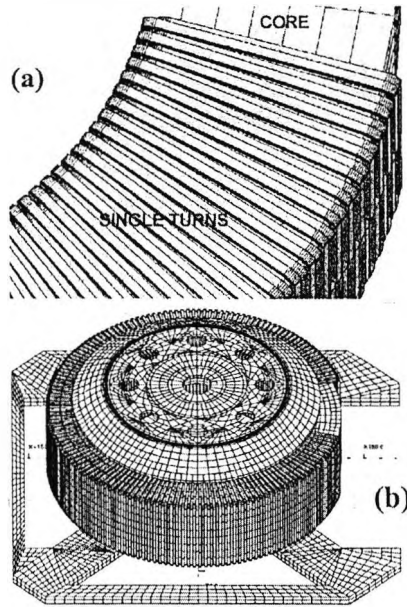


Fig. 3. Realization of 3D finite element models for variable transformers: (a) overlapping single turns replacing the continuous helical winding, (b) full 3D FE model of the TS 1225 commercial variable transformer under investigation.

This paper presents the results of such a 3D FE modeling study of variable transformers taking into account saturation nonlinearity of the core for various operational regimes and eddy current effects in the top plate.

II. FE MODELING OF VARIABLE TRANSFORMERS

A. Basic Field Equations

The 3D finite element (FE) modeling of variable transformers is mainly based on the mathematical modeling and computation of magnetic field distributions in the 3D problem domain $\Omega(x, y, z)$ by solving appropriate field equations. This leads, in general, to the solution of the following nonlinear Poisson's equation in terms of magnetic vector potential A and current density J [3], [4]:

$$\nabla \times \frac{1}{\mu} \nabla \times A = J \text{ in } \Omega(x, y, z). \quad (1)$$

Here the current density J consists of the source current density J_s and eddy current density J_c . Considering this and the necessary current continuity condition $\nabla \cdot J = 0$, and by explicitly applying Coulomb gauge condition $\nabla \cdot A = 0$, the vector potential formulation (A - V) of fields in the conducting sub-domains are given by the following governing equations:

$$\nabla \times \frac{1}{\mu} \nabla \times A + \sigma \left(\frac{\partial A}{\partial t} + \nabla V \right) = 0, \quad (2)$$

$$\nabla \cdot \sigma \left(\frac{\partial A}{\partial t} + \nabla V \right) = 0. \quad (3)$$

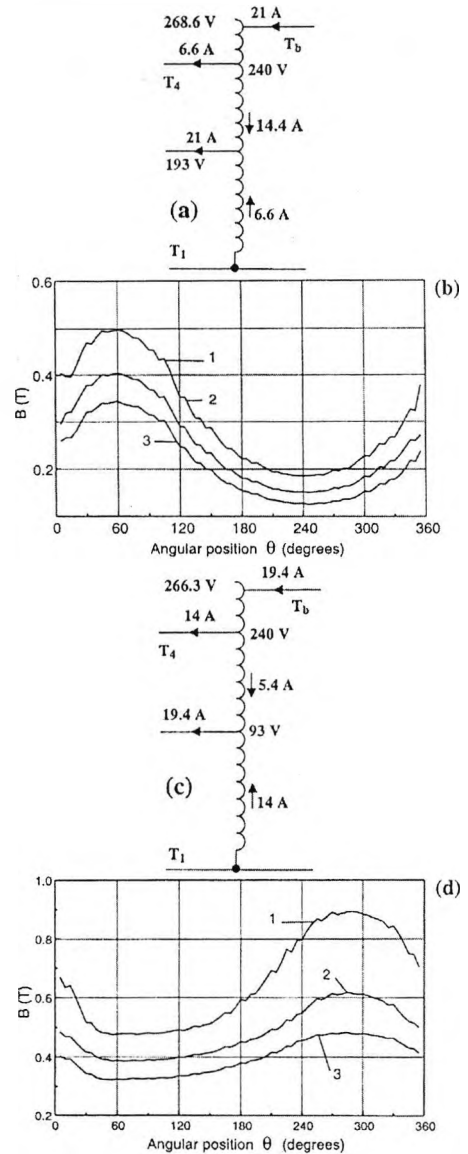


Fig. 4. Effects of operational regimes determined by brush (T_b) and tap positions (T_1, T_4 at turn 257, etc.) shown in (a) and (c) on the saturation level and distribution of core flux density in the TS 1225 variable transformer. The graphs in (b) and (d) show flux densities along three circular contours inside the core [near the inner (1) and outer (3) radii and in the middle (2) of the core] on xy -plane ($z = 0$, see Fig. 1).

This vector potential formulation of fields is directly combined with the reduced (ϕ) and total (ψ , $\nabla \cdot \mu \nabla \psi = 0$) magnetic scalar potential formulations of fields in the nonconducting sub-domains [3]. To exactly couple these field descriptions the equality of the normal flux and tangential field intensity

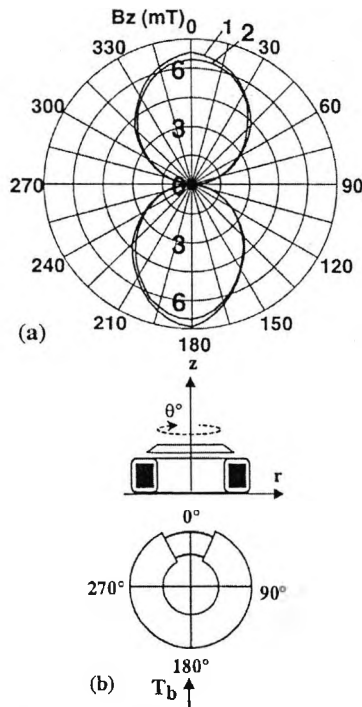


Fig. 5. Validation of FE modeling: comparison of flux density values (a) obtained by modeling (1) with corresponding experimental data (2) measured in air over the core (with the aluminum top plate) shown schematically on the right (b); $z = 117$ mm, $r = 87$ mm, $I_1 = 12.04$ A, $I_2 = 12.11$ A, total number of turns $N = 296$, taps T_1 at turn no. 1, T_5 at turn no. 296, T_3 the brush position (T_b) at turn no. 149 ($\theta = 180^\circ$).

interface conditions ($B_{n1} = B_{n2}$, $H_{\tau1} = H_{\tau2}$) are also imposed.

B. Realization of FE Models

Under appropriate boundary conditions, the above equations were solved by finite element method (FEM) using the commercial FE package Opera-3d [5] running on Sun workstations under Unix. For this, various 3D FE models like the one shown in Fig. 2 were developed. For all such models the continuous N -turn helical winding is replaced by N single-turn coils tightly and compactly wound around the toroidal core. This is justified given the closely wound helical winding and it simplifies the realization of FE models. In addition, these turns, although lie side by side on the outer surface of the core, overlap on its other surfaces owing to the difference in circumferential lengths between the inner and outer surfaces [Fig. 2(a)]. This complicates the realization of FE models. The typical FE model shown in Fig. 2(b) contains over 54 k 8-noded hexahedral elements with about 50 k nodes. The above models were used to obtain the steady-state and transient solutions of field equations by which the magnetic field distribution in the 3D problem domain $\Omega(x, y, z)$ of the transformer were obtained. Some of the modeling results were validated against corresponding experimental data obtained for

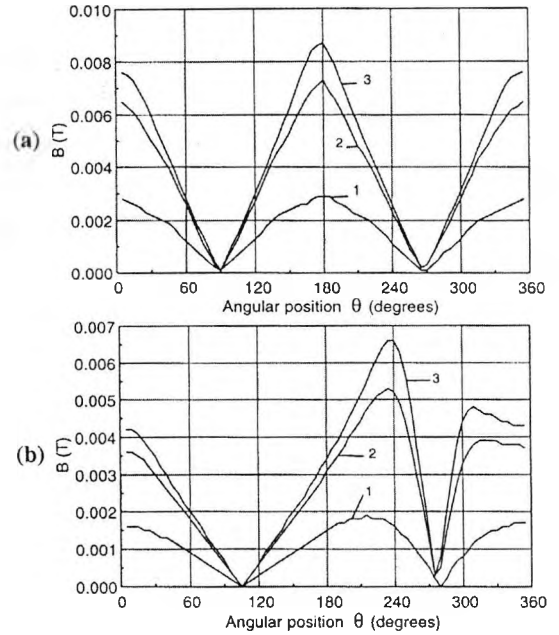


Fig. 6. Effects of core saturation and eddy currents in the top plate on magnetic field distribution in air above the core: (a) with top plate, $N = 296$, brush position at $\theta = 180^\circ$ [see Fig. 5(b)], (b) without top plate, $N = 258$, brush position at $\theta = 240^\circ$. The graphs show flux densities along three circular contours (with radius $r = 40, 80,$ and 110 mm) on xy -plane above the core ($z = 65.5$ mm).

various operational regimes and configurations of the TS 1225 variable transformer. The good agreement obtained [6] established confidence in the modeling methodologies adopted and helped refine subsequent FE models.

III. RESULTS AND DISCUSSIONS

Some of the modeling results are presented in Figs. 4-6. Fig. 4(a) and (c) show the schematics of two of the operational regimes of the TS 1225 variable transformer working as a stabilizer. The distribution of current in various sections of the winding, which is determined by brush (T_b) and tap positions (T_1, T_4 , etc.), also determines the distribution of magnetic flux in the core. Consequently, this also determines the saturation level in the core. For example, comparison of Fig. 4(b) and (d) shows that the particular brush and tap positions shown in Fig. 4(c) result in higher level of saturation and more uniform flux distribution in the core [Fig. 4(d)] than that obtained from Fig. 4(a) which gives higher nonuniformity and lower level of saturation [Fig. 4(b)]. These, together with eddy current effects in the top plate contribute to the distribution and magnitude of magnetic field in air around the core. This is evident from Fig. 6 which shows the distribution of flux density along three circular contours in air on xy -plane. It also shows that the peak flux density rotates with brush position T_b . Fig. 5 shows the comparison of modeling and experimental results for field distribution in air above the core. The good agreement

between these results validates the modeling methodologies used and establishes confidence in the results obtained. The stray magnetic field in air needs to be minimized in order to reduce losses due to possible circulating currents that may be induced in various constructive parts around the core. Modeling and computation of magnetic field distribution in air is also important in the investigation of the nature and magnitude of any magnetic forces acting on the winding turns for various tap and brush positions. This forces may cause the tightly wound turns to vibrate (at power and at higher frequencies in the presence of harmonics) which may result in insulation damage and ultimately lead to short-circuited winding turns.

IV. CONCLUSIONS

The effects of eddy currents and saturation on magnetic field distribution in and around the toroidal core of commercial variable transformers have been presented. It has been shown that this field distribution is dependent upon their operational regimes characterized by brush and tap positions which determine the current distribution in the winding. The FE models and the modeling methodologies developed are now being used for CAD and performance modeling of variable transformers for various design parameters (e.g., geometric, material and electrical) under no-load and full-load operational regimes. The FE models are also being used to calculate the copper and iron losses in variable transformers which may include eddy-current, hysteresis, and circulating-current losses

primarily in the transformer core and in any shorted winding turns.

ACKNOWLEDGMENT

The authors would like to thank W. Lyons and D. Maule at Claude Lyons Limited, UK for active collaboration over the years and for providing us with experimental facilities. They would also like to thank N. Lee and N. Gray at Claude Lyons for many useful discussions and assistance with the experimental work.

REFERENCES

- [1] J. P. G. Abreu, C. A. M. Guimaraes, and G. Paulillo, "A proposal for a power converter autotransformer," in *Proc. IEEE Int. Electrical Machines and Drives Conference*, Milwaukee, USA, 1997, pp. 6.1-6.4.
- [2] J.-P. Martin, J. Wendling, and Y. Tournier, "Specificities of the short-circuit behavior of concentrically-wound transformers and autotransformers," *IEEE Trans. Power App. and Sys.*, vol. 99, pp. 2069-2077, 1980.
- [3] K. J. Binns, P. J. Lawrenson, and C. W. Trowbridge, *The Analytical and Numerical Solution of Electric and Magnetic Fields*, 3 ed. Chichester: John Wiley & Sons, 1992.
- [4] S. Ramo, J. R. Whinnery, and T. V. Duzer, *Fields and Waves in Communication Electronics*, 3 ed. Chichester: John Wiley & Sons, 1993.
- [5] "Opera-3d Version 2.609 1997," Vector Fields Limited, Oxford, UK.
- [6] S. H. Khan, J. M. El-Shawish, L. Finkelstein, and K. T. V. Grattan, "Investigation of variable transformers by 3D field modeling—comparison of modeling and experimental results," in *Proc. ICEM 2000 Conference*, Helsinki, Finland, 2000, pp. 262-266.
- [7] "Tosca Version 6.6 1996," Vector Fields Limited, Oxford, UK.
- [8] "Elektra Version 2.6 1996," Vector Fields Limited, Oxford, UK.